The Upper Zone of the Bushveld Complex, South Africa: Parental Magma and Crystallization Processes

Von der Naturwissenschaftlichen Fakultät der

Gottfried Wilhelm Leibniz Universität Hannover

zur Erlangung des Grades

Doktor der Naturwissenschaften (Dr. rer. nat.)

genehmigte Dissertation
von

Lennart Alexander Fischer, M. Sc.

2018

Acknowledgments

Abstract

The Bushveld Complex in South Africa is the largest layered intrusion on Earth. Its upper part is known for huge resources of iron, titanium, vanadium and phosphorus. Associated with the layered character of the rocks, these economically valuable elements are enriched at certain levels of the intrusion. Thus it is important to understand the formation processes of those layers. Using samples from the Bierkraal drill cores, representing the entire Upper and Upper Main Zone in the Western Limb, this thesis gives detailed insights into magmatic processes and the parental magma as well as the prevailing conditions forming the Upper and Upper Main Zone of the Bushveld Complex.

A detailed study of modal proportions of the Bierkraal drill cores, contributed to a better understanding of the top part of the intrusion. The observed compositional cyclicity of the Upper and Upper Main Zone was recently explained by several magma injections with a plagioclase-laden magma. Anorthosite layers are produced by crystal settling of the transported plagioclase crystals and magnetitite layers crystallized from a hybrid melt, produced by mixing of resident and injected magma. However, further discussion of the prevailing magma conditions affecting the mineral compositions as well as detailed description of the sub-magmatic system is missing.

In this study, the investigation of melt inclusions in apatite from the Upper Zone showed a compositional range from Fe-rich to Si-rich liquids best explained by silicate liquid immiscibility. During late-stage magmatic evolution the liquid line of descent of the Upper Zone reaches the two-liquid field and immiscible melts start to segregate. The continuous range of melt inclusion compositions observed in this study is the result of cooling. Thus, the liquid evolves along the binodal of the two-liquid field, producing more and more contrasting compositions. The dense, low-viscous, Fe-rich liquid percolates downwards and the cumulates from this Fe- and P-rich immiscible melt form the nelsonite layers observed in the Upper Zone.

Trace-element distribution in titanomagnetite and clinopyroxene as well as major-element composition of clinopyroxene revealed two major compositional shifts towards more evolved signatures within the Upper Zone stratigraphy. These distinct changes in mineral composition are in correlation with bulk-rock vanadium concentrations. They can be explained by the injection of a more evolved magma. Compared to previously proposed cyclical shifts incomposition, these two events are much more pronounced, arguing against a continuously evolving staging chamber. In fact, this supports the hypothesis of a sub-compartmentalized Bushveld staging chamber as a source for the magma injections. Prevailing oxygen fugacity (fO_2) conditions in the Upper Zone were estimated using the V partitioning between titanomagnetite and clinopyroxene. The results show that fO_2 variations are minor in the Upper Zone and are approximately around FMQ - 2, which is 1.5 - 2 log units lower than previously assumed.

To discuss potential parental magmas of the Upper and Upper Main Zone, crystallization experiments were performed in an internally heated pressure vessel, aiming to reproduce the mineral assemblage above the Pyroxenite Marker. Previously proposed and new calculated compositions were tested at conditions relevant to the Bushveld Complex (2 kbar; 1080°C - 1140°C; ~FMQ -2). In contrast to previously proposed basaltic compositions, the experimental results show that the parental magma to the Upper and Upper Main Zone of the Bushveld complex must be andesitic. Moreover, experimentally produced mineral compositions revealed, that the Upper and Upper Main Zone parental magma contained a residual liquid from the underlying zones high in Mg and Ca also small amounts of H_2O (<1 wt%).

Zusammenfassung

Der Bushveld Komplex in Südafrika ist die größte Lagenintrusion der Erde. Dessen oberer Teil ist bekannt für seine großen Vorkommen an Eisen, Titan, Vanadium und Phosphor. Dem lagigen Charakter der Gesteine entsprechend, sind diese wirtschaftlich bedeutsamen Elemente in bestimmten Lagen der Intrusion angereichert. Aus diesem Grund ist es wichtig, die Prozesse, die diese Lagen bilden genau zu verstehen. Diese Arbeit gibt einen detaillierten Einblick in die magmatischen Prozesse und die Zusammensetzung des Stamm-Magmas der Upper und Upper Main Zone (UUMZ) und die vorherrschenden Bedingungen bei der Kristallisation. Dafür wurden Proben aus den Bierkraal Bohrkernen genommen, die die gesamte UUMZ im westlichen Teil der Intrusion repräsentieren.

Eine detaillierte Studie über den Modalbestand der Gesteinsproben aus den Bierkraal Bohrkernen, hat zu einem besseren Verständnis des oberen Teils der Intrusion beigetragen. Das von Yuan et al. (2017) entwickelte Entstehungsmodell erklärt die Zyklizität, die in Mineralzusammensetzungen beobachtet werden kann, mit mehreren Magma-Injektionen in die Bushveld Magmakammer. Dabei transportiert das injizierte Magma auch Plagioklas-Kristalle, die in der Magmakammer nach unten sinken und so Anorthosit-Lagen bilden. Die ökonomisch wichtigen Magnetit-Lagen kristallisieren aus einer Hybrid-Schmelze aus, die durch Mischung zwischen dem vorhandenen und injizierten Magma entsteht.

Schmelzeinschlüsse in Apatit aus der Upper Zone zeigen Zusammensetzungen von Fe-reichen bis Si-reichen Schmelzen. Diese Spanne von Zusammensetzungen kann man am besten mit der Entmischung zweier silikatischer Schmelzen erklären. Während der Kristallisation in der Upper Zone entwickelt sich die Schmelze hin zu einer Mischungslücke hin, in der sich zwei nicht-mischbare Schmelzen voneinander trennen. Die kontinueirliche Reihe der Zusammensetzungen der Schmelzeinschlüssen entsteht während der voranschreitenden Abkühlung, bei der sich die beiden nicht-mischbaren Schmelzen entlang der Binodalen der Mischungslücke entwickeln, und so immer starker gegensätzliche Zusammensetzungen erhalten. Die dichtere, niedrig-viskose, Fe-reiche Schmelze sickert nach unten. Kumulate aus diesen Fe- und P-reichen Schmelzen bilden dann die Nelsonit-Lagen in der Upper Zone.

Spurenelemente in Ti-Magnetiten und Klinopyroxenen sowie die Hauptelement-Zusammensetzung der Klinopyroxene zeigen zwei abrupte Veränderungen zu mehr entwickelten Zusammensetzungen im stratigraphischen Verlauf der Upper Zone. Diese markanten Sprünge in der Mineralzusammensetzung korrelieren mit Vanadium Konzentrationen im Gesamtgestein. Im Vergleich zu den bisher gezeigten Änderungen in Mineralzusammensetzungen die mit der Magma Injektion einhergehen (Yuan et al.,2017), sind diese viel ausgeprägter und sprechen gegen eine sich kontinuierlich entwickelte sub-Bushveld Magmakammer. Vielmehr spricht die Veränderung zu starker entwickelten

Mineralzusammensetzungen für eine weiter unterteilte sub-Bushveld Magmakammer als Quelle für die Magma-Injektionen.

Die Sauerstofffugazität (fO_2) und deren Entwicklung in der Upper Zone wurde über die Vanadium-Verteilung zwischen Magnetit und Klinopyroxen bestimmt. Die Ergebnisse zeigen, dass fO_2 in der Upper Zone nur gering variiert und sich im Bereich von FMQ -2 bewegt. Dies ist 1.5 bis 2 Log-Einheiten unterhalb der bisher angenommen Sauerstofffugazitäten für die Upper Zone.

Potentielle Stamm-Magmen der UUMZ wurden über Kristallisationsexperimente in intern beheizten Gasdruck Anlagen getestet. Das Ziel dieser Experimente war es, die ersten Kumulate der UUMZ direct oberhalb des Pyroxenit Markers zu reproduzieren. Hierzu wurden publizierte und neu berechnete Zusammensetzungen bei für den Bushveld Komplex relevanten Bedingungen getestet (2 kbar; 1080°C - 1140°C; ~FMQ -2). Im Gegensatz zu den bisherigen Annahmen, dass das Stamm-Magma eine basaltische Zusammensetzung hat, zeigen die Experimente, dass nur eine andesitische Zusammensetzung die Mineralvergesellschaftung oberhalb des Pyroxenit Markers reproduziert. Die Zusammensetzung der experimentellen Mineralphasen zeigt außerdem, dass das Stamm-Magma der UUMZ anteilig aus der Restschmelze der darunter liegenden Zone bestehen muss und zudem geringe Mengen an H_2O enthält (< 1wt%).

Table of Contents

Outline of the study

In total, this study consists of 4 chapters including 3 publications (two with Lennart A. Fischer as first author) published in peer-reviewed journals. In the following, short summaries for each chapter are given.

Chapter 1 - Introduction

Chapter 1 introduces the Geology of the Bushveld Complex and the importance of the research on this layered intrusion. The paper of the first section discusses the economic importance and the current view of the Bushveld Complex and gives an overview about recent debates and challenges. The Upper Zone is known for its huge resources of Fe, Ti, V and P. Associated with the layered character of the rocks, these resources are enriched at certain levels of the intrusion, which makes it important to understand the formation processes of those layers. An earlier version of the first section was published in the "Proceedings of the Royal Society of Tasmania" (Fischer & Yuan, 2016).

The second paper is introducing a new model for the formation of the Upper Zone of the Bushveld Complex. In this paper major element data for bulk rock and silicates for the Upper Zone are presented and discussed. Based on significant changes in compositions at certain levels of the intrusion it is concluded that the Bushveld Upper and Upper Main Zone grew by multiple emplacements of crystal-laden magmas coming from deep-seated chambers. Slow cooling in a shallow chamber explains the systematic bottom-up compositional evolution in the cumulate pile within individual cycles. This model was published in "Journal of Petrology" (Yuan et al., 2017).

Fischer, L.A. and Yuan, Q. (2016). Fe-Ti-V-(P) Resources in the Upper Zone of the Bushveld Complex, South Africa. *Papers and Proceedings of the Royal Society of Tasmania, 150 (1).*

Yuan, Q., Namur, O., **Fischer, L.A.**, Roberts, R.J., Lü, X., Charlier, B. (2017). Pulses of plagioclase-laden magmas and stratigraphic evolution in the Upper Zone of the Bushveld Complex, South Africa. *Journal of Petrology, 58(8), 1619-1643.*

Chapter 2 - Immiscible iron- and silica-rich liquids in the Upper Zone of the Bushveld Complex

This chapter was published in "Earth and Planetary Science Letters" (Fischer et al., 2016), presenting new geochemical data for apatite-hosted multiphase inclusions in gabbroic cumulates from the Bushveld Upper Zone. Inclusions re-homogenized at high-temperature (1060–1100°C) display a range of compositions in each rock sample, from iron-rich (35 wt% FeO_{tot}; 28 wt% SiO_2) to silica-rich (5 wt% FeO_{tot}; 65 wt% SiO_2). This trend is best

explained by an immiscible process and trapping of contrasted melts in apatite crystals during progressive cooling along the binodal of a two-liquid field. The coexistence of both Si-rich and Fe-rich immiscible melts in single apatite grains is used to discuss the ability of immiscible melts to segregate from each other, and the implications for mineral and bulk cumulate compositions. We argue that complete separation of immiscible liquids did not occur, resulting in crystallization of similar phases from both melts but in different proportions. However, partial segregation in a crystal mush and the production of contrasting phase proportions from the Fe-rich melt and the Si-rich melt can be responsible for the cyclic evolution from melanocratic (Fe–Ti–P-rich) to leucocratic (plagioclase-rich) gabbros which is commonly observed in the Upper Zone of the Bushveld Complex where it occurs at a vertical scale of 50 to 200 m.

Fischer, L.A., Wang, M., Charlier, B., Namur, O., Roberts, R.J., Veksler, I.V., Cawthorn, R.G. Holtz, F. (2016): Immiscible iron-and silica-rich liquids in the Upper Zone of the Bushveld Complex. *Earth and Planetary Science Letters, 443, 108-117.*

Chapter 3 - Magnetites in the Upper Zone of the Bushveld Complex: Emphasis on V distribution and constrains on fO_2

This chapter investigates the trace element distribution in magnetites and clinopyroxenes of the Upper Zone of the Bushveld Complex. Magnetite is variably enriched in vanadium along the stratigraphic column and is of critical economic importance for South Africa. However, the relevance of important ore-forming processes such as magma replenishments, cooling/fractionation, immiscibility, and oxygen fugacity have not been fully investigated for the Upper Zone of the Bushveld Complex.

Additionally, the partitioning of vanadium, a multivalent element that occurs in Fe-Ti-oxides and clinopyroxene is investigated to estimate the oxygen fugacity conditions during the crystallization of the Upper Zone. V distribution, fractionation of magnetite and oxygen fugacity are closely linked to each other. Therefore, oxygen fugacity calculations for a continuous sample set, as provided in this study, can help to understand the influence of different parameters contributing to the ore-forming process, such as magma replenishment and fractionation. V in magnetite ranges from 30 to 6670 ppm and in clinopyroxene to up to 290 ppm. Using data from published experimental studies on V partitioning between magnetite or clinopyroxene and melt, enables to calculate fO_2 from V partitioning between magnetite and clinopyroxene. The calculated oxygen fugacity varies around FMQ -2 (FMQ corresponds to the Fayalite-Magnetite-Quartz-buffer).

Chapter 4 - The parental magma to the Upper and Upper Main Zone of the Bushveld Complex

This chapter is an experimental study on the magma composition parental to the Upper and Upper Main Zone (UUMZ) of the Bushveld Complex. The study provides a large experimental dataset on basaltic to andesitic compositions at temperatures between 1080°C and 1140°C and a pressure of 2 kbar. Crystallization experiments were conducted in an Internally Heated Pressure Vessel at conditions relevant to the Upper and Upper Main Zone of the Buhveld Complex for four previously proposed compositions and two new calculated compositions. Natural samples from the base of the UUMZ provide compositions of minerals, which are assumed to be in equilibrium with the Upper and Upper Main Zone parental magma. Experimental run products are evaluated in terms of liquid and mineral evolution as well as in comparison to the natural cumulates. Moreover, the influence of different experimental procedures (oxide powder as starting material; glass powder as starting material; overheating prior to the experimental temperature) using the same composition is discussed.

Results reveal, that the magma, parental to the UUMZ must be andesitic in composition, rather than basaltic as previously assumed. However, adjustment of the new proposed composition is necessary and evaluated in terms of Mg#, CaO and H_2O concentration.

1 Introduction

Iron, titanium and vanadium are important resources for the world's economy. While iron is a major material in many industries, titanium and vanadium have become more important during the last decades. Both, titanium and vanadium are important alloying elements in the steel industry, improving the strength and toughness of steel. Especially in the aerospace industry those steel alloys are in great demand.

Continuous industrial development is reflected in the mine production of these elements and their ores or source minerals, which has greatly increased in the last 20 years. The mining of these resources has more than doubled, except for phosphorus production which has increased to a lesser extent (Figure 1.1; U.S. Geological Survey, 2015). World demand and limited reserves of those raw materials emphasize the importance of gaining a better understanding of the formation processes of their deposits.

Fe, Ti, V, and P never or only rarely occur as native elements in nature. Minerals, rich in one or more of these elements are mined and their components are extracted. One of the most commonly mined minerals for iron is magnetite (Fe_3O_4), which can also contain significant concentrations of titanium. The main source for titanium is ilmenite ($FeTiO_3$). Both Fe-Ti-oxides can contain economically valuable amounts of vanadium. Phosphorus is extracted from phosphate minerals such as apatite ($Ca_5(PO_4)_3(F,Cl,OH)$).
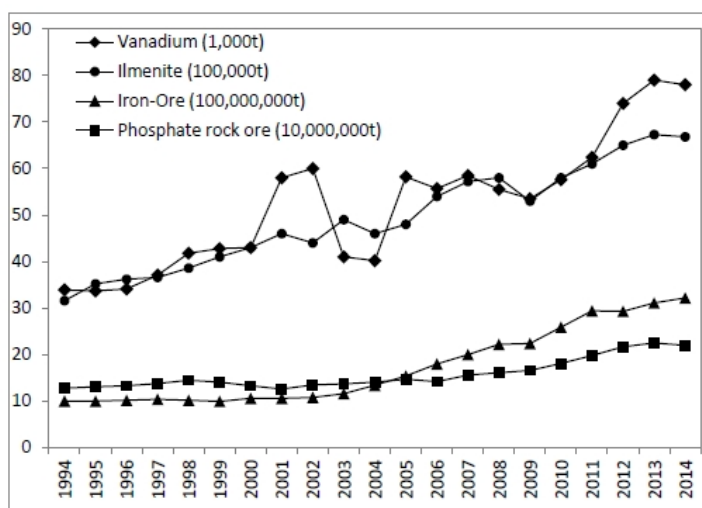
Figure 1.1 Annual world production of vanadium and major resource suppliers for iron, titanium and phosphorus. Units are given in the figure. Ilmenite supplies 90% of consumed titanium (U.S. Geological Survey 2015). Iron-Ore and phosphate rocks are mined for iron and phosphorus, respectively. Annual production data are taken from U.S. Geological Survey (2015).

Deposits mined for magnetite, ilmenite and/or apatite can have different origins. Magnetite can be formed by sedimentary, magmatic or biogenic processes. Concentrated magnetite rich sediment layers are produced by bacteria in marine environments (Devouard et al., 1998), volcanic activity (Nystrom & Henriquez, 1994) or fluvial transport (Fletcher & Walcott, 1991). Ilmenite has a magmatic origin and can be concentrated by fluvial transport (Garzanti et al., 2010). Apatite is commonly formed by magmatic processes (Green & Watson, 1982) or by biomineralisation (Hirschler et al., 1990). Importantly all three minerals are also found in high proportions in certain layers in some solidified magma chambers, called layered intrusions (Eales & Cawthorn, 1996; Song et al., 2013).

1.1   Layered intrusions

Layered intrusions are solidified magma chambers, showing a layering of rocks with different bulk compositions. The differences can be expressed in terms of the variety of minerals present and/or their proportions as well as their textures. Vertical sections of those horizontally layered rocks provide continuous sample sets showing the magmatic evolution of the intrusion. This advantage makes layered intrusion a great natural laboratory to study magmatic processes and the formation of their ore deposits. The layering is a product of processes occurring during cooling of the magma chamber. Magma is derived from a source within the Earth's mantle to the crust, and causes partial melting of the crust due to the heat excess, as well as updoming and rifting due to buoyancy of the ascending magma. Finally, this process results in an intrusion of magma into the crust. The intruding magma can reach the surface, resulting in a volcanic eruption or can remain in the crust, forming a magma chamber. The level to which the magma ascends depends on buoyancy and viscosity, which is controlled by the magma composition and temperature, as well as crustal structures, which provide conduits. The magma composition is determined by the compositions of the initial magma ascending from the mantle, crustal partial melts and potentially due to assimilation of magma chamber wall rocks.
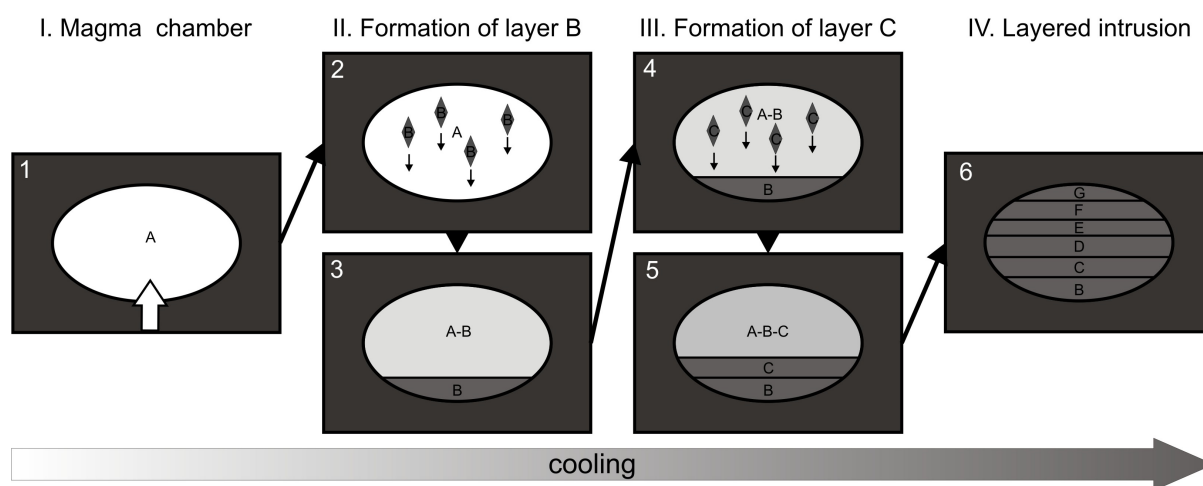
Figure 1.2 Simplified schematic illustration of the crystallization and settling process in a layered intrusion. The hot magma, with the composition A intrudes and remains in the crust (Fig. 1.2.1). The magma chamber cools down and crystallization of crystals with composition B starts (Fig. 1.2.2). Crystals settle at the bottom of the magma chamber and form a layer rich in cumulus minerals having the composition B. The residual magma has the composition A minus B (Fig. 1.2.3). Under different conditions (decreased temperature, different magma composition) crystallizing minerals have a different composition C (Fig. 1.2.4) and the resulting layer is different from the previous one (Fig. 1.2.5). With continuous cooling crystallization and settling produce more layers with different compositions until the magma chamber is solidified (Fig. 1.2.6). Note that the composition of the residual magma is also strongly dependent on the volume crystallizing from the magma but not shown in this simplified figure.

The emplaced magmas have temperatures up to 1250°C and are substantially hotter than the crustal host rocks (Figure 1.2). Consequently, the magma cools during and after its intrusion into the crust. Once the temperature is below the liquidus, crystallization begins. Most crystals sink to the bottom of the magma chamber due to their high density compared to their parental liquid, and form a layer of accumulated minerals (cumulus minerals). With time and progressive cooling more minerals crystallize and settle within the magma chamber, forming horizontal layering until the magma chamber is completely solidified. Since the extraction of crystals from the liquid is accompanied by a change in the liquid's composition, the composition of minerals and thus the rock shows a compositional progression, expressed by the typical layered structure (Figure 1.2). Rocks formed by crystallization and settling of minerals are named cumulates.

In nature this process is much more complex. Besides temperature, changes in oxygen fugacity can have dramatic effects on the crystallizing phases and thus the path of magmatic evolution (Namur et al., 2015). Also changes in the volatile content (H_2O and CO_2) and potential degassing events influence the crystallization sequence. Moreover, instead of a single crystal composition different minerals can crystallize at the same time, building up a cumulate rock layer. Crystal compositions can change between layers, but also the relative proportions of minerals or their textures can differ. Repeated layers with similar composition are observed in nature. In some cases new magma is injected into an existing magma chamber, affecting the magma compositions and thermodynamic properties of the system, which results also in a change of compositions and modes of crystallizing minerals. Depending on magma and crystal compositions, crystals can be more buoyant than the magma and therefore float (Campbell, 1978; Namur et al., 2011). However, these crystals are commonly found in cumulate layers in certain locations. To explain these occurrences other processes besides crystallization and settling have to be considered (Namur et al., 2011).

In summary, layered intrusions are a product of a vast number of magmatic processes, such as fractionation and crystal settling, magma mixing, magma replenishment or immiscibility. The occurrence of a variety of magmatic processes on a relatively small scale is challenging but also provides the opportunity to investigate complex magmatic systems. Moreover, the close relationship of layered intrusions and ore deposits make it important to study these systems and shed light on their formation.

1.2 The Bushveld Complex

The Bushveld Complex in South Africa (Figure 1.3) is the largest layered intrusion on Earth. Formed by 1 million km^3 of magma (Cawthorn & Walraven, 1998), it covers a 65000 km^2 area with a thickness of 7 – 9 km, emplaced in three limbs (western, eastern and northern limb). Within this giant volume, major resources of platinum group elements

(PGE), iron, titanium, vanadium, and chromium are hosted. Moreover, the Bushveld Complex is the world's largest resource of PGE. Discovered in the late 1860s by Carl Mauch, it is still one of the most important mining areas. Major resources of PGE's are hosted in the Merensky Reef (MR) and Upper Group 2 chromitite (UG2). Both in general 1.5 m thick layer packages containing pegmatoidal pyroxenites and chromite $((Fe,Mg)Cr_2O_4)$ dominated layers, respectively. Iron and titanium are concentrated in magnetite and ilmenite rich layers. Prominent examples are the Main Magnetite layer (MM) and the Magnetite Layer 21 (M21).
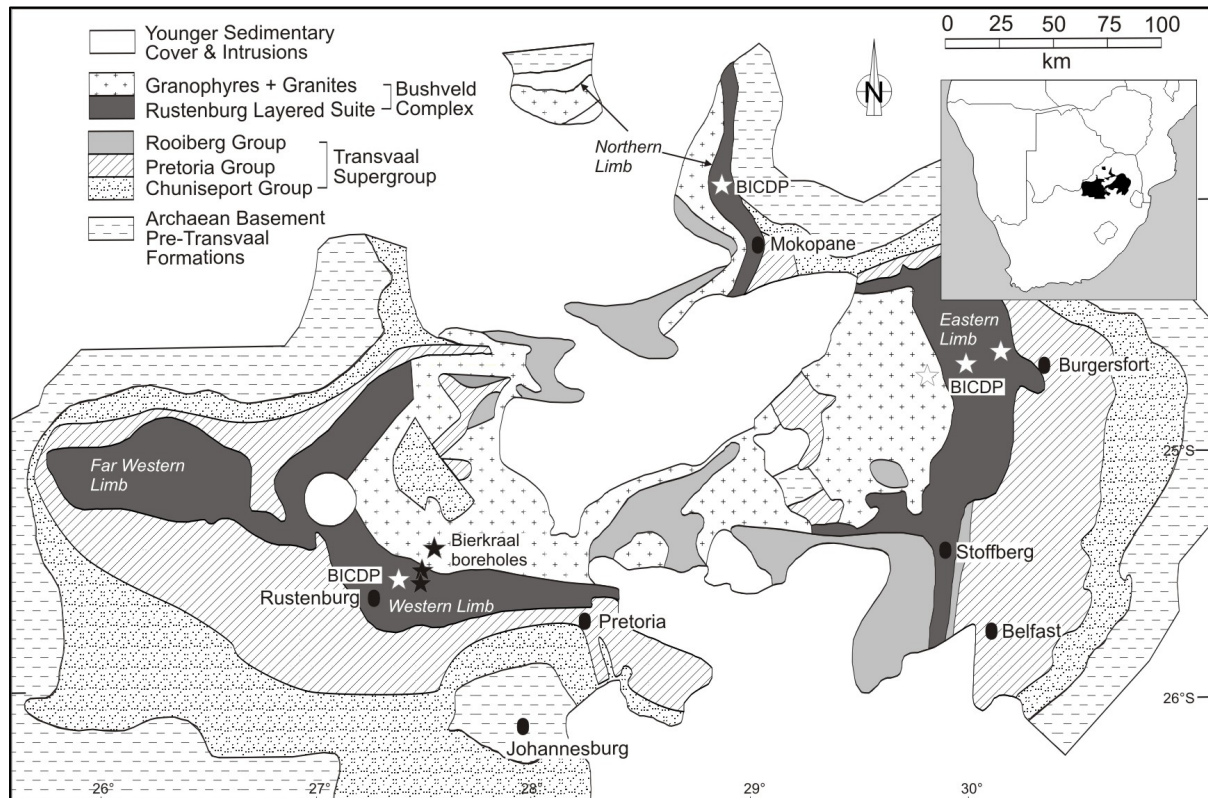
Figure 1.3 Geological map of the Bushveld Complex with location of the Bierkraal boreholes (black stars) and the potential drilling sites of the BICDP (white stars; Trumbull et al., 2015). Modified after Barnes & Maier (2002).

The chemistry of the Bushveld Complex and of its initial magma as well as later injected magmas has been estimated by several authors (e.g., Davies et al., 1980; Harmer & Sharpe, 1985; Barnes et al., 2010; VanTongeren et al., 2010). Although accurate magma compositions are hotly debated (see review in Cawthorn, 2015), the overall mineral assemblage implies a relatively Mg- and/or Fe-rich mafic silicate magma. Consequently, the rocks formed from these magmas are mostly ultramafic/mafic rocks. Common mafic minerals for the Bushveld Complex are pyroxene $((Mg,Fe,Ca)_2Si_2O_6)$, olivine $((Mg,Fe)_2SiO_4)$, magnetite and ilmenite.

Zircon U/Pb dating has revealed that the initial emplacement of magma in the Bushveld occurred at 2,055.91±0.26 Ma, and the whole intrusion cooled to below 650°C (solidified

magma chamber) in 1.02±0.63 Ma (Zeh et al., 2015). Cawthorn & Walraven (1998) proposed an even shorter crystallization time of 200,000 years.

The Bushveld cumulate rocks are divided into the Marginal, Lower, Critical, Main, Upper and Roof Zones and their corresponding subdivisions (Wager & Brown, 1968; Cawthron, 2013a), based on mineral assemblages (Figure 1.4). The initial horizontal layering of the Bushveld intrusion was displaced and is now dipping toward the center of the body (Figure 1.4). Cawthorn & Webb (2001) proposed that isostatic adjustment, induced by the huge mass of emplaced magma, is responsible for the tilted layers. Here, the focus is on the genetically related Upper and Upper Main Zone (UZa, UZb, UZc and MZu) hereinafter referred as UUMZ).

Figure 1.4 Simplified stratigraphic column (left) and cross-section (right) of the western and eastern limb of the Bushveld Complex with Zones and distinctive layers. Lower Zone (LZ), Critical Zone (CZ), Main Zone (MZ) and Upper Zone (UZ) are divided by solid lines. Subdivisions Upper Middle Zone (MZu), Upper Zone a (UZa), Upper Zone b (UZb) and Upper Zone c (UZc) are divided by dashed lines. The distinctive layers the Merensky Reef (MR), Pyroxenite Marker (PM), Main Magnetite layer (MM) and Magnetite layer 21 (M21) are marked with arrows. The thickness of the sequence varies between the eastern and western limbs. Above the UZ, felsic (Si-rich) rocks are located. The LZ is underlain by the Marginal Zone. The north to south cross-section shows the present configuration of the Bushveld layered intrusion. Modified after Eales & Cawthorn (1996) and Cawthorn & Webb (2001).

1.2.1 The Upper and Upper Main Zone

The UUMZ is commonly considered as representing the last injection of magma into the Bushveld magma chamber and is known as a world-class deposit of Fe, V, Ti, and P. The Pyroxenite Marker (PM) is located at the base of the UUMZ (Figure 1.4), indicating a major change of magma composition between UUMZ and the underlying part of the MZ. It is thought that an injection of new magma changed the overall magma composition within the Bushveld magma chamber and forced orthopyroxene (Ca-poor pyroxene) to crystallize, resulting in the orthopyroxene dominated, several meter thick PM (Cawthron et al., 1991).

The UZ can be further subdivided, based on the first appearance (first crystallization) of new cumulus minerals within the layered sequence. The base of the UZ (subzone UZa) is defined by the appearance of cumulus Ti-magnetite, which is followed by the appearance of olivine (UZb) and finally apatite (UZc).

The UZ stratigraphy is dominated by gabbros with intercalated layers of anorthosite, magnetitite and nelsonite (Figure 1.5). While anorthosite, a plagioclase-rich rock (plagioclase: mineral series with end-member-formulas $NaAlSi_3O_8 - CaAl_2Si_2O_8$) is economically unimportant, magnetitite (magnetite and ilmenite) and nelsonite (magnetite, ilmenite and apatite) rocks are enriched in iron, vanadium, titanium, and phosphorus. This makes it important to unravel the processes involved in the formation of these layers and the resulting enrichment or depletion of economically valuable elements.
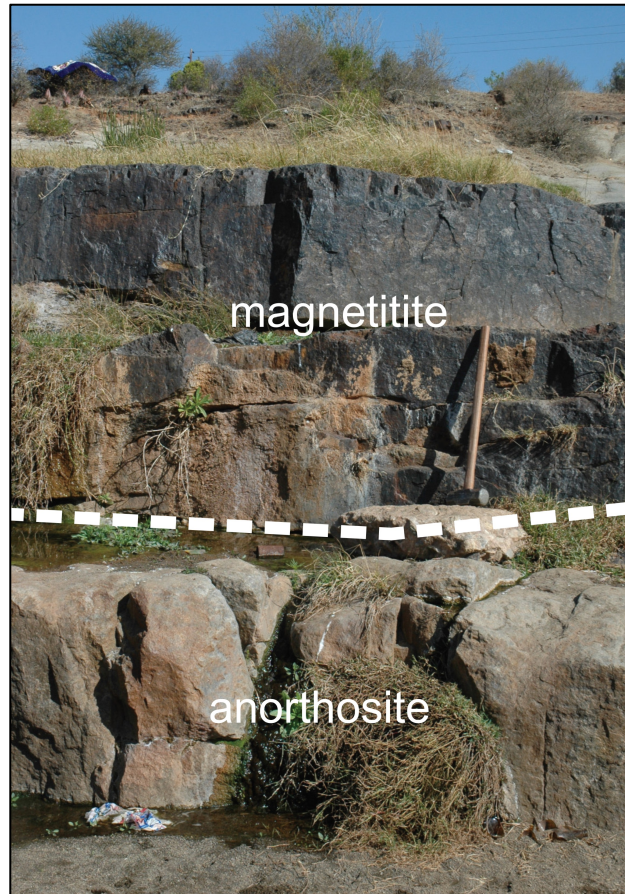
Figure 1.5 Photograph of the dark Main Magnetite layer overlaying a bright anorthosite layer in the Upper Zone. Photograph from (Scoon & Mitchell, 2012).

1.3   Scientific debates and controversies

Although the Bushveld Complex has been studied for more than 150 years, several recent debates and controversies emphasize the uncertainties in the understanding of this layered intrusion.

1.3.1   Link between limbs

The Bushveld Complex is exposed in three major limbs, namely the Western, Eastern and Northern Limbs. Gravity models and seismic tomography have shown that the Eastern and Western limbs are connected at depth (Webb et al., 2004; Kgaswane et al., 2012). This is also supported by the finding of similar layers and sequences in the two limbs. Cawthorn & Webb (2001) identified six equivalent layers in the Eastern and Western limbs and concluded that both limbs crystallized from a single magma chamber. The presently

exposed structure with two limbs is the result of isostatic depression (Cawthorn & Webb, 2001).

Connection between the Northern Limb and the Western and Eastern Limbs is also debated. Possibly equivalent layers were identified but no conclusive evidence could be provided (Kinnaird et al., 2005). Cawthorn (2015) suggested discrete evolution of the Northern limb at least for the Lower and Critical Zones, based on the lack of equivalent chromitite layers in the Western and Eastern limbs. Ashwal et al. (2005) found possibly correlating layers of the Main and Upper Zone within the Northern but also significant differences in the cumulus assemblage of the PM.

1.3.2 Closed- or open-system

Closed system crystallization means that the magma evolves and cools progressively in the magma chamber without magma eruptions or any input of new magma, usually referred to as magma replenishment. In case of the Bushveld Complex it is widely accepted that the whole intrusion formed by several magma batches probably originating in a sub-Bushveld staging chamber (Eales, 2002; Ashwal, 2005; McDonald & Howell, 2007, Roelofse & Ashwal, 2012). Whether the UUMZ in the Bushveld formed in a closed system has been debated in the last decades. Based on the generally consistent initial strontium isotope ratios (0.7073 ± 0.0002) of the host rocks, some researchers have concluded that the UUMZ formed by differentiation of a single magma body (Kruger et al., 1987; Cawthorn et al., 1991). Tegner et al. (2006) identified nine compositional cycles in the UZ, explained by magma mixing between two magma layers within a stratified magma chamber. In contrast to the closed system model, due to an observed significant loss of incompatible elements such as K and Zr, Cawthorn & Walraven (1998) proposed that up to 40% of the magma might have been erupted. In addition, the documented compositional reversals in the Northern (Ashwal et al., 2005) Eastern (Scoon & Mitchell, 2012) and Western (Yuan et al., 2017) limb strongly indicate that the UUMZ experienced a succession of magma pulses. The composition of the injected magma is unknown, but Yuan et al. (2017) proposed injection of a magma carrying up to 20 vol% plagioclase crystals.

1.3.3 Mush emplacement versus magma recharge

The difference between the emplacement of a crystal mush and a crystal-free silicate liquid is due to the crystal load transported by the magma. In contrast to the generally assumed crystal-free liquid in many models of magma evolution (Marsh, 2004; Latypov, 2009), recent studies suggest that most injected magma can carry crystals, with concentration of up to 55 vol% (Marsh, 2013). In addition, emplacement of plagioclase-rich mush has been proposed for the thick anorthosite layers in another layered intrusion such

as the Stillwater Complex in Montana (Raedeke, 1982) and is also regarded as a widely accepted process to form the Proterozoic massif type anorthosites (Ashwal, 1993). Based on the magnetic susceptibility and non-cotectic proportions of plagioclase, Ashwal et al. (2005) and Roelofse & Ashwal (2012) suggest that this mechanism may have occurred in the UUMZ and lower Main Zone, implying the existence of a sub-Bushveld magma chamber, progressively feeding the actual Bushveld chamber with evolved magma. Results from Yuan et al. (2017) provide evidence for several injections of a plagioclase laden magma within the UUMZ (see chapter 1.5 "Evolution of the Upper and Upper Main Zone").

1.3.4   Silicate liquid immiscibility

Silicate liquid immiscibility is the unmixing of two or more silicate liquids (magmas) with different compositions from a single parental magma. The unmixing of an iron-rich silicate liquid and a silica-rich silicate liquid has been identified in several locations with genetic similarities to the Bushveld Complex such as the Skaergaard intrusion in Greenland (Jakobsen et al., 2005) and the Sept Iles intrusion in Canada (Namur et al., 2012). In the case of the Bushveld Complex, the development of immiscible silicate liquids within the magma body has been debated and controversially interpreted. Cawthorn (2013b) challenged the occurrence of silicate liquid immiscibility, whereas von Gruenewaldt (1993) suggested that silicate liquid immiscibility might have produced the up to m-scale magnetitite and nelsonite layers. Alternatively, based on rare earth elements (REE) in apatite from the Eastern Limb, VanTongeren & Mathez (2012) argue that even large-scale separation of iron- and silica-rich melts at the hundreds-of-meter scale might have occurred. The latter model has been widely debated (Cawthorn, 2014; VanTongeren and Mathez, 2014) but consensus has not yet been reached. Results of this study investigating samples from the Western Limb (Fischer et al, 2016; see chapter 2 "Immiscible iron- and silica-rich liquids in the Upper Zone of the Bushveld Complex") suggest that silicate liquid immiscibility occurred on a smaller scale (50–200 m) in the UMMZ with sorting of immiscible melt droplets in the crystal mush forming Fe-Ti-P-rich layers within the UZ contradicting the hypothesis of large-scale separation of two layers of immiscible melts. This model was questioned by VanTongeren (2018), re-interpreting the dataset of Fischer et al. (2016) assuming that the analyzed melt inclusions originate from an Fe-rich section resulting from large-scale separation as proposed by VanTongeren & Mathez (2012). However, samples from Fischer et al. (2016) are significantly lower in the stratigraphy than those described in VanTongeren et al. (2012). In this lower section several compositional reversals are observed contradicting a large-scale separation. Moreover, her observation of VanTongeren (2018), that the proportion of the Si-rich melts inclusions is significantly lower than those of Fe-rich inclusions, is not comprehensible looking on the continuous compositional range presented in Fischer et al. (2016).

1.3.5   Bushveld Igneous Complex Drilling Project

The Bushveld Igneous Complex Drilling Project (BICDP; Trumbull et al., 2015) is part of the work of the International Continental Drilling Program (ICDP), an international organization supporting scientific continental drilling projects. Directed by two research groups from Germany (GFZ – German Research Centre for Geosciences) and South Africa (University of the Witwatersrand, Johannesburg) the BICDP started in 2014 and is currently in the planning stage. It comprises three different drill sites, one site at each limb of the intrusion (Figure 1.3). Combined with existing drill cores, those obtained from the BICDP will cover the complete Bushveld stratigraphy in each limb. In addition to other benefits, this allows researchers to investigate vertical and lateral variations and may resolve the controversy concerning the relationships between the different limbs.

1.4   Sampling and petrography

The exposed part of the Bushveld Complex provides only limited insights into deeper layers. For sampling of unexposed layers, drilling is necessary. The South African Geological Survey drilled three boreholes in the Bierkraal area (BK1, BK2 and BK3), north of Rustenburg intersecting the UUMZ and the PM (Figure 1.3). The combined cores provide a 2270 m thick section of the intrusion. Samples from these drillcores are representative of the UUMZ in the Western Limb of the Bushveld Complex. In total, 230 samples were provided to this study giving an average spacing of less than 10 m (Supplemental Table S1). To correlate samples from the three drill cores, we calculated the stratigraphic position below the roof of the intrusion following the calculations of Tegner et al. (2006) taking roof contact and dip angle into account. In the course of this study samples were investigated using a variety of methods including melt inclusions (Fischer et al., 2016), bulk rock compositions (Yuan et al., 2017), silicate compositions (Yuan et al., 2017), Fe-Ti-oxide compositions (chapter 3 "Magnetites in the Upper Zone of the Bushveld Complex: Emphasis on V distribution and constrains on fO_2"). This extensive database on a continuous sample set, representing the entire UUMZ allows precise insights into stratigraphy and formation processes.

The UUMZ is dominated by magnetite-free and magnetite bearing gabbros, gabbronorites, Ol-gabbros and troctolites. Additionally, anorthosites and the magnetite rich rocks, pmi-C (plagioclase + magnetite + ilmenite Cumulate), magnetitite and nelsonite are observed. Whereas gabbroic rocks are a common rock type found in many locations and formed by slowly cooling basaltic magma, the modes of formation of the latter two rock types need a more detailed investigation of the UUMZ.

1.4.1 Mineral modes

Mineral modes of 98 (average spacing of ~19 m) selected samples from BK1 and BK3 drill core were determined using FEI MLA 650 scanning electron microscope (SEM) at the Central Science Lab at the University of Tasmania, Australia. Per sample ~25 000 energy-dispersive X-ray (EDX) spectra were obtained on a representative 20 x 10 mm sample area. Using the Mineral Liberation Analysis (MLA) software package v3.1., recorded spectra were compared to a handmade reference spectra database including 34 minerals typical for the UUMZ (see Supplemental Table S2). In this way, every obtained EDX spectra was assigned to a specific mineral. However, precision of EDX spectra was not high enough to differ between pigeonite and orthopyroxene and are thus summarized as low-Ca-pyroxene. Results are presented in Yuan et al. (2017) and Supplemental Table S3.

Figure 1.6 shows the obtained mineral modes within the stratigraphy. Position of additional magnetite, nelsonite and anorthosite layers from Tegner et al. (2006) and Yuan et al. (2017) are indicated. Plagioclase is the dominant phase throughout the UUMZ. Pyroxenes are abundant in most samples. While clinopyroxene vary equal in the entire UUMZ, low-Ca-pyroxenes are less abundant in the upper part (UZc; after apatite saturation). Magnetite always coexists with smaller proportions of ilmenite, summarized as Fe-Ti-oxides in Figure 1.6. After olivine saturation (UZb) olivine proportions are relatively small compared to its abundance in UZc. Sulphides occur as accessory minerals in the entire UUMZ. Amphibole occurs repetitively in major proportions (up to 30 vol%) in the UUMZ probably indicating alteration by fluids. The top of the stratigraphic sequence is marked by the occurrence of kalifeldspar and quartz.

Figure 1.6 Mineral modes for the Upper Zone obtained via SEM MLA. Diamond symbols show positions of magnetite, nelsonite and anorthosite layers from Tegner et al. (2006) and Yuan et al. (2017) observed in samples from the same drill cores but not included in MLA of this study.

1.4.2   Gabbroic rocks

Gabbroic rocks are the dominant rock type in the UUMZ. They are typical for mafic intrusions and mainly consist of plagioclase ± pyroxene ± olivine. After magnetite (UZa) and apatite saturation (UZc) the gabbroic rocks can additionally contain Fe-Ti-oxides and apatite respectively. Distinctive for the UUMZ gabbroic rocks are their high proportions of plagioclase, magnetite and apatite. The latter mineral shows a cyclic vertical variation in abundance (Tegner et al., 2006; Yuan et al., 2017). Gabbroic rocks vary markedly throughout all subdivisions in terms of mineral modes and compositions as well as textures. Biotite, amphibole and sulphides commonly occur as accessory minerals. At the top of the intrusion also quartz and orthoclase are observed in minor proportions.
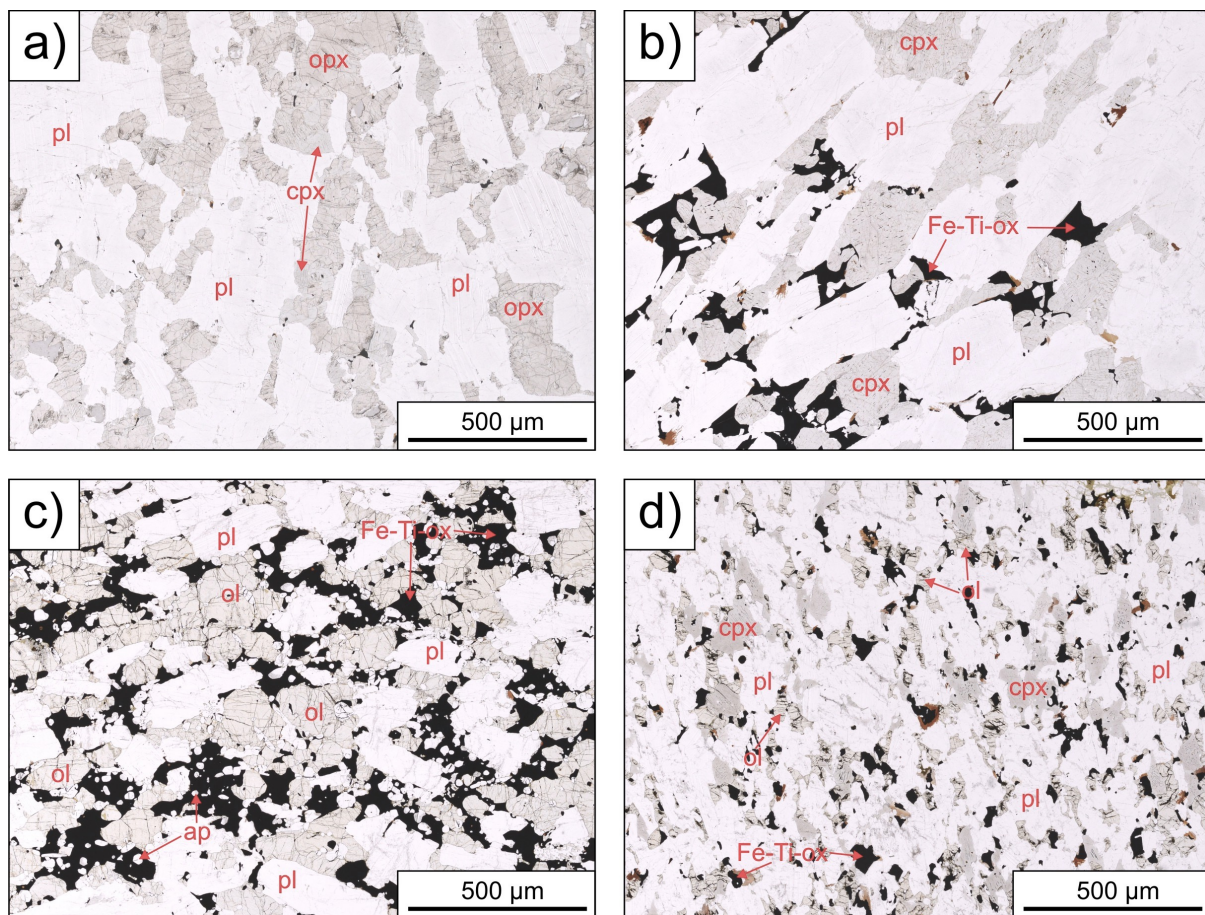
Figure 1.7 Thin section photographs with plane polarized transmitted light of gabbroic rocks of the UZ. **a)** Gabbronorite containing tabular plagioclase (pl), subhedral orthopyroxenes (opx) and anhedral clinopyroxene (cpx) often associated with the opx (BK3-1399.6). **b)** Magnetite-Gabbronorite containing tabular pl, anhedral cpx and interstitial Fe-Ti-oxides (Fe-Ti-ox) which are mainly titanomagnetites with few ilmenites (BK3-1321.3). **c)** Magnetite-Troctolite containing lath-shaped pl and subhedral olivine (ol). Typical for UZa are the euhedral apatites (ap) associated with the interstitial Fe-Ti-ox (BK1-1074). **d)** Ol-Gabbro containing lath-shaped pl, subhedral cpx and few anhedral ol. Few Fe-Ti-ox occur insterstitial and sometimes show brownish rims of biotite (BK1-1285.6).

Gabbronorites of the UUMZ contain abundant euhedral to subhedral, tabular plagioclase (Figure 1.7a). Clinopyroxene occurs subhedral whereas low-Ca-pyroxenes have an anhedral shape. Magnetite, if present, occurs as interstitial aggregates together with ilmenite (Figure 1.7b). Troctolites are finer grained compared to the gabbronorites (Figure 1.7c). Olivines have a subhedral shape and occur as single crystals or aggregates. Plagioclase is lath-shaped and less abundant than in the gabbronorites. In olivine-gabbros both pyroxenes have a sub- to anhedral shape (Figure 1.7c). Olivine in these rocks is subhedral. Fe-Ti-oxides occur, as in all gabbroic rocks, interstitial.

1.4.3   Anorthosite

Anorthosites occur as repetitive layers within the UUMZ and are in contrast to other rock types found in the UUMZ, classified as felsic rocks. They consist of mainly plagioclase with sometimes small proportions of poikilitic pyroxenes (Figure 1.8). Boundaries between plagioclase crystals are often serrated. Some anorthosite samples show slight local alteration, expressed in minerals formed after the cooling of the magma chamber (e.g., epidote, amphibole). Yuan et al. (2017) identified 28 anorthosite and 28 leucogabbroic layers in the UUMZ.
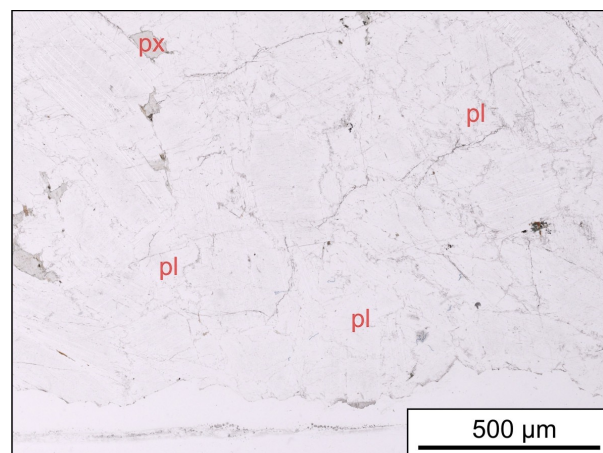
Figure 1.8 Thin section photograph with plane polarized transmitted light showing monomineralic anorthosite consisting of mainly plagioclase (pl) with few poikilitic pyroxenes (px) (BK3-1380.7).

Leucogabbros are also observed containing small amounts of interstitial Fe-Ti-oxides in addition to the anorthosite mineral assemblage.

1.4.4   Fe-Ti-rich rocks

Throughout the UZ magnetite-rich rocks are observed, namely magnetitite, nelsonite and pmi-C rocks. Tegner et al. (2006) identified 26 magnetite layers and six nelsonite layers in the Bierkraal drill-cores of the UUMZ, with a total thickness of 20.42 m. In addition Yuan et al. (2017) observed another 7 magnetite layers in the same drill-core. Usually, magnetitite consists of massive magnetite and ilmenite. Fe-Ti-oxides occur as massive aggregates. Several magnetite layers also contain few plagioclase and pyroxenes (Figure 1.9a). Layers with higher proportions of plagioclase (Figure 1.9b) are termed pmi-C (plagioclase, magnetite, ilmenite, Cumulate) after the nomenclature of Irvine (1982). Magnetite and ilmenite occur as massive aggregates containing subhedral, tabular shaped plagioclase crystals. Magnetites from the UUMZ show a relatively high Ti concentration, ranging from 5

to 20 wt% TiO_2 (Reynolds, 1985a). Nelsonites contain, in addition to the magnetitite assemblage, significant amounts of euhedral apatites.
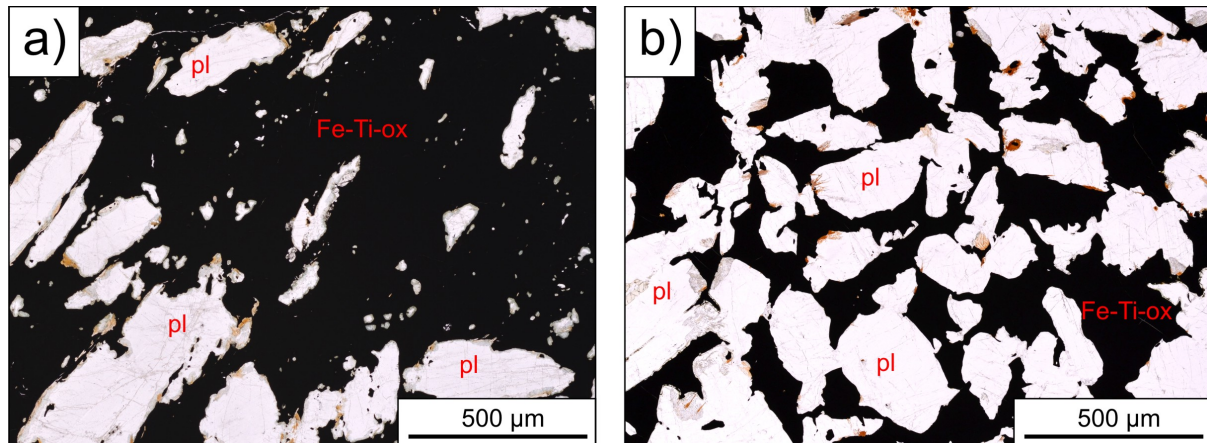
Figure 1.9 Thin section photographs with plane polarized transmitted light. **a)** Magnetitite from the Main Magnetite Layer containing massive Fe-Ti-oxides (Fe-Ti-Ox) which are mainly titanomagnetite with few ilmenites. Plagioclase (pl) occurs tabular (BK3-1343). **b)** pmi-C (plagioclase + magnetite + ilmenite, Cumulate) with abundant Fe-Ti-ox and pl (BK1-1119.3).

1.5 Evolution of the Upper and Upper Main Zone

This sub-chapter is part of Yuan et al. (2017) and was modified to fit in the frame of this thesis.

Yuan, Q., Namur, O., **Fischer, L.A.**, Roberts, R.J., Lü, X., Charlier, B. (2017): Pulses of plagioclase-laden magmas and stratigraphic evolution in the Upper Zone of the Bushveld Complex, South Africa. *Journal of Petrology, 58(8), 1619-1643.*

1.5.1.1 Compositional reversals in Bierkraal drill cores

Progressive mineral reversals have been widely documented in the Bushveld (PM of the Bushveld; Cawthorn et al., 1991; VanTongeren & Mathez, 2013) and in other well-studied layered intrusions such as the Fongen-Hyllingen intrusion (Wilson & Sorensen, 1996) or the Sept Iles intrusion (Namur et al., 2010). Such reversals are typically regarded as indicators of new magma recharge and mixing with the resident melt in the magma chamber. Reversals in mineral compositions in the Bushveld UUMZ have also been previously reported in the Northern Limb (Ashwal et al., 2005) and the Western Limb (Tegner et al., 2006).

For the Bierkraal data presented here, reversals have been identified in whole-rock and mineral compositions and are used to define cycles (cp. Figure 1.10). Trapped liquid shift effects may change the composition of mafic minerals (Barnes, 1986), but have no influence on plagioclase core compositions (Grove et al., 1984). We therefore define the boundaries

between cycles as the lowest anorthite content within each reversal. Gradual increases in anorthite content, the Cr content in magnetite separates, and the Mg# of high-Ca pyroxene are usually observed above the level of these minimum values. Following the reversal, these parameters usually exhibit a continuous decrease before the next cycle starts. Importantly, we observe that most of the reversals are closely associated with anorthosite or pmi-C, which are usually located at the bottom of the cycles (cycle II, III, VIII, IX, XI, XIII-XVI and XVIII).

Some of the reversals that we documented are stratigraphically close to reversals previously described by Tegner et al. (2006), such as those cycles defined by the disappearance of apatite (Figure 1.10). In Figure 1.10 An in plagioclase and bulk P_2O_5 are compared to illustrate these compositional variations. The reversals in UZa and UZb are best represented by An in plagioclase, whereas the reversals in UZc are documented perfectly by anorthite and bulk P_2O_5 (Figure 1.10).
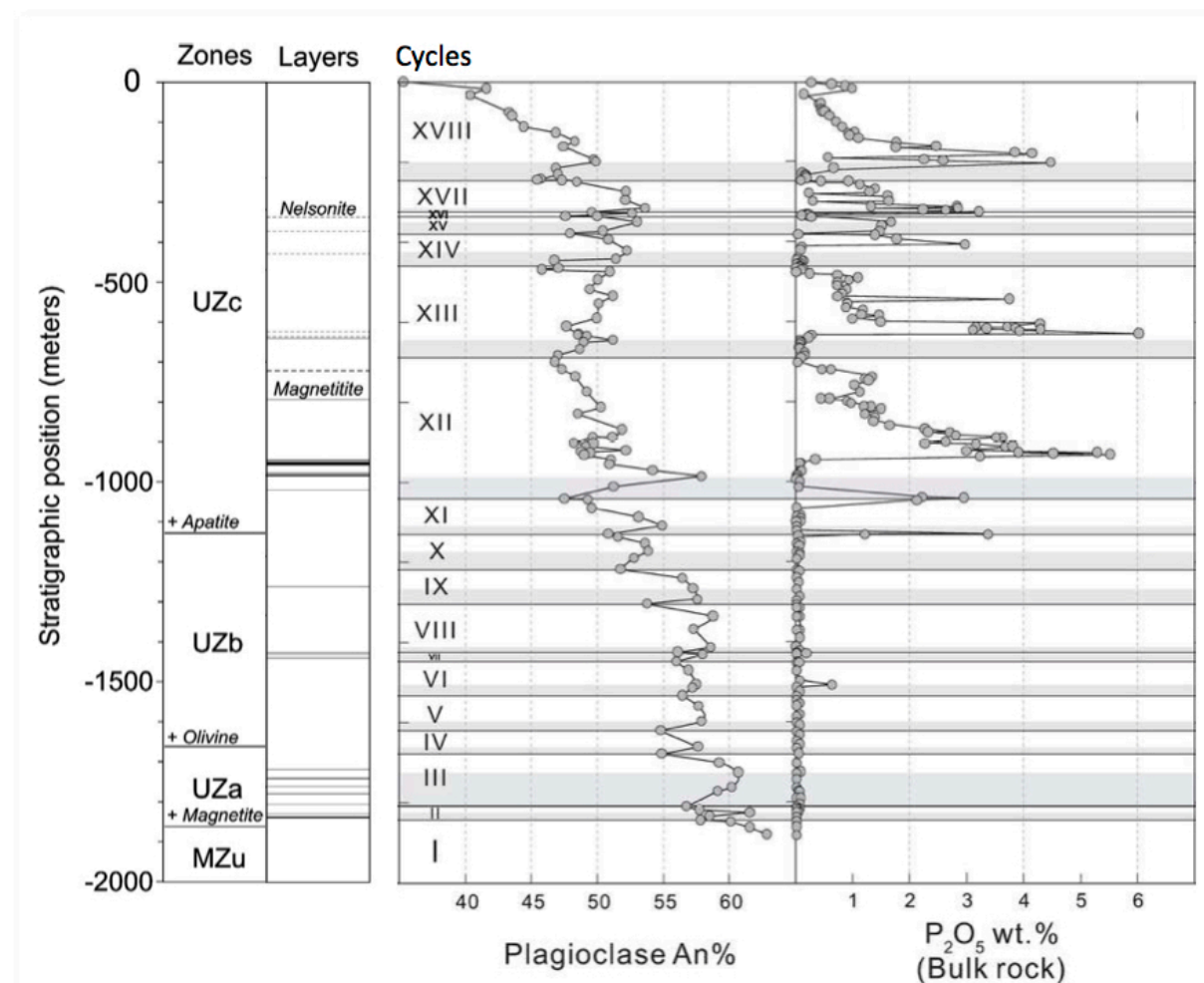
Figure 1.10 Plagioclase composition and bulk P_2O_5 content are shown for the UUMZ stratigraphy. Column „Zones" show the boundaries of Upper Zona a (UZa), Upper Zone b (UZb) and Upper Zone c (UZc). The base of the Upper Main Zone (MZu), marked by the PYroxenite Marker ist not shown. The „Layers" column shows the position of magentite (solid lines) and nelsonite (dashed lines) layers observed in the UUMZ. Roman numbers indicate the cycles proposed by Yuan et al. (2017) and the grey fields mark the position of the compositional reversal. Modified after Fischer et al. (2016) and Yuan et al. (2018).

1.5.1.2 Lithological cycles

UZa and UZb display cyclic patterns in FeO_{tot} above 1500 m, which correspond to a typical lithological sequence from anorthosite to leucogabbro, then to magnetite (olivine) gabbro/norite to oxide-rich layers, and then sharply to pmi-C rocks or anorthosite (Figure 1.11a-b). Locally the base of the sequence starts with leucogabbro (1503 to 1441 m) or ends with no magnetite layer (1247 to 1156 m). Magnetite layers in the Bierkraal drill cores (Tegner et al., 2006) usually occur above the magnetite (olivine) gabbro/norite.

UZc rocks consist of magnetite gabbro and magnetite troctolite with magnetite, nelsonite and anorthosite layers (Figure 1.7 - 1.9). The most conspicuous feature in UZc is the cyclicity of modal apatite, and accordingly the bulk P_2O_5 (Figure 1.10). Commonly the bottom of each cycle starts with leucogabbro and / or anorthosite. The plagioclase proportion gradually decreases to about 20 wt% in the magnetite-rich samples and apatite appears as a major cumulus phase in the upper portions of these magnetite-rich rocks, forming nelsonite layers. Higher up, the apatite proportion progressively decreases to 0.8-1 wt% and then declines sharply to near zero with the assemblage changing from magnetite troctolite to ferrogabbro and leucogabbro (Figure 1.11c-d). Concomitantly, the modal proportion of plagioclase behaves in an opposite way to the trend of apatite, starting with about 20 wt % plagioclase in magnetite troctolite, then gradually increasing to about 50 wt% in ferrogabbro, and jumping to 80 wt% in plagioclase-rich rocks (Fig. 13c). This pattern of apatite and plagioclase proportions occurs at intervals of 1040 to 687 m, 687 to 468 m and 246 to 0 m, except in the interval of 468 to 246 m where the samples show an alternation of anorthosite and ferrogabbro (with apatite) on a small scale of about 40 meters. In UZc, the evolution trend in Fe-Ti oxides is very similar to that in P_2O_5, but it is observed that not all magnetite layers contain cumulus apatite and usually the nelsonite is found slightly above the magnetite layers (Figure 1.11d).

At the bottom of the UUMZ, from the PM to the first appearance of cumulus Fe-Ti oxides, the samples display a near-continuous trend of upward decreasing anorthite content in plagioclase, Mg# in clinopyroxene and Mg# orthopyroxene. This trend lasts from 1877 to 1841m, followed upwards by 17 reversals at a scale of 30 to 340 m (Figure 1.10). Although some of these reversals are characterized by a minor increase of anorthite in plagioclase (2~3 An %), the majority are related to substantial increases in An %, Fo content and Mg# in clinopyroxene, documented in several successive samples such as the reversal in cycles III (An: 56.8-61), XI (An: 51-55), XIII (An: 47-51), XIV (An: 45.8-52.3), XV and XVI (An: 48-53), XVIII (An: 45-50), and the marked increase in An of about 22 mol % from 1039 m to 985 m depth in cycle XII (An from 47.5 to 58). These large variations clearly suggest perturbation in the crystallization process and strongly argue against closed-system crystal fractionation for the UUMZ. In addition, within several reversal intervals (cycles XII to XV and XVIII), there is also a remarkable increase of V_2O_5 content in magnetite (Cawthorn & Walsh, 1988). Similarly, in the detailed study of the UUMZ of the Bellevue drill core (Northern Limb),

Ashwal et al. (2005) attributed the reversals of An in plagioclase and Mg# in pyroxene to new magma replenishments. Importantly, as discussed above, the almost simultaneous reversals of Cr in magnetite and anorthosite in plagioclase present unarguable evidence for primitive magma recharge for the UUMZ.
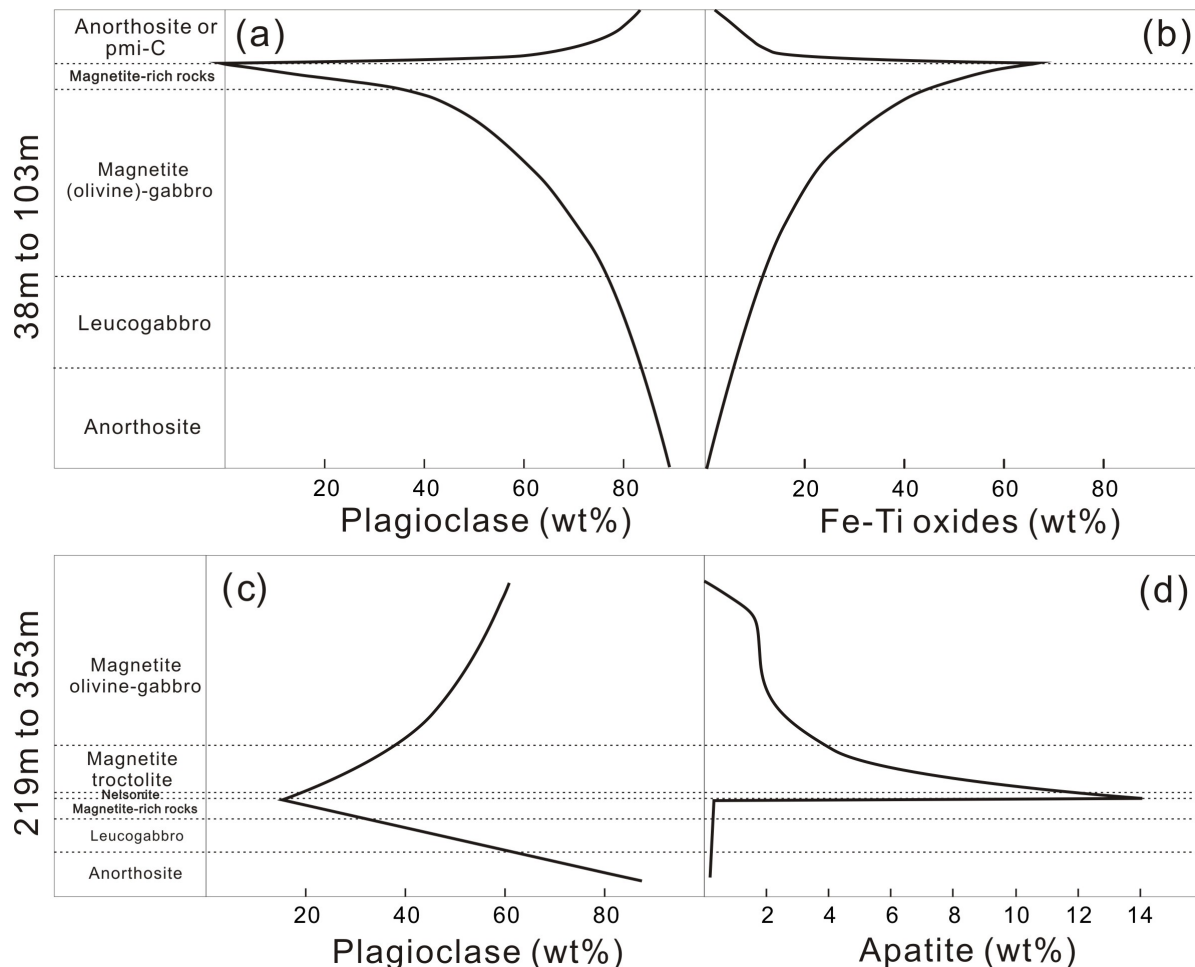
Figure 1.11 Schematic lithological section through an idealized cyclic sequence in UZb (a, b) and UZc (c, d). (a) and (b) are based on the interval from 1841 to 1749 m in UZb. (c) and (d) are based on the ideal unit between 690 and 470 m. In some units, some horizons may be missing. From Yuan et al. (2017).

1.5.1.3 *Plagioclase mush emplacement and anorthosite formation*

As mentioned in the petrography section, pmi-C rocks are common in UZb. This assemblage almost disappears in UZc and is replaced by a series of anorthosite layers. These layers are found in the intervals where cumulus apatite disappears in the upper cycles. The most remarkable feature of these plagioclase-rich horizons in the entire UZ is that most of them are within or near the reversals documented in anorthite content in plagioclase. Some of these plagioclase-rich rocks occur at the top of the reversals and some are located within the reversals, whereas the majority of such rocks lie at the beginning of these reversals. Where such rocks are located at the base of the cycle, a gradual decrease in plagioclase proportion is observed, with a progressive petrographic trend from anorthosite to

leucogabbro to gabbroic rocks. This phenomenon is best displayed in cycles XI and XII where reversal bases are plagioclase-rich (~80 wt%) and then gradually change to a magnetite troctolite with about 20 wt% plagioclase and a sharp increase in apatite. In UZa and UZb, an idealized cyclic unit comprises layers of anorthosite and pmi-C rocks, then magnetite (olivine) gabbro/norite and oxide-rich samples as described above.

Overall, all these features strongly suggest that the replenishing magma carried plagioclase crystals. According to the thickness ratio between the plagioclase-rich interval (52 m) and the total cycle thickness of cycle XII (296 m), which exhibits the most typical pattern, the plagioclase load of the replenishing magma is estimated at about 15-20 vol%. This amount of plagioclase phenocrysts is similar to that proposed in recent studies suggesting that most injected magmas can carry crystals at concentration of up to 55 wt% (Marsh, 2013).

However, whether these plagioclase crystals are formed in the feeder zone or on the way to the Bushveld magma chamber is not clear. Recent work on plagioclase crystallization during H_2O- and $H_2O–CO_2$-saturated magma decompression indicates that deep $H_2O–CO_2$ fluids could leave a lasting textural 'fingerprint' on erupted magmas (Riker et al., 2015), which may correlate with the alteration in some plagioclase-rich samples. In addition, emplacement of a plagioclase-rich mush has been proposed to explain the thick anorthosite layers in other layered intrusions (Raedeke, 1982; Czamanske & Bohlen, 1990; Bédard et al., 2007). Based on the magnetic susceptibility and non-cotectic proportions of plagioclase, it has been suggested that this process may have occurred in the UUMZ and in the Lower Main Zone, implying the existence of a sub-Bushveld magmatic staging chamber (Ashwal et al., 2005; Roelofse & Ashwal, 2012; Roelofse et al., 2015; Hayes et al., 2017). Importantly, as observed in our data, the most primitive plagioclase crystals within the reversal of each cycle nicely follow the overall differentiation trend of the UUMZ, which also indicates that the staging sub-chamber is continuously differentiating. Therefore, we conclude that the reversals documented in our study of the Bierkraal drill core samples, are caused by the emplacement of plagioclase-laden magmas, leading to the formation of plagioclase-rich layers within the reversal intervals of the UUMZ.

1.5.1.4   Origin of pmi-C rocks and magnetite layers in UZa and UZb

Substantial pmi-C horizons (including magnetite layers) are characteristic mineral assemblages within most cycles in UZa and UZb, but are mostly absent in UZc. Although the model of plagioclase mush emplacement can explain the basal anorthosites, another process is needed to account for the pmi-C and oxide-rich rocks in UZa and UZb.

Several lines of evidence indicate the pmi-C assemblage is produced by a hybrid melt created by magma mixing between the resident magma and the liquid of the new plagioclase-bearing batch. Firstly, the UUMZ sequences exhibit clear evidence for mush

emplacement as documented above. The emplacement of plagioclase-laden magma and the formation of anorthosite were then followed by mixing between the resident magma and the new magma batch. Magma mixing produces a hybrid melt that can be saturated in uncommon mineral assemblages (such as plagioclase and Fe-Ti oxides in this study). This is also confirmed by the first occurrence of magnetite (1832 m), which is in a pmi-C rock. The high Cr and primitive anorthite content of these pmi-C rocks, also indicate a correlation with the replenishing magma. A similar hybrid liquid with a magnetite/feldspar ratio of 30/70 has been observed in an experimental study by (Roeder & Osborn, 1966). Differences in the magnetite:plagioclase ratios in our samples can be explained by post-depositional modification. The PM, about 300 m below our cycle I, contains no Fe-Ti oxides. We therefore argue that some degree of fractionation, leading to the enrichment of FeO before magma mixing, is also needed to produce these pmi-C rocks.

Magnetite layers in the Bierkraal drill cores have been extensively studied and reported in previous publications. These layers commonly show a sharp lower contact with underlying anorthosite and a gradual contact with overlying anorthosite (McCarthy et al., 1985; Reynolds, 1985a; Cawthorn et al., 2005). This is also the case for our samples, as indicated in the lithological cycle. Crystal settling and sorting has typically been proposed to explain the magnetitite and chromitite layers in many layered intrusions (Cawthorn et al., 2005; Bai et al., 2012; Namur et al., 2015). However, the absence of pyroxene, which has an intermediate density between magnetite and plagioclase, leads to a gravity problem for a sorting mechanism (Cawthorn et al., 2005; Cawthorn & Ashwal, 2009) because the typical Bushveld magma saturated in plagioclase and magnetite is also saturated in pyroxene. The formation of hybrid magmas after mixing with plagioclase-laden magmas can solve this issue and explains the absence of pyroxene above the magnetite layers. We therefore propose that magnetite layers are the result of crystal settling from the pmi-C saturated magma, which is produced by magma mixing.

1.5.1.5 Synthesis model for the crystallization of the Upper Zone

After magma addition at the PM, the residual magma in the UUMZ chamber progressively evolved on a Fe-enrichment trend. Pulses of plagioclase-laden magmas were emplaced, forming the anorthosites at the bottom of each cycle (Figure 1.12a-c). Mush emplacement was subsequently followed by magma mixing between the resident magma and the new liquid; the mixing leads to a hybrid melt that produces a number of pmi-C rocks (Figure 1.12d). After the deposition of these pmi-C rocks, further cooling and differentiation drove the melt to become saturated with pyroxenes and olivine, and magnetite (olivine) gabbro norites crystallized (Figure 1.12e). A similar mush emplacement and magma mixing process occurred cyclically and produced the pmi-C liquid. Crystal sorting further led to the formation of the magnetite layer above the magnetite (olivine) gabbro-norite (Figure 1.12f-g).
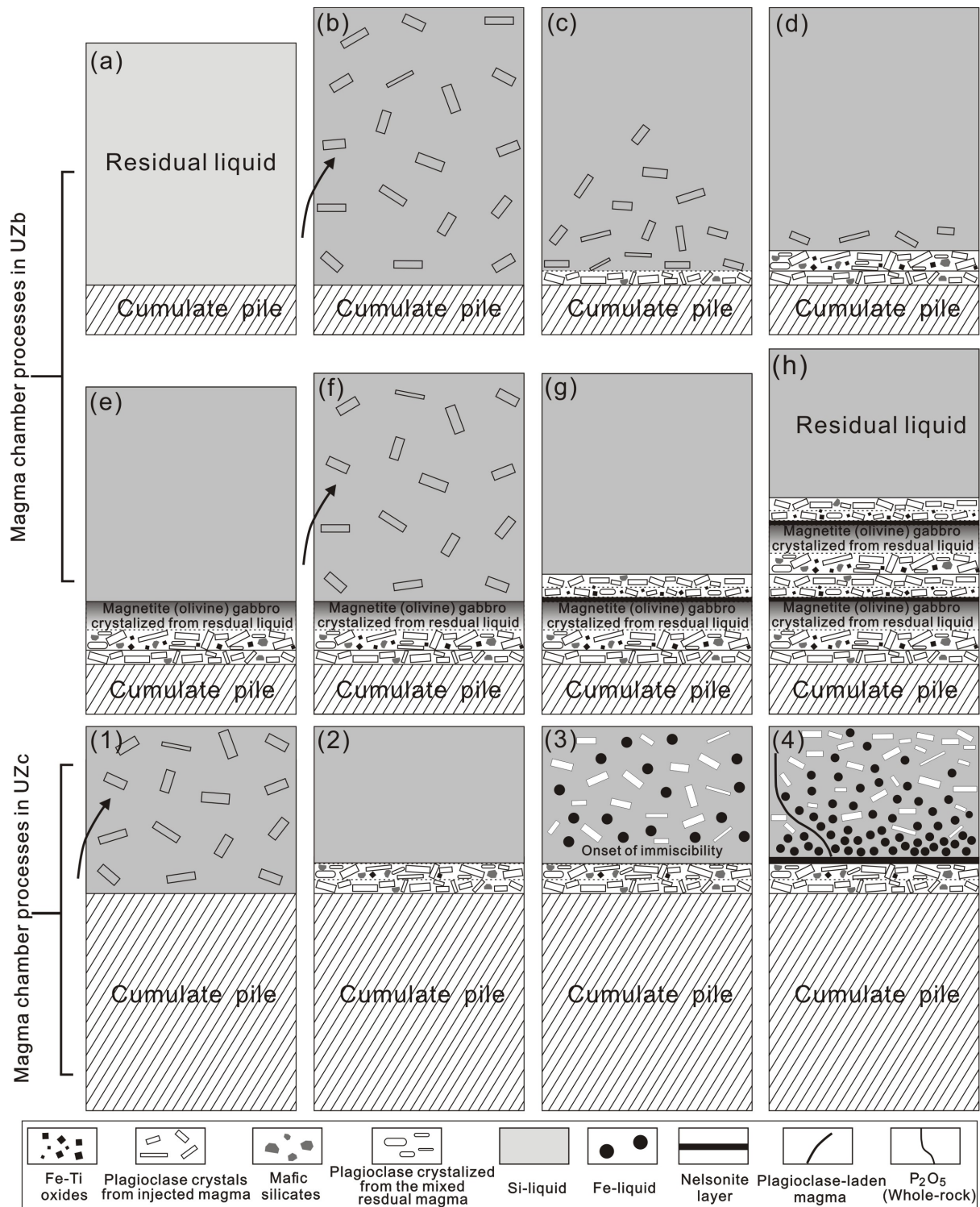
Figure 1.12 Schematic illustration of magma chamber processes in the Bushveld Complex, which can account for the typical litholo- gical sequence of anorthosite, pmi-C, magnetite (olivine) gabbro and oxide-rich rocks in UZb, and anorthositic, magnetite layer, nelsonite, magnetite troctolite and magnetite olivine gabbro observed in the phosphorus cycles in UZc. From Yuan et al. (2017).

In UZc, subsequent to the replenishment of crystal-laden magma, anorthosites formed in the basal part of each cycle (Figure 1.12i-j), followed by magnetite layers formed from hybrid magmas similar to those in UZa and UZb. After apatite saturation, immiscibility occurred immediately, preventing the formation of leucogabbros (Figure 1.12k) and leading

to downward percolation of the dense immiscible iron-rich liquid (Fischer et al., 2016; chapter 2 "Immiscible iron- and silica-rich liquids in the Upper Zone of the Bushveld Complex"). This resulted in the formation of a layer with a high proportion of Fe-Ti oxides, apatite and olivine, accumulated adjacent to the basal anorthosite, forming nelsonites and magnetite troctolites (Figure 1.12l).

Our model relies on new evidence for the close association between magnetite layers and anorthosite layers. The intermediate assemblage of pmi-C documented in UZa and UZb, closely related to the magnetite layers, is a cumulate product formed after mixing of the residual magma with replenished plagioclase-laden magma. This rock type provides a link between the formation of anorthosite and magnetite layers. Our model can explain the progressive upper contact with anothosite formed during the mush emplacement and the sharp lower contacts with anorthositic rocks (von Gruenewaldt, 1973; Molyneux, 1974). In addition, our model for UZc can also account for the sequence of magnetite, nelsonite, magnetite troctolite and magnetite olivine gabbro layers followed by magnetite-rich rocks in the typical lithological section of the phosphorous cycle. Finally, we can clearly identify different mechanisms for formation of magnetitite (magma mixing; Yuan et al., 2017) and nelsonite layers (immiscibility; Fischer et al., 2016) in the UUMZ, which may also shed light on the Fe-Ti-P layers in other mafic layered intrusions.

1.6   Summary

The Bushveld Complex contains world major resources of PGE's, iron, titanium, vanadium and other elements. With increasing demand for these elements, the Bushveld deposits are of significant economic interest. The distribution of valuable elements follows the characteristics of a layered intrusion in that certain elements are concentrated at distinct levels of the intrusion. However, the actual processes involved in the formation of these layers are still controversially debated. This study (Fischer et al., 2016; Yuan et al., 2017; this thesis) has produced a systematic dataset for whole rock compositions, mineral modes and silicate and Fe-Ti-oxide compositions for the Upper and Upper Main Zone of the Bushveld Complex. Using this database, allows to identify magmatic processes occurring during the formation of this part of the intrusion. The UUMZ is marked by several injections of a plagioclase-laden magma resulting in compositional reversal observed in e.g. plagioclase and bulk P_2O_5. Settling of transported plagioclase crystals formed the anorthosite layers and gabbroic rocks are the result of fractionation. The magnetite and pmi-C layers crystallize from a hybrid melt produced by mixing of resident and injected magma and nelsonite layers are formed by cumulates from immiscible Fe-P-rich silicate liquids.

2 Immiscible iron- and silica-rich liquids in the Upper Zone of the Bushveld Complex

Lennart A. Fischer [a,b], Meng Wang [a], Bernard Charlier [a,c], Olivier Namur [a], R. James Roberts [d], Ilya V. Veksler [e,f], R. Grant Cawthorn [g], François Holtz [a]

[a] *Institut für Mineralogie, Leibniz Universität Hannover, 30167 Hannover, Germany*
[b] *School of Physical Sciences, University of Tasmania, Hobart 7001, Australia*
[c] *Department of Geology, University of Liege, 4000 Sart Tilman, Belgium*
[d] *Department of Geology, University of Pretoria, Hatfield, Pretoria, 0002, South Africa*
[e] *Department of Mineralogy and Petrology, Technical University Berlin, 13355 Berlin, Germany*
[f] *Perm State University, Geological Department, Bukireva 15, 614990 Perm, Russia*
[g] *School of Geosciences, University of the Witwatersrand, PO Wits 2050, South Africa*

Abstract

The Bushveld Complex (South Africa) is the largest layered intrusion on Earth and plays a considerable role in our understanding of magmatic differentiation and ore-forming processes. In this study, we present new geochemical data for apatite-hosted multiphase inclusions in gabbroic cumulates from the Bushveld Upper Zone. Inclusions re-homogenized at high-temperature (1060–1100 °C) display a range of compositions in each rock sample, from iron-rich (35 wt.% FeO_{tot}; 28 wt.% SiO_2) to silica-rich (5 wt.% FeO_{tot}; 65 wt.% SiO_2). This trend is best explained by an immiscible process and trapping of contrasted melts in apatite crystals during progressive cooling along the binodal of a two-liquid field. The coexistence of both Si-rich and Fe-rich immiscible melts in single apatite grains is used to discuss the ability of immiscible melts to segregate from each other, and the implications for mineral and bulk cumulate compositions. We argue that complete separation of immiscible liquids did not occur, resulting in crystallization of similar phases from both melts but in different proportions. However, partial segregation in a crystal mush and the production of contrasting phase proportions from the Fe-rich melt and the Si-rich melt can be responsible for the cyclic evolution from melanocratic (Fe–Ti–P-rich) to leucocratic (plagioclase-rich) gabbros which is commonly observed in the Upper Zone of the Bushveld Complex where it occurs at a vertical scale of 50 to 200 m.

2.1 Introduction

Silicate liquid immiscibility and the unmixing of an iron-rich silicate melt and a silica-rich silicate melt has been identified in tholeiitic and andesitic magmas, both in volcanic settings (e.g. Philpotts, 1982; Charlier et al., 2013) and in plutonic environments (e.g. Jakobsen et al., 2005 Namur et al., 2012; Kamenetsky et al., 2013; Veksler & Charlier, 2015). In the case of the Bushveld Complex, South Africa (Figure 2.1), the development of immiscibility has been suggested to occur in the Upper Zone (UZ). Reynolds (1985a) and von Gruenewaldt (1993) suggested that the numerous (up to m scale) magnetitite and nelsonite layers in the UZ formed from an immiscible Fe-rich liquid. Scoon & Mitchell (1994) interpreted the occurrence of Fe-rich pegmatites in the Upper Critical Zone and the Lower Main Zone as having crystallized from an immiscible Fe-Ti-rich silicate melt derived from the UZ. This model was challenged by Cawthorn (2015) who presented several physical and chemical reasons for its implausibility. Based on a detailed study of rare earth element (REE) concentrations in apatite, VanTongeren & Mathez (2012) suggested a large-scale immiscibility process in the UZ, with a complete physical separation of the buoyant Si-rich melt from the dense Fe-rich melt. Data were re-interpreted by Cawthorn (2013b) who suggested that compositional variability in apatite results from re-equilibration with interstitial liquid in the crystal mush. The role of large-scale immiscibility on the differentiation of the Bushveld UZ has been further debated (Cawthorn, 2014; VanTongeren & Mathez, 2014) but consensus has not yet arisen, mainly because of the absence of any direct evidence for the existence of melts in cumulate rocks. This debate highlights the large uncertainty regarding the significance of liquid immiscibility for magma differentiation in plutonic settings.
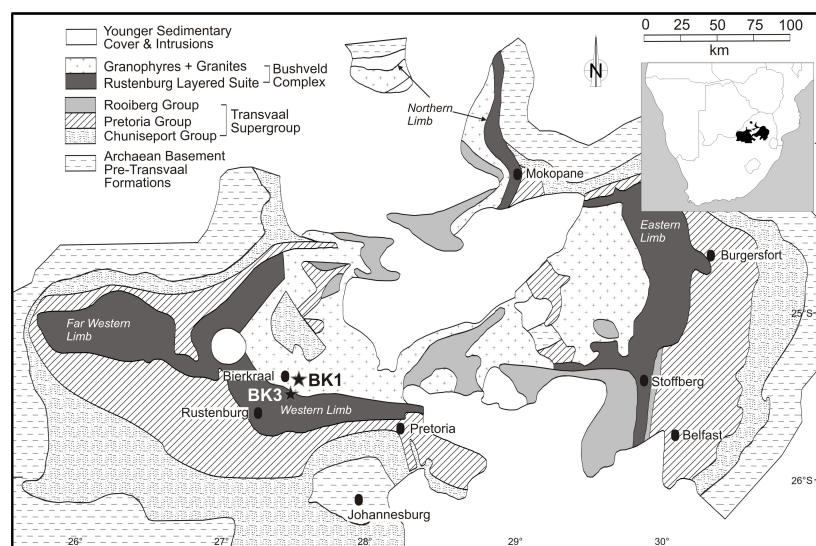
Figure 2.1 Geological map of the Bushveld Complex with location of BK1 and BK3 drill-cores (modified after Barnes & Maier (2002). Enlarged version in chapter 1 (Figure 1.3).

In this study, we investigated the petrography of polycrystalline apatite-hosted melt inclusions that we interpret as crystallized melt inclusions. For selected samples, we re-homogenized the inclusions at high temperature and measured their major element compositions. Based on these data, we present the first evidence for the coexistence of immiscible melts during the crystallization of the UZ of the Bushveld Complex. The coexistence of immiscible melts within gabbroic rocks formed by magma at the transition between basaltic and rhyolitic magmatism has implications for the dynamics of magma chambers, the density distribution of silicate melts and cumulate rocks, and the ore-forming processes of Fe-Ti-P-rich layers. This has also implications for the formation of evolved lavas (quartz monzonitic and rhyolitic compositions), which are closely associated to the Bushveld (Cawthron, 2013a; Mathez et al., 2013).

2.2   The Upper Zone of the Bushveld Complex

The Bushveld Complex, South Africa (Figure 2.1), includes a 7 km thick mafic cumulate sequence emplaced in three limbs. These cumulates are divided into the Marginal, Lower, Critical, Main, Upper and Roof Zones and their corresponding subdivisions (Wager & Brown, 1968). The base of the UZ (subzone UZa) is defined by the appearance of cumulus titanomagnetite, which is followed by the appearance of olivine (UZb) and finally apatite (UZc). The initial emplacement of magma in the Bushveld occurred at 2055.91±0.26 My, and the whole intrusion cooled to below 650°C in 1.02±0.63 My (Zeh et al., 2015). Cawthorn & Walraven (1998) proposed an even shorter crystallization time of 200.000 years.

The Upper Zone and Upper Main Zone above the Pyroxenite Marker (hereinafter referred to as UUMZ) are generally considered as having crystallized from a single batch of magma following a large event of magma chamber replenishment (Cawthorn et al., 1991; Tegner & Cawthorn, 2010; VanTongeren & Mathez, 2013).

The UUMZ interval is famous for the occurrence of numerous layers of magnetitite and nelsonite (Molyneux, 1974; von Gruenewaldt et al., 1985; von Gruenewaldt, 1993), the major World resource for vanadium. Tegner et al. (2006) identified 26 magnetite and 6 nelsonite layers in the UZ in the Western Limb of the Bushveld Complex. Crystallization of abundant Fe-rich minerals drove residual liquids towards SiO_2-enrichment (Tegner et al., 2006; Tegner & Cawthorn, 2010). The roof sequence of the Bushveld is poorly defined and the uppermost rocks of the layered intrusion could be either quartz monzonites (Cawthorn, 2013a) or mafic cumulates if evolved residual melts were erupted from the magma chamber (Tegner et al., 2006; VanTongeren et al., 2010).

Although there is a distinct overall differentiation up-section in the UUMZ Figure 2.2), compositional reversals in minerals and significant changes in bulk rock chemistry were described, possibly indicating multiple events of magma replenishment (von Gruenewaldt, 1973; Molyneux, 1974; Ashwal, 2005; Scoon & Mitchell, 2012). Tegner et al. (2006) defined

nine cyclic units based on whole-rock and mineral compositions (whole-rock P_2O_5 content, anorthite in plagioclase, Mg# in pyroxenes and olivine, and V_2O_5 in magnetite). Six cycles with apatite-bearing rocks (nelsonites, gabbros) occur in the upper half of the UZ (Figure 2.2) of the western Bushveld (subzone UZc). In each of these cycles (50 to 200 m-thick), P_2O_5 in the whole-rock first increases from very low concentrations (<0.2 wt%) up to 10 wt.% (23 wt.% apatite) and then decreases continuously upwards to 0.5 wt.% (Figure 2.2).
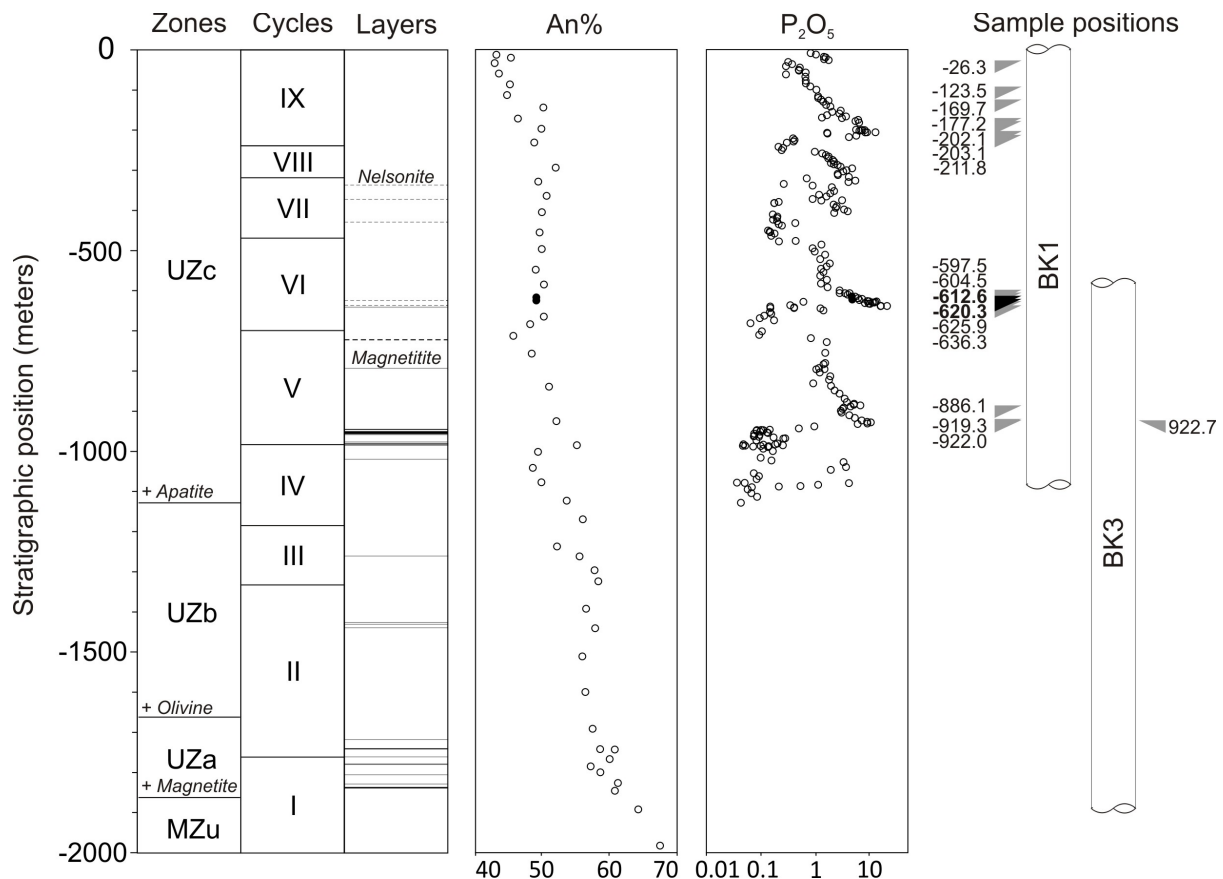
Figure 2.2 Schematic stratigraphic column of the upper part of the Bushveld Complex showing cycles, magnetite and nelsonite layers, plagioclase composition (An%) (all from Tegner et al., 2006), P2O5 concentration in whole rock (Cawthorn and Walsh, 1988), and samples in drill-cores BK1 and BK3. Subzones are defined by the appearance of cumulus titanomagnetite (UZa), of olivine (UZb) and apatite (UZc). Dashed lines correspond to nelsonite layers, solid lines to magnetitite layers. Black symbols along the drill cores correspond to samples selected for re-homogenization while symbols in grey are samples used for petrographic description and geochemical mapping of un-homogenized melt inclusions.

It is commonly assumed that evolved, rhyolitic magma escaped from the Bushveld magma chamber during the late stages of differentiation (Cawthorn & Walraven, 1998; Tegner et al., 2006; VanTongeren et al., 2010). The most recent investigation of the parental magma (VanTongeren et al., 2010) of the UUMZ is based on a careful summation of cumulate compositions to which 15-25 vol. % of rhyolitic magma (average compositions of the Damwal, Kwaggasnek, Schrikkloof and Rashoop formations) was added. This amount of

rhyolite is required to stabilize orthopyroxene, clinopyroxene and plagioclase, which are the first liquidus phases in the UUMZ (Tegner et al., 2006; VanTongeren et al., 2010). Potential parental magmas for the UUMZ are therefore not typical ferrobasalts such as those observed in mid-ocean ridges or continental flood basalts (Charlier et al., 2013). They are enriched in SiO_2 (> 50 wt.%), CaO and Al_2O_3, making them more similar to iron-rich tholeiitic andesites.

2.3   Methods

2.3.1   Sampling

The samples selected for this study come from the Bierkraal (BK) drill-cores BK1 and BK3 (Kruger et al., 1987; von Gruenewaldt, 1993; Tegner et al., 2006;Figure 2.2), and cover the entire UZc of the Western Limb of the Bushveld Complex. To correlate samples from both drill-cores we calculated the inferred stratigraphic position for each sample following the equations of Tegner et al. (2006) taking dip angle and roof contact into account.

We have investigated 17 samples from 3 different cycles from the UZc (IX, VI and V; Fig. 2). The rocks can be characterized as Fe-Ti-oxide troctolites, consisting mainly of plagioclase, olivine, Fe-Ti-oxides and apatite (see Supplemental Table S4). For all samples, we performed a detailed petrographic examination, including a study of apatite-hosted inclusions. Such inclusions are commonly interpreted to represent equilibrium melts trapped during the growth of their host minerals, and in other intrusions they have been shown to provide unambiguous evidence for the development of immiscibility (Jakobsen et al., 2005; Charlier et al., 2011; Liu et al., 2014). Among studied samples, we selected two rock samples from cycle VI (Tegner et al., 2006) at calculated stratigraphic depths of -612.6 m (sample BK1-1085: 1085 m being the original sample depth in drill-core) and -620.3 m (sample BK1-1094), with the '0 m' reference corresponding to the top of the ferrodioritic cumulates identified at a depth of 415m in the BK1 drill-core. In these two rock samples, we re-homogenized apatite-hosted melt inclusions at high temperature and performed a detailed geochemical analysis of these inclusions.

2.3.2   Re-homogenization of melt inclusions

Minerals from samples BK1-1085 and BK1-1094 were separated using high voltage pulses with a SELFRAG fragmentation system at the Goethe University Frankfurt. Minerals were then sieved and we kept the fraction with grain sizes between 250 to 1500 µm, corresponding to the observed sizes of apatite grains. Olivines and Fe-Ti-oxides were separated using a FRANTZ magnetic separator. Apatites were then separated from

plagioclase using LST heavy liquid (solution of sodium heteropolytungstates in water; specific gravity: 2750 kg/m^3).

Only non-fractured apatite crystals with multiphase inclusions were selected for re-homogenization in an internally heated pressure vessel (IHPV; Berndt et al., 2002). Apatite crystals were loaded in open Pt-capsules together with graphite to reach reducing conditions. The IHPV was pressurized with Ar to a final pressure of 100 MPa and then heated isobarically from 25°C to 1060°C or 1100°C in 2 hours. These temperature conditions were necessary to produce crystal-free melt inclusions and correspond to the liquidus temperature of evolved monzonitic magmas (Charlier et al., 2011; Charlier & Grove, 2012). When final temperature was reached, it was held constant for 30 min before we rapidly quenched the samples on a copper plate. The cooling rate was ~ 150°C/s. Temperature was controlled using two S-type thermocouples (stable within ± 2°C) and two additional S-type thermocouples were used to monitor the sample temperature. Temperature gradient across the sample is generally less than 5°C. Classical melt inclusion homogenization on a heating stage failed at keeping apatite grains from cracking.

2.3.3 Analytical method

Standard thin sections of the rocks were prepared for petrographic and mineral analyses. Individual crystals of apatite were mounted in epoxy and polished to expose the re-homogenized inclusions. The homogenized melt inclusions and minerals were analyzed by electron probe micro-analyzer (EPMA) using a Cameca SX100 at the Institute of Mineralogy in Hannover, Germany. Analyses were conducted with an acceleration voltage of 15 kV. Raw data were corrected with the software "Peak Sight" and "PAP" matrix (Pouchou & Pichoir, 1991). Minerals were analyzed with a beam current of 15 nA and a focused beam (1 µm). The counting time for each element was 10 s. Glasses were analyzed using a beam current of 4 nA for major elements. The beam size was 5 µm. The counting time for individual elements varied between 4 and 30 s. The following standards were used: wollastonite for Si and Ca, Al_2O_3 for Al, Fe_2O_3 for Fe, MgO for Mg, rutile for Ti, albite for Na, orthoclase for K, Mn_3O_4 for Mn, apatite for P_2O_5. Geochemical mapping of apatite-hosted inclusions before homogenization was performed with a Hitachi SU-70 field emission scanning electron microscope (FE-SEM) and processed with the Oxford Instruments AZtec software at the University of Tasmania.

2.4 Results

2.4.1 Petrography of host rocks

Samples BK1-1085 and BK1-1094 are coarse-grained Fe-Ti-oxide troctolites, containing mainly plagioclase (modal proportion: 37%), olivine (26%), Fe-Ti-oxide (25%), apatite (10%) as well as minor clinopyroxene (2%) (Figure 2.3A). Sulfides, chlorite and biotite occur as accessory minerals. Plagioclase is anhedral to subhedral in shape, ranges in size from 1 to 5 mm and shows no zoning. The anorthite content is 49 ± 2 mol%, similar to the data reported by Tegner et al. (2006) for nearby samples in BK1. Olivine crystals are anhedral to subhedral with a size ranging between 0.5 and 2 mm. Olivines from sample BK1-1094 have a forsterite (Fo = molar $100*[Mg/(Mg+Fe)]$; with Mg and Fe in molar proportions) content of Fo26 and are slightly more magnesian than those from BK1-1085 (Fo22). Olivines from both samples have slightly higher Fo content than olivines from similar depth reported by Tegner et al. (2006). This may be due to diffusive re-equilibration with abundant Fe-Ti

Figure 2.3 Microphotographs of apatite-bearing troctolites from the Upper Zone of the Bushveld intrusion, and melt inclusions in apatite. **A:** Apatite-bearing troctolite (transmitted polarized light; sample BK1-1094); **B:** Unhomogenized multiphase in- clusions trapped in a single grain of apatite (transmitted polarized light; sample BK1-1094); **C:** Homogenized Si-rich inclusion at the top of the photograph and Fe- rich inclusion at the bottom of the photograph (transmitted polarized light; sample BK1-1094). Scale bars are 2 mm (A), 100 μm (B), and 50 μm (C).

oxide minerals (Pang et al., 2009). Fe-Ti oxides (Ti-magnetite and ilmenite) occur as anhedral patches often associated with apatite. The TiO_2 concentration in magnetite varies between 15 and 25 wt.%. Apatites are 0.2 - 1.5 mm in size, euhedral in shape and can be characterized as fluorapatite.

2.4.2 Petrography of apatite-hosted inclusions

All 17 studied samples contain apatite grains with abundant multiphase inclusions (Figure 2.3B) however, in most samples, apatite crystals are very small (< 200-500 μm). Single apatite crystals often host several inclusions, locally with different daughter mineral

assemblages. Inclusions are rounded to elongated in shape, generally orientated parallel to the crystallographic c-axis of apatite, and their sizes range from 10 µm to 100 µm (Figure 2.3B). The inclusions are fully crystallized and their mineralogy was assessed from multi-element mapping. Elemental maps show that single inclusions contain different minerals in various proportions, the major phases being feldspar, pyroxene, amphibole and olivine (Fig. 4). Minor phases such as ilvaite, chlorite, biotite and Fe-Ti-oxides are locally observed. Feldspars and clinopyroxenes are the dominant phases, whereas chlorite and biotite occur predominantly in inclusions in cracked apatites. We interpret the presence of these hydrous phases as a result of alteration processes in inclusions which were not closed. Crystallized inclusions with highly contrasted mineral modes can be observed in a single apatite grain. Feldspars show a variety of compositions and are mostly present as albite or orthoclase, but can occur with oligoclase to andesine or anorthoclase composition. Olivines have a forsterite content lower than Fo35 but rarely occur as pure fayalite. Crystal boundaries between feldspars are often blurred but sharp to other phases (Figure 2.4A). Clinopyroxene shows only minor variations in composition and can mostly be classified as hedenbergite. Orthopyroxene occurs in Fe-rich inclusions (Figure 2.4B) with Mg# (molar [Mg/(Mg+Fe)]*100) ranging between 59 and 71. Amphiboles show a wide range in
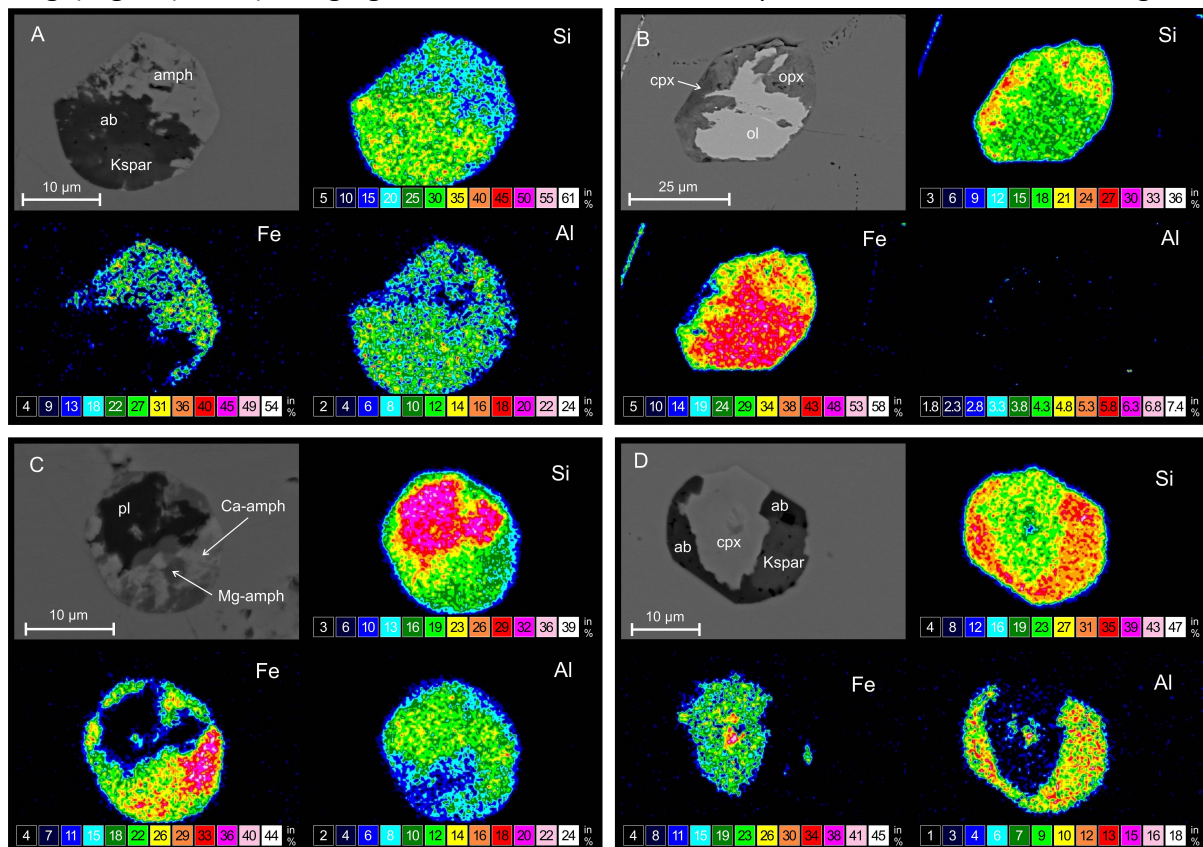
Figure 2.4 Geochemical mapping and corresponding BSE image, of un-homogenized apatite-hosted inclusions, showing multiple daughter phases. **A:** Si-rich inclusion with amphibole (amph), albite (ab) and orthoclase (Kspar) as daughter phases. **B:** Fe-rich inclusion with orthopyroxene (opx), clinopyroxene (cpx) and olivine (ol). No Al-bearing phase is visible but feldspar is likely to be present and not exposed at the surface. **C:** Inclusion with intermediate composition with plagioclase (pl), calcic amphibole and magnesian amphibole. **D:** Inclusion with intermediate composition with albite, clinopyroxene and orthoclase.

composition from calcic- to Mg-amphiboles with relatively high FeO (Figure 2.4C). Ilvaite shows no compositional variations and occurs as small homogeneous crystals.

As illustrated in Figure 2.4, inclusions show a large spectrum of daughter phases in different proportions independently of the sample location. Considering the lack of three-dimensional information in geochemical maps (Figure 2.4) and the chemical heterogeneity of some crystals, the bulk composition of the inclusions can only be determined from the analysis of glasses obtained after re-homogenization in order to get reliable and unambiguous liquid compositions.

2.4.3 Compositions of re-homogenized inclusions

We studied 99 homogenized melt inclusions in 62 apatite grains from samples BK1-1085 (38 inclusions in 22 apatites) and BK1-1094 (61 inclusions in 40 apatites). Homogenized inclusions show no residual crystal phases and usually contain a gas bubble (Figure 2.3C). Chemical profiles across the inclusion-apatite boundary show no compositional gradient. Results of EPMA measurements for inclusions are presented in Figure 2.5 and Supplemental Table S5, in which each melt inclusion is represented by one data point. Inclusions cover a wide compositional range from iron-rich (35 wt.% FeO_{tot}; 28 wt.% SiO_2), to silica-rich (5 wt.% FeO_{tot}; 65 wt.% SiO_2) (Figure 2.5A). Intermediate compositions are also observed but a compositional gap occurs between 40 and 50 wt.% SiO_2 in sample BK1-1094. Multiple inclusions in a single apatite grain always display distinctly contrasted compositions. Overall, Al_2O_3 (Figure 2.5B), Na_2O and K_2O increase linearly with SiO_2, whereas MgO and P_2O_5 decrease. CaO does not show a simple linear trend (Figure 2.5C). When plotted against SiO_2, the CaO content first increases from 12 to 17 wt.% with SiO_2 increasing from 28 to 39 wt.%, and then decreases down to 3 wt.% at 65 wt.% SiO_2. The highest CaO values that we observe are surprising high compared to typical basaltic magmas (e.g. 10-12 wt.% CaO; Jenner & O'Neill, 2012), ferrobasalts (e.g. 8-10 wt.% CaO; Toplis & Carroll, 1996; Thy et al., 2009, andesitic magmas (8-11 wt.% CaO; Wilkinson, 1986) and even Fe-rich immiscible melts (6-14 wt.% CaO; Charlier et al., 2011; Charlier & Grove, 2012). An obvious reason for this high CaO content would be substantial melting of apatite during melt inclusion homogenization. However, considering a melt with 40 wt.% SiO_2 and using equations from Harrison & Bruce (1984), we calculated that melting above the liquidus from 1050°C to 1100°C would produce an increase from 3.38 to 3.96 wt.% P_2O_5 in the silicate melt, corresponding to an increase of 0.75 wt.% CaO. This increase in solubility of apatite with temperature does not explain the extremely high CaO values of the melt inclusions compared to the estimated CaO contents of Bushveld UZ magmas (~ 10 wt.% CaO at F = 1 to < 4 wt.% CaO at F = 0.2; with F being the residual liquid fraction; Tegner et al., 2006).
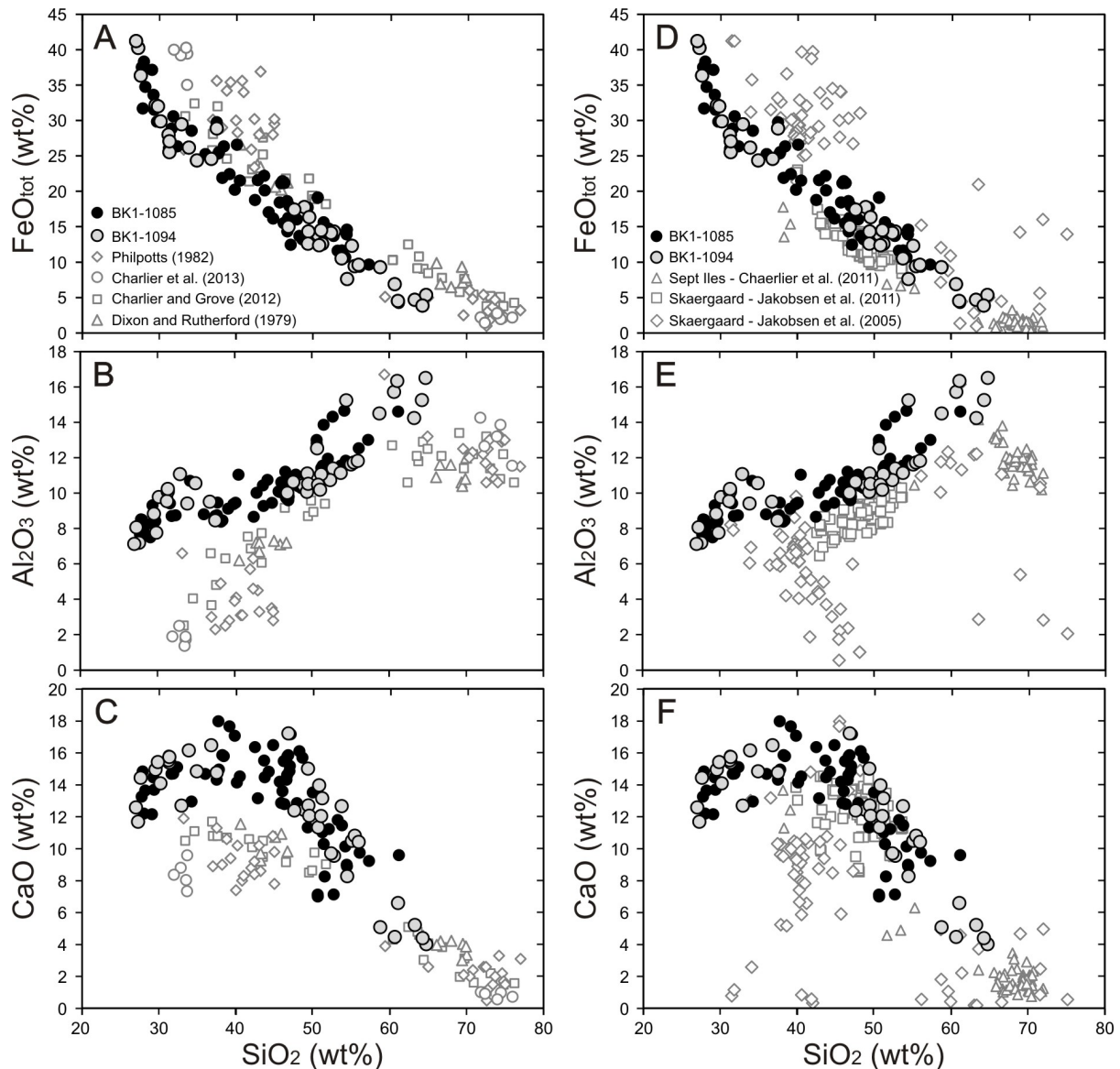
Figure 2.5 Compositional variations of re-homogenized melt inclusions for FeO$_{tot}$; Al$_2$O$_3$; CaO as a function of SiO$_2$ (wt.%). Dataset is compared to **A–C:** Immiscible melts observed in experiments (Dixon & Rutherford, 1979; Charlier & Grove, 2012) and in natural tholeiitic basalts (Philpotts, 1982; Charlier et al., 2013); **D–F:** Melt inclusion compositions from Skaergaard (Jakobsen et al., 2005; 2011) and Sept Iles (Charlier et al., 2011).

2.5 Discussion

2.5.1 Liquid line of descent and onset of immiscibility

Daughter phase compositions of the analyzed melt inclusions differ significantly from cumulate mineral compositions. Olivine in inclusions span a very large compositional range (Fo0 to Fo35), whereas cumulus olivines show a more restricted range between Fo22 and Fo26. Plagioclase in inclusions is mostly present as albite or orthoclase endmember composition (~ An0), whereas the cumulate plagioclase composition is around An50. This compositional differences between cumulate and daughter minerals imply that the studied inclusions represent crystallized liquid compositions rather than trapped minerals.

The large compositional variations of these melt inclusions may be explained either by the entrapment of liquids reflecting different differentiation stages or by liquid immiscibility. To test the first hypothesis we calculated possible liquid lines of descent (LLD) for the UUMZ with the MELTS thermodynamic algorithm (Ghiorso & Sack, 1995) for 8 different starting compositions at oxygen fugacities (fO_2) between FMQ-1 and +1 (FMQ: corresponding to the quartz-fayalite-magnetite buffer) and initial H_2O contents of 0.1 and 1.0 wt.% (VanTongeren et al., 2010; Figure 2.6 and Supplemental Figure S1). The 8 different starting compositions were proposed by VanTongeren et al. (2010) and correspond to a mixture between the bulk composition of the UUMZ and 15 - 25 wt% of various rhyolite melts which are assumed to have escaped from the magma chamber (VanTongeren et al., 2010). According to petrographic study of VanTongeren et al., (2010) we only present LLDs in which orthopyroxene

Figure 2.6 FeO_{tot} (wt.%) vs. SiO_2 (wt.%) diagram showing potential liquid lines of descent (LLD) for the Upper and Upper Main Zone (UUMZ) of the Bushveld Complex. Grey lines represent results of MELTS calculations (Ghiorso and Sack, 1995) at three dif- ferent oxygen fugacity conditions (FMQ+1, FMQ and FMQ–1). Dashed black lines represent LLDs from Tegner et al. (2006) and Tegner and Cawthorn (2010). We used 8 starting compositions (see Supplemental Table S6 and Supplemental Figure S1) repre- senting a mixture between the bulk composition of the UUMZ (VanTongeren et al., 2010) and 15–25 wt.% of a rhyolite formation (Damwal, Kwaggasnek, Schrikkloof and Rashoop). Calculations were performed for initial H_2O contents of 0.1 and 1.0 wt.%. We only present LLDs for which orthopyroxene crystallizes as the first cu- mulus phase (VanTongeren et al., 2010). Black arrow outlines the average fractional crystallization trend from the MELTS calculations.

crystallizes as the first cumulus phase (Supplemental Figure S1). Whatever the fO_2 conditions, the initial water content and the parent magma used in the calculations, the UUMZ magmas first record a stage of iron-enrichment before titanomagnetite saturation. The maximum FeO_{tot} content of the melt at titanomagnetite saturation is usually close to 15 wt.%. After magnetite saturation, residual melts evolved towards SiO_2-enrichment and FeO depletion. Although MELTS may have some limitations in Fe-rich and Si-rich systems (Ghiorso & Sack, 1995), our calculations are in very good agreement with the results obtained by Tegner et al. (2006) and Tegner and Cawthorn (2010) using detailed mass balance calculations between liquid and cumulate rocks and analysis of FeO in cumulus plagioclase.

Homogenized melt inclusions in apatite show a compositional range much larger than the inferred LLDs (Figure 2.6). Evolved melt inclusions with 60-65 wt.% SiO_2 could have been produced by fractional crystallization of the UUMZ parental magma (Tegner et al., 2006; VanTongeren et al., 2010; Supplemental Figure S1; Figure 2.6) but the iron-rich melts that we observe in melt inclusions plot away from any potential trend of fractional

crystallization. This suggests that at least some melts trapped in apatite grains were not produced by a simple fractional crystallization process (Figure 2.6). Instead, we interpret the existence of Fe-rich compositions with more than 18 wt.% FeO as an indication that silicate liquid immiscibility developed during crystallization of the UUMZ. In addition, the large compositional variation of melt inclusions would indicate that the melt inclusions of one sample have been trapped over a temperature interval, as discussed below. Following this reasoning, the evolved, silica-rich melt inclusions, could also have been produced by immiscibility and could represent the conjugate Si-rich melts of the Fe-rich melt inclusions. In this hypothesis, the calculated LLDs hit the two-liquid field during evolution from iron-rich basaltic andesite to silica-rich compositions leading to the separation of an Fe-rich melt and a Si-rich melt (Charlier & Grove, 2012; Namur et al., 2012; Figure 2.7).

Immiscible melt inclusions have also been described in the Skaergaard (Jakobsen et al., 2005; 2011) and Sept Iles layered intrusions (Charlier et al., 2011; Namur et al., 2012). Melt inclusions in Skaergaard are observed in apatite and olivine from the Upper Zone (Jakobsen et al., 2005) and in plagioclase from the top of the Lower Zone (LZc) to the Upper Zone (Jakobsen et al., 2011). Apatite hosted inclusions are larger (10-200 μm) compared to those from this study but have a similar appearance. When combined with the plagioclase hosted inclusions, data show a similar continuous Fe-rich to Si-rich compositional range (Figure 2.5D). This was interpreted by Jakobsen et al. (2011) as trapping of droplets of both liquids in different proportions. Charlier et al. (2011) presented inclusions hosted in apatite from the most evolved cumulates of the Sept Iles layered intrusion. Their melt inclusions are similar in shape and size (10-120 μm) to the inclusions from this study. Melt inclusions from Sept Iles show a smaller compositional range from 18 wt.% FeO_{tot} and 38 wt.% SiO_2 to 0.5 wt.% FeO_{tot} and 70 wt.% SiO_2 (Charlier et al., 2011), with a complete absence of intermediate compositions.

2.5.2 Trapping of melt inclusions and compositional evolution during cooling

The compositional range that we observe in a single sample is much broader than expected if two immiscible end-members were trapped at a single temperature. Incomplete segregation of two immiscible end-members at a μm-scale (e.g. Jakobsen et al., 2011), and trapping of melt along the binodal surface during cooling (e.g. Charlier and Grove, 2012), can result in a wide compositional range for melt inclusions. Simple mixing of different proportions of paired melts produces linear trends for all major elements. Although we observe linear trends for most elements, the behaviour of CaO cannot be explained by simple mixing of two immiscible poles and as demonstrated above was not significantly affected by apatite melting during the experiments. Although we cannot exclude that some melt inclusions represent an emulsion of unsegregated immiscible melts, we suggest that most of the compositional range that we observe is controlled by a temperature-dependent evolution of element partitioning between immiscible melts. This is confirmed by

experimental data showing that CaO partitioning between the Fe- and Si-rich liquids is indeed strongly dependent on temperature, melt composition, and melt structure (Bogaerts & Schmidt, 2006; Charlier & Grove, 2012), which results in a non-linear CaO vs. SiO_2 trend of immiscible pairs (Figure 2.5C). The expansion of the two-liquid field during cooling is responsible for the formation of increasingly contrasted melts as temperature decreases (Charlier and Grove, 2012). Trapping inclusions along the binodal surface produces a large range of compositions between conjugate melts. Si-rich and Fe-rich melts are presumably close in composition at high temperatures (when the liquid line of descent first hits the solvus) and then become increasingly contrasted as temperature decreases (Figure 2.7).

Considering that the range of liquid compositions that we observe represents trapping of melt inclusions at different temperatures rather than trapping an emulsion of immiscible melts, we can use experimental data to estimate the degree of crystal mush cooling during apatite crystallization. Experimental immiscible melt pairs reported in Charlier and Grove (2012) show that, depending on where the LLD hits the binodal surface, it is possible to produce pairs with 60-65 wt.% SiO_2 and 8-11 wt.% FeO_{tot} vs. 42-50 wt.% SiO_2 and 19-22 wt.% FeO_{tot} at 1020°C, and 73-76 wt.% SiO_2 and 4-6 wt.% FeO_{tot} vs. 31-36 wt.% SiO_2 and 25-32 wt.% FeO_{tot} at ca. 960°C. This compositional range is relatively similar to the melt inclusion compositions that we observe, which suggests that melt inclusions were trapped during apatite growth on a temperature interval of ~ 60°C. No estimate of liquidus temperature exists for the Bushveld UZ but we note that our calculated interval of 60°C (1020-960°C) is almost identical to that between apatite saturation and the solidus of the Skaergaard magma (1040-980°C; Thy et al., 2009). We therefore suggest that this temperature interval can realistically span the liquidus temperature down to the complete solidification of the crystal mush.
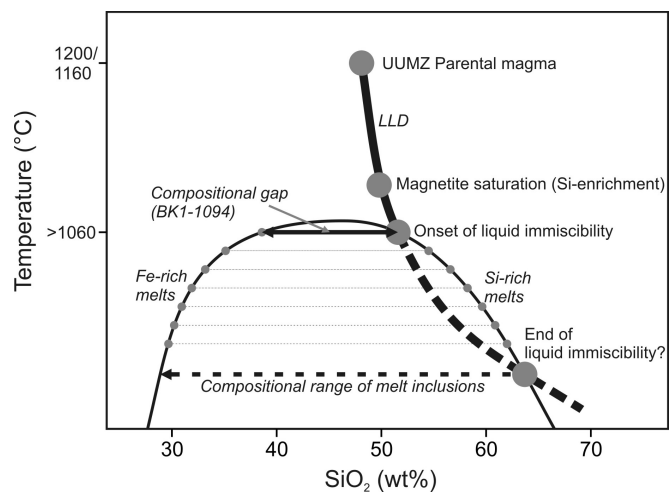
Figure 2.7 Schematic liquid line of descent (LLD) for the Bushveld UUMZ parental magma plotted in a temperature (no precise scale) vs. SiO_2 (wt.%) diagram. Upon cooling, the LLD (solid line) becomes saturated in magnetite and then reaches the two-liquid field (onset of immiscibility), below 1060◦C (minimum tempera- ture for melt inclusion homogenization). Pairs of Fe- and Si-rich melts are then formed. With cooling, the immiscibility field expands and melt pairs become more contrasting in composition. No liquid between 40 and 50 wt.% SiO_2 is produced (compositional gap observed in sample BK1-1094). Intermediate compositions in sample BK1-1085 are explained by incomplete separation of the immiscible melts (Jakobsen et al., 2011). The heavy dashed line represents the evolution of the bulk liquid (Fe-rich + Si-rich). The most contrasting compositions of melt inclusions are reached just before the bulk liquid possibly leaves the two-liquid field.

2.5.3 Migration of immiscible melts in a crystal mush and formation of layering

Immiscible Fe-rich and Si-rich pairs have contrasting physical properties, i.e. higher density and lower viscosity for the Fe-rich melt (Philpotts, 1982; Charlier & Grove, 2012; Namur et al., 2015). However, their ability to separate is also dependent on other parameters such as cooling rate, globules coarsening, interfacial tension, and wetting properties with cumulus phases (Martin & Kushiro, 1991; Mungall & Su, 2005; Chung & Mungall, 2009; Veksler et al., 2010), which makes difficult any prediction for a specific plutonic environment. Moreover, owing to the dome-like shape of the immiscibility binodal surface (Figure 2.7), if two immiscible liquids form and segregate, each liquid will exsolve its conjugate as the temperature decreases. Consequently, even if perfect segregation of the paired melts is reached at the onset of immiscibility, both liquids will keep evolving on the binodal surface that will continue to diverge with falling temperature.

The hypothesis of large-scale separation of two layers of immiscible melts in the Bushveld Complex, illustrated on Figure 2.8A, was based on an abrupt change of the REE content of cumulus apatite between two horizons of the UZ in the Eastern limb (VanTongeren & Mathez, 2012). This process was inferred to result in the formation of a lower, dense, 300 m-thick, cumulate section with low concentration of REE in apatite, representing the crystallization products of the iron-rich melt, and an upper, buoyant 325 m cumulate section with REE-rich apatites, formed by crystallization of the silica-rich melt. This model requires that the two melts separate completely and diverge from the equilibrium compositions following their own LLD (VanTongeren & Mathez, 2014). In the Western limb, REE data in apatite presented by Cawthron (2014) show a relatively continuous increase from the most primitive apatite-bearing gabbros to the top of the intrusion. This pattern suggests continuous evolution of the main magma body by fractional crystallization rather than segregation and chemical isolation of two thick layers of immiscible melts (VanTongeren et al., 2012). It is therefore possible that the processes of crystallization in the different limbs of the Bushveld are different which is perhaps suggested by the different bulk rock stratigraphic trends in the Western limb (Figure 2.1), the Northern limb (Ashwal et al., 2005) and the Eastern limb (Scoon & Mitchell, 2012). In the Western limb where we observe a succession of 200-300 m thick cycles with a bottom made up of melano-gabbro followed by progressively more leuco-gabbroic rocks, we suggest that immiscibility occurred repetitively as already suggested for the Sept Iles layered intrusion (Charlier et al., 2011). Sorting of immiscible melt droplets in the crystal mush led to the development of horizons dominated by Fe-rich melt at the bottom (which mostly crystallized Fe-Ti oxide minerals and apatite) and Si-rich melt at the top (which mostly crystallized plagioclase-rich rocks). Nevertheless, during cooling, Fe-rich and Si-rich liquids stay in equilibrium and minerals with identical compositions but different proportions crystallize from the two liquids. The reversals in mineral compositions (plagioclase An-content and the Mg number of mafic
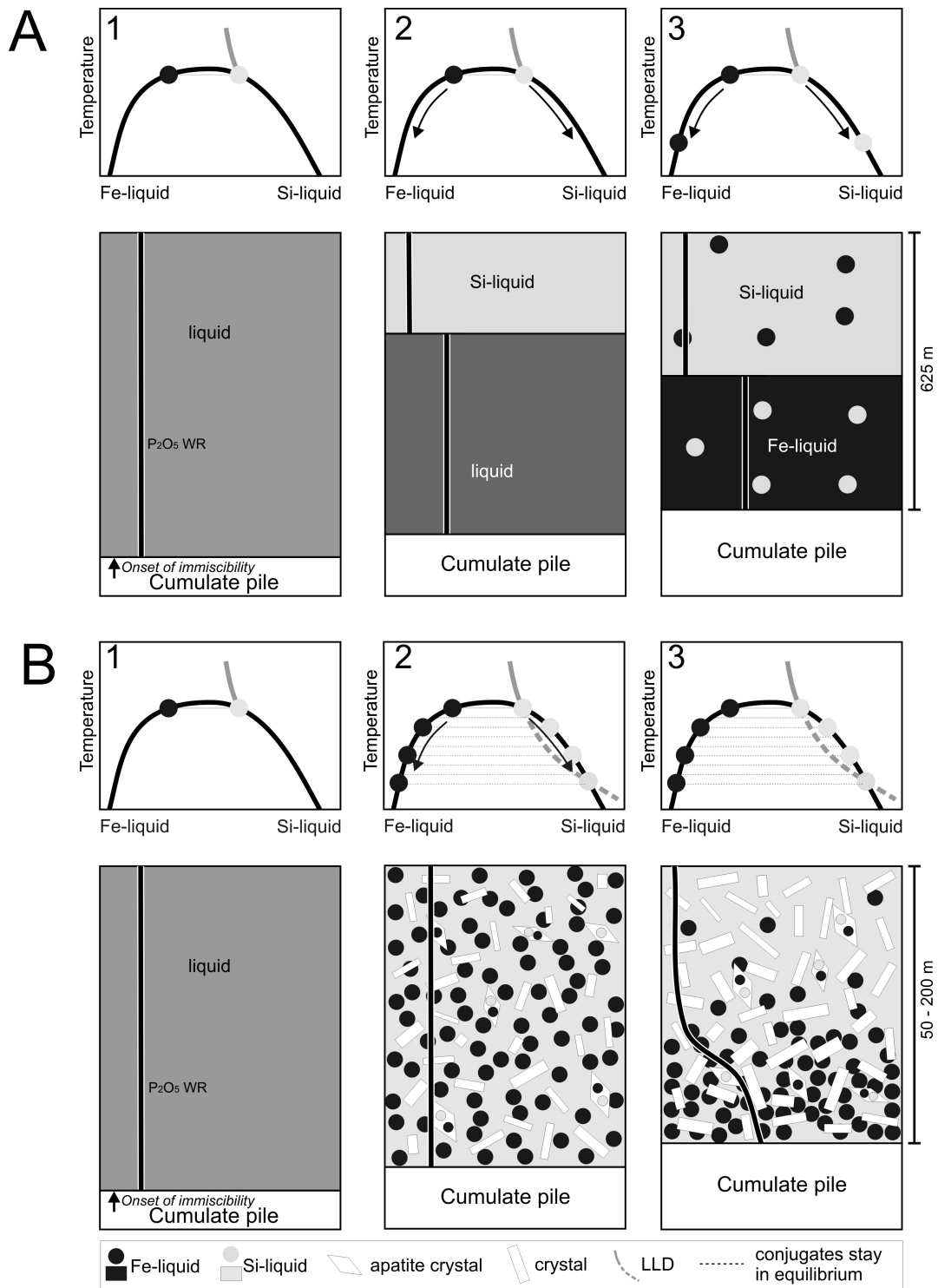
Figure 2.8 Schematic illustration of the liquid immiscibility process on two different scales in the Bushveld Complex. A: The large-scale separation of two immiscible layers as proposed by VanTongeren and Mathez (2012); 1: Bulk liquid composition reaches the two liquid field and Fe- and Si-rich melt start segregate. 2: With cooling liquids become more distinct in composition and separate from each other by density differences. 3: Both liquids diverge from equilibrium and separate into a thick 300 m Fe-rich layer and an overlaying 325 m thick Si-rich layer. B: The equilibrium immiscibility model as proposed in this study. 1 Bulk liquid composition reaches the two liquid field and Fe- and Si-rich melt start to segregate with a progressive enrichment of the dense Fe-rich melt at the base of the crystal mush. 2: With cooling liquids become more distinct in composition but stay in equilibrium 3: Melt droplets are sorted in the crystal mush and crystallized mela- to leucogabbros.

minerals) at the bottom of each cycle could be related to magma chamber replenishments (von Gruenewaldt, 1973; Molyneux, 1974; Ashwal et al., 2005; Scoon & Mitchell, 2012) producing hybrid melts with a bulk composition falling out of the two-liquid field or to a process of density inversion due to instable magma density stratification (Tegner et al., 2006). Successive stages of immiscibility would then be produced by cooling and compositional evolution of the residual melts after each compositional reversal.

2.6   Conclusions

This study of melt inclusions in apatite demonstrates that immiscibility played an important role in the formation of cumulate rocks in the Upper Zone of the Bushveld Complex. Inclusions in apatite are observed in gabbros and nelsonites of the entire Upper Zone. The wide range in melt compositions, from iron-rich to silica-rich, is interpreted to be the result of entrapment at different temperatures along the binodal surface. Particularly, the iron-rich compositions observed in this study cannot have been produced by fractional crystallization and thus strongly support an immiscibility process. The sorting of immiscible melt droplets in the crystal mush possibly explains the formation of Fe-Ti-P-rich and (leuco-)gabbroic layers in the Upper Zone of the Bushveld Complex.

3 Magnetites in the Upper Zone of the Bushveld Complex: Emphasis on V distribution and constrains on fO_2

3.1 Introduction

Fe-Ti-oxides are commonly observed in mafic environments often within magnetite-bearing gabbros in layered intrusions (e.g., Sept Iles, Canada; Namur et al., 2012; Panzhihua, China; Zhou et al., 2008) and massiv anorthosites (e.g., Labrieville and St-Urbain, Canada; Owens & Dymek, 1992). Also pure Fe-Ti-Oxide layers with economically significant ore potential are often recognized in layered intrusions. Zhou et al. (2005) and Song et al. (2013) described these ores as lenses and stratiform layers for the Panzhihua intrusion (China) with layer thicknesses of up to 60 m. For the Sept Iles layered intrusion in Canada, Namur et al. (2010) described up to 1 m thick pure Fe-Ti-oxide layers as tabular or lense-shaped, massive ore bodies. Often those intrusions also host significant amounts of V, enriched in the Fe-Ti-oxides (e.g., Windimurra Complex, Australia; Mathison & Ahmat, 1996). A prominent example for massive oxide layers and an important V deposit is the Bushveld Complex in South Africa. It is well known for its PGE resources but also hosts significant amounts of V in chromite (Maier et al., 2013; Junge et al., 2014) and magnetite (Reynolds, 1985b). Magnetite is variably enriched in vanadium along the stratigraphic column and is of critical economic importance for South Africa.

The UZ of the Bushveld Complex is dominated by gabbroic rocks with intercalated layers of anorthosite, magnetitite and nelsonite, where the two latter host major resources of vanadium. Gabbronorites, gabbros and troctolites of the UZ can contain up to 35 vol% Fe-Ti-oxides often correlating with the observed compositional cyclicity (Yuan et al., 2017) but remain overall constant till ~200 m below the roof. Yuan et al. (2017) observed an increase in magnetite proportion with height within each cycle, explained by Fe enrichment of the differentiating melt. In the Western Limb 33 magnetitite layers are reported (Tegner et al., 2006; Yuan et al., 2017). Additionally, Yuan et al. (2017) described several magnetite-rich pmi-C rocks for the UZ. Although recent studies provided convincing evidence for the concept of magma injections into the UZ, a detailed knowledge about prevailing conditions (e.g., oxygen fugacity) during important ore-forming processes such as magma replenishments, cooling/fractionation, immiscibility and the nature of incoming magma are lacking for the UZ of the Bushveld Complex. Dare et al. (2012) showed, that trace element variations in magnetite are a useful tool for interpreting the formation of igneous rocks. Magnetites show distinct trace element compositions, depending on their formation environment and post-magmatic changes, thus providing insights into processes relevant for the UZ. The role of oxygen fugacity changes in the formation of massive magnetite ores is debated (e.g., Panzhihua, China; Ganino et al., 2008). To constrain fO_2 conditions for cumulate rocks, usual mineral-melt oxybarometer cannot be applied. Therefore, this study uses the distribution of the fO_2-sensitive element V between magnetite and clinopyroxene to estimate fO_2 conditions for the UZ.

3.1.1 Models for the formation of magnetitite layers in the UZ

The formation of the magnetitite layers is controversially discussed in the last decades and several models of formation were proposed. Wager & Brown (1986) proposed a crystallization and settling model in which the dense magnetite grains are sorted in the magma chamber forming magnetitite layers. However, they also noted that pyroxene with an intermediate density between magnetite and plagioclase is missing, making an only gravity-controlled process from a simple evolving magma problematic. A required process to explain the non-appearance of pyroxene crystallization was not presented.

Abrupt changes in liquid composition are assumed for the Bushveld magma chamber caused by contamination with silicic roof rocks (Irvine, 1975) or by magma mixing either within a stratified magma chamber (Kruger & Smart, 1987; Harney et al., 1990) or by injection of a new magma (Ashwal et al., 2005; Scoon & Mitchell, 2012). Reynolds (1985b) and Tegner et al. (2006) modified the model of a stratified chamber, proposing that magnetite layers originate from simple fractional crystallization. This high magnetite crystallization then caused a density decrease of the residual liquid, initiating magma mixing with the overlaying magma layer. Yuan et al. (2017) presented evidence for magma chamber replenishments in the UUMZ. According to their model the magnetite layers crystallized from a hybrid melt formed by magma mixing of the new injected and the resident magma also producing the unusual mineral assemblage of only magnetite and plagioclase.

Similar to Cameron's (1978) model on the formation of chromitite layers, Cawthorn & McCarthy (1980) proposed a pressure induced process to form monomineralic magnetitite layers rather than an abrupt change in liquid composition. In this model pressure increase shifts the phase boundaries, so that only magnetite crystallizes from the Bushveld liquid. Nucleation of CO_2 bubbles after magma input (Lipin, 1993) or external tectonic processes (Carr & Groves, 1994) are assumed to cause the pressure increase.

The concept of an immiscible Fe-rich silicate liquid forming the magnetite layers has been proposed for the UUMZ by Reynolds (1985b) and von Gruenewaldt (1993). Based on melt inclusion compositions, Fischer et al. (2016) confirmed the existence of immiscible silicate liquids in the UZc. However, the Fe-rich (and P-rich) liquid contains ~40 wt% FeO_{tot} which cannot account for the massive magnetitite layers. More likely, cumulates of the immiscible Fe-P-rich liquid produced the nelsonite layers of the UZc.

Von Gruenewaldt et al. (1985) and Klemm et al. (1985) proposed an alternative model, in which a fluid derived from the country rocks increases the oxygen fugacity of the liquid, forcing crystallization of magnetite. Tegner et al. (2006) questioned this hypothesis, given that source and transport of such a fluid is not demonstrated and probably would occur on a more local scale, not explaining the observed continuity of the magnetitite layers. Moreover, although textural evidence for higher fO_2 is given in magnetitites (Reynolds,

1985b), it remains unclear if the increase in fO_2 caused magnetite crystallization or vice versa (Toplis & Carroll, 1996).

3.1.2 Vanadium Partitioning

Vanadium is a multivalent element with V^{3+} and V^{4+} being the dominant species in magmatic systems, and generally compatible in members of the spinel group (e.g. magnetite, ilmenite) and clinopyroxene under magmatic conditions. The proportions of these two species are sensitive to variations in fO_2. The dependence of V_{bulk} mineral/melt partitioning on fO_2 was shown in several experimental (e.g., Duke, 1976; Lindstrom, 1976; Canil & Fedortchouk, 2000; Toplis & Corgne, 2002; Karner et al., 2007; Mallmann & O'Neill, 2009; Laubier et al., 2014; Sievwright et al., 2017) and natural (e.g., Canil, 1997; Connolly & Burnett, 1999) studies with a trend towards higher mineral/melt partition coefficients with decreasing oxygen fugacity. Effects of temperature (Geßmann & Rubie, 1998; Herd et al., 2002), liquid composition (Arató & Audétat, 2017) and mineral composition (Horn et al., 1994; Righter et al., 2006; Papike et al., 2014) on the V partitioning are reported. Pressure effects are less constrained but Canil (1999) showed that these are minor at least for orthopyroxene. Nevertheless, V partitioning between mineral and melt is a good indicator for prevailing oxygen fugacity conditions and is used in several studies as oxybarometer (e.g., Herd, 2006; Karner et al., 2006; Papike et al., 2013). Ratios of V isotopes (Schuth et al., 2017) and V valence states (Balan et al., 2006) can also be used to estimate fO_2 conditions. In the case of the Bushveld sample-set, however, V isotopes and valence states cannot be easily applied to the high-Ti magnetites of the Bushveld (interferences of Ti and V) or require a high analytical effort (XANES) not applicable for a large data set as in this study.

In the Bushveld Complex V is almost absent in olivine and plagioclase but compatible in magnetite and clinopyroxene. Both, magnetite and clinopyroxene, prefer to incorporate V^{3+} over V^{4+} on the octahedral sites. Additionally, V^{4+} can be incorporated in both minerals similar to the process of Ti^{4+} in clinopyroxene on the M1 site (Toplis & Corgne, 2002) and in titanomagnetite on the octahedral site (Toplis & Corgne, 2002; Balan et al., 2006). However, the substitution by V^{4+} is much less frequently than that by V^{3+} (Giuli et al. 2004). Thus, the V_{bulk} partitioning between mineral/melt and mineral/mineral is mainly controlled by V^{3+} whose abundance is affected by fO_2. This implies for natural systems, that the V distribution between co-crystallizing minerals and the liquid they are crystallizing from are closely linked to the prevailing oxygen fugacity conditions, which in turn can be affected by several magmatic processes such as fractionation, magma replenishment or fluid rock interaction. Therefore, oxygen fugacity calculations for a continuous sample set linked to a petrogenetic study of magnetites, as provided in this study, can help to understand the influence of different parameters contributing to the ore-forming process.

3.2 Methods

3.2.1 Petrography of selected samples

Major and trace element analyses of titanomagnetite and clinopyroxene for 54 representative magnetite and clinopyroxene bearing samples were determined in this study. Samples were selected from each cycle defined in Yuan et al. (2017) with focus on cycle XII, representing a typical cycle of the UZc. Selection was based on the appearance of magnetite to exclude those magnetites showing alteration, secondary ilmenite exsolutions or postcumulus modification as often observed for Fe-Ti-oxides (Butcher & Merkle, 1987). A list of the selected samples and their rock type is presented in Table 3.1.

The UUMZ is dominated by magnetite-free and magnetite bearing gabbros, gabbronorites, Ol-gabbros and troctolites. Additionally anorthosites and the magnetite rich rocks, pmi-C, magnetitite and nelsonite are observed. A petrographic overview of these lithologies for the same sample set can be found in Yuan et al. (2017). Representative samples, selected for trace element study of magnetite and clinopyroxene are coarse-grained gabbros, gabbronorites, Ol-gabbros, troctolites, leucogabbros and anorthosites (Table 3.1; Figure 1.7). These samples contain always coexisting magnetite and clinopyroxene. Modal proportions of magnetite in the selected samples vary between 0.03 and 18.7 vol%. Investigated troctolites have clinopyroxene contents above 2 vol%. Gabbros and gabbronorites are variable in their mineral modes independent from their stratigraphic position. Anorthosites, only contain small amounts of magnetite and clinopyroxene.

Table 3.1 Overview of selected samples for LA-ICP-MS analysis of magnetites and clinopyroxenes.

Sample[1] core-depth	strat. pos.[2] (m)	Zone[3]	Cycle[4]	Rock type[5]	modal proportions (vol%)[6]		
					Mt	Ilm	cpx
BK1-610.4	178,51	UZc	XVIII	Ol-Gabbro	3,29	6,09	0,91
BK1-633.8	199,88	UZc	XVIII	Ol-Gabbro	9,82	7,37	6,83
BK1-667.8	230,94	UZc	XVIII	Gabbro	0,03	0,04	21,63
BK1-715	274,06	UZc	XVII	Ol-Gabbro	2,13	3,41	9,63
BK1-759.8	314,99	UZc	XVII	Ol-Gabbro	8,09	4,18	3,29
BK1-771.2	325,31	UZc	XVII	Ol-Gabbro	-	-	-
BK1-775.3	329,15	UZc	XVI	Anorthosite	3,04	2,12	9,53
BK1-822.8	372,54	UZc	XV	Ol-Gabbro	1,83	4,01	23,10
BK1-922	463,17	UZc	XIV	Ol-Gabbro	0,91	1,95	13,52
BK1-955	493,31	UZc	XIII	Ol-Gabbro	1,96	2,24	11,13
BK1-1082.2	609,52	UZc	XIII	Troctolite	11,82	3,50	1,56
BK1-1103.5	628,98	UZc	XIII	Troctolite	18,73	4,50	0,63
BK1-1145	666,89	UZc	XIII	Ol-Gabbro	1,75	1,98	19,24
BK1-1260.4	772,31	UZc	XII	Ol-Gabbro	2,68	2,11	18,13
BK1-1401.2	900,94	UZc	XII	Ol-Gabbro	3,54	2,88	24,20
BK1-1403.32	902,88	UZc	XII	Troctolite	-	-	-

Sample[1] core-depth	strat. pos.[2] (m)	Zone[3]	Cycle[4]	Rock type[5]	modal proportions (vol%)[6]		
					Mt	Ilm	cpx
BK3-360.1	909,07	UZc	XII	Troctolite	5,28	3,25	5,33
BK1-1411.03	909,92	UZc	XII	Troctolite	-	-	-
BK1-1421.1	919,12	UZc	XII	Troctolite	6,54	3,95	4,20
BK1-1427.95	925,38	UZc	XII	Troctolite	-	-	-
BK1-1433.3	930,26	UZc	XII	Troctolite	14,70	8,68	1,22
BK3-396.6	942,41	UZc	XII	Ol-Gabbro	4,34	2,21	14,56
BK1-1447	942,78	UZc	XII	Troctolite	11,59	2,38	1,53
BK1-1458.12	952,94	UZb	XII	Anorthosite	-	-	-
BK1-1475.7	969,00	UZb	XII	Anorthosite	6,38	2,31	4,00
BK3-426.5	969,73	UZb	XII	Ol-Gabbro	-	-	-
BK3-433.7	976,31	UZb	XII	Ol-Gabbro	6,00	2,02	16,14
BK1-1492.8	984,62	UZb	XII	Troctolite	17,13	6,36	0,64
BK3-445.6	987,18	UZb	XII	Troctolite	6,27	1,34	28,28
BK3-468.0	1007,64	UZb	XII	Anorthosite	5,39	2,77	1,06
BK1-1520.4	1009,83	UZb	XII	Anorthosite	7,95	2,33	1,70
BK3-494.8	1032,12	UZb	XII	Ol-Gabbro	2,21	1,65	8,47
BK3-502.6	1039,25	UZb	XII	Troctolite	8,42	2,71	0,92
BK1-1556.6	1042,90	UZb	XI	Troctolite	4,59	2,57	2,40
BK3-530	1064,28	UZb	XI	Troctolite	18,25	5,21	1,72
BK1-1584.1	1068,03	UZb	XI	Anorthosite	7,51	3,26	1,67
BK3-540	1073,42	UZb	XI	Ol-Gabbro	-	-	-
BK3-555	1087,12	UZb	XI	Ol-Gabbro	13,33	3,50	12,30
BK3-578	1108,13	UZb	XI	Gabbro	10,77	2,44	19,53
BK1-1649.8	1121,65	UZb	XI	Gabbronorite	9,84	2,52	18,87
BK3-667.1	1189,53	UZb	X	Ol-Gabbro	6,93	2,13	22,29
BK3-750	1265,26	UZb	IX	Ol-Gabbro	7,75	1,10	13,54
BK3-780	1292,67	UZb	IX	Anorthosite	2,39	1,07	5,04
BK3-825.1	1333,87	UZb	VIII	Troctolite	10,29	2,77	14,78
BK3-908.8	1410,33	UZb	VIII	Leucogabbro	2,13	0,44	4,83
BK3-948.7	1446,78	UZb	VII	Gabbronorite	4,13	0,99	16,61
BK3-1010.5	1503,24	UZb	VI	Troctolite	3,20	2,09	19,69
BK3-1020.3	1512,19	UZb	VI	Ol-Gabbro	9,22	1,57	9,75
BK3-1041.2	1531,28	UZb	VI	Ol-Gabbro	10,68	1,44	13,96
BK3-1137	1618,80	UZb	V	Ol-Gabbro	8,99	1,56	14,32
BK3-1200	1676,36	UZa	IV	Gabbro	6,06	2,02	20,44
BK3-1301.9	1769,45	UZa	III	Gabbro	4,53	1,88	7,76
BK3-1369.9	1831,57	UZa	II	Anorthosite	6,64	1,04	5,11
BK2-167,2	1833,67	UZa	I	Gabbronorite	-	-	-

[1] Depth in the Bierkraal drill cores BK1, BK2 and BK3 in meter
[2] calculated stratigraphic position following Tegner et al. (2006)
[3] Subzone of the Upper Zone
[4] Cycle as defined by Yuan et al. (2017)
[5] Rock type obtained from thin section microscopy
[6] modal proportions of magnetite, ilmenite and clinopyroxene from chapter 1.4.1

3.2.2 LA-ICP-MS

Magnetites and clinopyroxenes were analyzed for major and trace element compositions using inductively coupled plasma mass spectrometry (LA-ICP-MS) at the Institut für Mineralogie, Leibniz Universität Hannover. Spots of interest were ablated using an inhouse build laser ablation system based on a Spectra-Physics Solstice femtosecond system coupled to a ThermoScientific Element XR fast scanning sector field inductively coupled plasma mass spectrometer. The laser system consists of a 100 fs Ti:sapphire regenerative amplifier with a fundamental wavelength of 775 nm and an frequency quadrupled output beam of 194 nm and was operated with a pulse energy of ~1.5 J/cm^2 and a repetition rate of 10 Hz. The ablation cell has a volume of ~35 cm^3 and He was used as carrier gas with flow rates of ~0.65 l/min. The plasma of the mass spectrometer was generated using argon with sample gas flow of ~1.1 l/min and auxiliary gas flow rates of 0.6 - 0.8 l/min. A Ni X-type skimmer cone with a Ni Jet sampler cone were used. Points of interest were analyzed using raster ablations (40 x 40 μm). The acquisition time for each analysis was 185 s including 30 s for background scanning (gas blank). Each acquisition included 120 cycles with the elements ^{23}Na, ^{25}Mg, ^{27}Al, ^{29}Si, ^{43}Ca, ^{45}Sc, ^{49}Ti, ^{51}V, ^{53}Cr, ^{55}Mn, ^{57}Fe, ^{59}Co, ^{61}Ni, ^{65}Cu, ^{66}Zn, ^{88}Sr, ^{89}Y, ^{91}Zr, ^{93}Nb, ^{95}Mo, ^{137}Ba, ^{139}La, ^{140}Ce, ^{141}Pr, ^{143}Nd, ^{147}Sm, ^{153}Eu, ^{157}Gd, ^{159}Tb, ^{169}Tm, ^{177}Hf, ^{181}Ta, ^{208}Pb, ^{232}Th and ^{238}U. Repeated measurements on the external glass reference NIST SRM 610 (Pearce et al., 1997) were used for external calibration and to monitor analytical precision. To control a potential drift of the device, the reference material was checked between every analytical set of 16 analyses. Evaluation of the complete data set was carried out with ICPMSDataCal software (Liu et al., 2008). Analyzed spots were checked afterwards via BSE images with EMPA to ensure homogeneity within analyzed crystals.

3.2.3 Calculation of oxygen fugacity

Several studies have used mineral compositions of Fe-Ti-oxides (Buddington & Lindsley, 1964; Herd et al., 2001; Duchesne et al., 2007; Sauerzapf et al., 2008) or pyroxenes (Schnetzler & Philpotts, 1970; Wadhwa, 2001) as oxybarometer. However, these methods are highly sensitive to re-equilibration, especially due to rapid reaction rates of ilmenite (Hammond & Taylor, 1982). To avoid the negative effect of ilmenite, partitioning of fO_2 sensitive elements such as V between minerals can be used to calculate fO_2. As mentioned above, in the case of the Bushveld Complex V is incorporated in magnetite and clinopyroxene. To calculate fO_2 from the V distribution in Bushveld cumulate rocks, knowledge about the relationship of V partitioning between titanomagnetite and clinopyroxene and fO_2 is necessary. Unfortunately, experimental studies at known fO_2 on V for these two minerals are rare. Only Lindstrom (1976) and Toplis & Corgne (2002) investigated V partitioning in a magnetite and clinopyroxene saturated systems and published mineral/melt partition coefficients. Knowing that magnetite and clinopyroxene

incorporate V^{3+} but V^{4+} is predominantly incorporated in titanomagnetites a dependence of the V partitioning between magnetite and clinopyroxene can be assumed. However, the calculated magnetite/clinopyroxene partition coefficient for experimental studies of Lindstrom (1976) and Toplis & Corgne (2002) does not reveal a dependence on fO_2, probably due to experimental and analytical uncertainties. Therefore, in this study, a dataset for V distribution between magnetite or clinopyroxene and silicate melt is compiled from experimental studies conducted under known oxygen fugacity conditions for ultramafic to intermediate compositions at an fO_2 range between log fO_2 of -4 and -14, temperatures between 1068°C and 1560°C and pressures between 1 atm and 30 kbar (Supplemental Table S7; Duke, 1976; Lindstrom, 1976; Hart & Dunn, 1993; Hauri et al., 1994; Jenner et al., 1994; Skulksi et al., 1994; Canil & Fedortchouk, 2000; Herd et al., 2002; Toplis & Corgne, 2002; Karner et al., 2008; Mallmann & O'Neill, 2009; Laubier et al., 2014; Sievwright et al., 2017). This dataset includes 46 experimental determined partition coefficients for magnetite/melt and 93 for clinopyroxene/melt. As shown in Figure 3.1, trends for both distribution coefficients show a clear correlation with fO_2. V partition coefficients for magnetite/melt range between 0.11 and 66 in the experimental dataset and show a much stronger increase with decreasing fO_2 than for clinopyroxene/melt ranging between 0.06 and 9.18. Although covering a wide range of oxygen fugacities the experimental dataset is poor in V partition coefficents for magnetite for lower fO_2, having only two data points below log fO_2 -10.
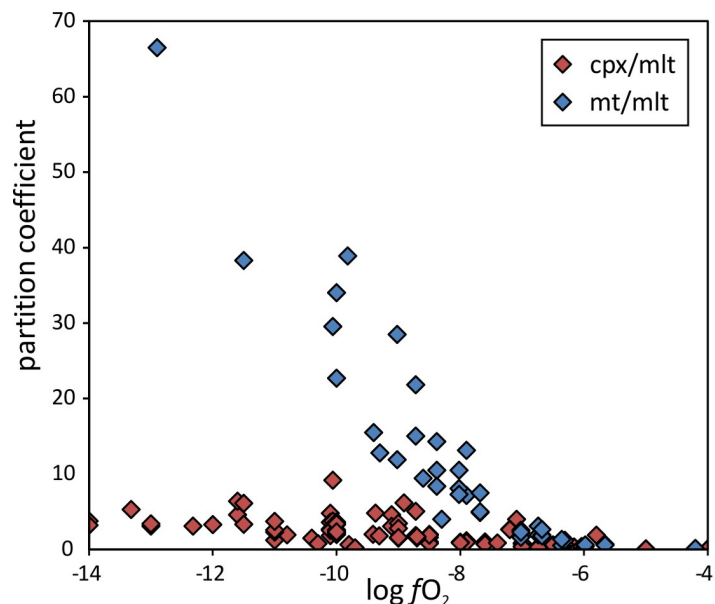
Figure 3.1 Vanadium mineral/melt partition coefficients for magnetite and clinopyroxene plotted against oxygen fugacity.

Partition coefficients were obtained in experimental studies relevant for basaltic to andesitic systems (Duke, 1976; Lindstrom, 1976; Hart & Dunn, 1993; Hauri et al., 1994; Jenner et al., 1994; Skulksi et al., 1994; Canil & Fedortchouk, 2000; Herd et al., 2002; Toplis & Corgne, 2002; Karner et al., 2008; Mallmann & O'Neill, 2009; Laubier et al., 2014; Sievwright et al., 2017).

To constrain fO_2 conditions from partition coefficients other possible controlling factors, such as liquid composition, mineral composition, pressure and temperature need to be discussed. Previous studies showed that the composition of pyroxenes (Mg# 65 - 90, Toplis & Corgne, 2002; wollastonite component of 13 and 33, Papike et al., 2014) can affect the V partitioning between pyroxene and silicate melt. In the latter study a higher wollastonite component of the pyroxene promotes higher cpx/melt partition coefficients of V. A comparison of cpx/melt partition coefficients with pyroxene compositions of the

experimental dataset used in this study did not reveal a compositional dependence. In contrast to the study of Papike et al. (2014) the pyroxenes of the experimental dataset have a generally higher wollastonite component and show a smaller compositional range as in Toplis & Corgne (2002), thus not significantly effecting V partitioning. A dependence of the V $D_{mineral/melt}$ on the magnetite composition is not expected (Arató & Audétat, 2017). Although not reported in literature, pressure and temperature effects on the V mineral/melt partition coefficient were checked for the experimental dataset. The majority of experiments was performed at 1 atm and only a small number of spinel free experiments were conducted at pressures between 10 and 30 kbar thus only clinopyroxenes were checked but did not show a pressure dependence of the V mineral/melt partition coefficient. A recent study by Arató & Audétat (2017) showed that the $D_{mineral/melt}$ of V is dependent on the liquid composition in silicic magmas. To test the experimental dataset used in this study, V partition coefficients for magnetite/melt and clinopyroxene/melt are plotted against ASI (molar ratio: $Al_2O_3/(CaO+Na_2O+K_2O)$) representing the coexisting liquid composition (Figure 3.2). Experimentally determined partition coefficients were grouped by their known fO_2 in one log-unit intervals (log fO_2 -10 corresponds to the interval of log fO_2 -9.5 to -10.5). Although some fO_2 intervals do no reveal a clear trend, probably due to the variable parameters from the different experimental studies, a dependence of $D_{mineral/melt}$ on ASI can be observed (Figure 3.2). V partition coefficients between magnetite or clinopyroxene and melt are both increasing with increasing ASI, more expressed at lower oxygen fugacities. Above log fO_2 -7 no effect is visible. Since the V mineral/melt partition coefficient for both, magnetite and clinopyroxene, is affected similarly, the partitioning of V between these two minerals is negligible. Thus, the dependence of the V distribution between titanomagnetite and clinopyroxene on fO_2 can be calculated by fitting two functions for $D_{mineral/melt}$ for magnetite and clinopyroxene from the experimental dataset (Figure 3.2).
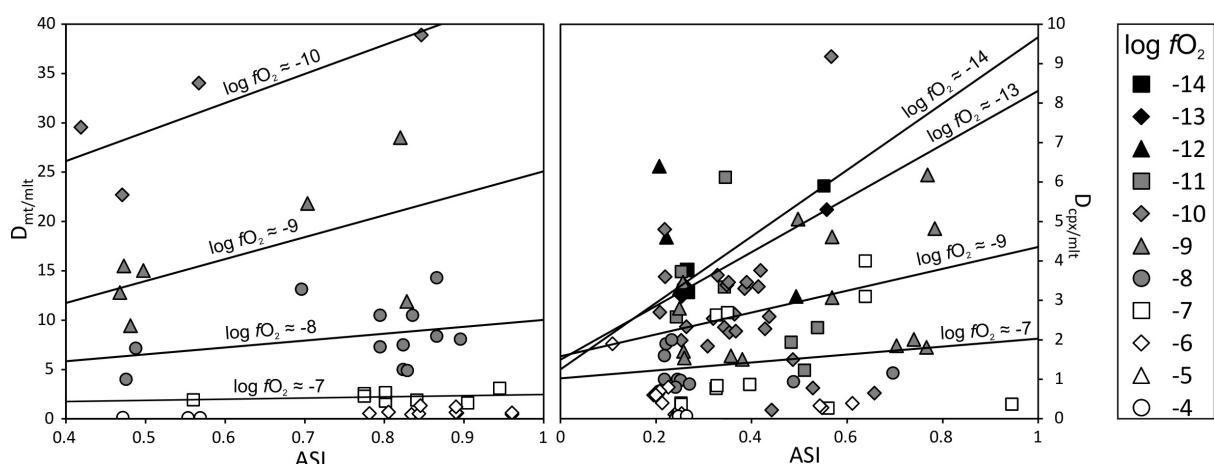
Figure 3.2 Dependence of the V partition coefficient on melt composition expresses as ASI (molar ratio: $Al_2O_3/(CaO+Na_2O + K_2O)$). Mineral and melt compositions from the experimental dataset (see Figure 3.1 for references). Different symbols represent fO_2 ranges ±0.5. Regression lines for selected fO_2 ranges show the dependence oft he mineral/melt partition coefficeint on melt composition.

Exponential regressions for the compiled experimental dataset were fitted using the Curve Fitting Toolbox of MATLAB with the Trust-region algorithm and the least absolute residuals (LAR) method to minimize the influence of extreme values. The dependence of the magnetite/melt partition coefficient on the fO_2 can be described with the function

$$f_1 = D^V_{mt/mlt} = a_1 \cdot e^{b_1 \cdot log fO_2} \tag{3.1}$$

with the variables a_1 = 0.1695 (±0.0327; with 95% confidence bounds) and b_1 = -0.4713 (±0.0167) with an r^2 coefficient of determination of 0.9877. The dependence of the clinopyroxene/melt partition coefficient on the fO_2 can be described with the function

$$f_2 = D^V_{cpx/mlt} = a_2 \cdot e^{b_2 \cdot log fO_2} \tag{3.2}$$

with the variables a_2 = 0.2209 (±0.0309) and b_2 = -0.2294 (±0.0168) with an r^2 of 0.9733. Consequently, the dependence of V partitioning between magnetite and clinopyroxene ($D^V_{mt/cpx}$) can be calculated by dividing f_1 and f_2 resulting in

$$f_3 = D^V_{mt/cpx} = \frac{f_1}{f_2} = \frac{a_1 \cdot e^{b_1 \cdot log fO_2}}{a_2 \cdot e^{b_2 \cdot log fO_2}} \tag{3.3}$$

To calculate a fO_2 for a known $D^V_{mt/cpx}$ the function 3.3 needs to be solved for log fO_2 resulting in

$$log\, fO_2 = \frac{ln D^V_{mt/cpx} - ln a_1 + ln a_2}{b_1 - b_2} \tag{3.4}$$

After inserting the variables a_1, a_2, b_1 and b_2 determined by MATLAB the following equation can be used to calculate log fO_2 for a known $D^V_{mt/cpx}$.

$$log\, fO_2 = \frac{ln D^V_{mt/cpx} + 3.285}{-0.2419} \tag{3.5}$$

The error for log fO_2 in function 3.4 and 3.5 respectively can be calculated following the Gaussian error propagation using the partial derivatives for the variables $D^V_{mt/cpx}$, a_1, a_2, b_1 and b_2, and their errors σ ($D^V_{mt/cpx}$), σ(a_1), σ(a_2), σ(b_1) and σ(b_2) giving the equation

$$\sigma(log\, fO_2) = \sqrt{ \left(\frac{1}{D^V_{mt/cpx}(b_1-b_2)} \right)^2 \cdot \sigma\left(D^V_{mt/cpx}\right)^2 + \left(\frac{1}{a_1(b_2-b_1)} \right)^2 \cdot \sigma(a_1)^2 + \left(\frac{1}{a_2(b_1-b_2)} \right)^2 \cdot \sigma(a_2)^2 + \left(\frac{ln D^V_{mt/cpx}-ln a_1+ln a_2}{(b_1-b_2)^2} \right)^2 \cdot \left(\sigma^2(b_2) + \sigma^2(b_1)\right) } \tag{3.6}$$

The exponential function 3.5 derived from mineral/melt partition coefficient regression lines enables to calculate the prevailing oxygen fugacity conditions from cumulate rocks containing magnetite and clinopyroxene as it is the case for the UZ in the Bushveld Complex.

Figure 3.3 Shows the regression lines for $D^V_{cpx/melt}$ (red) and $D^V_{mt/melt}$ (blue) fitted with MATLAB. Green line represents the calculated function for $D^V_{mt/cpx}$ (equation 3.5).
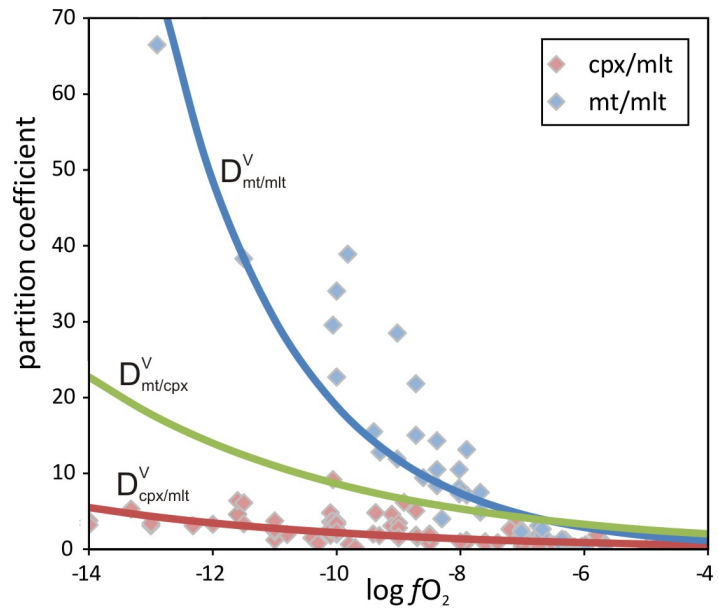
3.3 Results and Discussion

3.3.1 Textural features of Upper Zone magnetites

Titanomagnetite is a member of the spinel group and defines the intermediate compositions of the solid solution between magnetite and ulvöspinel. It occurs in the UZ either interstitial in gabbroic rocks or as densely packed aggregates in massive magnetite layers. Homogenous magnetites typically occur in volcanic systems with rapid cooling (Mücke, 2003). In plutonic environments, titanomagnetites are susceptible to subsolidus processes, such as re-equilibration and oxidation (Buddington & Lindsley, 1964; Frost & Lindsley, 1991). Furthermore, a common feature for titanomagnetites is the large variety of exsolutions (Buddington & Lindsley, 1964; Haggerty, 1991). In the case of the Bushveld Complex, exsolved phases are ulvöspinel now oxidized to ilmenite and pleonast (aluminous spinel) with a general increase of exsolved ilmenite proportion up section (Willemse, 1969; Reynolds, 1985b; von Gruenewaldt et al., 1985). Additionally, primary ilmenite is observed in most of the samples often in contact with the titanomagnetite. BSE imaging of Fe-Ti-oxides in this study was performed using a Cameca SX-100 EMPA at the Institut für Mineralogie, Leibniz Universität Hannover, Germany. To describe the different observed exsolution textures in samples from this study, the terms defined and summarized by Haggerty (1991) are used.

The position and shape of the magnetite-ulvöspinel solid solution solvus remains in question (Vincent et al., 1957; Kawai et al., 1954; Basta, 1960; Lindsley, 1981; Spencer & Lindsley, 1981; Pucher, 1969) and the effect of minor element components is discussed (Price 1981). Pucher (1969) observed a miscibility gap in the solid-solution series at a temperature of ~750°C. Proposed solvus temperatures are in the range between ~450°C - ~750°C. Exsolution of ulvöspinel is common throughout the UZ samples and is ascribed to the presence of a miscibility gap in the magnetite-ulvöspinel solid-solution series
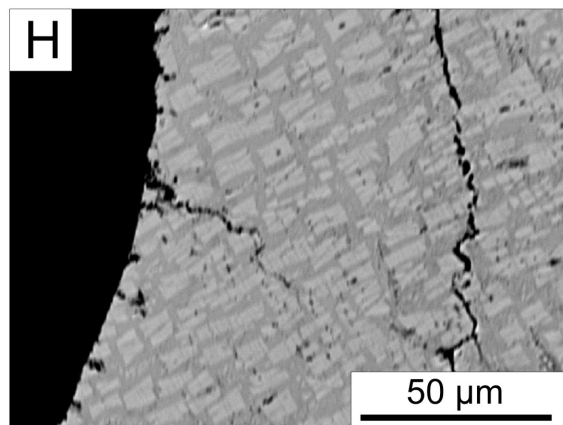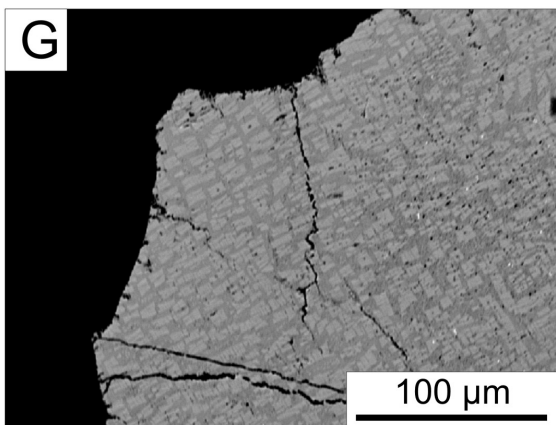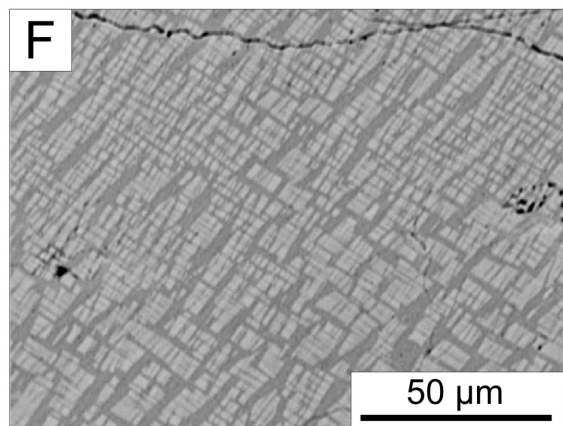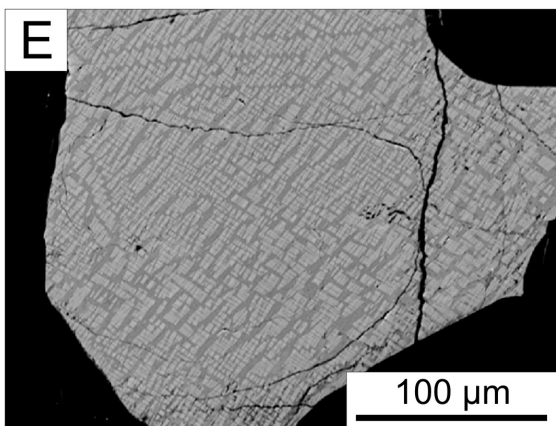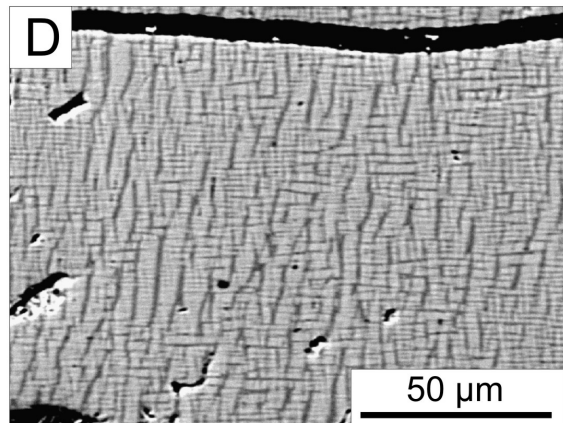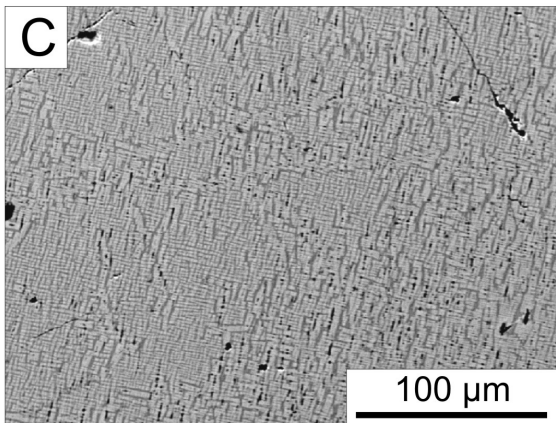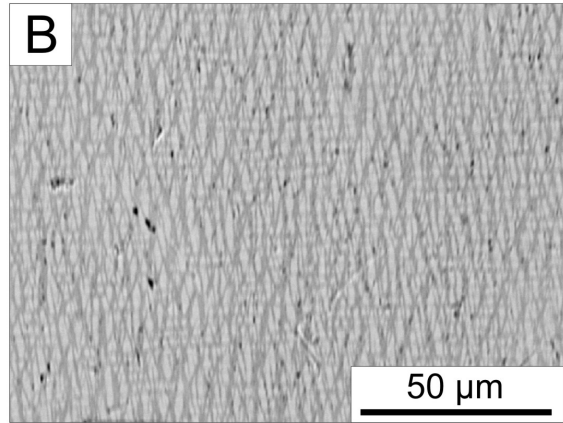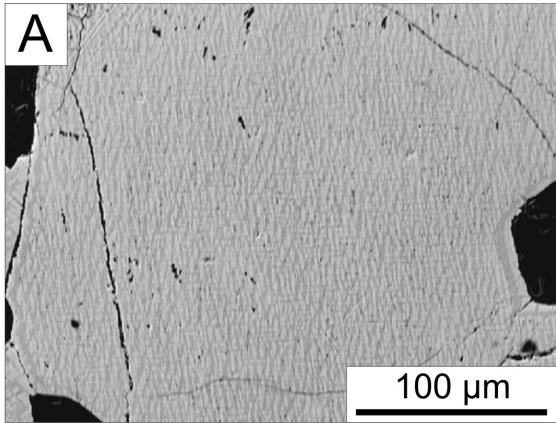
Figure 3.4 BSE images of cloth-type exsolution textures. Temperature and oxygen fugacity are assumed to decrease from top to bottom (see text for details). Left and right image show same magnetite grain at different magnification. Darker phase corresponds to ulvöspinel exsolutions now oxidized to ilmenite. Brighter phase corresponds to the titanomagnetite host. Areas around cracks do not show textural modifications indicating cracking during sample preparation. Images **A and B** (sample: BK1-759.8; stratigraphic position: 274.06 m; zone: UZc; cycle: XVII; rock type: Ol-gabbro) showing very fine-scale exsolutions <1 μm. **C and D** (BK3-1020.3; 1512.19 m; UZb; VI; Ol-gabbro) with more developed exsolutions compared to A and B. **E and F** (BK1-1421.1; 919.12 m; UZc; XII; troctolite) showing <5μm exsolution textures. **G and H** (BK1-1447; 942.78 m; UZc; XII; troctolite) showing a larger scale exsolution network >5 μm.

(Price, 1980; 1981). The exsolution of ulvöspinel results in a fine-scale network texture (Figure 3.4). The size and extent of these cloth-texture networks depends on Ti-concentration in the solid solution, stage of oxidation and cooling rate (Haggerty, 1991). However, comparison of bulk Ti-contents (host + exsolutions) in analyzed titanomagnetites with different scales of cloth-texture revealed no dependence on Ti content. For example titanomagnetites from sample BK1-759.8 (Figure 3.4A) with a <1 μm exsolutions and sample BK1-1421.1 (Figure 3.4E) with ~5 μm exsolutions have similar compositions with TiO_2 concentrations of 16.9 and 15.6 wt% respectively. Fine-scale networks as shown in Figure 3.4A and B result from lower oxidation stages and higher temperatures owing the solvus of the magnetite-ulvöspinel solid solution. With cooling or further oxidation the amount of exsolved ulvöspinel increases, resulting in a larger spaced network (Figure 3.4C-F). Given that ulvöspinel is only stable at very low fO_2 and high temperatures, oxidation of exsolved ulvöspinel occurs, resulting in the formation of ilmenite. Such formed ilmenite is termed protoilmenite (Willemse, 1969) and the cloth-texture is still preserved after oxidation, as it is the case for the UZ.

Besides the exsolution textures described above, abundant lamellae of ilmenite are observed in those samples where cloth-texture exsolutions are absent (Figure 3.5). Ilmenite lamellae vary in size from <1 μm to >10 μm scale between different samples. They occur along all directions of the (111) planes of the magnetite and are marked by tapered terminations. These ilmenite exsolution lamellae are called "trellis-type" exsolution. The formation of trellis-type ilmenite exsolutions is controversially discussed in literature and ascribed to either oxy-exsolution (Buddington & Lindsley, 1964) or exsolution from cation-deficient titaniferous spinels (Lattard, 1995). Both processes occur above the magnetite-ulvöspinel solvus. While the oxy-exsolution process is controlled by relatively oxidizing conditions the exsolution of ilmenite from cation-deficient titanomagnetite occurs during cooling of the system. Tan et al. (2016) showed that both processes can occur in the same magnetite grain resulting in two generations of ilmenite exsolutions in which oxy-exsolved ilmenite tend to form larger lamellae. Furthermore, inter-oxide re-equilibraiton forms small lenticular exsolutions of ilmenite. This texture of two-generation exsolution is also observed in the UZ titanomagnetites (e.g., sample BK3-360.1; Figure 3.5C, D and G). Similar to the evolution of cloth-texture exsolutions, the size of trellis-type exsolutions depends on the kinetics of cooling and oxidation, resulting in relatively larger lamellae where cooling was slower or more oxidized (Haggerty, 1991).
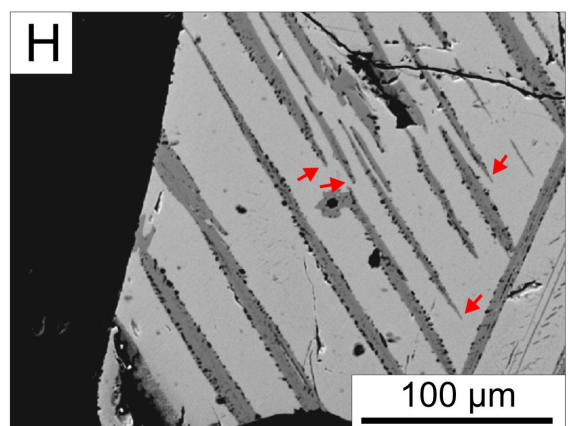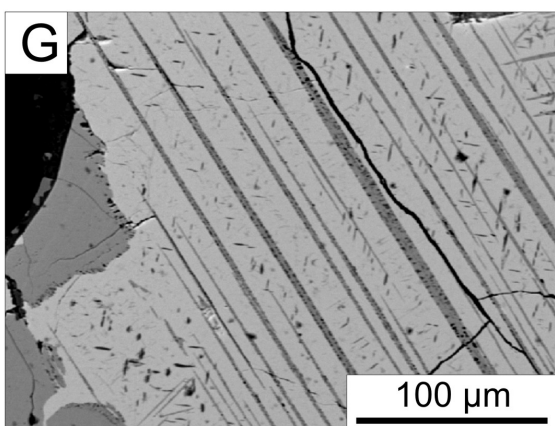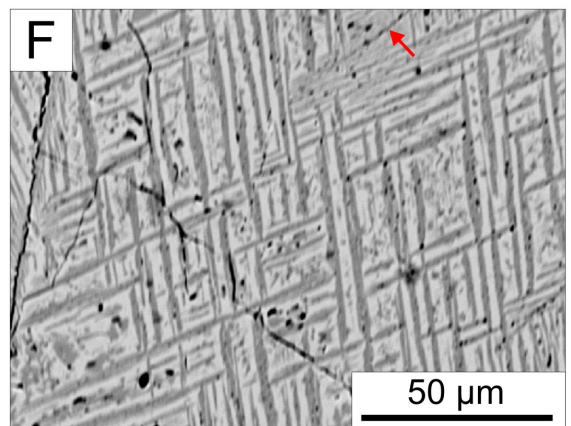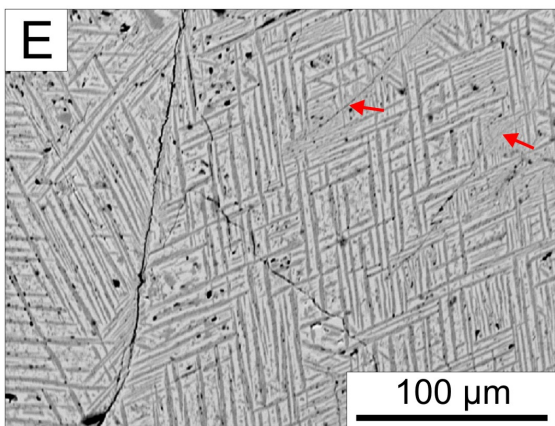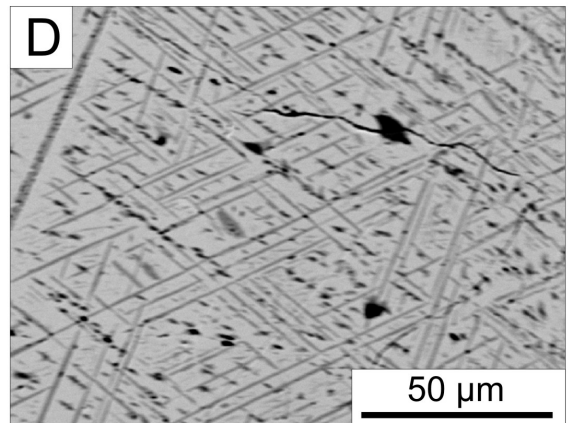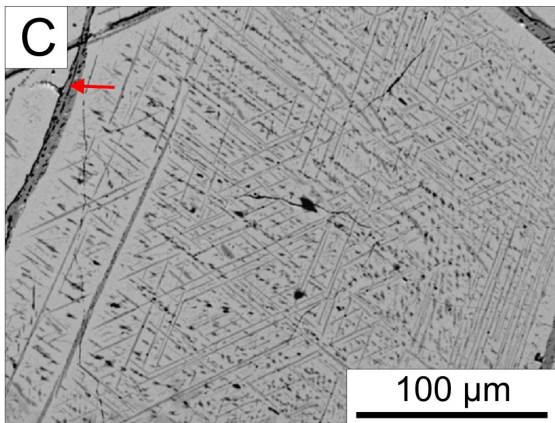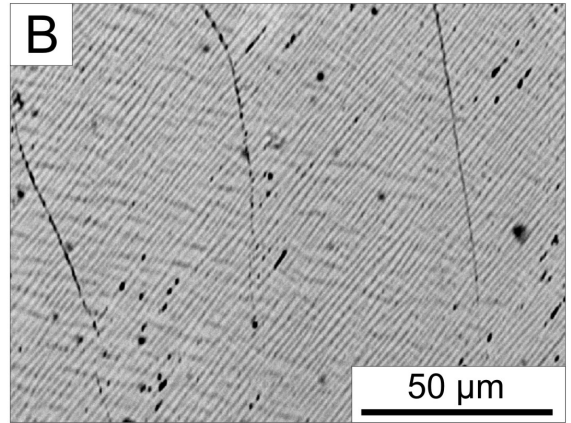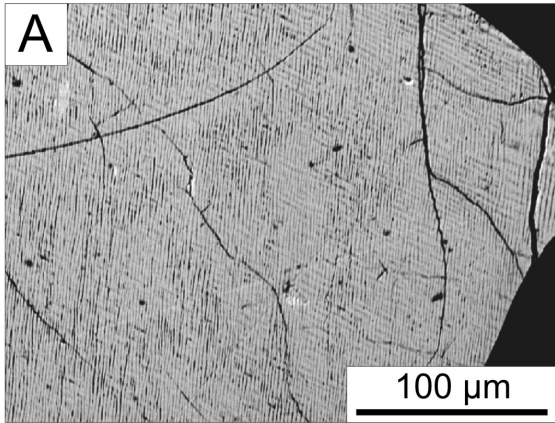
Figure 3.5 BSE images of trellis-type exsolution textures. Temperature and oxygen fugacity are assumed to decrease from top to bottom (see text for details). Left and right image show same magnetite grain at different magnification. Darker phase corresponds to ilmenite exsolutions. Brighter phase corresponds to the titanomagnetite host. Images **A and B** (sample: BK1-1179.5; stratigraphic position: 698.41 m; zone: UZc; cycle: XII; rock type: troctolite) showing very fine-scale exsolutions <1 μm. Darker areas correspond to holes from polishing. **C and D** (BK3-360.1; 909.07 m; UZc; XII; troctolite) with more developed exsolutions compared to A and B. On the left site in image C a larger dark grey ilmenite developing from a crack can be observed (indicated by the red arrow). The area of the titanomagnetite directly in contact with this ilmenite does not show exsolutions. **E and F** (BK1-1433.3; 930.26 m; UZc; XII; troctolite) showing <5μm exsolution textures. Secondary oxidation can be observed around cracks indicated by red arrows. **G and H** (BK3-360.1; 909.07 m; UZc; XII; troctolite) showing a larger scale exsolution network >5 μm. These ilmenite exsolution lamellae can be distinguished from primary ilmenite laths by their typical tapred terminations (indicated by red arrows in H).

Titanomagnetites in massive magnetite layers show in addition to cloth-texture exsolutions abundant lamellae of pleonast. Pleonast lamellae occur along the (111) magnetite planes and are usually less developed than the ilmenite exsolution lamellae (Figure 3.6A). Their size is uniform with a thickness of <5 μm and does not change between samples from different stratigraphic positions. Those pleonast exsolutions are usually interpreted to result from the intersection of the magnetite-pleonast solid solution solvus which has a maximum temperature of 870°C and thus lies at a higher temperature than that of the magnetite-ulvöspinel solid solution (Turnock & Eugster, 1962; Haggerty, 1991).

Primary, always homogeneous, ilmenite is commonly present in the selected samples as discrete grains, large laths within titanomagnetites or rarely as granules within titanomagnetites. Discrete ilmenite grains occur in most of selected samples. Where in contact to titanomagnetites, reaction rims can be observed extinguishing the exsolution textures in the titanomagnetite. The size of the reaction rims rarely exceeds 10 μm (Figure 3.5C). Within some samples large (up to 50 μm) lamellae of ilmenite are observed in addition to the above described titanomagnetites (BK1-1179.5; Figure 3.6B). In contrast to the similarly appearing trellis-type exsolutions no tapered terminations are observed. Those sandwich-type lamellae are primary ilmenites and not exsolution products (Mücke, 2003), and can act as nucleation point for the titanomagnetite crystallization (Haggerty, 1991). Diffusion processes between primary ilmenite laths and titanomagnetite can change the mineral composition.

Some samples show alteration features, such as veins and abundant secondary hydrous minerals. Titanomagnetites are directly affected by this alteration due to oxidizing fluids. Altered titanomagnetite crystals show a patchy alteration and the titanomagnetite/ulvöspinel/ilmenite is oxidized to maghemite (Bowles et al., 2011).

In both cases of cloth-texture and trellis-type exsolutions, the bulk composition (magnetite + ilmenite exsolutions) represents the primary magmatic composition (Dare et al., 2012). Moreover, it is necessary to analyse magnetite with its exsolutions to neglect the effect of interdiffusion of e.g. Fe and Ti (Freer & Hauptman, 1978). Although, it was shown that the solvus of magnetite-ulvöspinel solid solution can be decreased to temperatures below 600°C, Cawthorn et al. (1983) noted a zonation in Cr content in single magnetite crystals, indicating a primary magmatic signature of the UZ magnetites, arguing that subsolidus Cr diffusion was prevented by ilmenite lamellae.

To ensure analysis of primary magmatic compositions, only titano-magnetite with homogeneous cloth- and trellis-type textures were chosen. Since each analysis-raster via LA-ICP-MS ablates an area of 40 x 40 µm in titanomagnetites were chosen with exsolution textures <5 µm. Titanomagnetites showing larger-spacing networks (Figure 3.4G-H), large and irregular ilmenite lamellae (Figure 3.5G-H), primary ilmenite laths (Figure 3.6B) or secondary alteration (Figure 3.6C) were excluded from this study. Additional to samples with clear alteration textures, these criteria also exclude samples were the bulk analysis by LA-ICP-MS can be effected by proportions of a single lamellae and by those textures where it cannot be resolved if oxidation was driven by a change in fO_2 of the system or by the presence of oxidizing fluids.
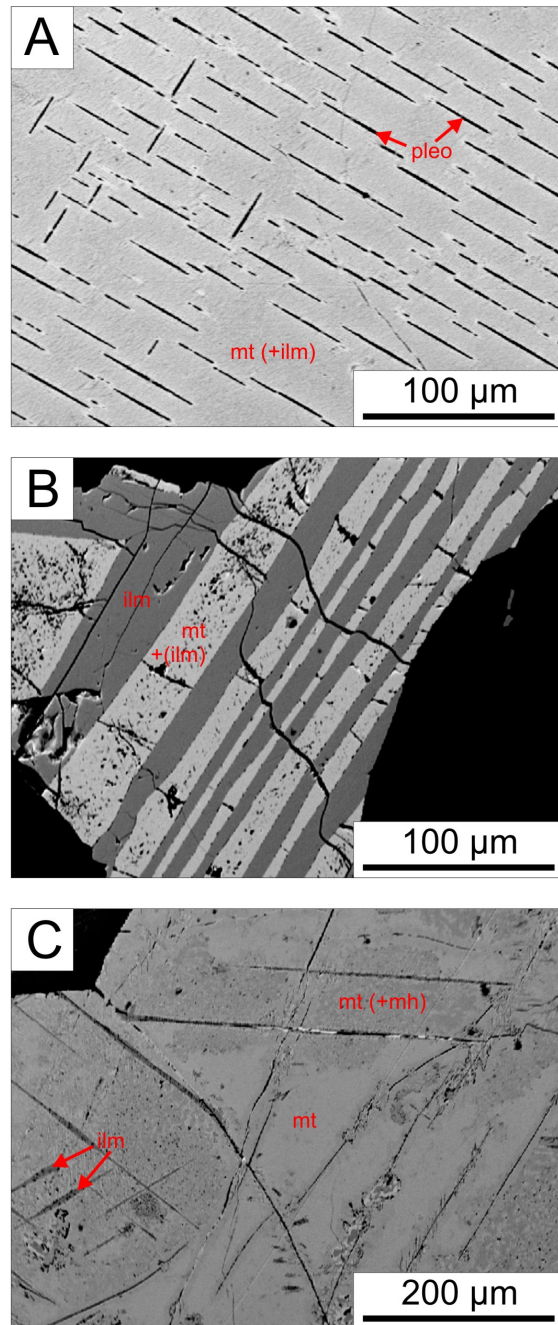
Figure 3.6 BSE images of titanomagnetites. **A** (sample: BK1-1343; stratigraphic position: 1806.99 m; UZa; III; magnetitite) showing black pleaonast exsolutions (pleo) typical for massive magnetites. Grey titanomagnetite host has a very fine-scale cloth-texture with ulvöspinel exsolutions now oxidized to ilmenite (mt(+ilm)). **B** (BK1-1179.5; 698.4 m; UZc; XII; troctolite) showing a sandwich-type intergrowth of dark grey primary ilmenite lath with light grey titanomagnetite inbetween. Titanomagnetite shows trellis-type exsolutions of ilmenite. **C** (BK1-1460; 954.7 m; UZb; XII; pmi-C) showing strong alteration of titanomagnetite resulting in a patchy network with exsolution oxidized to maghemite (mh). Some large trellis-type ilmenite exolsutions are still present.

3.3.2 Textural features of the Upper Zone clinopyroxenes

As with the titanomagnetites, clinopyroxenes in the UZ show abundant exsolution textures. Exsolution textures in pyroxenes are a common feature in basic intrusive rocks (Bown & Gay, 1959) and are mainly controlled by temperature and are therefore used as geothermometer in many studies (Lally et al., 1975; Fleet et al., 1980; Doukhan et al., 1990; Besson & Poirier, 1994). For the investigated clinopyroxenes two exsolution types can be distinguished. One expressed in small titanomagnetite rods and the other consisting of fine pigeonite lamellae, both orientated parallel along the (001) and (100) planes of the clinopyroxene (Figure 3.7). BSE imaging and EDX phase identification was performed using a Hitachi SU-70 FE-SEM at the Central Science Lab at the University of Tasmania, Australia. Exsolutions of magnetite in magmatic rocks are ascribed to exsolutions during cooling (Robinson et al., 1971; Fleet et al., 1980) or oxidation-exsolution (Morse, 1975) processes. Feinberg et al. (2004) ruled out the oxidation-exsolution process arguing that the generated SiO_2 during oxidation is not observed in clinopyroxenes with magnetite inclusions. Zhu et al. (2017) showed that exsolutions of spinel in clinopyroxene is promoted by removal of O_2 from the system, and thus magnetite crystallization can trigger spinel exsolutions in clinopyroxene. Lamellae of low-Ca-pyroxenes in clinopyroxene are the result of subsolidus exsolution (Hess, 1941) and are assumed to result from heterogeneous nucleation and growth or spinodal decomposition during cooling (Champness & Lorimer, 1976 and references therein), whereas the former occurs more
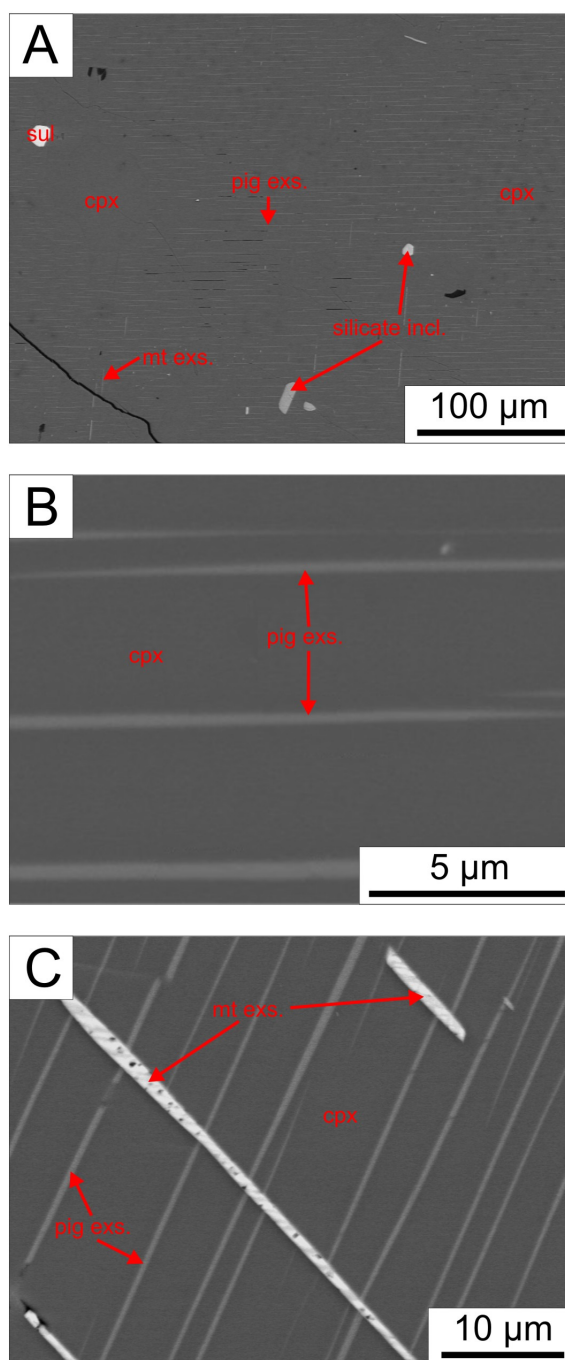
Figure 3.7 BSE images of clinopyroxenes with exsolution lamellae. **A** (sample: BK1-433; stratigraphic position: 16.4 m; UZc; XVIII; Ol-gabbro) showing abundant pigeonite exsolution lamellae (pig exs.), few magnetite exsolution lamellae (mt exs.) and inclusions of silicates (silicate incl.) and sulfides (sul). **B** (BK1-433; 16.a m; XVIII; Ol-gabbro) shows the same clinopyroxene grain as A at a higher magnification showing the pigeonite exsolution lamellae. **C** (BK1-1019.8; 552.5 m UZc; XIII; Ol-gabbro) showing pigeonite and magnetite exsolution lamellae in clinopyroxene.

likely in plutonic environments (Copley et al., 1974). The described exsolutions in clinopyroxenes are subsolidus processes. Calculations using the exsolution orientation revealed exsolution temperatures between 510°C and 720°C (Doukhan et al., 1990). Analog to the titanomagnetites, the bulk composition of clinopyroxene and its exsolutions represents the magmatic composition prior to the subsolidus process. Thus, only bulk analysis of the clinopyroxene can provide information on prevailing magmatic conditions.

The majority of the clinopyroxenes in this study contain both, pigeonite and titanomagnetite exsolutions. Clinopyroxenes with only titanomagnetite exsolutions are not observed. Pigeonite exsolutions occur as up to 150 μm long lamellae with tapered terminations. The width of pigeonite lamellae never exceeds 1 μm with sharp boundaries to the clinopyroxene host (Figure 3.7B). Spacing between the lamellae is constant within and between samples and is around 5 μm. Titanomagnetite exsolutions occur as non-continuous rods usually 10 - 20 μm long with angular terminations, and rarely wider then 1 μm (Figure 3.7C). Compared to the pigeonite exsolution they are less abundant in the particular clinopyroxene. In addition to the lamellar exsolution textures, silicate, oxide and sulfide inclusions are observed in clinopyroxenes (Figure 3.7A). Areas with such inclusions were not measured. In contrast to exsolutions in titanomagnetite, clinopyroxene hosted exsolutions do not show a varation within the stratigraphy, neither in exsolution abundance, exsolution size nor exsolution type.

3.3.3 Composition of magnetite

Titanomagnetites of the UZ vary in composition as solid solution of magnetite and ulvöspinel (Figure 3.8) supporting that the bulk analysis via LA-ICP-MS represents titanomagnetite with exsolutions of ulvöspinel oxidized to ilmenite and/or ilmenite rather than a mixture of primary magnetite and ilmenite. There is no correlation between titanomagnetite composition and rock type. The overall gradual upward increase of TiO_2 in magnetite noted by von Gruenewaldt et al. (1985) is not observed. Instead, an increase of TiO_2 in magnetite within some cycles is noted (Figure 3.9). Sample

Figure 3.8 UZ magnetite compositions plotted in the ternary diagram rutile, hematite and wüstite. Each datapoint represents the average composition of magnetite in a single sample.

spacing in this study is too large to demonstrate this for every cycle. In cycles XII and XIII reversals in TiO_2 in magnetite are recognized located above the reversals in anorthite observed by Yuan et al. (2017). Highest Ti concentrations in magnetite are reached below and above the anorthite reversal of cycle XII and above the anorthite reversal of cycle XIII.
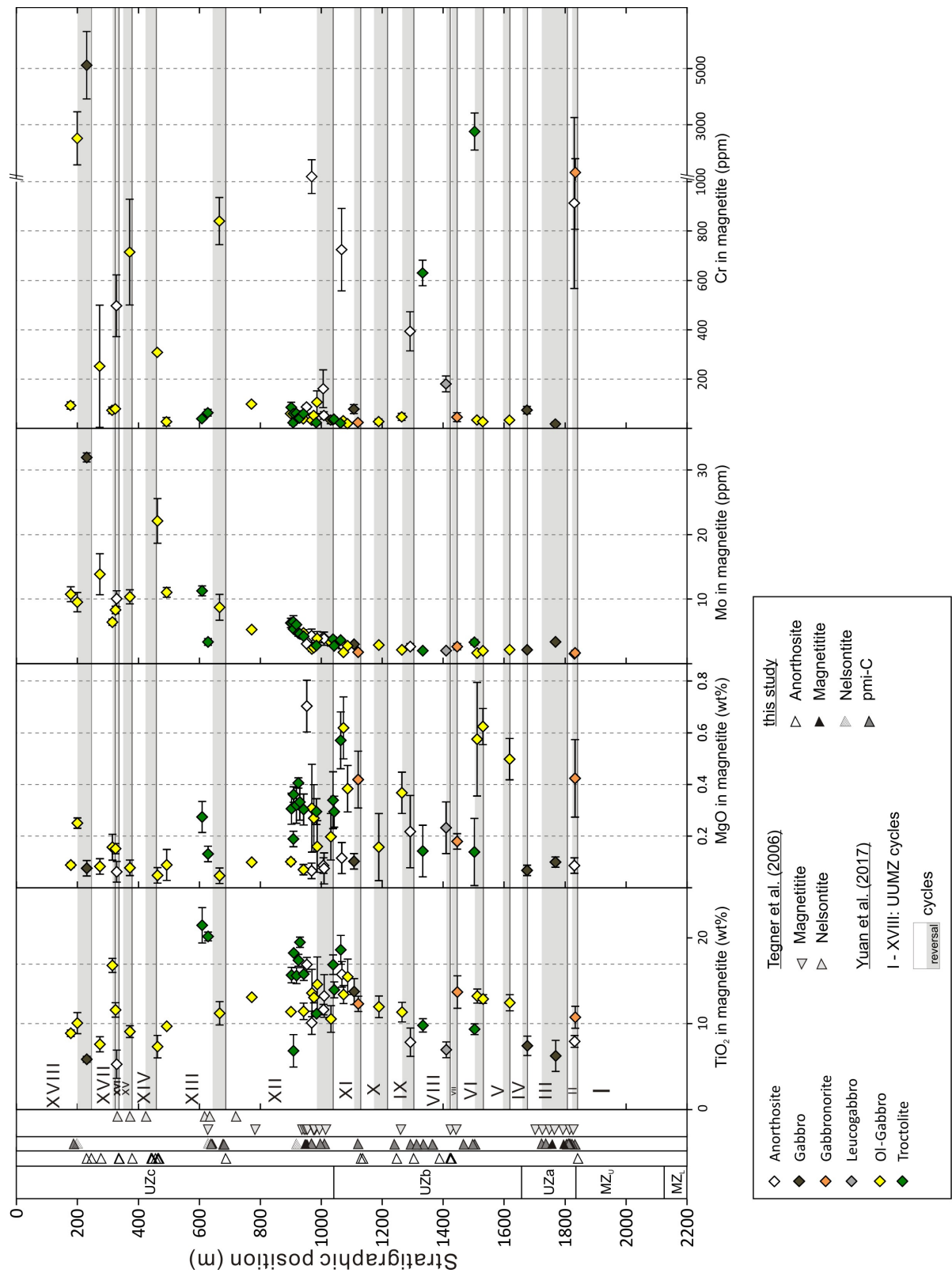
Figure 3.9 TiO$_2$, MgO, Mo and Cr contents of UZ magnetites with stratigraphic position. Each datapoint represents the average magnetite composition in a single sample. Error bars indicate the standard deviations and colors indicate the rock type. Also marked are positions of magnetitite, nelsonite and anorthosite layers (Tegner et al., 2006; Yuan et al., 2017) and cycles with reversals (Yuan et al., 2017).

Major and trace element compositions of titanomagnetite are presented in Supplemental Table S8. The environment in which the magnetite forms controls its chemical signature. Temperature, pressure, liquid composition, and presence of a fluid strongly influence the partitioning behavior between magnetite and melt or fluid. Thus, multi-element pattern of magnetites can help to understand the formation environment, crystal fractionation and timing of magnetite crystallization. Dare et al. (2014) proposed a multi-element pattern to distinguish between different magmatic and hydrothermal environments. In this, elements are normalized to bulk continental crust to reflect changes in magnetite composition relative to a slightly evolved liquid, which is assumed to be saturated in magnetite. Figure 3.10 shows continental crust-normalized multi element pattern for the UZ titanomagnetites, with elements sorted by compatibility into magnetite with increasing compatibility from left to right. Multi element pattern of magnetite normalized to bulk continental crust should increase from incompatible to compatible. Deviations from this pattern are typical for certain environments. In the case of magmatic systems deviations can show evidence for changes in liquid composition and/or changes of the partition coefficient as a result of changes in for example fO$_2$ or crystallizing phases.

Normalized elements increase from incompatible to compatible with negative anomalies for Zr, Ca, Al, Nb, Mg and Ni and marked peak for Mo. High variations between different samples are observed for Zr, Hf, Nb, (Ti), V and Cr. The two most incompatible elements in magnetite, Si and Ca are, as expected, highly depleted. The less depleted Si
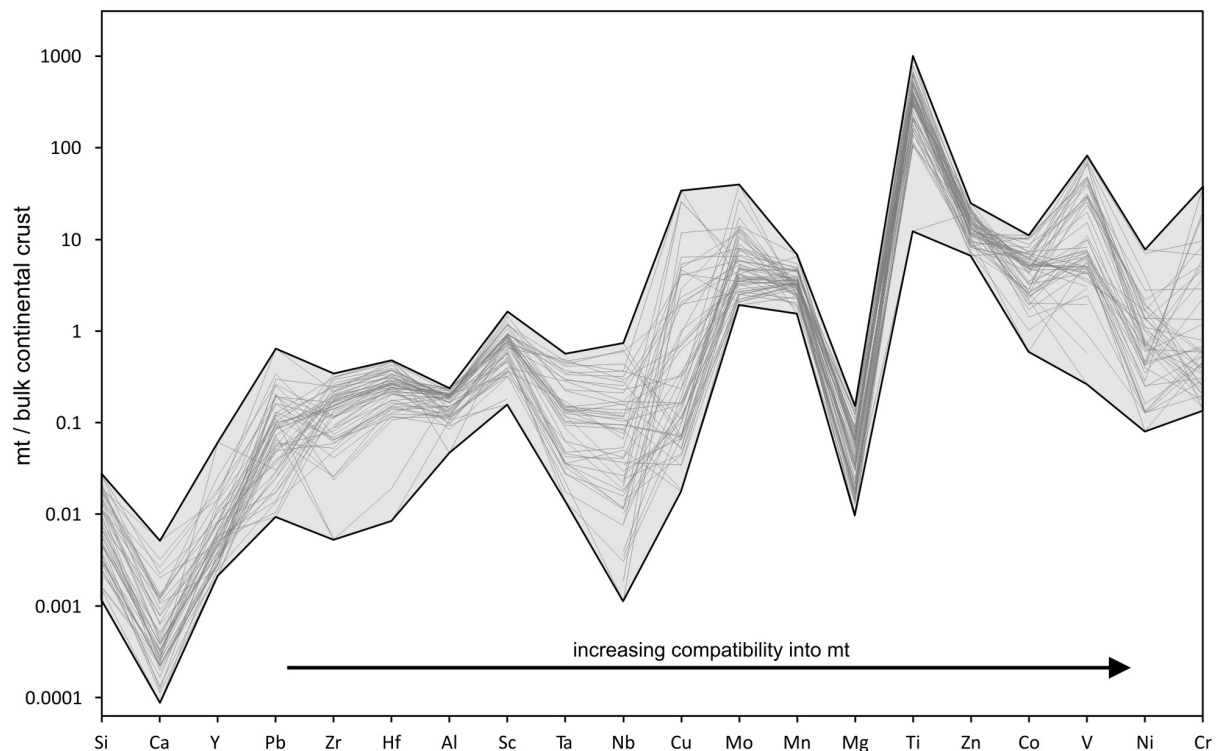
Figure 3.10 Multi element diagram for UZ magnetites, normalized to bulk continental crust (Rudnick & Gao, 2003) as proposed by Dare et al. (2014). Light gray field indicates the compositional range of magnetites in the selected samples from the UZ. Dark gray lines represent average magnetite composition of each selected sample.

values relative to Ca are possibly the result of nano-scale silicate inclusions in magnetite as observed by Newberry et al. (1982) and discussed by Nadoll & Koenig (2011). The relative depletion in Zr, Hf, Ta, Nb, Mg reflect the presence of co-crystallizing ilmenite, where these elements are highly compatible (Duran et al., 2016). Chalcophile elements, such as Pb, Cu, Co and Ni show a high variability between the samples indicating the co-crystallization of sulphides in the UZ. As shown by Maier et al. (2003) crystallization of magnetite can trigger S-saturation of the melt resulting in sulphide crystallization. V is highly enriched in the UZ magnetites and shows similar to Cr a high variability between the samples. This probably results from changes in oxygen fugacity since both are multivalent elements and sensitive to changes in fO_2.

To illustrate fractionation of the silicate melt and possible magma chamber processes, changes of single trace elements in magnetite are discussed with the stratigraphic position. Continuous fractionation in a closed system leads to an enrichment in elements incompatible in the fractionated phases, whereas compatible elements in turn are depleted. Deviations from this trend can reflect changes in liquid composition and/or fO_2 and are an indicator for magma chamber replenishments.

MgO is a major component of olivine and pyroxenes and compatible in magnetite, thus it should decrease with stratigraphic height. As shown in Figure 3.9 MgO does not show an overall decreasing trend upwards, supporting the open system model. Next to V, Mo is the only element in magnetite showing an overall trend with stratigraphy (Figure 3.9). Concentrations of Mo in UZa and UZb are constantly below ~3 ppm. With apatite saturation at the base of UZc, Mo increases upwards in cycle XII till concentrations around 10 ppm and keeps those higher values till the top of the intrusion. Mo mineral/melt partitioning is positively affected by a decrease in fO_2 (Tacker & Candela, 1987), a decrease in temperature (Righter et al., 2010) and a decrease of the Ca concentration in the silicate melt (O'Neill & Eggins, 2002). A correlation with other redox sensitive elements (e.g., Cr and V) is not observed ruling out a strong change in fO_2. Apatite crystallization consumes Ca, P, F and Cl from the silicate melt. While, F and Cl do not affect Mo partitioning (Candela & Holland, 1984), Ca depletion in the melt results in increasing $D^{Mo}_{mineral/melt}$. However, evidence for Ca depletion in the melt is not given by other phases (e.g., An in plagioclase from Yuan et al., 2017). Dare et al. (2014) noted that elevated Mo concentrations in magnetites are a common feature in magmatic systems where apatite is present but did not further discuss an explanation. Cr in magnetite shows a high variability from almost absent till <0.5 wt% (Figure 3.9). The majority of the selected samples show Cr concentrations in magnetite below 100 ppm. However, several exceptions can be observed. At first glance it is noticeable that magnetites in anorthosites show high concentrations. Four out of seven analyzed anorthosite samples show Cr in magnetite concentrations >400 ppm. This is best explained by the low amount of magnetite and the absence of olivine where Cr is also compatible. For the other rock types Cr in magnetites has local maxima often correlating with the reversal intervals observed by Yuan et al. (2017).

3.3.4 Composition of clinopyroxene

In contrast to the titanomagnetites, clinopyroxenes of the UZ show overall trends within the entire UZ sequence rather than compositional variations or scattering within cycles. Major and trace element compositions of clinopyroxenes are presented in Supplemental Table S9. The major element compositon of the UZ clinopyroxenes is presented in Figure 3.11 for Mg# and wollastonite component (Wo, calculated after Deer et al., 1992). Clinopyroxene compositions show a clear dependence on the stratigraphic position in two intervals. Mg# and wollastonite component in clinopyroxene decrease slightly from ~65 to ~55 mol% and ~40 to ~35 mol% respectively from the base of UZa till above the reversal in cycle XII. Within cycle XII the clinopyroxene composition changes abrupt to lower Mg# and higher Wo followed by an increase in Mg# and a decrease in Wo. A dependence on the rock type is not observed. Compositional changes in pyroxene towards more evolved compositons are known from the trapped liquid shift effect (Barnes, 1986). In this, the cumulus mineral equilibrates with trapped intercumulus liquid, changing the cumulus composition of the mineral. However, the magnitude of this effect strongly depends on the modal abundance of ferromagnesian phases, with a larger effect at low modal amounts. The shift observed in this study occurs in samples from a short interval with variable mineral assemblages and modes to a similar extent, thus arguing against an effect of the trapped liquid shift. Moreover the compositional shift occurs at the level of proposed magma influx. Thus, it is most likely, the observed abrupt changes towards more evolved clinopyroxene compositions and the thickness of cycle XII reflect the addition of a large amount of significantly more evolved magma at the base of UZc.

Similar to the major element composition of clinopyroxene Eu, Sr, Co and Sc show a twofold trend (Figure 3.12). Sr and Eu are incompatible in clinopyroxene and Sc behaves compatible. Nevertheless, all three show same trends with stratigraphic position similar to the Wo component with first constant values till cycle XII followed by an abrupt increase within cycle XII. While Eu and Sr stay constant at higher values, Sc decreases upwards. Moreover, Eu is highly compatible in apatite, thus an increase in Eu in clinopyroxene together with apatite saturation is not expected. Co, compatible in clinopyroxene, follows the opposite trend with constantly higher values in UZa and UZb with an abrupt decrease within cycle XII. Alltogether, the similar behavior of compatible and incompatible elements in clinopyroxene and the abrupt changes within cycle XII independent of co-crystalizing phases, strongly argue for a drastic change in melt composition, probably due to the injection of a evolved silicate liquid enriched in Eu, Sr and Sc and depleted in Co.
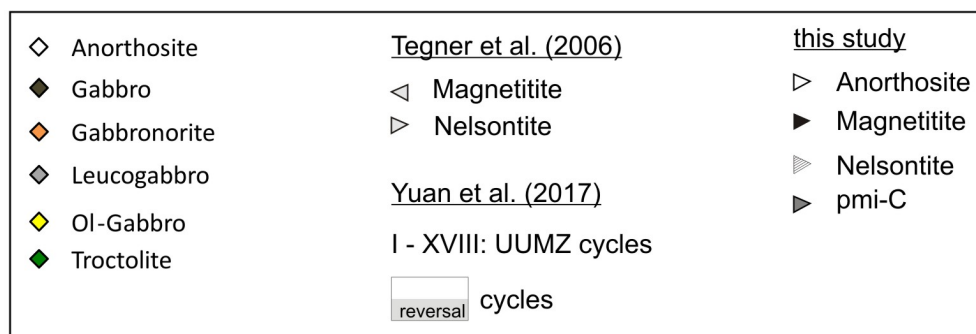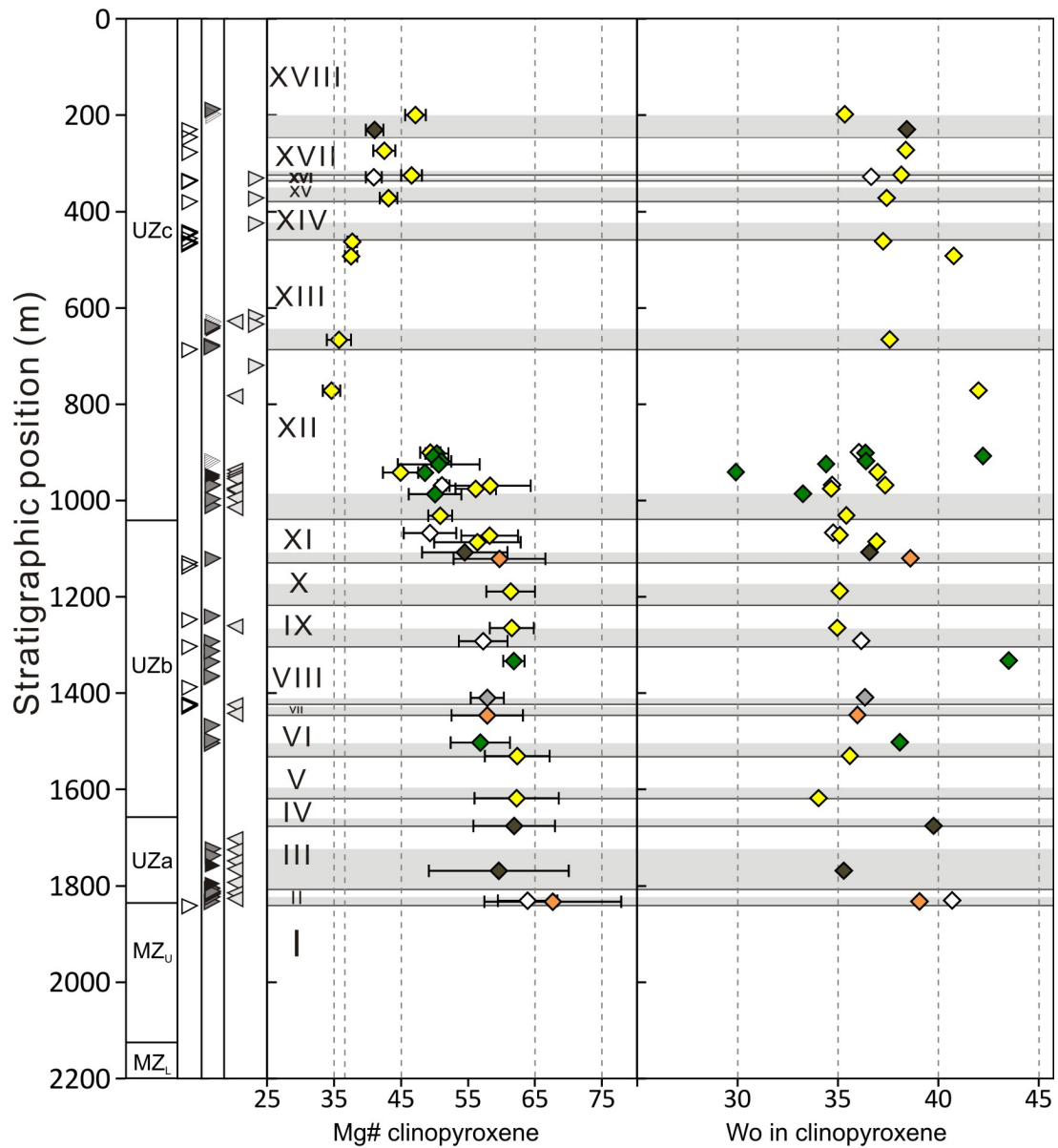
Figure 3.11 Compositional variation of UZ clinopyroxenes with stratigraphic position. Each datapoint represents the average magnetite composition in a single sample. Error bars indicate the standard deviations and colors indicate the rock type. Also marked are positions of magnetitite, nelsonite and anorthtosite layers (Tegner et al., 2006; Yuan et al., 2017) and cycles with reversals (Yuan et al., 2017).
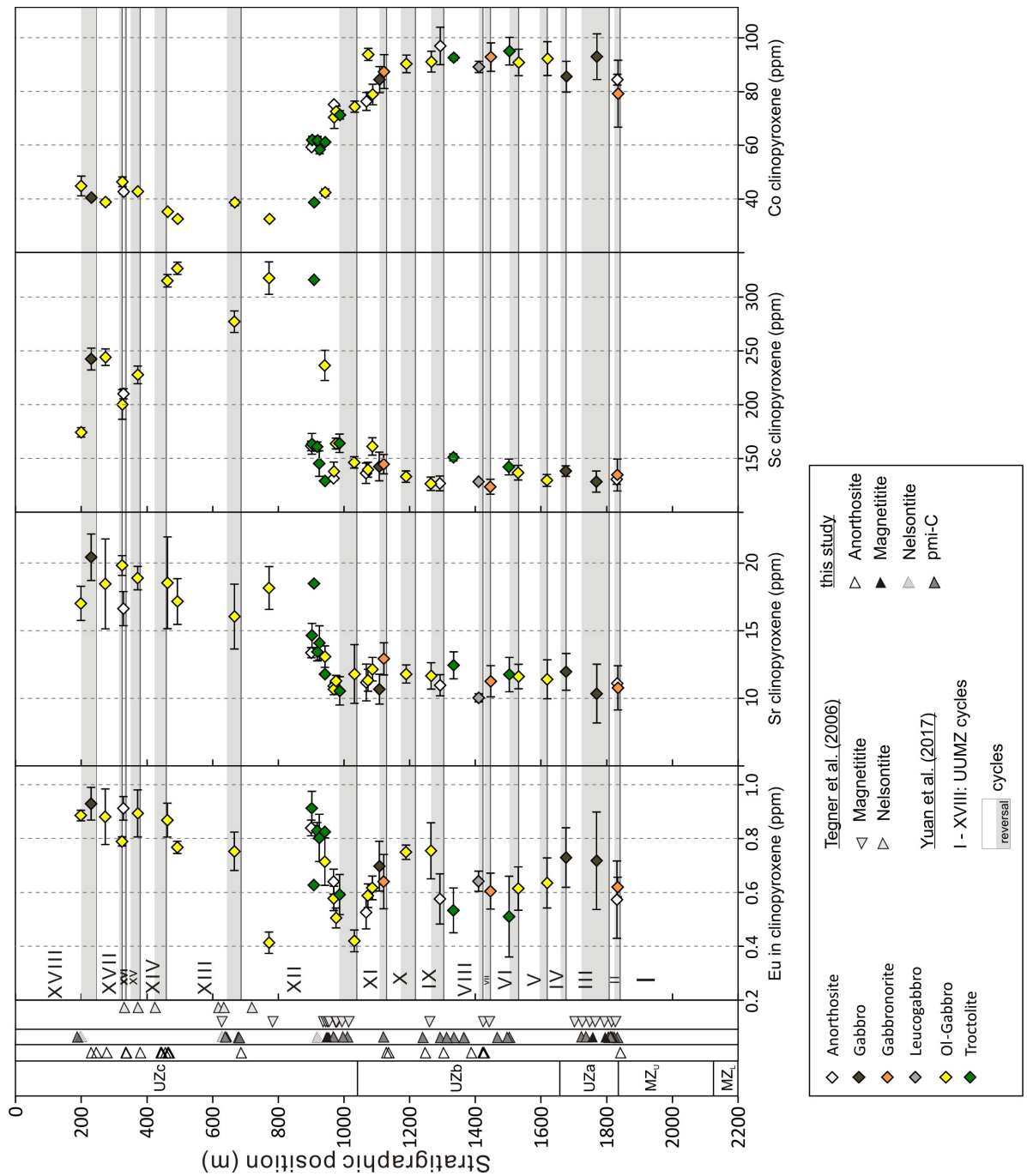
Figure 3.12 Selected trace elements in clinopyroxene with stratigraphic position. Each datapoint represents the average magnetite composition in a single sample. Error bars indicate the standard deviations and colors indicate the rock type. Also marked are positions of magnetitite, nelsonite and anorhtosite layers (Tegner et al., 2006; Yuan et al., 2017) and cycles with reversals (Yuan et al., 2017).

3.3.5 V concentrations in bulk rock, magnetite and clinopyroxene

As discussed above, the partitioning of V between magnetite and clinopyroxene is sensitive to changes in fO_2. Cr, which is also a multivalent element, could generally act in the same way, as proxy for fO_2 conditions. However, Cr concentrations are much lower in all phases, especially in clinopyroxene where it is often below the detection limit. Therefore special attention is drawn to V distribution in the UZ rocks. V concentrations in magnetite range between 10 and 13600 ppm, and in clinopyroxene between up top 400 ppm. V in magnetite and clinopyroxene follows the same trend as bulk rock V concentration. However, compared to the overall trend several samples show more variable V concentrations in both minerals showing peaks towards higher concentrations. These variations show a clear correlation between V in magnetite and clinopyroxene. Thus, similar process of magma injection (Yuan et al., 2017) causing the cyclicity of the stratigraphy might have influenced both minerals. Magnetite is the first mineral crystallizing in the UUMZ where V is highly compatible. Thus, the appearance of magnetite also marks the maximum peak in bulk rock V at a depth of 1758 m (base of UZa).
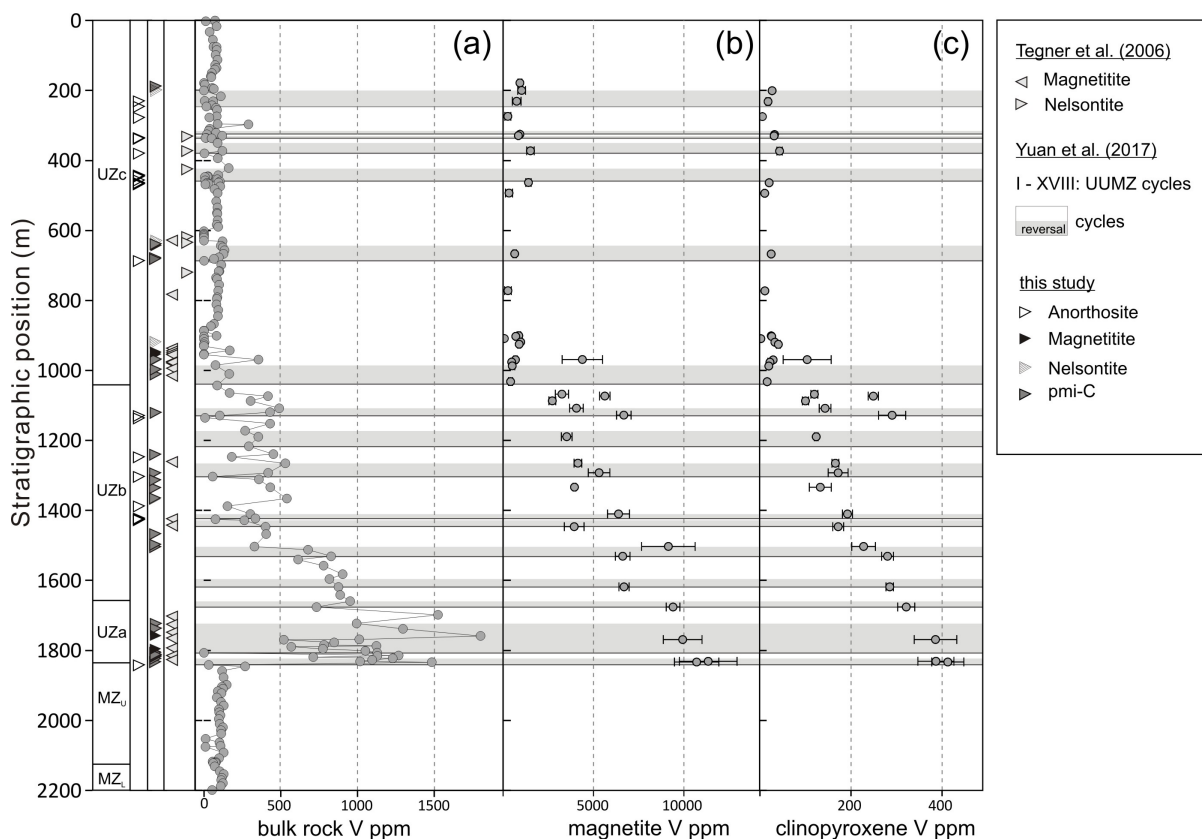
Figure 3.13 V concentrations in bulk rock, magnetite and clinopyroxene. Bulk rock data are from Yuan et al. (2017) from the same drill core as samples from this study. Magnetite and clinopyroxene V concentrations are from this study. Each datapoint represents the average magnetite composition in a single sample. Error bars indicate the standard deviations. Also marked are positions of magnetitite, nelsonite and anorhtosite layers (Tegner et al., 2006; Yuan et al., 2017) and cycles with reversals (Yuan et al., 2017).

In Figure 3.13 the evolution of bulk rock V within the UUMZ stratigraphy is shown. V shows a high variation in bulk rock, ranging between 0 and 1801 ppm. Overall, V concentrations in 2200 m to 1800 m depth are constant between 80 and 100 ppm repeatedly with single depleted samples in between. Moreover, there is a 900 m sequence marked by a peak in V concentration of 1800 ppm at a depth of 1758 m followed by a decrease upwards down to a concentration of 80 ppm at a depth of 900 m. This decrease, in turn, is interrupted at a depth of 1500 m with a shift to lower V concentrations. Similar to the reported reversals in anorthite (Yuan et al., 2017), the overall decrease is interrupted by several reversals in bulk V towards higher concentrations, which are also observed in the predominantly constant sequence above 900 m depth. These reversals correlate well with those observed in anorthite.

3.3.6 Petrologic implications for the UUMZ

Previously reported compositional reversals (Yuan et al. 2017) evidence the concept of multiple magma injections into the UUMZ of the Bushveld Complex. The comprehensive dataset for V in bulk rock, magnetite and clinopyroxene is most appropriate to describe the evolution the UUMZ. Its stratigraphy is marked by a strong and abrupt increase in V and the highest V concentrations in bulk rock at around 1800 m depth (cp. Figure 3.13) reflected by maximimum V concentrations in magnetites and clinopyroxenes from this depth. This is also the level of the first magnetite crystallization showing that magnetite is the first mineral where V is a major component. This peak in V is followed by a decrease in V concentration in both, bulk rock and mineral compositions till ~1500 m depth, indicating a fractional crystallization. Yuan et al. (2017) noted three magma injections in this interval, implying that the injected magma had a similar decrease in V concentration as the resident magma, although slightly enriched in V, or the proportion of the injected magma was too small to influence the bulk V concentration. At the depth of ~1500 m the continuous decrease in V is interrupted and shows a gap towards lower V values. This jump in V concentration occurs at the level of a new magma injection, implying that the injected magma was strongly depleted in V compared to the resident magma at this stage. From this level of the intrusion bulk rock V decreases upwards to a concentration of ~80 ppm at within cycle XII and then stays constant till the top of the intrusion. This level of the intrusion shows also marked characteristics in magnetite and clinopyroxene compositions as discussed above. Mo in magnetites and major and trace element composition of clinopyroxenes show an abrupt compositional change within cycle XII in the UZc. The lower Mg# in clinopyroxene above this abrupt change suggests that the injected magma was much more evolved in composition than the resident magma and enriched in Mo, Eu, Sr, Sc and depleted in Co. Although, showing reversals in e.g. An content in plagioclase and bulk P the overall compositional trend of the UUMZ follows a fractionation trend upwards. The source of the magma injections, causing the observed compositional reversals is not known. Several authors

proposed the existence of a sub-Bushveld magmatic staging chamber, which most likely is the source of injected magma (Eales, 2002; Ashwal, 2005; McDonald & Howell, 2007, Roelofse & Ashwal, 2012). Based on the overall fractionation trend in An in plagioclase, Yuan et al. (2017) concluded that this staging chamber is continuously differentiating. The strong compositional shift in the UZ observed in V at cycle VI and in clinopyroxene in cycle XII are discriminated against the cycles described by Yuan et al. (2017) by their characteristic compositional shift being significantly more pronounced. Thus, they are in conflict with a continuous evolving sub-Bushveld magma staging chamber. Aiming to explain the different crustal contamination signatures of Main Zone rocks, Roelofse & Ashwal (2012) proposed a sub-compartmentalized staging chamber. In their model segmented parts of the staging chamber are located in different depth within the crust and thus are variably contaminated by contaminants from upper or lower crust. The abrupt compositional changes in cycle VI and XII could result from magmas derived from different parts of a sub-compartmentalized staging chamber. V in magnetite and clinopyroxene is homogenously distributed within most of the samples. However, some samples show a large scattering in their mineral V concentrations. As shown in Figure 3.13 these samples are often located within or directly above the reversals described by Yuan et al. (2017). Compared to magnetites at the top of the underlying cycles, these magnetites show an average composition with higher V concentrations. The scattering can be explained by crystallization of magnetite during magma mixing, supporting an early magnetite crystallization after magma replenishment.

As shown above, the oxygen fugacity is a function of V ratio of magnetite/clinopyroxene (V_{mt}/V_{cpx}), thus, changes in V_{mt}/V_{cpx} reflect changes in the prevailing fO_2. Figure 3.14 shows that the Vmt/Vcpx within the UZ stratigraphy. In general Vmt/Vcpx shows only slight variations within the errors and is independent of whole rock V concentrations and host rock. This is in agreement with Balan et al. (2006) who observed constant fO_2 throughout the UZ stratigraphy. Similar to the mostly continuously evolving bulk rock vanadium concentrations, the constant V_{mt}/V_{cpx} ratios imply that the injected magma had a similar fO_2 as the resident magma. Nevertheless, peaks towards higher V_{mt}/V_{cpx} ratios are observed at depth of 1400, 900 and 300 m, thus not correlating with proposed magma injections. When comparing these peaks with the modal abundance of magnetite it is conspicuous that the high V_{mt}/V_{cpx} ratios are from samples with locally lowest magnetite proportions marking the end of a decrease in magnetite from a high magnetite sample approximately 100 m below. This correlation suggests that the extensive crystallization of magnetite lowers significantly the fO_2 conditions for the following magnetite crystallization. This is supported by Toplis & Carroll (1996) who showed that high magnetite crystallization removes Fe^{3+} from the melt, thus lowering the fO_2. Moreover, Balan et al. (2006) observed changes in fO_2 within single massive magnetite layers, with lower fO_2 at the top of a single magnetite layer.

The only constrain on oxygen fugacity for the UUMZ was proposed by VanTongeren et al. (2010). Based on the experiments of Toplis & Carroll (1996), the appearance of cumulus

magnetite and the further presence of fayalitic olivine, VanTongeren et al. (2010) proposed that the prevailing fO_2 conditions for the UZ were close to the FMQ (Quartz-Fayalite-Magnetite) buffer. Using the equation (3.5) enables the estimation of fO_2 from the obtained V_{mt}/V_{cpx} ratios of this study. Calculations reveal fO_2 values from log fO_2 -14 to -18, which is more reducing than previously proposed (assuming a solvus temperature for titanomagnetite of 900°C; log fO_2 -14 corresponds to FMQ - 1.5) and is closer to the proposed NNO conditions of UZ magnetitite layers (Balan et al., 2006). However, calculated fO_2 are in a range with only poor experimental data and the propagated errors from fits and analysis are larger than the calculated variability. Nevertheless, the ratio of V in magnetite versus clinopyroxene shows that relative changes in fO_2 appear outside the error limits.
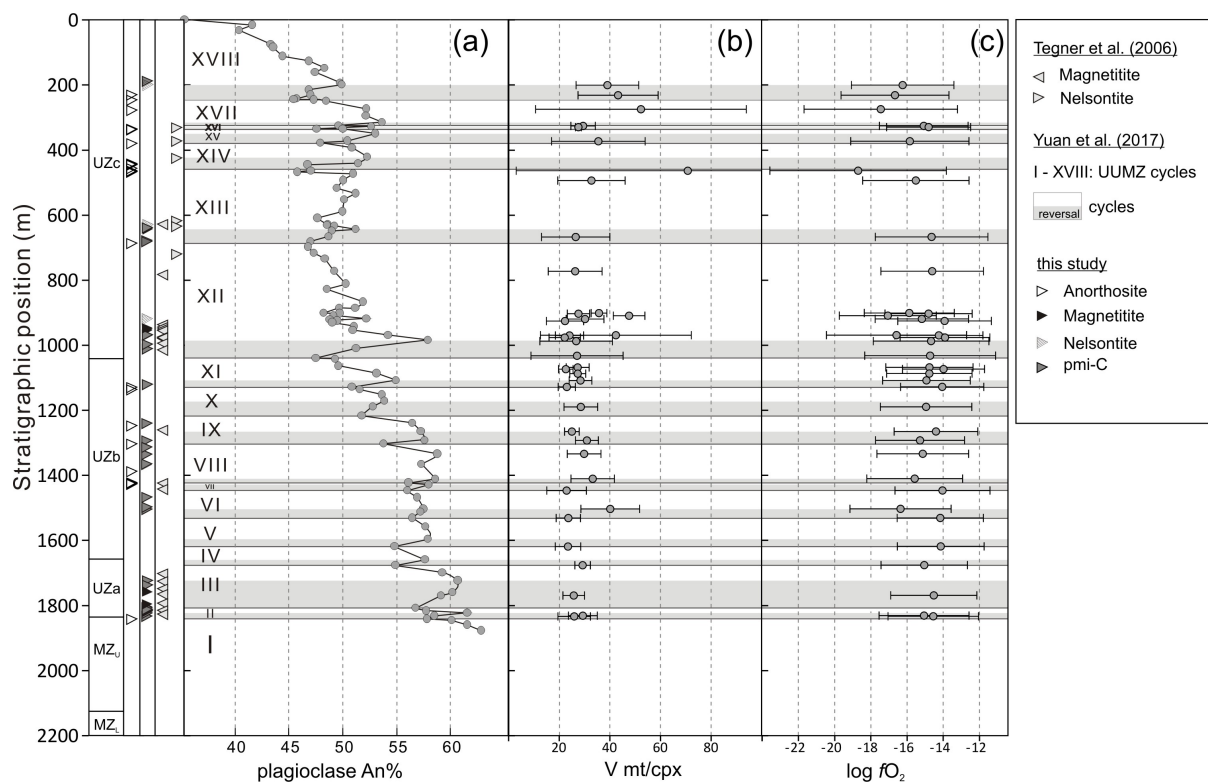
Figure 3.14 showing the An content in plagioclase, the ratio of V in magnetite versus clinopyroxene and the estimated fO_2. Plagioclase data are from Yuan et al. (2017) from the same drill core as samples from this study. V ratio are from this study with each datapoint calculated from average mineral compositions in a single sample. Error bars indicate the propagated errors. Also marked are positions of magnetitite, nelsonite and anorhtosite layers (Tegner et al., 2006; Yuan et al., 2017) and cycles with reversals (Yuan et al., 2017).

3.3.7 Comparison with the magnetite-ilmenite oxy-barometer

The mineral-equilibrium Fe-Ti-oxide geo-thermometer and oxy-barometer was introduced by Buddington & Lindsley (1964) and is continuous developed and re-calibrated (e.g., numerical fits by Spencer & Lindsley, 1981; Sauerzapf et al., 2008). Ghiorso & Evans (2008) revised the Fe-Ti-oxide oxy-barometer by taking the entropy of the solid solution into account. Duchesne et al. (2007) presented an empirical calibrated oxy-barometer based on

the V distribution between magnetite and ilmenite. These oxy-barometers require equilibrium of magnetite and ilmenite and the absence of any subsolidus modification. For comparison with our results we chose the magnetite-ilmenite oxy-barometer calibrated by Sauerzapf et al. (2008), which is applicable to high temperatures and low to moderate fO_2. In comparison Ghiorso & Evans (2008) modified version is applicable to more oxidizing conditions in silicic systems and thus not relevant for the Bushveld Complex.

Calculations with the thermo-oxybarometer by Sauerzapf et al. (2008) revealed log fO_2 values between -12 and -17 and thus are in a similar range as fO_2 obtained in this study. Figure 3.15 shows the comparison of both fO_2 calculations showing a similar trend but large deviations from the 1:1 line. Ilmenite crystals, as used in the Sauerzapf et al. (2008) oxybarometer, experienced low-temperature re-equilibrating expressed in their Mg/Mn ratio (Bacon & Hirschmann, 1988). Calculations of the magnetite-ilmenite equilibrium using Mg/Mn ratios reveal disequilibrium for most ilmenite-magnetie pairs (Figure 3.15a). Where magnetite and ilmenite are in equilibrium smaller deviations from the 1:1 line are implying low temperature modifications of the ilmenite. The use of V distribution between clinopyroxene and magnetite, using magnetite bulk composition (magnetite + exsolution) reveals the magmatic fO_2 conditions. In contrast the oxybarometer by Sauerzapf et al. (2008) applied to slow cooled cumulates gives the, more oxidizing, fO_2 conditions during low temperature modification.
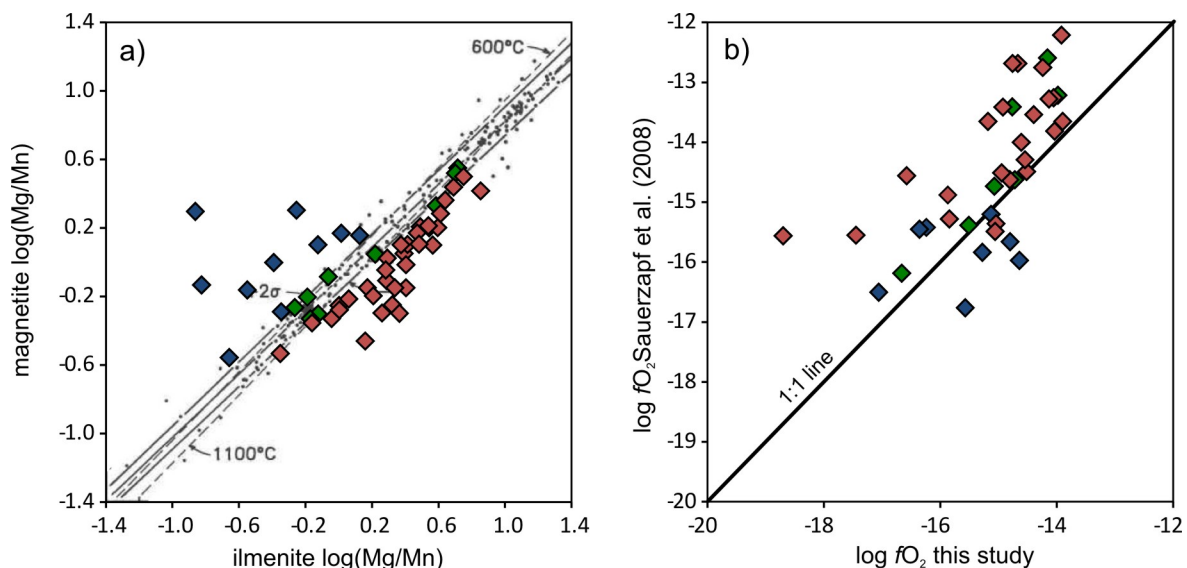
Figure 3.15 a) Test for equilibrium between magnetite and ilmenite after Bacon & Hirschmann (1988). Deviations from the marked field indicate disequilibrium. Only green symbols are in equilibrium. **b)** Comparison of fO_2 calculations from this study and the magnetite/ilmenite oxybarometer of Sauerzapf et al. (2008). Colors are from a) and indicate equilibrium of magnetite and ilmenite used for fO_2 calculations.

3.4 Conclusions

In this study on vanadium distribution between magnetite and clinopyroxene, and trace element composition of titanomagnetite and clinopyroxenes of the UUMZ of the Bushveld Complex compositional variations in titanomagnetite and clinopyroxene are observed, supporting the model of multiple magma injections into the Bushveld chamber (Yuan et al., 2017). Moreover, two strong compositional shifts are observed indicating a more complex evolution of the sub Bushveld magma staging chamber as proposed by Roelofse & Ashwal (2012). Heterogeneous V distribution between different magnetite grains from the same sample observed within proposed reversal suggest an early magnetite crystallization directly after magma mixing of injected and resident magma. Moreover, estimated fO_2 showed that injected magma did not change the prevailing fO_2 conditions. The variations in fO_2 are rather related to the crystallization of high proportions of magnetite. Calculated oxygen fugacities are in the range of log fO_2 -14 to -17 and thus lower than previously proposed suggestions. Comparison with the oxybarometer of Sauerzapf et al. (2008) showed a systematic discrepancy, caused by low-temperature modifications of the Fe-Ti-oxides.

4 The parental magma to the Upper and Upper Main Zone of the Bushveld Complex

4.1 Introduction

It is widely accepted that the Bushveld Complex was formed by multiple magmatic injections with changing compositions (Hamilton, 1977; Kruger, 1992; 1994). However, the liquid compositions of these magma injections have been strongly debated. Feeder structures, giving information on composition or geometry of magma injections are missing. In general it is assumed that the Bushveld Complex was formed by two types of magma. Based on marginal rock compositions, Harmer & Sharpe (1985) proposed a high-Mg basaltic-andesite composition named B1 (Bushveld 1) and a tholeiitic basalt, referred to as B2 and B3 (Bushveld 2 and Bushveld 3). Moreover, Harmer & Sharpe (1985) assumed B1 to be parental to the Lower Zone and the Lower Critical Zone, whereas the Main Zone cumulates could be the product of B2 and B3 magma compositions. The Upper and Upper Main Zone (UUMZ) are traditionally considered to be crystallized from a single batch of magma. However, recent studies have shown that magma replenishment events occurred also within the UUMZ interval (Ashwal et al., 2005; Scoon & Mitchell, 2012; Yuan et al., 2017). Nevertheless, compositions of incoming and resident magmas for the UUMZ are unknown.

This chapter experimentally investigates several proposed and new calculated possible parental compositions for the magmas of the UUMZ. Experiments are designed to simulate the crystallization of the first cumulates above the PM, to study phase relations of MZu cumulates. Additionally thermodynamic models, using rhyolite-METLS are tested and compared with the experimental results.

4.1.1 Base of the UUMZ

The base of the UUMZ is defined by the PM, a 2 - 3 m thick pyroxenite layer (Kruger et al., 1987; Cawthorn et al., 1991, Maier et al., 2001). The PM is observed in all limbs of the Bushveld Complex supporting connectivity between them (see chapter 1.3.1 "Link between limbs"). However, PM samples from different localities differ in their mineralogy. Maier et al. (2001) presented the mineralogy of PM samples from the Western, Eastern and Northern Limb. Based on the majority of the samples, including one from the Bierkraal drill core, the PM is composed of orthopyroxene (70 - 90 vol%), plagioclase (10 - 20 vol%) and clinopyroxene (5 - 15 vol%). However, also clinopyroxenitic PM with >80 vol% clinopyroxene is observed in the Western Limb. Figure 4.1a shows a thin section photograph of a norite from the Bierkraal drill core, typical for the upper part of the PM in the Western Limb.

In general, the PM is considered to have been formed after a major magma replenishment event. Based on compositional reversals at the level of the PM, the injected magma is assumed to be more primitive compared to the resident magma (von

Gruenewaldt, 1973; Kruger et al., 1987; Cawthorn et al., 1991). Based on the $^{87}Sr/^{86}Sr$ isotopic ratio Cawthorn et al. (1991) estimated the relative proportions of the mixing magmas to be equal. Klemm et al. (1985) proposed that the crystallization of the PM was not controlled by the composition of the injected magma but rather by the pressure increase resulting from magma replenishment. This pressure increase would lead to an increase of the orthopyroxene stability field. Maier et al. (2001) suggested an injection of a crystal mush at the base of the residual magma. The relatively cold temperatures of the crystal mush would then lead to supercooling and kinetic suppression of plagioclase crystallization, producing the pyroxenite. Although, specific compositions are unknown, most authors agree that resident magma and injected magma mixed, producing a homogeneous magma parental to the UUMZ.
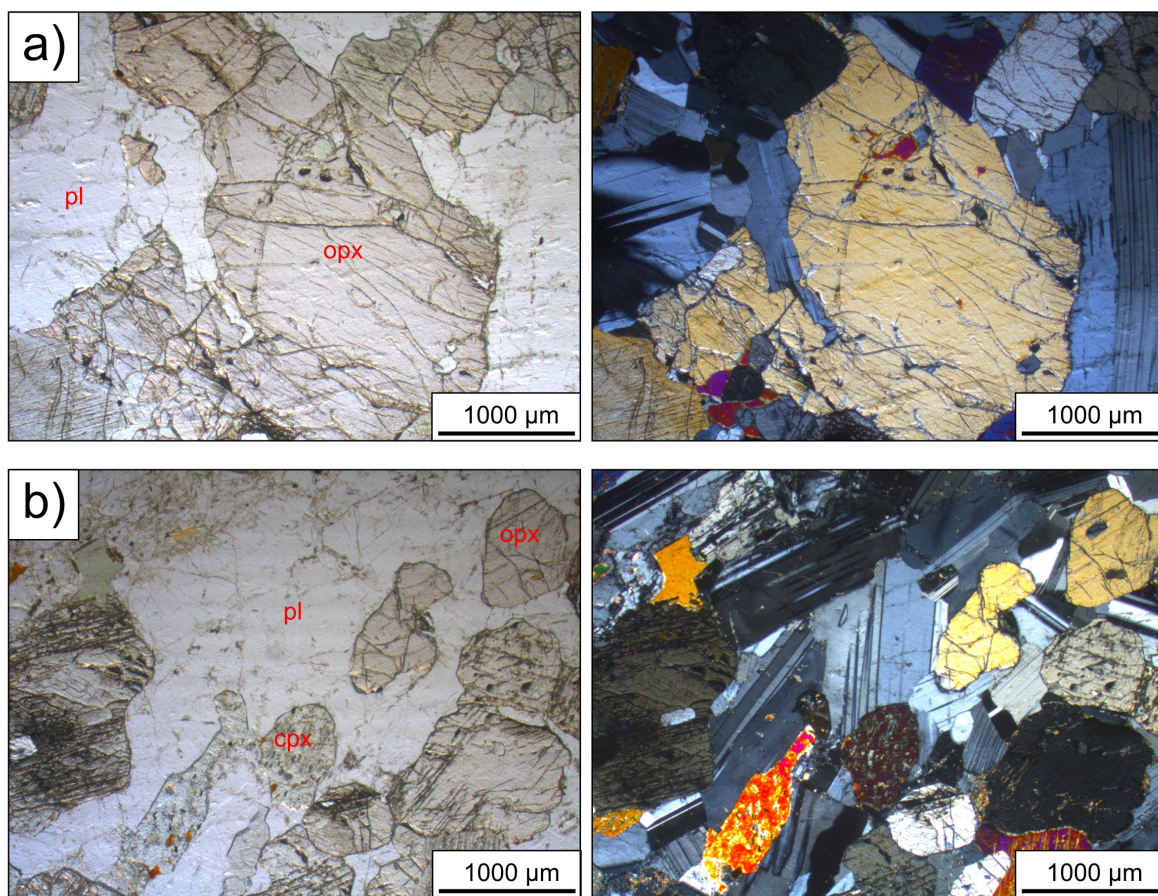
Figure 4.1 Thin section photographs with polarized light and under crossed polars for **A:** Upper part of the Pyroxenite Marker with plagioclase (pl) and orthopyroxene (opx) and **B:** Gabbronorite with plagioclase (pl), orthopyroxene (opx) and clinopyroxene (cpx) located ~30 m above the Pyroxenite Marker in the Western Limb.

In the Western Limb the PM is overlain by gabbronorites (Figure 4.1b), containing cumulus plagioclase, orthopyroxene and clinopyroxene. The compositions of the first cumulate phases of the UUMZ determined in this study in a sample located ~30 m above the PM are given in Table 4.1. Plagioclase composition with An 66 - 74

(molar [Ca/(Ca + Na)]*100) is slightly more primitive than those observed by Cawthorn et al. (1991) in the same drill core for the PM with An ~67. In these rocks, plagioclase has a tabular, euhedral to subhedral shape. Both pyroxenes mostly occur as subhedral grains and are 2 – 4 mm in size. Clinopyroxene crystals show fine exsolution lamellae of orthopyroxene. Clino- and orthopyroxene have a Mg# (molar [Mg/(Mg+Fe)]*100) ranging between 77 - 81 and 71 - 73, respectively. These three phases, plagioclase orthopyroxene and clinoproxene, are assumed to be equilibrium precipitates of the parental magma of the UUMZ.

Table 4.1 Major element compositions in wt% of cumulate minerals of the gabbronorite ~30 m above the Pyroxenite Marker, determined by electron microprobe. Italic values give the standard deviation (1 σ) of each value.

	no.	SiO_2	TiO_2	Al_2O_3	FeOt	MnO	MgO	CaO	Na_2O	K_2O	Total	An/Mg#
pl	11	50.53 *0.74*	b.d.	31.03 *0.37*	0.3 *0.05*	b.d.	b.d.	14.59 *0.55*	3.24 *0.3*	0.19 *0.03*	99.88	70.56
opx	12	54.17 *0.21*	0.23 *0.05*	0.84 *0.07*	17.62 *0.55*	0.39 *0.03*	25.34 *0.45*	1.67 *0.91*	b.d.	b.d.	100.25	71.94
cpx	10	52.61 *1.32*	0.29 *0.13*	1.33 *0.38*	6.97 *0.29*	0.22 *0.03*	15.02 *0.5*	22.54 *0.84*	0.21 *0.05*	b.d.	99.2	79.34

b.d.	below detection limit
no.	number of analyses
An	molar [Ca/(Ca + Na)]*100
Mg#	molar [Mg/(Mg + Fe)] *100

4.1.2 Felsic rocks related to the Bushveld Complex

The mafic Bushveld Complex (or Rustenburg Layered Suite after SACS, 1980), as described above, is part of a larger geodynamic setting located in the Kaapvaal craton which hosts the Transvaal sedimentary rocks. Several magmatic events occurred after stabilization of the craton 2.7 b.y. ago, including the intrusion of mafic sills and eruption of mafic to felsic magmas termed Dullstroom Group (mainly basalt, andesite to minor dacite). Rocks of the Dullstroom Group are located below the Bushveld rocks, which in turn are overlain by the Rooiberg Group comprising of the upper part of the Damwal Formation (dacites and rhyolite) and rhyolites of the Kwaggasnek Formation and the Schrikkloof Formation. After emplacement of the ultramafic to monzonitic rocks of the up to 9 km thick Bushveld Complex, 2.06 b.y. ago, intrusion of granites occurred (Lebowa Granite Suite) which is genetically unrelated to the other suites (Schweitzer et al., 1997).

The relation of the felsic volcanic rocks from the Rooiberg Group with the mafic Bushveld Complex is controversially discussed in literature. The Rooiberg Group rocks show similar ages as the Bushveld Complex suggesting an intrusion between the Dullstroom and Damwal Formations (VanTongeren et al., 2010 and references therein). The origin of these felsic melts was explained by different models including crustal and mantle sources. Hatton & Schweitzer (1995) proposed that partial melting of the lower crust produced the Rooiberg rhyolites. Furthermore, Maier et al. (2000) suggested that these crustal partial melts were mixed with mafic magma resulting in those composition found in the Rooiberg rhyolites.

However, on the basis of trace element compositions Buchanan et al. (2002) reconsidered the partial melting model and suggested a mantle derived melt which was contaminated by crustal assimilation which then further differentiated. VanTongeren et al. (2010) revised the previous models and proposed a cogenetic relationship of the Rooiberg Rhyolites and the Bushveld Complex, where the rhyolites are the residual liquid from differentiation which then escaped from the mafic cumulates as shown by Cawthorn & Walraven (1998). Although agreeing with the model of the escaped liquid formed by differentiation, Cawthorn (2013a) questioned the conclusions of VanTongeren et al. (2010), arguing that the rhyolites were emplaced before and metamorphosed by the intrusion of the mafic Bushveld. As equivalent for the residual liquid he proposes a monzonitic composition found in a rock succession located below the Rooiberg Group. However, monzonite and rhyolite are similar in major element composition. Major element compositions of the rhyolites and monzonite are given in Table 4.2.

Table 4.2 Published major element compositions for calculated UUMZ bulk rock and natural felsic lithologies.

		SiO$_2$	TiO$_2$	Al$_2$O$_3$	FeOt	MnO	MgO	CaO	Na$_2$O	K$_2$O	P$_2$O$_5$	total
UUMZ Bulk	Tegner et al. (2006)	47.6	1.2	17.3	13.5	0.2	5.6	11.0	2.7	0.4	0.44	99.94
UUMZ Bulk	VanTongeren et al. (2010)	47.03	1.7	16.4	15.6	0,2	6.48	9.39	2.46	0.36	0.38	100.01
Damwal	Schweitzer et al. (1997)	68.30	0.60	12.20	7.18	0,14	1.09	2.31	2.84	4.17	0.15	98.98
Kwaggasnek	Schweitzer et al. (1997)	72.30	0.35	11.60	5.24	0.14	0.66	0.69	2.69	5.07	0.05	98.94
Schrikkloof	Schweitzer et al. (1997)	74.40	0.24	11.60	3.20	0.03	0.61	0.24	2.26	5.82	0.02	98.78
Rashoop	Schweitzer et al. (1997)	73.91	0.25	11.97	3.45	0.08	0.53	0.30	3.12	5.48	0.03	99.12
Monzonite	Cawthorn (2013a)	69.94	0.46	12.13	5.97	0.1	0.27	1.70	3.01	4.17	0.10	97.85

4.1.3 Previous assumptions of UUMZ parental magma

Several assumptions were made on the UUMZ parental magma composition. As mentioned above, the injection of a new magma at the level of the PM is widely accepted. A first estimation of the composition of the UUMZ parental magma was proposed by Davies & Cawthorn (1984). They identified a hypersthene gabbro body which intruded into the cumulates of the Critical Zone. Based on field relations they suggested that this body is probably representative of the magma parental to the UUMZ. Cawthron et al. (1991) studied relative changes between resident and injected magma suggesting a lower silica activity and higher La/Sm ratio of the injected magma but similar REE signature for both. Two more recent studies provide additional estimated compositions of possible parental magmas (Tegner et al., 2006; VanTongeren et al., 2010). Both studies made the same assumption as Cawthorn & Walraven (1998) that 20 % of an unknown magma escaped from the magma chamber and that the components of the segregated magma are now missing in the cumulate UUMZ sequence. Based on UUMZ bulk rock compositions from von Gruenewaldt (1971), Tegner et al. (2006) calculated an average composition for the entire

UUMZ above the PM by adding 20 % of a calculated liquid in equilibrium with the cumulus phases at the top of the intrusion (olivine, clinopyroxene, plagioclase, ilmenite and magnetite). The bulk composition of the UUMZ without the 20% missing component is presented in Table 4.2 and the bulk composition including the 20% segregated liquid is given in Table 4.3. Similar to this attempt VanTongeren et al. (2010) calculated possible magma compositions, parental to the UUMZ. They calculated the bulk UUMZ composition from data published by Molyneux (1974) completed by new analyses from the same section (composition is presented in Table 4.2). They proposed the Rooiberg rhyolites as an equivalent of the missing component, which was squeezed out during the crystallization of the Bushveld Complex. Following these assumptions they added different proportions (15%; 25%) of four different rhyolitic compositions found on top of the Bushveld Complex (Schweitzer et al., 1997) to the UUMZ bulk composition resulting in possible parental magma compositions.

Table 4.3 shows the proposed parental magma compositions of Davis & Cawthorn (1984), Tegner et al. (2006) and VanTongeren et al. (2010) with basaltic to basaltic-andesite compositions. VanTongeren et al. (2010) tested their compositions and those of Tegner et al. (2006) by MELTS calculations (Ghiorso & Sack, 1995). Their calculations revealed a crystallization sequence of orthopyroxene -> orthopyroxene + plagioclase -> pigeonite + clinopyroxene + plagioclase. This does not perfectly resemble the natural occurring cumulates, suggesting an earlier crystallization of clinopyroxenes together with orthopyroxene and plagioclase. The authors argue that this discrepancy is caused by the MELTS program, which works with a Gibbs free energy minimization algorithm. Since the difference in the Gibbs free energy between both pyroxenes is very small, there may be a large error on the prediction of the stabilities of orthopyroxene, pigeonite and clinopyroxene.

Considering that MELTS may not be successful to model the crystallization processes accurately for the proposed parental compositions, experiments to determine phase equilibria in possible parental magma compositions are necessary to test the validity of hypotheses formulated in VanTongeren et al. (2010).

Table 4.3 Proposed parental magma composition in wt% for the Upper and Upper Main Zone.

	Davies & Cawthorn (1984)	Tegner et al. (2006)	VanTongeren et al. (2010)							
escaped liquid	n.A.	20%	15% Damwal	15% Kwaggasnek	15% Schrikkloof	15% Rashoop	25% Damwal	25% Kwaggasnek	25% Schrikkloof	25% Rashoop
SiO$_2$	49.72	51.40	50.22	50.82	51.14	51.06	52.35	53.35	53.87	53.75
TiO$_2$	0.81	1.00	1.56	1.53	1.51	1.51	1.45	1.39	1.36	1.36
Al$_2$O$_3$	15.67	16.60	15.75	15.66	15.66	15.71	15.33	15.18	15.18	15.27
FeO$_{tot}$	12.74	11.70	14.34	14.05	13.74	13.78	13.50	13.01	12.50	12.56
MnO	0.19	0.10	0.19	0.19	0.18	0.19	0.19	0.19	0.16	0.17
MgO	6.08	4.60	5.67	5.60	5.60	5.58	5.13	5.02	5.01	4.99
CaO	10.83	9.70	8.32	8.08	8.01	8.02	7.62	7.21	7.10	7.11
Na$_2$O	2.94	2.90	2.51	2.49	2.48	2.56	2.55	2.51	2.50	2.62
K$_2$O	0.25	0.70	0.93	1.06	1.18	1.13	1.31	1.54	1.72	1.64
P$_2$O$_5$	-	0.40	0.34	0.33	0.32	0.33	0.32	0.30	0.29	0.29
Total	99.23	99.10	99.83	99.81	99.82	99.87	99.75	99.70	99.69	99.76

4.2 Methods

4.2.1 Choice of starting compositions

For the evaluation of potential parental compositions of the UUMZ, the cumulate phases of the gabbronorite, plagioclase, orthopyroxene and clinopyroxene, overlaying the PM are used (Table 4.1). The aim of this study is to reproduce the phase assemblage of those gabbronorites in order to identify their parental magma composition. It is assumed that the UUMZ parental magma was in equilibrium with the three phases. Thus, the main aim of the experimental approach is to constrain the conditions, mainly temperature and bulk composition representative of the UUMZ parental magma composition, at which the three phases crystallize within a small temperature interval below the liquidus. Also, the mineral compositions from experimental products must reproduce the composition of the minerals observed above the PM. Moreover, proposed formation conditions for the UUMZ, such as temperature and pressure and the influence of oxygen fugacity and melt water content have to be verified.

In total six possible parental compositions were tested in this study and are presented in Table 4.4. In addition to possible parental compositions presented in literature (compositions A, B, C and D) two more possible parental magma compositions were calculated (compositions E and F) and were prepared as starting material for the experiments. Compositions A and B are calculated mixtures of bulk UUMZ (VanTongeren et al., 2010) and monzonite (Cawthorn, 2013a). The proportions of 15% and 25% felsic component were proposed by VanTongeren et al. (2010). The monzonite corresponds to the

liquid which is supposed to have been escaped from the Bushveld magma chamber (Cawthorn & Walraven, 1998; VanTongeren et al., 2010). As noted above, there is no significant difference between the proposed escaped liquid composition of VanTongeren et al. (2010) and Cawthorn (2013a). Thus we only tested mixtures with one proposed felsic composition which is sufficient to test the hypothesis of VanTongeren et al. (2010). Composition C and D are from Tegner et al. (2006) and Davies & Cawthorn (1984) respectively.

E and F are new compositions which were tested in this study. In the course of this study we noted that the silica activities in the four investigated compositions A, B, C and D were too low for the stabilization of orthopyroxene. In order to obtain systems with higher silica activities, the amount of added felsic component to the UUMZ bulk composition was increased. Composition E is a mixture of 60% bulk UUMZ (VanTongeren et al., 2010) and 40% monzonite (Cawthorn, 2013a) resulting in an andesitic composition. Composition F was prepared considering that a clinopyroxene component was missing in the silica-rich composition E. The composition of the added clinopyroxene component is corresponding to the clinopyroxene composition observed in the first cumulates above the PM (see Table 4.1 for composition). While felsic components are found at the top of the Bushveld Complex and are supposed to represent an escaped liquid (VanTongeren et al., 2010; Cawthorn, 2013a), high amounts of clinopyroxene are observed in some parts of the PM, underlying the UUMZ (Maier et al., 2001). To calculate the amount which needs to be added to bulk UUMZ and monzonite, the exchange partition coefficient of Mg and Fe between clinopyroxene/orthopyroxene and liquid is used. The Kd^{Fe-Mg}_{px-liq} of 0.21 was obtained from experimental runs in this study using composition E. This value, although slightly lower, is in the range of those proposed by (Baker & Eggler, 1987; Bédard et al., 2007). Using composition E, clinopyroxene was added step by step until the Mg# for the natural orthopyroxene was in equilibrium with the new liquid composition. After addition of 8 wt% of clinopyroxene component to composition E, the Mg# of the calculated equilibrium orthopyroxene is in agreement with those observed above the PM.

In contrast to previous assumptions on UUMZ parental magma the new composition F is andesitic and not basaltic (Table 4.4).

Table 4.4 Calculated starting compositions for crystallization experiments. All values are given in wt%.

	SiO$_2$	TiO$_2$	Al$_2$O$_3$	FeO	MnO	MgO	CaO	Na$_2$O	K$_2$O	P$_2$O$_5$	total	Mg#
A	50.62	1.55	15.79	14.20	0.19	5.56	8.26	2.55	0.93	0.34	100	41.1
B	53.04	1.43	15.40	13.27	0.17	4.95	7.50	2.61	1.32	0.31	100	39.9
C	51.87	1.00	16.75	11.82	0.10	4.64	9.78	2.93	0.71	0.40	100	41.2
D	50.43	0.82	15.89	11.92	0.20	6.17	10.98	2.98	0.25	0.35	100	48.0
E	56.68	1.24	14.80	11.85	0.16	4.03	6.37	2.70	1.90	0.27	100	37.7
F	57.65	1.56	13.33	11.28	0.19	3.51	7.29	2.57	2.22	0.41	100	35.7

totals are normalized to 100%
A: 15% escaped liquid
B: 25% escaped liquid
C: Tegner et al., 2006
D: Davies & and Cawthorn, 1984
E: 40% escaped liquid
F: monzonite + clinopyroxene
Mg#: molar [Mg/(Mg + Fe)] *100

4.2.2 Preparation of starting compositions

Starting compositions were prepared as mixed powders from oxide, carbonate, phosphate and synthesized mineral powders. SiO$_2$ was used for silica, TiO$_2$ for titanium, Al$_2$O$_3$ for aluminum, Fe$_2$O$_3$ and fayalite for iron, MnO for manganese, MgO for magnesium, wollastonite for calcium, albite for sodium, orthoclase for potassium and Ca$_3$PO$_4$ for phosphorus. Prior to weighing, powders were dried at 110°C over night. To account for the hydroscopic behavior of SiO$_2$, Al$_2$O$_3$ and MgO, these powders were annealed at 800°C for 12 h in a muffle-furnace. The powders were mixed with ethanol in an agate mortar and then grinded in a disk mill for 20 min to attain homogenization.

Additionally, composition F was prepared as oxide powder mixture (F$_{ox}$) and glass (F$_{gl}$). For the starting glass, SiO$_2$ was used for silica, TiO$_2$ for titanium, Al$_2$O$_3$ for aluminum, Fe$_2$O$_3$ for iron, Mn$_3$O$_4$ for manganese, MgO for magnesium, CaCO$_3$ for calcium, Na$_2$CO$_3$ for sodium, K$_2$CO$_3$ for potassium and (NH$_4$)H$_2$PO$_4$ for phosphorus. After homogenization in a mortar mixed powders were loaded into Pt-crucibles and melted at 1600°C and 1 atm in air for 2 h before quenching in water. During heating volatile components (H$_2$, NH$_4$, CO$_2$) degas. Quenched glass was then grinded in a disc mill for 20 min. This procedure was repeated to obtain a homogeneous glass.

To prepare samples for the experimental runs, starting powders (oxide or glass) were loaded into Pt-graphite-double-capsules. Pt-capsules with an outer diameter of 4.4 and an inner diameter of 4.0 mm were annealed at 950°C for 10 minutes and quenched in water. After drying, one end was welded with a PUK fine welding system (Lampert PUK3). Around 30 mg of each starting powder or glass were filled in a single graphite crucible, and dried

again at 400°C for 2 hours. Graphite crucibles were closed with a lid and graphite crucibles were loaded into Pt-capsules and welded shut.

4.2.3 Experimental setup

To simulate crystallization of the possible parental magma compositions an Internally Heated Pressure Vessel (IHPV) at the Institut für Mineralogie, Leibniz Universität Hannover, Germany was used. Analyses on experimental run products were obtained via electron microprobe (EMPA) in the same institute.

The experiments were performed at 2 kbar between 1080°C and 1140°C, which are conditions relevant to the Bushveld Complex. Crystallization pressures for the UUMZ were estimated to be between 1.5 kbar for the upper part (Wallmach et al., 1995) and 2 kbar for the lower part (VanTongeren et al., 2010). Liquidus temperatures for potential parental magmas were calculated to be <1200°C. The experiments were conducted using Pt-graphite double capsules (Husen et al., 2016) and have an oxygen fugacity, defined by the graphite-CO-CO_2 (CCO ≈ FMQ -2) buffer (Hirschmann et al., 2008). The fO_2 conditions during experiments were confirmed using the partitioning of Fe between plagioclase and melt (Phinney, 1992). The presence of graphite from the double-capsule technique leads to anhydrous conditions during the experiments (Holloway et al., 1992). Run duration for the experiments was ≥24 h.

Experiments were conducted in an IHPV equipped with a rapid quench device, which avoids the formation of quench crystal phases. The vessel is pressurized with Ar gas. The temperature inside the furnace is monitored and controlled by four thermocouples. Deviations in temperature were observed to be below ±5°C. Pressure is monitored with a strain gauge manometer with an uncertainty of ±50 bar. A detailed description of the IHPV and rapid quench device is given in Berndt et al. (2002).

In addition to the different starting materials glass or oxide mixture, two different temperature paths were used at the beginning of the experiments. The first temperature path consisted in heating with a ramp of 50 K/min till 20°C below the experimental temperature. Final temperature was then reached with a ramp of 10 K/min to avoid overshooting of the temperature. Experimental temperature was then hold for >24 h. In a second approach the sample was heated above the liquidus to 1200°C with a ramp of 50 K/min to melt the sample prior to crystallization. After holding 1200°C for two hours, temperature was dropped down to the experimental run conditions and held for 48 h. The latter temperature path was only applied to oxide mixture starting material. Table 4.5 shows the experimental run conditions for each experiment.

Table 4.5 Experimental run conditions and run products

composition	run	T (°C)	t (h)	phases
A	BU1_01 *	1143	24	gl, ol, pl †
	Y244	1200 → 1140	47	gl, ol, pl
	Y079	1120	62	gl, ol, pl †
	BU1_03 *	1105	44	gl, ol, pl, pig †
	Y237I	1200 → 1100	48	gl, ol, pl, pig
	Y235I	1200 → 1080	48	gl, ol, pl
B	BU1_01 *	1143	24	gl, ol, pl †
	Y244	1200 → 1140	47	gl, pl
	Y079	1120	62	gl, ol, pl, pig †
	BU1_03 *	1105	44	gl, ol, pl, pig †
	Y237I	1200 → 1100	48	gl, ol, pl, pig
	Y209	1080	52	gl, pl, pig †
	Y235I	1200 → 1080	48	gl, ol, pl, pig
C	BU1_01 *	1143	24	gl, ol, pl, cpx †
	Y075	1140	48	gl, ol, pl †
	Y244	1200 → 1140	47	gl, pl
	BU1_03 *	1105	44	gl, ol, pl. pig, cpx †
	Y237I	1200 → 1100	48	gl, ol, pl, pig, cpx
	Y209	1080	52	gl, pl †
	Y235I	1200 → 1080	48	gl, ol, pl, cpx
D	BU1_01 *	1143	24	gl, ol, pl, cpx
	BU1_03 *	1105	44	gl, ol, pl, cpx †
	Y237II	1200 → 1100	48	gl, ol, pl, cpx
	Y235II	1200 → 1080	48	gl, pl, opx
E	Y075	1140	48	gl, pl, cpx
	Y079	1120	62	gl, pl, pig †
	Y237II	1200 → 1100	48	gl, pl, opx
	Y209	1080	52	gl, pl, pig †
	Y235II	1200 → 1080	48	gl, ol, pl, cpx
Fox	Y258	1200 → 1140	52	gl
	Y253	1120	49	gl, pl, pig, cpx †
	Y257	1200 → 1120	48	gl, pl, pig, cpx
	Y252	1100	49	gl, pl, cpx †
	Y251	1200 → 1100	48	gl, pl, pig, cpx
	Y255	1080	48	gl, pl, cpx †
Fgl	Y253	1120	48	gl, pl, pig, cpx
	Y252	1100	49	gl, pl, pig, cpx
	Y255	1080	48	gl, pl, pig, cpx

* Experiments from Hövelmann (2014)
† Pure Al_2O_3 observed in experiments
1200 → Experimental approach with initial heating of 1200°C

4.2.4 Electron Microprobe

The experimental melts and minerals were analyzed by a Cameca SX-100 electron microprobe, equipped with five spectrometers. Two analytical beam conditions were used to account for beam sensitivity of glass. The setting for minerals was operating with an acceleration voltage of 15 kV, a beam current of 15 nA and a focused beam. Glasses were analyzed with an acceleration voltage of 15 kV, a beam current of 10 nA and a beam diameter of 10 μm. Analyzed major elements were Si (crystal TAP), Ti (LPET), Al (TAP), Fe (LLIF), Mn (LLIF), Mg (TAP), Ca (PET), Na (TAP), K (LPET) and P (PET). Counting time for all elements was 10 s. Calibration standards were wollastonite (Si, Ca), TiO_2 (Ti), kyanite (Al), Fe_2O_3 (Fe), Mn_3O_4 (Mn), MgO (Mg), jadeite (Na), orthoclase (K) and apatite (P). Raw data were corrected using the PAP matrix correction (Pouchou & Pichoir, 1991) and secondary standard for glass measurements (VG2).

4.3 Results

This study includes eight experiments performed in the frame of a MSc thesis (Hövelmann, 2014) using the same starting compositions A, B, C and D as in this study. Experiments from Hövelmann (2014) are marked in Table 4.5.

4.3.1 Appearance of experimental run products

Back scattered electron images of representative experimental run products are presented in Figure 4.2, illustrating differences and similarities between starting materials (oxide or glass powder) and temperature paths (with or without initial heating to 1200°C). In general, plagioclase occurs as euhedral lath shaped crystals and is the dominant mineral phase in all experimental run products. Intergrowth of plagioclase crystals appears frequently throughout all experiments. Olivine is subhedral to euhedral in shape and can be intergrown by plagioclase. Pyroxenes appear anhedral to euhedral, depending on the starting material. In experiments using glass powder, pyroxenes are anhedral to subhedral in shape, whereas they appear euhedral in experiments using oxide powders. Experimentally produced crystals do not show zonation or reaction rims.

In addition to the general temperature dependence of the crystal size, with larger crystals at lower temperatures, there is also an effect of both temperature path and starting material on the crystal size. Experiments using glass powder as starting material show the smallest crystals, which can have only a few μm in size. The use of oxide powders as starting material leads to slightly larger crystals in those experiments without initial heating above the liquidus but are still tiny compared to those observed in experiments with a two-step
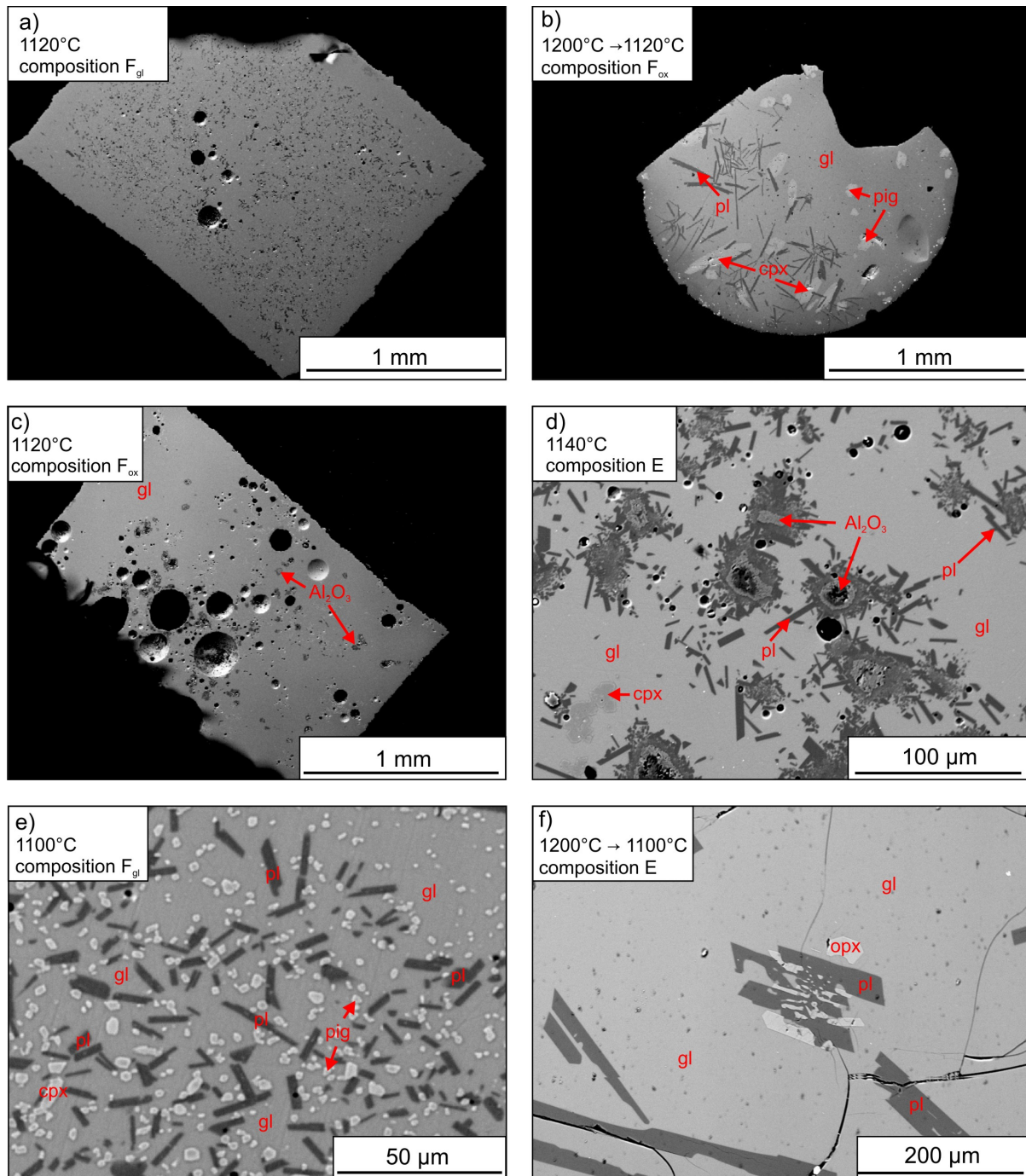
Figure 4.2 BSE images of representative experimental run products. a - c show experimental run products of composition F at the same temperature but from the three different experimental approaches. Phases in **a)** are glass as matrix, plaguioclase as dark grey crystals and clinopyroxene and pigeonite as light grey crystals. **b)** shows the same phases as A but crystals are much larger in size, resulting from the two-step heating procedure. **c)** shows glass and Al_2O_3 relics. Plagioclase crystals are located around Al_2O_3 relics. **d)** shows the experimental run product for composition **e)** wihtout overheating with the typical Al_2O_3 relics surrounded by plagioclase crystals. E shows the experimental run products using glass powder as starting material with the typical tiny crystal size especially for pyroxenes. **f)** shows the intergrowth of orthopyroxene and plagioclase, typical for experiments with two-step heating. Abbreviations are gl: glass; pl: plagioclase; opx: orthopyroxene; pig: pigeonite; cpx: clinopyroxene: Al_2O_3: relictic Al_2O_3.

temperature path, first reaching 1200°C. In these experiments crystals can reach a size of up to 0.5 mm but crystals have more irregularly shapes with embayments and intergrowth structures (Figure 4.2f). In general, plagioclase crystals are larger than olivine and pyroxenes, which are equal in size within each experiment. Experiments, using glass powder as starting material show a crystal free rim in contact with the graphite, but without compositional differences of the glass (Figure 4.2a). Except for these experiments, crystals are always evenly distributed.

In some experiments with oxide powders as starting material, and conducted without initial heating to 1200°C, pockets of Al_2O_3 are observed which are always surrounded by plagioclase crystals. These experiments are marked in Table 4.5.

4.3.2 Crystallization sequence

The crystallization sequences for each starting composition are presented in Figure 4.3. Plagioclase is present in all experimental run products below the liquidus (experiments at 1140°C). Olivine crystallizes together with plagioclase at 1140°C in experiments using the starting composition A, B, C and D. For composition E olivine is the last phase to crystallize after plagioclase and pyroxenes at 1080°C. Olivine is absent in the experimental products from composition F. Low-Ca pyroxenes are observed in all six starting compositions, but at different temperatures. In experiments with the starting compositions B, E and F, low-Ca pyroxenes crystallize at 1120°C and are stable at the lower experimental temperatures. Low-Ca pyroxenes appear only at 1100°C in composition A and C and only at 1080°C in composition D. In experiments with compositions C, E and F low-Ca pyroxenes can coexist with clinopyroxene, which appears sometimes at higher temperature (C and E) or at the same temperature (F). In experiments using composition D low-Ca pyroxene crystallizes at the expense of clinopyroxene at 1120°C. Experiments, where pockets of Al_2O_3 solid phases are present show a slightly different crystallization sequence marked by a higher crystallization temperatures for low-Ca pyroxene in composition B, for olivine and clinopyroxene in composition C and for low-Ca pyroxene and clinopyroxene in composition E. Those stability fields are indicated by grey dashed lines in Figure 4.3.

The liquidus temperature of composition A, B, C and D were determined in Hövelmann (2014) and are between 1140°C and 1160°C for A and B and between 1180 and 1200°C for C and D. The liquidus temperatures for compositions E and F are between 1140°C and 1160°C and between 1120°C and 1140°C respectively.
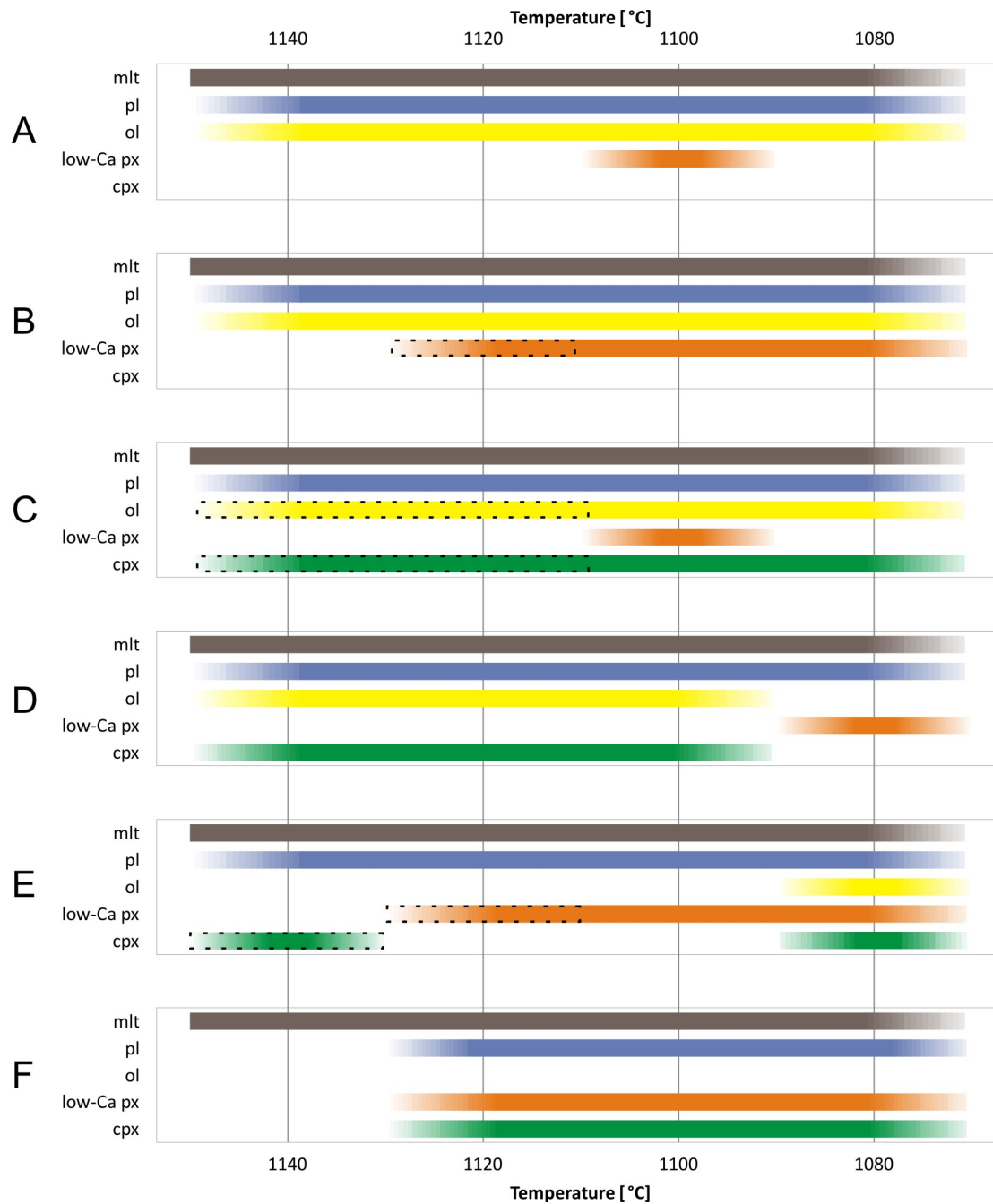
Figure 4.3 Phases present in the experimental run products. The color fading indicates extrapolation of upper and lower temperature limit of the phase stability between two, above or below the experimental run temperatures. Phase stabilities in dashed boxes are only confirmed by experiments with Al$_2$O$_3$ relics (cp. chapter 4.4.1 " Attainment of equilibrium and influence of experimental procedure"). mlt: melt; pl: plagioclase; ol: olivine; low-Ca px: low-Ca pyroxene; cpx, clinopyroxene.

4.3.3   Composition of experimental run products

4.3.3.1   Liquid composition

Major element compositions of the experimental liquids are presented in Table 4.6 and Figure 4.4. Figure 4.4 shows all experimental results, irrespective of the experimental approach that was applied. The liquid evolution is marked by a systematic decrease in MgO and Mg# with decreasing experimental temperature. In general, the different starting compositions produce similar, typical tholeeitic fractionation trends with decreasing Al_2O_3 and CaO and increasing SiO_2, TiO_2 and K_2O with decreasing MgO. FeO, MnO and Na_2O show a different behavior depending on the starting composition. For compositions A and B a slight increase in FeO with decreasing MgO can be observed. Compositions C and F produce a trend where FeO is first decreasing before increasing with decreasing MgO. In contrast to C and F, FeO in D and E experiments first increase before decreasing with decreasing MgO. Na_2O is decreasing with decreasing MgO experiments with starting composition A. In compositions C, and D Na_2O increases with decreasing MgO. E and F experiments show first a decrease in Na_2O followed by an increase at the lowest temperatures.
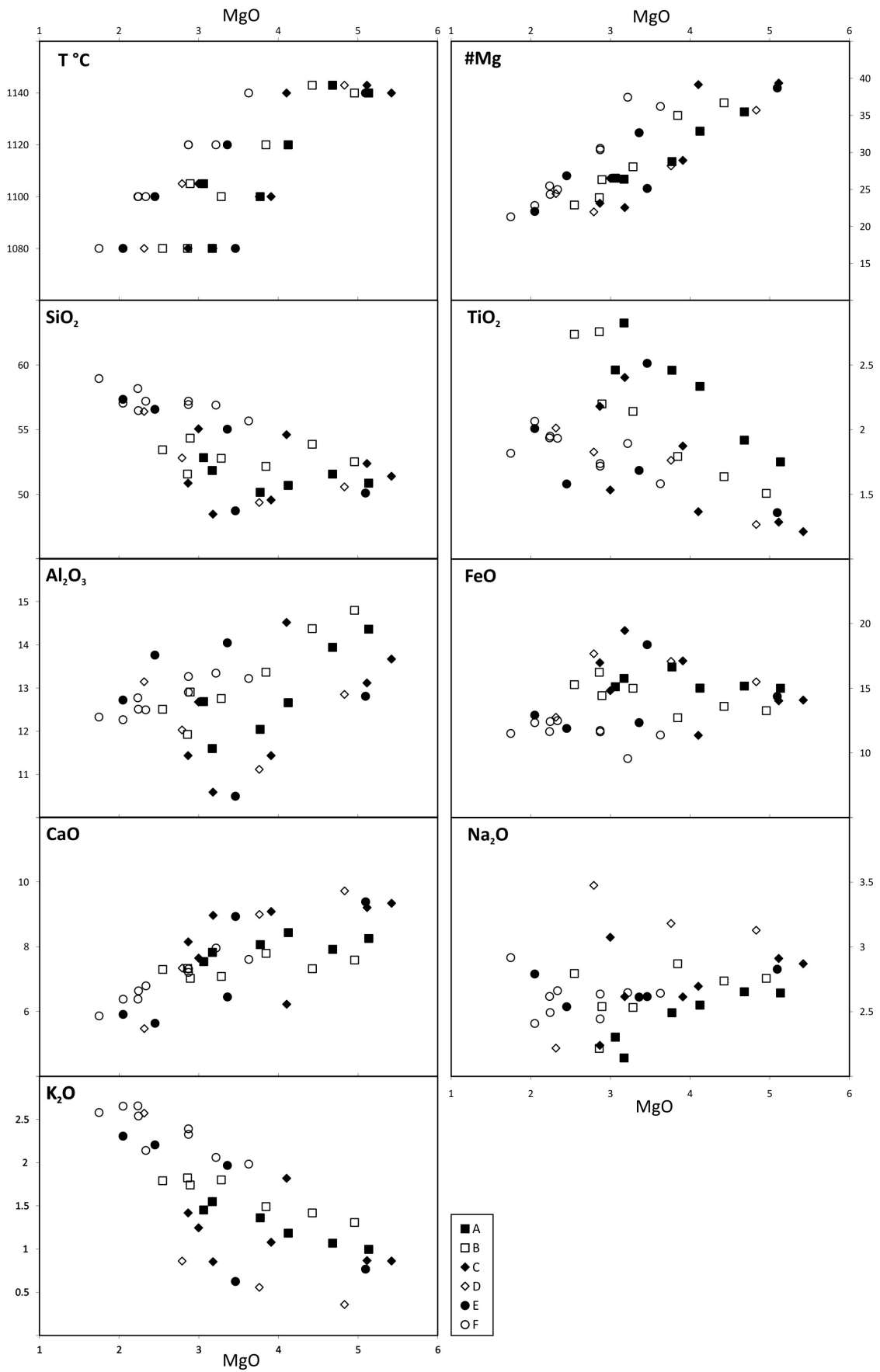
Figure 4.4 Compositional variation diagrams with synthetic starting and experimental liquid compositions. Oxides are given in wt%. Different starting compositions are indicated by different symbols.

4.3.3.2 Mineral compositions

Mineral compositions of the experimental run products are presented in Table 4.6 and Figure 4.5. Mineral phases are homogeneous within single experiments but can vary significantly between different starting compositions or between the different experimental procedures for a certain experimental temperature. The An content in plagioclase is constantly decreasing with decreasing temperature in all experiments, ranging between 55 and 67 mol% with few outliers down to 45 mol% An (cp. Figure 4.5A). Olivine composition is changing systematically with temperature showing the highest Fo contents, ~Fo65 (Fo being the molar [Mg/(Mg + Fe)] *100), in experiments at the highest temperature and decreasing down to ~Fo46 at the 1080°C experiments (cp. Figure 4.5B). Similar to olivine, both pyroxenes also show a decrease in Mg# with decreasing temperature. Low-Ca pyroxenes have slightly higher Mg# and larger variation between experiments at a certain temperature compared to clinopyroxenes (cp. Figure 4.5C-D).
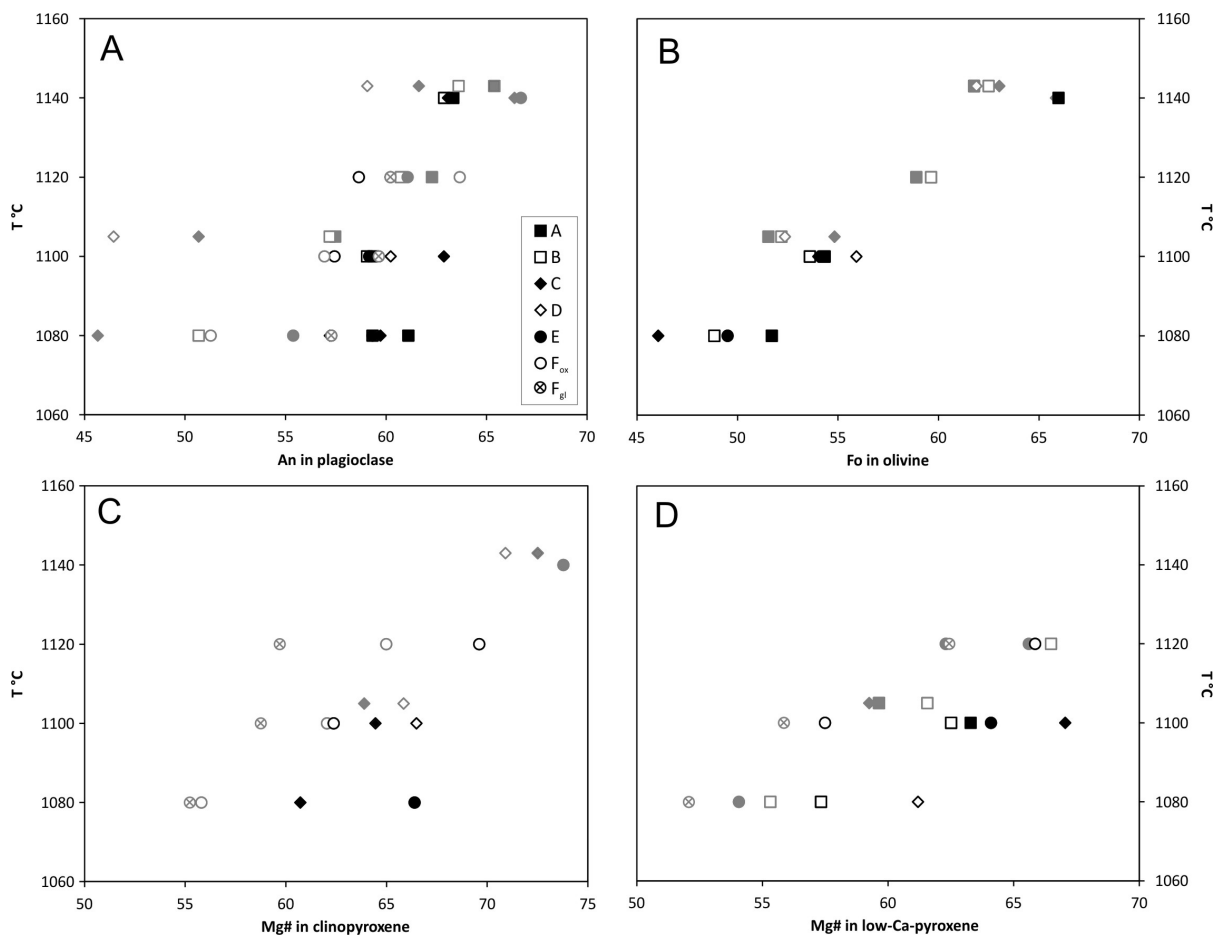
Figure 4.5 Mineral compositions plotted versus temperature for **A:** Anorthite content in plagioclase. **B:** Forsterite content in olivine **C:** Mg# of clinopyroxene, **D:** Mg# of low-Ca pyroxenes. Colors indicate the experimental approach with black for experiments with initial heating to 1200°C and grey for experiments without intitial heating. Data points are average compositions (cp. Table 4.6).

Table 4.6 Compositions of the experimental run products obtained via EMPA for all compositions. Given is the average composition with the 1σ standard deviation in italic numbers. Number of analyses is given in brackets.

composition A

Run	T°C	Phase	SiO$_2$	TiO$_2$	Al$_2$O$_3$	FeO	MnO	MgO	CaO	Na$_2$O	K$_2$O	P$_2$O$_5$	Total	An/Fo/Mg#
BU1_01 †	1143	gl (14)	51.56 *0.63*	1.92 *0.07*	13.94 *0.13*	15.17 *0.39*	0.26 *0.05*	4.68 *0.08*	7.92 *0.09*	2.65 *0.11*	1.07 *0.05*	0.43 *0.09*	99.61	35.48
		ol (7)	36.67 *0.30*	0.07 *0.02*	0.05 *0.05*	33.47 *0.41*	0.42 *0.06*	30.34 *0.31*	0.36 *0.06*	0.00 *0.03*	0.01 *0.01*	-	101.39	61.77
		pl (6)	51.49 *0.29*	0.08 *0.03*	29.94 *0.39*	0.82 *0.15*	0.01 *0.01*	0.16 *0.06*	13.39 *0.24*	3.78 *0.09*	0.21 *0.01*	-	99.88	65.39
Y244	1200 → 1140	gl(5)	50.87 *0.15*	1.75 *0.03*	14.36 *0.16*	15.00 *0.23*	0.23 *0.05*	5.13 *0.09*	8.25 *0.10*	2.64 *0.07*	1.00 *0.04*	0.44 *0.04*	99.68	37.88
		pl(5)	53.21 *0.66*	0.07 *0.02*	29.59 *0.18*	0.55 *0.06*	0.00 *0.00*	0.18 *0.04*	13.37 *0.10*	4.11 *0.17*	0.25 *0.02*	-	101.32	63.35
		ol(2)	36.57 *0.21*	b.d.	b.d	29.85 *0.45*	0.35 *0.02*	32.47 *0.24*	0.24 *0.01*	b.d.	0.00 *0.00*	-	99.50	65.97
Y079 †	1120	gl (2)	50.69 *0.13*	2.34 *0.04*	12.66 *0.10*	15.02 *0.36*	0.28 *0.04*	4.12 *0.02*	8.43 *0.06*	2.55 *0.05*	1.18 *0.03*	0.61 *0.00*	97.89	32.86
		ol (2)	35.21 *0.02*	0.06 *0.01*	b.d.	34.66 *0.46*	0.41 *0.06*	27.86 *0.14*	0.48 *0.08*	b.d.	b.d.	-	98.68	58.90
		pl (2)	52.12 *0.15*	0.09 *0.02*	28.93 *0.30*	0.88 *0.16*	b.d.	0.16 *0.02*	13.07 *0.08*	4.17 *0.09*	0.31 *0.00*	-	99.73	62.28
BU1_03 †	1105	gl (6)	52.84 *0.24*	2.46 *0.06*	12.69 *0.12*	15.12 *0.65*	0.22 *0.04*	3.06 *0.17*	7.54 *0.05*	2.30 *0.08*	1.45 *0.05*	0.50 *0.07*	98.18	26.51
		ol (5)	35.28 *0.23*	0.09 *0.01*	0.05 *0.04*	40.41 *0.74*	0.47 *0.09*	24.11 *0.25*	0.49 *0.02*	0.04 *0.05*	0.02 *0.01*	-	100.96	51.54
		pig (5)	52.50 *0.07*	0.44 *0.13*	0.96 *0.61*	22.58 *0.64*	0.43 *0.07*	18.73 *0.86*	4.57 *0.72*	0.11 *0.08*	0.05 *0.09*	-	100.37	59.64
		pl (6)	54.75 *0.21*	0.10 *0.01*	28.32 *0.25*	1.01 *0.13*	0.02 *0.03*	0.14 *0.04*	11.65 *0.06*	4.52 *0.13*	0.37 *0.03*	-	100.89	57.47
Y237I	1200 → 1100	gl (5)	50.16 *0.51*	2.46 *0.10*	12.04 *0.15*	16.65 *0.52*	0.25 *0.03*	3.77 *0.08*	8.06 *0.22*	2.49 *0.07*	1.36 *0.05*	0.58 *0.02*	97.83	28.76
		ol (5)	35.54 *0.25*	0.06 *0.01*	b.d.	37.94 *0.23*	0.47 *0.03*	25.33 *0.28*	0.34 *0.06*	b.d.	b.d.	-	99.69	54.33
		pl (8)	53.87 *0.81*	0.08 *0.01*	28.45 *0.39*	0.68 *0.12*	b.d.	0.16 *0.03*	12.25 *0.54*	4.42 *0.23*	0.33 *0.06*	-	100.25	59.35
		pig (3)	52.45 *0.22*	0.48 *0.11*	1.47 *0.43*	21.34 *0.81*	0.39 *0.06*	20.64 *0.03*	3.08 *0.61*	b.d.	b.d.	-	99.86	63.29
Y235I	1200 → 1080	gl (5)	51.85 *0.72*	2.82 *0.15*	11.60 *0.07*	15.77 *0.50*	0.27 *0.02*	3.17 *0.06*	7.82 *0.21*	2.14 *0.13*	1.55 *0.07*	0.66 *0.07*	97.66	26.38
		ol (3)	35.15 *0.17*	0.10 *0.02*	0.15 *0.00*	39.43 *0.17*	0.50 *0.01*	23.68 *0.13*	0.45 *0.11*	b.d.	b.d.	-	99.47	51.70
		pl (10)	53.58 *0.59*	0.10 *0.01*	28.44 *0.31*	0.93 *0.13*	b.d.	0.21 *0.02*	12.38 *0.32*	4.12 *0.19*	0.35 *0.02*	-	100.11	61.11

Table 4.6 continued

composition B

Run	T°C	Phase	SiO$_2$	TiO$_2$	Al$_2$O$_3$	FeO	MnO	MgO	CaO	Na$_2$O	K$_2$O	P$_2$O$_5$	Total	An/Fo/Mg#
BU1_01 †	1143	gl (15)	53.87 *0.47*	1.64 *0.08*	14.38 *0.13*	13.61 *0.27*	0.27 *0.08*	4.43 *0.10*	7.32 *0.14*	2.74 *0.11*	1.42 *0.04*	0.35 *0.09*	100.02	36.70
		ol (6)	36.68 *0.21*	0.05 *0.02*	0.04 *0.01*	32.92 *0.10*	0.56 *0.08*	30.78 *0.38*	0.31 *0.04*	0.01 *0.01*	0.01 *0.01*	-	101.36	62.49
		pl (6)	52.48 *0.46*	0.08 *0.01*	30.02 *0.21*	0.73 *0.08*	0.01 *0.02*	0.14 *0.04*	13.03 *0.23*	3.95 *0.15*	0.26 *0.02*	-	100.70	63.61
Y244	1200 → 1140	gl(5)	52.52 *0.16*	1.51 *0.06*	14.80 *0.07*	13.27 *0.19*	0.29 *0.04*	4.96 *0.12*	7.59 *0.15*	2.76 *0.07*	1.31 *0.04*	0.38 *0.02*	99.38	39.96
		pl(5)	53.09 *0.55*	0.06 *0.01*	29.44 *0.27*	0.55 *0.07*	0.03 *0.04*	0.13 *0.02*	13.11 *0.32*	4.08 *0.21*	0.30 *0.02*	-	100.74	62.89
Y079 †	1120	gl (1)	52.16	1.79	13.37	12.73	0.44	3.84	7.79	2.87	1.49	0.54	97.03	34.99
		ol (2)	35.18 *1.17*	0.23 *0.10*	0.39 *0.37*	32.75 *1.19*	0.63 *0.03*	27.14 *1.09*	0.78 *0.05*	b.d.	b.d.	-	97.10	59.63
		pig (2)	51.91 *0.02*	0.40 *0.01*	1.28 *0.14*	18.54 *0.81*	0.54 *0.05*	20.63 *0.14*	5.12 *1.02*	b.d.	b.d.	-	98.42	66.48
		pl (2)	53.18 *0.86*	0.07 *0.02*	29.02 *0.03*	0.87 *0.28*	b.d.	0.19 *0.05*	12.35 *0.01*	4.17 *0.35*	0.37	-	100.20	60.74
BU1_03 †	1105	gl (6)	54.35 *0.36*	2.20 *0.05*	12.91 *0.18*	14.44 *0.99*	0.28 *0.03*	2.89 *0.26*	7.02 *0.08*	2.54 *0.10*	1.74 *0.04*	0.43 *0.11*	98.79	26.32
		ol (5)	35.57 *0.20*	0.09 *0.01*	0.08 *0.03*	40.07 *0.51*	0.59 *0.05*	24.53 *0.20*	0.49 *0.06*	0.02 *0.01*	0.02 *0.02*	-	101.46	52.18
		pig (5)	52.93 *0.39*	0.36 *0.07*	0.85 *0.21*	22.20 *0.94*	0.61 *0.04*	19.95 *0.42*	4.16 *0.40*	0.07 *0.02*	0.02 *0.01*	-	101.14	61.56
		pl (5)	54.89 *0.40*	0.10 *0.04*	28.54 *0.45*	0.87 *0.08*	0.00 *0.01*	0.15 *0.04*	11.64 *0.37*	4.55 *0.09*	0.40 *0.02*	-	100.75	57.20
Y237I	1200 → 1100	gl (5)	52.79 *0.58*	2.14 *0.13*	12.76 *0.07*	15.01 *0.41*	0.30 *0.04*	3.28 *0.19*	7.08 *0.32*	2.53 *0.11*	1.80 *0.11*	0.45 *0.04*	98.15	28.05
		ol (3)	35.13 *0.27*	0.07 *0.01*	b.d. *0.00*	38.07 *0.33*	0.58 *0.05*	24.67 *0.38*	0.34 *0.05*	b.d. *0.00*	b.d. *0.00*	-	98.87	53.60
		pl (8)	53.64 *0.65*	0.08 *0.02*	28.29 *0.31*	0.65 *0.10*	b.d. *0.00*	0.17 *0.00*	12.12 *0.39*	4.40 *0.17*	0.38 *0.04*	-	99.73	59.05
		pig (3)	52.30 *0.30*	0.40 *0.07*	1.00 *0.26*	21.99 *0.32*	0.57 *0.03*	20.57 *0.11*	2.77 *0.08*	b.d. *0.00*	0.40 *0.02*	-	99.60	62.51
Y209 †	1080	gl(4)	53.44 *0.75*	2.74 *0.13*	12.51 *0.73*	15.29 *0.47*	0.24 *0.03*	2.55 *0.17*	7.30 *0.25*	2.79 *0.11*	1.79 *0.12*	0.78 *0.23*	99.43	22.89
		pig (2)	51.08 *0.44*	0.62 *0.03*	0.96 *0.04*	23.07 *0.19*	0.62 *0.01*	16.02 *0.76*	7.60 *0.80*	0.17 *0.10*	0.06 *0.01*	-	100.19	55.31
		pl (3)	55.15 *0.28*	0.23 *0.18*	26.65 *0.94*	1.47 *0.85*	b.d. *0.00*	0.20 *0.10*	10.20 *0.20*	5.08 *0.30*	0.62 *0.08*	-	99.59	50.68
Y235I	1200 → 1080	gl (5)	51.57 *0.92*	2.76 *0.12*	11.93 *0.16*	16.24 *0.38*	0.31 *0.03*	2.86 *0.11*	7.33 *0.21*	2.22 *0.12*	1.82 *0.10*	0.58 *0.12*	97.62	23.88
		ol (4)	34.17 *0.22*	0.07 *0.01*	b.d.	41.01 *1.12*	0.65 *0.02*	21.97 *0.38*	0.35 *0.04*	b.d.	b.d.	-	98.22	48.84
		pig (4)	51.51 *0.33*	0.51 *0.09*	1.20 *0.23*	23.97 *0.65*	0.60 *0.04*	18.07 *0.59*	3.35 *0.47*	0.08 *0.01*	b.d.	-	99.29	57.33
		pl (8)	53.67 *1.12*	0.09 *0.02*	28.22 *0.50*	0.79 *0.17*	b.d.	0.14 *0.02*	11.97 *0.36*	4.25 *0.16*	0.44 *0.07*	-	99.55	59.33

Table 4.6 continued

composition C

Run	T°C	Phase	SiO$_2$	TiO$_2$	Al$_2$O$_3$	FeO	MnO	MgO	CaO	Na$_2$O	K$_2$O	P$_2$O$_5$	Total	An/Fo/Mg#
BU1_01 [†]	**1143**	gl (12)	52.38 *0.42*	1.29 *0.05*	13.12 *0.41*	14.04 *0.37*	0.20 *0.07*	5.11 *0.46*	9.21 *0.24*	2.91 *0.16*	0.87 *0.05*	0.50 *0.10*	99.62	39.37
		ol (5)	37.81 *0.65*	0.14 *0.06*	0.87 *0.56*	30.76 *0.93*	0.36 *0.04*	29.42 *1.40*	1.11 *0.45*	0.20 *0.13*	0.07 *0.04*	-	100.74	63.03
		aug (7)	52.07 *0.21*	0.47 *0.04*	2.44 *0.18*	10.58 *0.29*	0.27 *0.03*	15.66 *0.35*	18.53 *0.61*	0.20 *0.02*	0.01 *0.01*	-	100.24	72.51
		pl (6)	53.48 *0.25*	0.06 *0.02*	29.59 *0.25*	0.81 *0.07*	0.02 *0.03*	0.20 *0.01*	12.69 *0.14*	4.24 *0.12*	0.18 *0.02*	-	101.28	61.63
Y075 [†]	**1140**	gl (3)	54.61 *0.42*	1.37 *0.07*	14.52 *0.19*	11.36 *0.70*	0.18 *0.01*	4.10 *0.17*	6.22 *0.18*	2.70 *0.11*	1.82 *0.10*	0.96 *0.26*	97.84	39.15
		ol (2)	36.51 *0.11*	0.06 *0.01*	b.d.	30.09 *0.47*	0.26 *0.03*	32.55 *0.11*	0.24 *0.02*	b.d.	b.d.	-	99.72	65.85
		pl (3)	50.97 *0.99*	0.13 *0.05*	29.20 *0.26*	1.17 *0.38*	b.d.	0.38 *0.19*	13.26 *0.43*	3.47 *0.36*	0.37 *0.03*	-	98.93	66.39
Y244	**1200 → 1140**	gl (5)	51.40 *0.22*	1.21 *0.02*	13.67 *0.10*	14.09 *0.14*	0.21 *0.03*	5.42 *0.10*	9.34 *0.08*	2.87 *0.06*	0.86 *0.03*	0.47 *0.07*	99.55	40.67
		pl (5)	52.88 *0.43*	0.06 *0.01*	29.28 *0.29*	0.63 *0.03*	0.00 *0.00*	0.18 *0.03*	13.41 *0.39*	4.20 *0.21*	0.20 *0.02*	-	100.81	63.08
BU1_03 [†]	**1105**	gl (7)	55.07 *0.46*	1.53 *0.05*	12.68 *0.16*	14.82 *0.47*	0.18 *0.07*	3.00 *0.18*	7.65 *0.21*	3.07 *0.10*	1.25 *0.02*	0.57 *0.05*	99.81	26.50
		ol (4)	35.89 *0.22*	0.06 *0.01*	0.13 *0.07*	37.76 *0.69*	0.45 *0.05*	25.71 *0.29*	0.63 *0.07*	0.04 *0.05*	0.01 *0.01*	-	100.69	54.83
		pig (6)	53.22 *0.25*	0.34 *0.06*	1.05 *0.40*	22.31 *0.64*	0.44 *0.05*	18.20 *0.62*	5.42 *0.53*	0.12 *0.06*	0.05 *0.04*	-	101.16	59.25
		aug (4)	52.65 *0.41*	0.56 *0.10*	1.87 *0.56*	13.66 *0.98*	0.27 *0.02*	13.56 *0.14*	17.84 *1.09*	0.29 *0.07*	0.07 *0.04*	-	100.76	63.89
		pl (6)	56.83 *0.43*	0.07 *0.01*	27.46 *0.19*	0.76 *0.06*	0.01 *0.02*	0.13 *0.02*	10.47 *0.19*	5.42 *0.08*	0.32 *0.01*	-	101.46	50.68
Y237l	**1200 → 1100**	gl (4)	49.57 *0.68*	1.87 *0.14*	11.44 *0.13*	17.12 *0.80*	0.23 *0.01*	3.91 *0.19*	9.08 *0.27*	2.61 *0.13*	1.08 *0.08*	0.71 *0.05*	97.62	28.92
		ol (4)	35.12 *0.27*	b.d.	b.d.	38.12 *0.22*	0.47 *0.05*	25.12 *0.10*	0.49 *0.01*	b.d.	b.d.	-	99.32	54.02
		pig (2)	50.34 *0.28*	0.61 *0.11*	2.33 *0.62*	16.65 *1.46*	0.35 *0.03*	19.02 *0.32*	8.37 *1.65*	b.d.	b.d.	-	97.67	67.05
		aug (2)	50.96 *0.08*	0.61 *0.06*	1.79 *0.43*	13.99 *2.94*	0.29 *0.10*	14.23 *1.24*	16.75 *4.22*	0.15 *0.01*	b.d.	-	98.77	64.45
		pl (10)	52.51 *0.54*	0.07 *0.01*	28.79 *0.42*	0.75 *0.06*	b.d.	0.23 *0.04*	13.01 *0.40*	4.10 *0.20*	0.22 *0.02*	-	99.67	62.88
Y209 [†]	**1080**	gl (3)	48.47 *0.18*	2.40 *0.02*	10.59 *0.37*	19.47 *0.19*	0.28 *0.05*	3.18 *0.10*	8.97 *0.10*	2.62 *0.09*	0.85 *0.02*	2.01 *0.15*	98.83	22.55
		pl (1)	57.20	0.08	27.12	0.87	b.d.	0.10	9.12	5.70	0.46	-	100.66	45.66
Y235l	**1200 → 1080**	gl (5)	50.86 *0.82*	2.18 *0.09*	11.44 *0.26*	16.98 *0.65*	0.25 *0.04*	2.87 *0.15*	8.15 *0.21*	2.24 *0.30*	1.42 *0.10*	0.80 *0.11*	97.19	23.13
		ol (4)	34.01 *0.12*	b.d.	b.d.	43.17 *0.21*	0.53 *0.05*	20.68 *0.18*	0.50 *0.06*	b.d.	b.d.	-	98.89	46.05
		aug (8)	50.90 *0.38*	0.74 *0.14*	2.44 *1.05*	16.81 *1.21*	0.36 *0.02*	14.58 *1.05*	13.40 *2.05*	0.15 *0.07*	b.d.	-	99.37	60.72
		pl (5)	53.78 *0.56*	0.08 *0.02*	27.92 *0.26*	0.94 *0.18*	b.d.	0.21 *0.04*	12.13 *0.28*	4.31 *0.19*	0.33 *0.03*	-	99.69	59.72

Table 4.6 continued

composition D

Run	T°C	Phase	SiO₂	TiO₂	Al₂O₃	FeO	MnO	MgO	CaO	Na₂O	K₂O	P₂O₅	Total	An/Fo/Mg#
BU1_01	**1143**	gl (12)	50.58 *0.16*	1.27 *0.05*	12.85 *0.12*	15.50 *0.23*	0.33 *0.08*	4.83 *0.10*	9.72 *0.18*	3.13 *0.08*	0.36 *0.02*	0.68 *0.12*	99.25	35.70
		ol (6)	37.01 *0.21*	0.05 *0.03*	0.22 *0.28*	32.96 *0.17*	0.53 *0.03*	30.03 *0.46*	0.78 *0.27*	0.06 *0.09*	0.01 *0.01*	-	101.66	61.89
		aug (5)	52.49 *0.55*	0.42 *0.11*	2.66 *1.06*	10.91 *0.50*	0.29 *0.01*	14.92 *1.11*	18.57 *1.23*	0.41 *0.22*	0.03 *0.03*	-	100.70	70.91
		pl (6)	54.02 *0.47*	0.05 *0.02*	29.26 *0.36*	0.85 *0.08*	0.02 *0.03*	0.18 *0.06*	12.22 *0.31*	4.62 *0.26*	0.10 *0.01*	-	101.30	59.07
BU1_03 †	**1105**	gl (7)	52.82 *0.60*	1.83 *0.07*	12.03 *0.31*	17.67 *0.83*	0.30 *0.04*	2.79 *0.17*	7.34 *0.33*	3.47 *0.20*	0.86 *0.08*	0.60 *0.10*	99.72	21.96
		ol (5)	35.65 *0.45*	0.11 *0.07*	0.64 *0.25*	38.51 *0.47*	0.56 *0.05*	23.75 *0.40*	0.85 *0.05*	0.15 *0.07*	0.03 *0.03*	-	100.25	52.36
		aug (7)	52.69 *0.51*	0.54 *0.07*	1.50 *0.43*	12.78 *0.62*	0.33 *0.06*	13.83 *0.73*	18.33 *0.84*	0.28 *0.08*	0.03 *0.02*	-	100.31	65.85
		pl (5)	57.75 *0.29*	0.07 *0.01*	26.91 *0.23*	0.77 *0.12*	0.03 *0.04*	0.12 *0.05*	9.64 *0.20*	6.01 *0.11*	0.20 *0.02*	-	101.50	46.45
Y237II	**1200 → 1100**	gl (5)	49.37 *0.33*	1.76 *0.08*	11.12 *0.10*	17.09 *0.26*	0.32 *0.07*	3.76 *0.37*	9.00 *0.13*	3.18 *0.10*	0.56 *0.03*	0.85 *0.05*	97.00	28.18
		ol (3)	35.22 *0.05*	b.d.	b.d.	36.81 *0.31*	0.54 *0.06*	26.20 *0.34*	0.48 *0.05*	b.d.	b.d.	-	99.24	55.91
		aug (4)	51.85 *0.26*	0.56 *0.07*	1.99 *0.89*	13.62 *0.87*	0.36 *0.04*	15.16 *0.58*	15.89 *0.89*	0.21 *0.07*	b.d.	-	99.63	66.49
		pl (8)	53.15 *0.42*	b.d.	28.44 *0.36*	0.79 *0.12*	b.d.	0.24 *0.09*	12.53 *0.37*	4.51 *0.20*	0.10 *0.02*	-	99.76	60.23
Y235II	**1200 → 1080**	gl (5)	56.41 *0.75*	2.01 *0.16*	13.15 *0.19*	12.76 *0.40*	0.17 *0.01*	2.31 *0.14*	5.47 *0.11*	2.22 *0.21*	2.57 *0.14*	0.63 *0.09*	97.71	24.43
		opx (11)	51.69 *0.38*	0.51 *0.05*	2.09 *0.96*	22.47 *2.23*	0.42 *0.05*	19.88 *1.28*	2.47 *0.22*	b.d.	b.d.	-	99.52	61.19
		pl (5)	54.75 *0.67*	0.10 *0.02*	27.67 *0.42*	0.73 *0.05*	b.d.	0.15 *0.02*	11.55 *0.43*	4.45 *0.15*	0.49 *0.06*	-	99.90	57.20

Table 4.6 continued

composition E

Run	T°C	Phase	SiO$_2$	TiO$_2$	Al$_2$O$_3$	FeO	MnO	MgO	CaO	Na$_2$O	K$_2$O	P$_2$O$_5$	Total	An/Fo/Mg#
Y075	**1140**	gl (4)	50.10 *0.63*	1.36 *0.11*	12.81 *0.11*	14.38 *0.73*	0.24 *0.04*	5.09 *0.19*	9.38 *0.18*	2.83 *0.09*	0.77 *0.06*	0.85 *0.53*	97.82	38.71
		aug (2)	51.69 *0.19*	0.44 *0.00*	2.14 *0.03*	10.22 *0.45*	0.19 *0.02*	16.13 *0.04*	18.57 *0.17*	0.24 *0.08*	b.d. *0.00*	b.d.	99.62	73.78
		pl (11)	50.60 *2.14*	0.11 *0.06*	29.23 *1.58*	1.36 *0.70*	b.d.	0.48 *0.29*	13.46 *1.05*	3.58 *0.74*	0.20 *0.05*	-	99.02	66.71
Y079 †	**1120**	gl (2)	55.04 *0.00*	1.69 *0.05*	14.05 *0.08*	12.35 *0.31*	b.d.	3.36 *0.01*	6.45 *0.06*	2.61 *0.13*	1.97 *0.11*	b.d.	97.51	32.66
		pig (2)	52.11 *0.06*	0.31 *0.02*	1.22 *0.07*	20.63 *0.33*	0.31 *0.01*	22.08 *0.24*	2.77 *0.22*	b.d.	0.03 *0.00*	-	99.47	65.60
		pl (3)	53.33 *0.30*	0.08 *0.00*	28.83 *0.27*	0.78 *0.10*	b.d.	0.13 *0.04*	12.58 *0.16*	4.15 *0.14*	0.42 *0.02*	-	100.32	61.07
Y237II	**1200 → 1100**	gl (5)	56.58 *0.79*	1.58 *0.11*	13.76 *0.33*	11.90 *0.52*	0.18 *0.04*	2.45 *0.32*	5.63 *0.08*	2.54 *0.09*	2.21 *0.09*	0.45 *0.03*	97.28	26.84
		opx (8)	52.13 *0.30*	0.46 *0.04*	1.81 *0.32*	21.18 *1.45*	0.38 *0.04*	21.21 *0.94*	2.03 *0.10*	b.d.	b.d.	-	99.20	64.10
		pl (5)	54.40 *0.27*	0.08 *0.01*	27.81 *0.28*	0.55 *0.07*	b.d.	0.15 *0.02*	11.88 *0.27*	4.25 *0.26*	0.43 *0.02*	-	99.53	59.16
Y209 †	**1080**	gl (5)	57.35 *1.08*	2.01 *0.09*	12.72 *0.12*	12.93 *0.89*	0.19 *0.04*	2.05 *0.21*	5.91 *0.39*	2.79 *0.10*	2.31 *0.14*	0.65 *0.17*	98.91	22.02
		pig (4)	51.61 *0.69*	0.60 *0.19*	1.80 *1.46*	24.09 *1.94*	0.46 *0.03*	15.91 *2.21*	4.51 *0.18*	0.25 *0.26*	0.15 *0.11*	-	99.37	54.06
		pl (4)	55.02 *0.28*	0.19 *0.12*	27.85 *0.74*	1.36 *0.63*	b.d.	0.19 *0.10*	11.11 *0.28*	4.58 *0.19*	0.56 *0.13*	-	100.85	55.38
Y235II	**1200 → 1080**	gl (4)	48.73 *0.24*	2.51 *0.08*	10.50 *0.10*	18.38 *0.35*	0.34 *0.03*	3.46 *0.05*	8.93 *0.27*	2.62 *0.45*	0.62 *0.03*	1.14 *0.06*	97.23	25.13
		ol (3)	34.23 *0.08*	b.d.	b.d.	40.96 *1.04*	0.68 *0.06*	22.53 *1.11*	0.52 *0.03*	b.d.	b.d.	-	98.91	49.51
		aug (5)	50.16 *0.53*	1.14 *0.22*	3.68 *0.94*	11.53 *1.04*	0.28 *0.05*	12.78 *0.38*	19.71 *0.77*	0.24 *0.04*	b.d.	-	99.53	66.39
		pl (8)	53.93 *0.68*	0.07 *0.02*	27.99 *0.60*	0.83 *0.17*	b.d.	0.24 *0.07*	12.10 *0.66*	4.50 *0.41*	0.14 *0.03*	-	99.78	59.33
		ox (1)	0.12	0.08	b.d.	82.91	b.d.	b.d.	0.15	b.d.	b.d.	-	83.26	

Table 4.6 continued

Run	T°C	Phase	SiO₂		TiO₂		Al₂O₃		FeO		MnO		MgO		CaO		Na₂O		K₂O		P₂O₅		Total	An/Fo/Mg#
											composition F_{ox}													
Y258	1200 → 1140	gl(6)	55.68	0.80	1.58	0.07	13.22	0.19	11.39	0.54	0.20	0.05	3.63	0.10	7.61	0.29	2.64	0.14	1.98	0.10	0.50	0.11	98.42	36.21
Y253 †	1120	pl(5)	52.99	1.30	0.14	0.09	28.84	0.56	1.05	0.38	b.d.		0.24	0.09	13.13	0.72	3.80	0.46	0.52	0.05	-		100.71	63.67
		gl(5)	56.94	0.94	1.74	0.07	12.90	0.16	11.74	0.57	0.19	0.01	2.87	0.17	7.31	0.35	2.44	0.06	2.39	0.13	0.50	0.10	99.00	30.35
		cpx(5)	51.77	0.55	0.77	0.14	2.08	0.69	13.80	0.66	0.41	0.08	14.37	0.55	17.32	0.87	0.17	0.03	0.08	0.04	-		100.77	64.98
		pig(3)	53.38	0.77	0.34	0.04	1.03	0.53	20.83	0.41	0.52	0.04	19.31	0.59	5.05	0.16	b.d.	0.00	b.d.	0.00	-		100.46	62.30
Y257	1200 → 1120	gl(6)	56.90	1.55	1.89	0.20	13.35	0.41	9.57	0.87	0.25	0.05	3.22	0.31	7.96	0.50	2.65	0.13	2.06	0.17	0.52	0.17	98.35	37.45
		pl(4)	54.38	0.54	0.12	0.09	27.97	0.43	0.63	0.21	b.d.		0.22	0.12	11.90	0.32	4.31	0.10	0.50	0.07	-		100.02	58.65
		pig(5)	52.27	0.50	0.59	0.06	1.42	0.17	18.67	0.45	0.47	0.04	20.20	0.39	5.93	0.65	0.07	0.00	b.d.	0.00	-		99.61	65.85
		cpx(5)	51.65	0.38	1.02	0.17	2.06	0.42	12.86	0.58	0.39	0.05	16.52	0.37	14.94	0.70	0.15	0.03	b.d.	0.00	-		99.61	69.60
Y252 †	1100	gl(5)	57.20	1.51	1.93	0.08	12.50	0.16	12.50	0.98	0.22	0.03	2.34	0.22	6.79	0.59	2.66	0.17	2.14	0.20	0.73	0.18	99.01	24.98
		cpx(8)	51.56	0.16	0.79	0.06	1.17	0.33	13.88	0.42	0.35	0.05	12.73	0.38	19.77	0.61	0.38	0.08	0.07	0.04	-		100.69	62.04
		pl(6)	55.15	0.33	0.12	0.09	27.80	0.76	1.05	0.47	b.d		0.19	0.10	11.70	0.31	4.57	0.03	0.49	0.10	-		101.06	56.93
Y251	1200 → 1100	gl(5)	56.48	0.97	1.95	0.19	12.51	0.27	12.43	0.92	0.21	0.04	2.24	0.15	6.64	0.37	2.49	0.09	2.54	0.19	0.49	0.06	97.98	24.33
		pl(7)	54.17	0.26	0.11	0.03	27.69	0.36	0.86	0.16	b.d.		0.15	0.04	11.70	0.19	4.39	0.08	0.61	0.04	-		99.67	57.43
		pig(4)	50.97	0.11	0.60	0.15	1.80	1.13	22.05	2.18	0.45	0.04	16.73	0.52	6.60	1.14	0.16	0.12	b.d.	0.00	-		99.37	57.49
		cpx(7)	50.74	0.23	0.83	0.11	2.72	0.50	17.21	1.09	0.40	0.05	16.01	1.06	11.56	1.36	0.13	0.03	0.02	0.03	-		99.61	62.37
Y255 †	1080	gl(8)	58.95	1.43	1.82	0.06	12.33	0.17	11.51	1.06	0.20	0.03	1.75	0.11	5.86	0.44	2.92	0.10	2.58	0.18	0.49	0.14	98.41	21.30
		pl(7)	55.79	0.34	0.31	0.29	25.19	1.97	2.09	1.68	0.06	0.08	0.42	0.30	10.23	0.56	4.89	0.20	0.73	0.21	-		99.72	51.28
		cpx(11)	51.55	1.54	0.82	0.11	2.28	1.00	15.78	0.69	0.34	0.04	11.18	0.63	16.70	1.28	0.51	0.16	0.30	0.20	-		99.46	55.80

100

Table 4.6 continued

Run	T°C	Phase	SiO$_2$	TiO$_2$	Al$_2$O$_3$	FeO	MnO	MgO	CaO	Na$_2$O	K$_2$O	P$_2$O$_5$	Total	An/Fo/Mg#
						composition F$_{gl}$								
Y253	**1120**	gl(10)	57.20 *0.98*	1.72 *0.10*	13.27 *0.23*	11.63 *0.56*	0.17 *0.02*	2.87 *0.16*	7.21 *0.30*	2.64 *0.10*	2.33 *0.13*	0.48 *0.10*	99.52	30.55
		pig(7)	52.83 *0.37*	0.39 *0.10*	1.03 *0.34*	20.95 *0.52*	0.46 *0.04*	19.54 *0.46*	5.61 *0.71*	0.09 *0.04*	0.05 *0.03*	-	100.88	62.44
		pl(7)	54.23 *0.10*	0.18 *0.06*	27.07 *0.47*	1.73 *0.29*	b.d	0.67 *0.29*	12.21 *0.18*	4.07 *0.04*	0.59 *0.08*	-	100.75	60.22
		cpx(2)	53.21 *0.34*	0.93 *0.16*	5.14 *1.12*	15.16 *0.43*	0.29 *0.07*	12.60 *1.27*	11.19 *1.46*	0.79 *0.30*	0.65 *0.29*	-	99.97	59.70
Y252	**1100**	pl(6)	54.75 *0.29*	0.25 *0.11*	26.70 *0.99*	1.87 *0.62*	0.05 *0.05*	0.51 *0.29*	11.98 *0.33*	4.03 *0.08*	0.68 *0.11*	v	100.80	59.64
		gl(10)	58.18 *1.53*	1.94 *0.20*	12.77 *0.29*	11.66 *0.86*	0.20 *0.04*	2.24 *0.21*	6.38 *0.45*	2.62 *0.11*	2.66 *0.22*	0.52 *0.12*	99.12	25.47
		pig(8)	52.72 *1.08*	0.55 *0.12*	1.73 *1.07*	22.54 *1.19*	0.48 *0.04*	16.00 *1.22*	6.69 *1.30*	0.23 *0.24*	0.17 *0.20*	-	101.03	55.85
		cpx(4)	51.89 *0.98*	0.76 *0.12*	2.75 *0.78*	18.08 *1.02*	0.40 *0.03*	14.45 *1.69*	12.11 *0.87*	0.30 *0.27*	0.23 *0.20*	-	100.98	58.75
Y255	**1080**	gl(8)	57.05 *0.25*	2.07 *0.07*	12.27 *0.21*	12.35 *0.29*	0.21 *0.03*	2.05 *0.11*	6.38 *0.14*	2.41 *0.09*	2.65 *0.06*	0.54 *0.08*	97.96	22.83
		pl(8)	54.94 *0.57*	0.43 *0.17*	24.39 *1.28*	2.87 *0.89*	b.d.	0.80 *0.30*	11.13 *0.35*	4.00 *0.13*	0.89 *0.13*	-	99.45	57.28
		pig(4)	52.48 *1.08*	0.77 *0.07*	3.65 *1.13*	21.98 *1.39*	0.47 *0.02*	13.40 *0.76*	6.33 *0.50*	0.60 *0.27*	0.60 *0.19*	-	100.28	52.06
		cpx(4)	51.10 *0.79*	0.86 *0.06*	2.70 *0.42*	19.35 *0.81*	0.42 *0.05*	13.39 *0.87*	11.56 *0.67*	0.32 *0.14*	0.23 *0.06*	-	99.93	55.23

Mg#: molar [Mg/(Mg + Fe)] *100
An: molar [Ca/(Ca + Na)] *100
† Pure Al$_2$O$_3$ observed in experiments
1200 → Experimental approach with initial heating of 1200°C

4.4 Discussion

4.4.1 Attainment of equilibrium and influence of experimental procedure

Using experimental studies to investigate phase stabilities requires a critical evaluation if local and/or global equilibrium conditions were achieved during the experimental runs. Most experiments from this study have minimum run durations of 48 h (except for two experiments of 24 h at the highest temperature; Table 4.5). In this study three different experimental procedures were applied and the attainment of equilibrium is discussed separately for the three approaches.

Conducting experiments with glass as starting material is the best method to reach equilibrium among the three approaches that have been tested. The nucleation is enhanced along the initial glass grains and problems related to possible mineral zoning due to progressive changes of the melt composition with increasing crystallinity are minor. Freise et al. (2009) conducted time dependent experiments using the same approach on alkali basalts under dry conditions and showed near equilibrium conditions are reached within 3 h.

The experimental approach using non-fused oxide and silicate powders as starting material has been tested by Sisson & Grove (1993) who showed that close to equilibrium conditions are reached after 36 h in experiments above 1050°C for basaltic water-bearing compositions. However, previous studies (e.g., Kinzler, 1997) noted that experiments using oxide-silicate powders as starting material only attain local equilibrium also when conducted with longer run durations (<100 h). In this study, pockets of Al_2O_3 can be observed in the products of experiments performed with oxide powder and without initial heating above the liquidus. These Al_2O_3 solid phases are most probably remnants of undissolved starting material, questioning the attainment of equilibrium in these experiments. The uncomplete dissolution of the Al-bearing oxide may also affect the melt composition in terms of Al concentration and thus the phase equilibria. A lower Al content in the melt would affect the plagioclase composition resulting in lower An concentrations (Panjasawatwong et al., 1995). A comparison of plagioclase compositions from experiments conducted at similar temperatures with and without Al_2O_3 relics, show that the plagioclase composition is indeed different, with a lower An in experiments with Al_2O_3 relics with few exceptions for higher temperature experiments (e.g., F; 1120°C; Figure 4.5). These compositional differences are confirmed by lower concentrations of Al in the melt in those experiments were relics of Al_2O_3 are observed. Compared to the bulk composition, the higher Ca/Al ratio in the reactive assemblage during the experiments also influences the stability of clinopyroxene as observed in experiments (crystallization at higher temperatures) with compositions C and E experiments (cp. Table 4.5 and Figure 4.3). To understand the crystallization sequence starting from a parental magma, global equilibrium is necessary. Thus, since the effect of Al_2O_3 relics in some experimental runs is not negligible

and can even change the observed phase assemblage, those experiments are excluded in the further discussion on the phase stability.

To avoid remnants of Al_2O_3 in the experimental run products, the two-step temperature path with initial heating above the liquidus was applied. A remarkable feature of the two-step experiments is the large crystal size (up to 0.5 mm; Figure 4.2B) resulting from a low nucleation and rapid growth of crystals. Due to the large size of the phases, the minerals could show compositional zoning related to the changes of melt composition with ongoing crystallization. However, the crystallinity is generally low in the run products of this study and phases formed in the two step experiments show no crystal zonation or compositional heterogeneity between crystals, supporting the attainment of equilibrium between melt and solid phases. The textures obtained in the two-step experiments also indicate a strong undercooling which could influence the phase equilibria determined in this study. For example, due to undercooling, a mineral phase which should be present at equilibrium may not be observed in the experimental products. This possible problem was tested with composition F. In addition to two-step experiments using oxide powder, runs with composition F were also performed using a glass powder with the same composition. In contrast to the overheated experiments, minerals in experiments performed with glass powder as starting material are tiny (cp. Figure 4.2). The advantage of using a glass powder is that nucleation is strongly favored at the interface between initial glass grains. Thus, problems due to undercooling are reduced, enabling attainment of global equilibrium. Experimental run products of both approaches reveal the same mineral assemblage, indicating that undercooling problems may not affect the presence of solid phases such as plagioclase and pyroxenes at equilibrium. However, small deviations in the mineral compositions are observed (Figure 4.6). An in plagioclase is slightly lower in those experiments performed with oxide powders, whereas Mg# of both pyroxenes is higher. On the other hand, the strong nucleation in experiments performed with glass powder leads to the formation of small phases, which causes a problem during EMPA measurements, because the activation volume can include matrix glass. Especially, pyroxenes are rarely larger than a few μm. Compared to the pyroxenes the residual liquid has a much lower Mg#. A mixed analysis would lead to a decrease in the Mg# of the pyroxenes as observed in this study. This explanation is supported by elevated Al concentrations in some pyroxenes of those runs, probably originating from contamination of the analyses by surrounding glass. Glass compositions, representing the residual melt show only minor compositional variations expressed in identical (1100°C) or slightly higher (1120°C) MgO contents in glasses from experiments using oxide powders as starting material (Figure 4.6). Alltogether, experiments using glass powder and two-step experiments using oxide powder as starting material are in agreement with each other. Thus, results from both are used for further discussion.
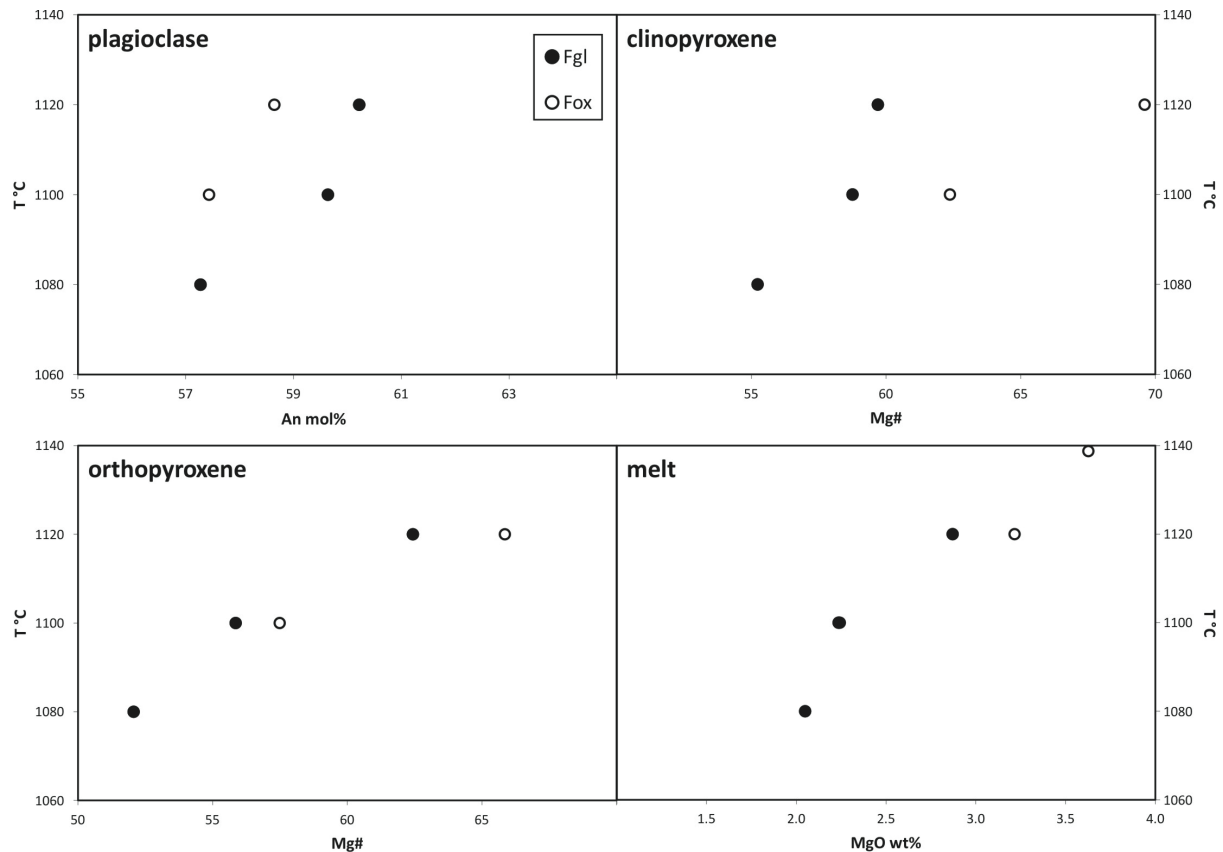
Figure 4.6 Compositions from experimental run products using starting composition F are plotted againgst experimental temperature, showing the effect of different starting materials.

In addition to global equilibrium, test for local equilibrium conditions can be conducted, using Fe-Mg exchange between melt and pyroxenes (Duke, 1976). For K_D(Mg-Fe) the following equation is used:

$$K_D(Mg - Fe)^{cpx-liq} = \frac{X_{FeO}^{cpx}}{X_{FeO}^{liq}} \times \frac{X_{MgO}^{liq}}{X_{MgO}^{cpx}}$$

Calculated K_D(Mg-Fe)$^{cpx-liq}$ range between 0.15 and 0.3 and decrease with decreasing temperature. This range and the decrease with temperature are in agreement with published values by Putirka (2008) supporting the achievement of equilibrium during the experiments. Since Fe-Mg exchange equilibrium does not ensure Na-Al or Ca-Na exchange equilibrium, several studies suggest to calculate mineral compositions and compare to observed mineral compositions (e.g., Rhodes et al., 1979; Putirka, 1999; 2008). Following these authors, clinopyroxene compositions were calculated after Putirka (1999) and presented in Figure 4.7. Data points plot close to the 1:1 line supporting equilibrium conditions. However, outliers for EnFs composition are observed, corresponding to clinopyroxenes from experiments using the starting glass F. Again, as discussed above, this is probably caused by analytical problems (glass contamination).

Another indicator for the achievement of equilibrium conditions is the accuracy of already calibrated geothermometers. The plagioclase-melt thermometer of Putirka (2005) was applied to the experimental run products. Figure 4.7 shows that the maximal deviation from the expected temperature using the model of Putirka (2005) is ~20°C. These results show a good agreement within the error of calculated and experimental temperatures. As expected deviations from the 1:1 line are slightly higher at lower temperatures.

In conclusion, calculations of exchange coefficients, mineral components and temperatures using plagioclase, clinopyroxene and melt compositions argue in the favor of local equilibrium conditions in experiments using oxide powders and two-step heating, and those using glass powders as starting material. Moreover, experiments conducted with glass powder as starting material reached global equilibrium. Since the equilibrium phase assemblage of the two-step experiments is identical to experiments starting from glass powder and since the phase compositions are similar (especially glass) it can be concluded that global equilibrium was also reached in the two-step experiments.
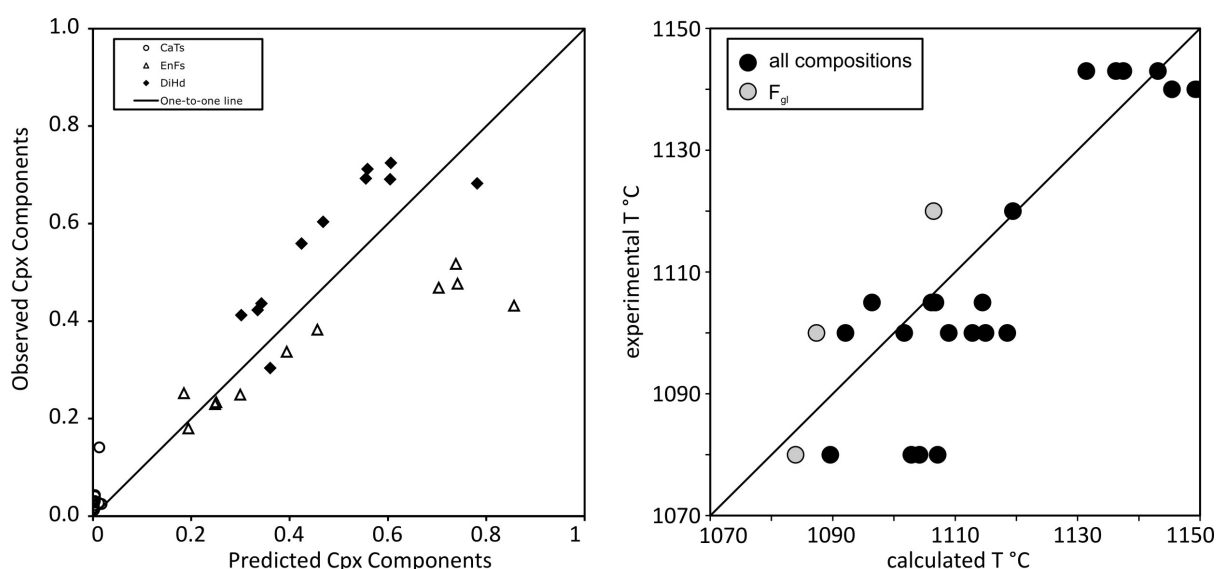

Figure 4.7 Left: Predicted clinopyroxene compositions, calculated using the Excel spreadsheet provided by Putirka (2008) versus pyroxene compositions observed in experimental run products (Putirka, 2008). **Right:** Calculated and observed experimental temperatures, calulated following Putirka (2005). Experiments where Al_2O_3 relics are present are excluded in both figures.

4.4.2   MELTS thermodynamic modeling

One aim of this study was to test the ability of MELTS to predict accurately the phase equilibria in systems relevant for the UUMZ since the constraints on the parental compositions proposed by VanTongeren et al. (2010) were based on calculations with MELTS. Therefore, MELTS calculations were performed at different conditions for all starting

compositions used in this study, enabling comparison with experiments from this study and previously proposed parental magma compositions tested by MELTS modeling.

4.4.2.1 *Previous assumptions on parental magmas using MELTS*

VanTongeren et al. (2010) proposed several possible UUMZ parental magma compositions based on calculation with MELTS (Ghiorso & Sack, 1995) and assuming that (1) the initial phases are orthopyroxene ± clinopyroxene ± plagioclase. (2) oxygen fugacity conditions are around FMQ based on the appearance of magnetite. (3) A melt water content of 1 wt% H_2O was postulated based on the observation of the absence of hydrous phases such as hydroxyl-apatite, biotite and hornblende in the UUMZ stratigraphy and UUMZ bulk rock analysis by Bowes et al. (1997). (4) A pressure of 2 kbar was assumed. (5) Closed system fractional crystallization was assumed.

VanTongeren et al. (2010) argued that their basaltic parental magma compositions reproduce the paragenetic sequence observed in UUMZ drill cores (magnetite saturation after 25% crystallization and apatite saturation after 70% crystallization). However, two major points need to be addressed here. Gualda et al. (2012) showed that MELTS and rhyolite-MELTS calculations are only accurate in crystallization interval between 0 and 50 vol% crystals. Thus the appearance of phases after this point in model calculations needs to be interpreted with caution. Moreover, as shown by several authors (e.g., Ashwal et al., 2005; Scoon & Mitchell, 2012; Yuan et al., 2017) the UUMZ is not the result of closed system fractional crystallization. Thus, MELTS results are only presented and discussed here for the crystallization sequence revealed before magnetite crystallization. In nature, this is the level where Yuan et al. (2017) identified the first magma injection for the UUMZ.

Modeling results of VanTongeren et al. (2010) confirmed the assumptions of Cawthorn & Walraven (1998) that the bulk UUMZ is not in equilibrium with the first cumulates above the PM, composed of plagioclase, orthopyroxene and clinopyroxene. Further modeling was performed, using compositions similar to A and B as well as the composition proposed by Tegner et al. (2006) similar to composition C in this study. Whereas the Tegner et al. (2006) composition failed to produce orthopyroxene, other calculated compositions showed the crystallization sequence orthopyroxene -> orthopyroxene + plagioclase -> pigeonite + clinopyroxene + plagioclase. This sequence satisfies the criteria of VanTongeren et al. (2010) leading them to the conclusion that these basaltic compositions (similar to A and B of this study) are possible UUMZ parental magma compositions. However, in contrast to VanTongeren et al. (2010) we argue that all three phases, orthopyroxene, clinopyroxene and plagioclase, which are observed directly above the PM, should crystallize simultaneously from a potential UUMZ parental magma.

4.4.2.2 Comparison of experimental products with MELTS

In this study the modeling of the crystallization sequence was performed for compositions A to F using rhyolite-MELTS (Gualda et al., 2012; Ghiorso and Gualda, 2015). Input parameters were 2 kbar pressure and isobaric fractional crystallization. Temperature was decreased in 10 degree intervals and stopped at 700°C. Oxygen fugacity was fixed to CCOH throughout the entire crystallization sequence to compare directly the experimental runs of this study with MELTS. Additional calculations were also performed at an oxygen fugacity fixed at FMQ to compare with results of VanTongeren et al. (2010) and to discuss the possible effect of oxygen fugacity. The effect of the addition of 1 wt% H_2O was also tested for the six compositions. Results are presented in Figure 4.8 with the proportions of remaining liquid given in vol%.

The experimental results with the parental magma compositions A - D, proposed in previous studies as possible parental melts, revealed the crystallization of olivine early in the sequence together with plagioclase and (A, B; Figure 4.3) or plagioclase and clinopyroxene (C and D; Figure 4.3). Olivine is present in all experimental products between 1140°C and 1080 °C for compositions A and D and in all experimental products between 1120 and 1080 °C for compositions B and C. However, the presence of this phase is not predicted by MELTS in this temperature range and for the corresponding crystallinity (0 to 25% crystals) in the dry systems. At the CCO oxygen buffer, MELTS predicts pigeonite and plagioclase after 10% crystallization in the four compositions A - D. For composition E, melts indicates that orthopyroxene is the liquidus phase, but that this mineral is replaced by pigeonite after 2% crystallization. Plagioclase is expected to crystallize after the formation of 5 % crystals with MELTS. This differs from our experiments in which plagioclase is the liquidus phase. In composition F, the three phases plagioclase, pigeonite and clinopyroxene are coexisting in the experiments at 1120°C, but clinopyroxene is only predicted at high crystallinity above 30 vol% using MELTS, which again differs from the experimental observations. In conclusion, MELTS does not fully reproduce the observed experimental phase assemblage. Since MELTS is not calibrated for all possible natural compositions, a complete and perfect overlap could not be expected between MELTS and our experimental products. However, the most important feature which is crucial in this study is that olivine is only predicted at a late crystallization stage by MELTS, which is contrasting with the experimental results. The experimental results show that the compositions assumed so far as parental melts should lead to the presence of olivine in the early cumulates, which is not observed in the UUMZ where olivine enters the sequence after magnetite (UZb). Thus, a direct application of MELTS to constrain the role of the composition of parental magma on the crystallization sequence in the UUMZ may leads to misinterpretations.

Although MELTS may not reproduce exactly the experimental results, the model can be used to estimate qualitatively the effect of oxygen fugacity and water on phase equilibria. MELTS modeling using the same conditions but oxygen fugacity fixed at different

buffers (FMQ and CCO) reveal similar results for crystallization <50% confirming previous assumptions that oxygen fugacity does not influence phase equilibria before magnetite saturation. Thus, even if the natural conditions are slightly more oxidizing than the experimental ones, strong differences are not expected. Notable here is the crystallization of magnetite and clinopyroxene in composition A that occurs much earlier at FMQ conditions. The addition of 1 wt% H_2O to the parental magma compositions influences significantly the initial phase assemblages in the MELTS calculations. Plagioclase is suppressed in all compositions. Orthopyroxene is stabilized in compositions B and E but disappears with ongoing crystallization. Clinopyroxene becomes stable earlier in the sequence. This argues against the presence of high amounts of H_2O at this level of the UUMZ.

One of the important observations made by VanTongeren et al. (2010) to constrain the parental magma of the UUMZ was that olivine should not be an early cumulus phase. The absence of early olivine in the parental compositions A to D proposed by VanTongeren et al. (2010) was confirmed by MELTS. However, our experiments clearly demonstrate that this phase is expected to be present in the possible parental magmas calculated by VanTongeren et al. (2010). Clearly, compared to the natural stratigraphy with cumulus orthopyroxene, plagioclase and clinopyroxene, the mineral assemblage observed experimentally for the compositions A - D is not matching. Olivine is absent in the lowest gabbronorites and enters the sequence much later (UZb).
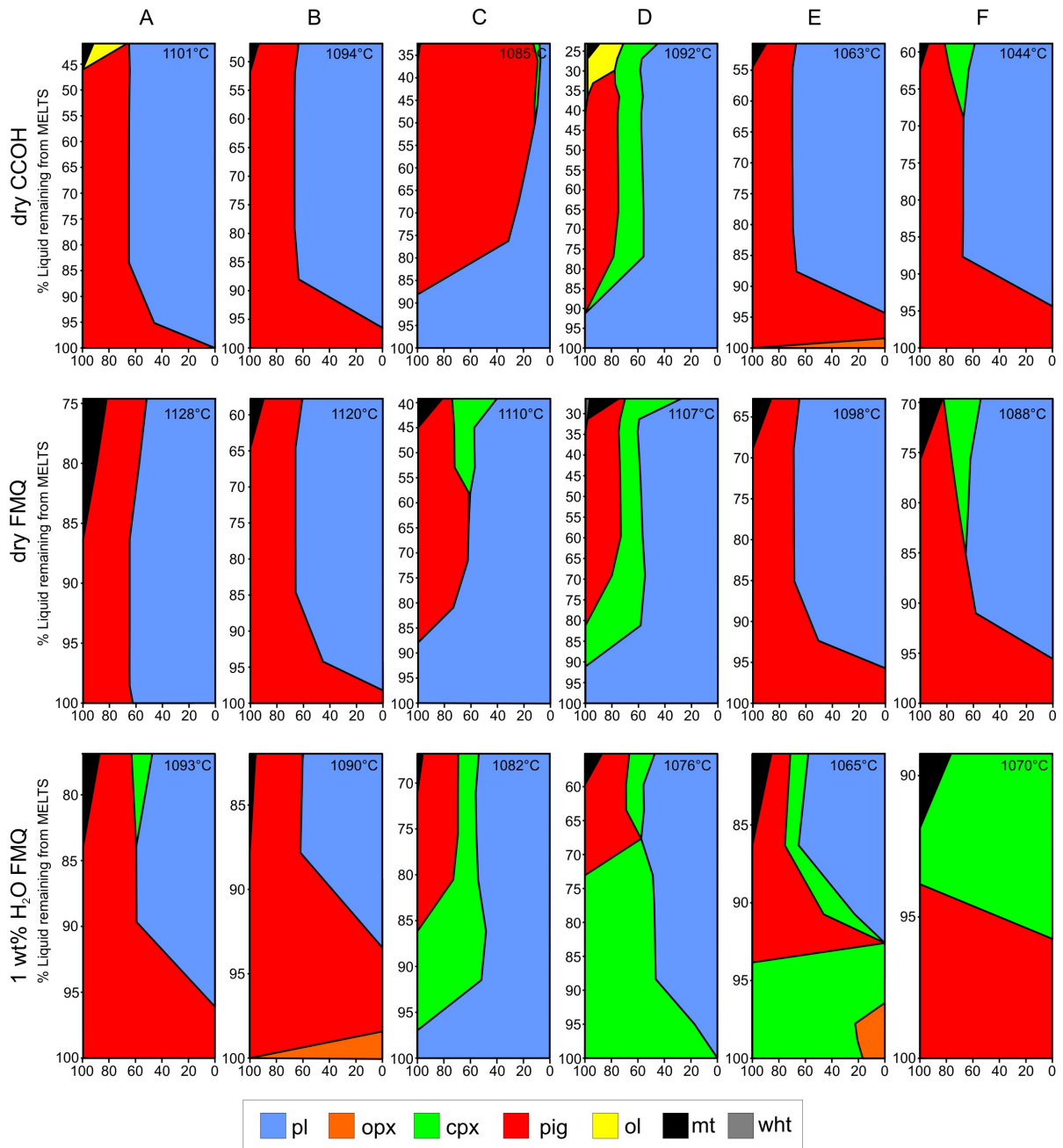
Figure 4.8 Modal abundances prdicted by rhyolite-MELTS calculations for compostions A, B, C, D, E and F for three different conditions: dry and CCO, dry and FMQ and 1 wt% H_2O and FMQ. X-axis shows the proportions in vol% of crystallizing minerals normalized to 100 for every temperature step. Y-axis shows the liquid fraction remaining from MELTS calculations. Results are shown from liquidus (100% liduid remaining) till the crystallization of magnetite (at the given T°C), marking the level of the first magma injection into the UUMZ. Predicted phases are plagioclase (pl), orthopyroxene (opx), clinopyroxene (cpx), pigeonite (pig), olivine (ol) magnetite (mt) and whitlockite (wht).

4.4.2.3 The role of felsic components in the UUMZ parental melts

Experiments with proposed parental magma compositions A - D revealed crystallization of olivine early in the sequence together with plagioclase and orthopyroxene (A and B) or clinopyroxene (C and D). This is in contrast to the natural stratigraphy, where

olivine is absent in the lowest gabbronorites and enters the sequence late (UZb). The stability of either orthopyroxene or olivine is controlled by the silica activity with orthopxroxene crystallization at higher silica activities (e.g., Nicholls et al., 1971). Thus, in the course of this study, more Si-rich compositions (E and F) were tested to reproduce the early cumulate phases. Due to the higher proportion of monzonite in composition E, the silica activity is increased compared to compositions A - D, promoting orthopyroxene stability at the expense of olivine. Experiments conducted with composition E, indeed show that the stability of orthopyroxene is shifted to higher temperatures compared to compositions A and D, and olivine appears at lower temperatures compared to A - D (Figure 4.3). However, clinopyroxene crystallization occurs only in the low temperature experiment (E; 1080°C), and olivine is also observed at this temperature, which again does not reproduce the mineral assemblage of the cumulates in the lowest gabbronorites. To shift the clinopyroxene stability to higher temperatures, so that this phase crystallizes approximately in the same temperature range as plagioclase and orthopyroxene (1120°C to 1140°C) a clinopyroxene with a composition similar to that analyzed in the first cumulates above the PM was added to composition E (see details above; chapter 4.2.1 "Choice of strating compositions"). Compared to the previously proposed basaltic parental magmas, the two new compositions E and F from this study are andesitic and have a higher silica activity. Early clinopyroxene crystallization, together with plagioclase and low-Ca-pyroxene is attained in composition F. The SiO_2 and CaO contents of experimental melts coexisting with clinopyroxene and low-Ca-pyroxene are shown in Figure 4.9 where stability fields of olivine and pyroxenes are also plotted. Figure 4.9 indicates that melts which may correspond to the parental compositions of the UUMZ must have SiO_2 contents above ~56 wt%. Compare to previous proposed compositions (tested here with compositions A - D), composition F is much more enriched in SiO_2 and contains less Al_2O_3 and MgO.
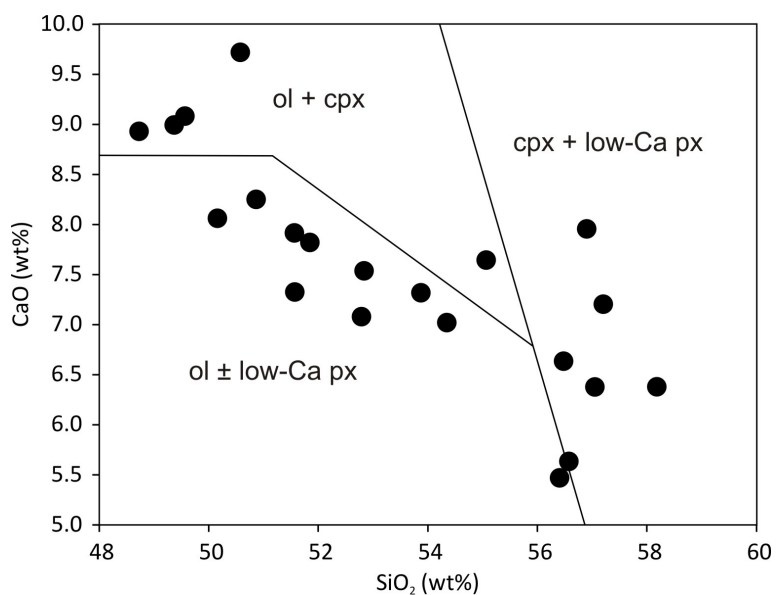

Figure 4.9 SiO_2 and CaO compositions of experimental residual liquids. Phase stability fields are estimated from pahses stable in the experiments. ol: olivine; cpx: clinopyroxene; low-Ca px: low-calcium pyroxene.

4.4.3 Comparison with Bushveld Complex

The aim of this study is, to constrain experimentally a magma composition, which is parental to the UUMZ. The chosen experimental conditions in this study (2 kbar; dry; CCO) are considered to be relevant for the UUMZ. Previous assumptions include the presence of H_2O (VanTongeren et al., 2010) and oxygen fugacity conditions above FMQ (Tegner et al., 2010), at FMQ (VanTongeren et al., 2010) or below FMQ (Balan et al., 2006; for magnetite layers). The latter is in agreement with findings from this study suggesting oxygen fugacity conditions around FMQ -2. However, Toplis & Carroll (1995) showed that there is only minor influence on fO_2 on the phase equilibria before magnetite saturation. Thus, since the experiments aim to simulate the crystallization directly above the PM where magnetite is absent, no significant influence of fO_2 is expected. Assumptions on the melt water content for the UUMZ are scarce in literature. Generally the UUMZ is considered to be more H_2O rich than the lower zones (Wallmach et al., 1995) and VanTongeren et al. (2010) suggests an H_2O content of the UUMZ parental magma of around 1 wt%. Owing the incompatible behavior of H_2O, the absence of hydrous phases in the MZu and the early crystallization of plagioclase, H_2O contents of 1 wt% or below this value are expected for the melts at the base of the UUMZ.

The UUMZ parental magma must crystallize plagioclase, low-Ca-pyroxene and clinopyroxene, which are the first cumulus phases of the UUMZ. This mineral assemblage is only achieved in experiments with the composition F, where all three phases crystallize at near liquidus conditions around 1120°C at CCO and dry conditions. Compared to the other starting compositions, F is more enriched in silica and alkalis and contains relatively low MgO concentrations. Although, experiments with composition F produce the same mineral assemblage as observed above the PM, the mineral compositions differ from those observed in the MZu (Figure 4.10). Plagioclases produced in the F experiments are lower in An compared to their natural equivalents. An content of plagioclase is mainly controlled by Ca, Al_2O_3 and H_2O contents of the liquid, all promoting higher An contents (Panjasawatwong et al., 1995). This can be observed in experiments using starting compositions C, which is higher in CaO and Al_2O_3, and thus crystallizes plagioclase with An contents more similar to MZu (Figure 4.10A). Moreover, Husen et al. (2016) showed in an experimental study, using synthetic basalts, that already ~0.5 wt% water in the liquid can increase the An in plagioclase by up to 15 mol%. Knowing that H_2O was present during crystallization of the UUMZ, it is most likely that small amounts of H_2O stabilized crystallization of high-An plagioclase at the base of the UUMZ.

Also pyroxene compositions differ between experimental run products and MZu samples. While the cumulates above the PM contain orthopyroxene (Mg# ~70), experimental run products show pigeonite (Mg# = 55 - 65). The transition of orthopyroxene and pigeonite is mainly controlled by temperature and liquid Mg# (Kilinc et al., 1983; Lindsley & Andersen, 1983; Davidson & Lindsley, 1985; Grove & Juster, 1989). These authors

show that pigeonite is destabilized in the favor of orthopyroxene at lower temperatures and higher Mg# of the liquid. For conditions applied to experiments from this study at a temperature of 1140°C the transition is around Mg# = 50 (Grove & Juster, 1989; Figure 4.11), which is much higher than in all used starting compositions (cp. Table 4.4). The Bushveld stratigraphy below the PM is marked by a change from primary orthopyroxene to primary pigeonite (von Gruenewaldt, 1973; Molyneux, 1974), suggesting that conditions are close to the boundary of both stability fields. This is supported by the occurrence of inverted pigeonite (secondary orthopyroxene), which is supposed to be a result of modification during cooling of the primary pigeonite (Cawthorn et al., 1991).
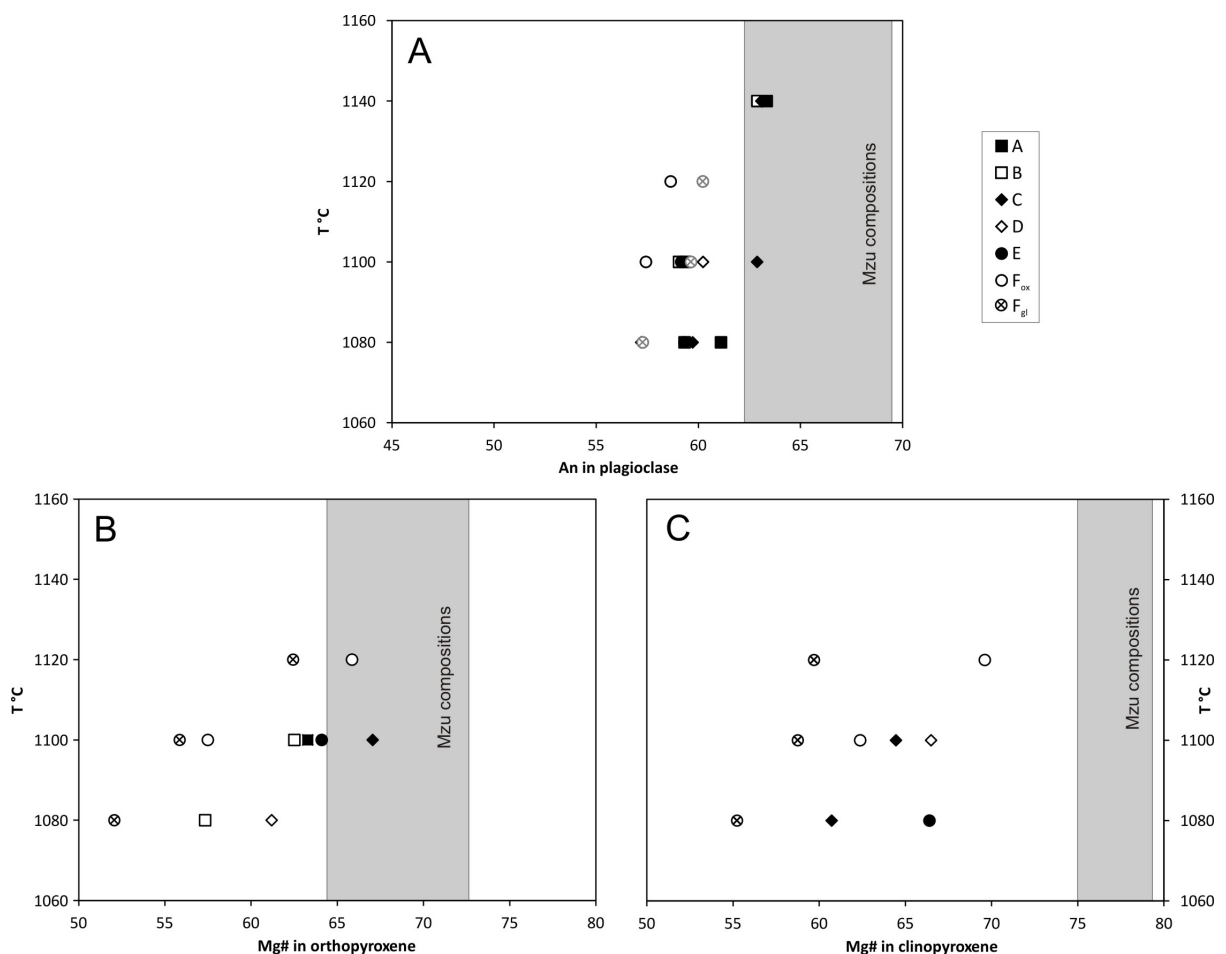

Figure 4.10 Comparison of experimental run products with natural minerals of the MZu. Grey fields mark the compositional range of MZu minerals. Symbols represent average compositions of experimentally produced minerals.

As emphasized above, the estimated parental composition F has a relatively low MgO concentration. There is evidence from marginal sills, that magmas from the underlying Critical and Main Zone (B1, B2 and B3) are much more enriched in Mg compared to composition F of this study. Barnes & Maier (2002) estimated compositions for the high-Mg basaltic andesite and tholeiitic basalt revealing Mg# of 71 and 53, respectively. Addition of such a liquid component would drive the magma composition towards the orthopyroxene stability field (cp. Figure 4.11). Experimentally produced plagioclases are lower in An compared to natural plagioclases
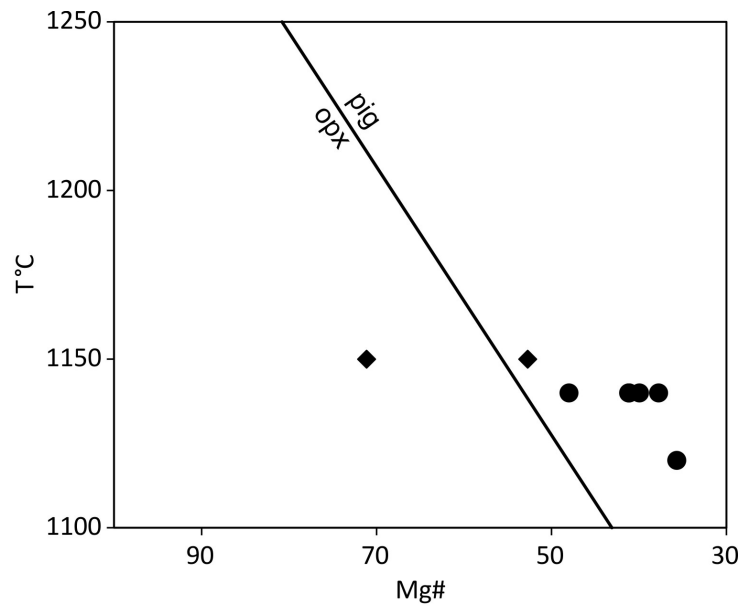

Figure 4.11 Stability of pigeonite (pig) and orthopyroxene (opx) depending on temperature and Mg# oft he liquid. Circles correspond to the experimental starting compositions with the temperature of the first experiment below the liquidus. Diamonds correspond to estimated liqiuid compostions from Critical and Main Zone of Barnes & Maier (2002). Although liquidus temperatures for these compositions are much higher (1200°C - 1300°C; Harmer & Sharpe, 1985), a temperature of 1150°C is plotted, which is estimated for the magma below the PM (Cawthorn et al., 1991).

observed in the MZu. The B1 - B3 liquids are also enriched in CaO, promoting crystallization of more An-rich plagioclase (Panjasawatwong et al., 1995) and stabilizing clinopyroxene (Ross & Huebner, 1979). Thus, further calculations of a parental magma composition should include a contribution of residual liquids from underlying zones leading to an increase in the Mg# of the melt, stabilizing orthopyroxene crystallization at the expense of pigeonite, as observed in the UUMZ cumulates. A higher Mg# is also assumed when looking on mineral Mg# of both pyroxenes. Compared, to the natural compositions of ortho- and clinoyproxene in the BK2 drill core, experimental pyroxenes are lower in Mg# (Figure 4.12).
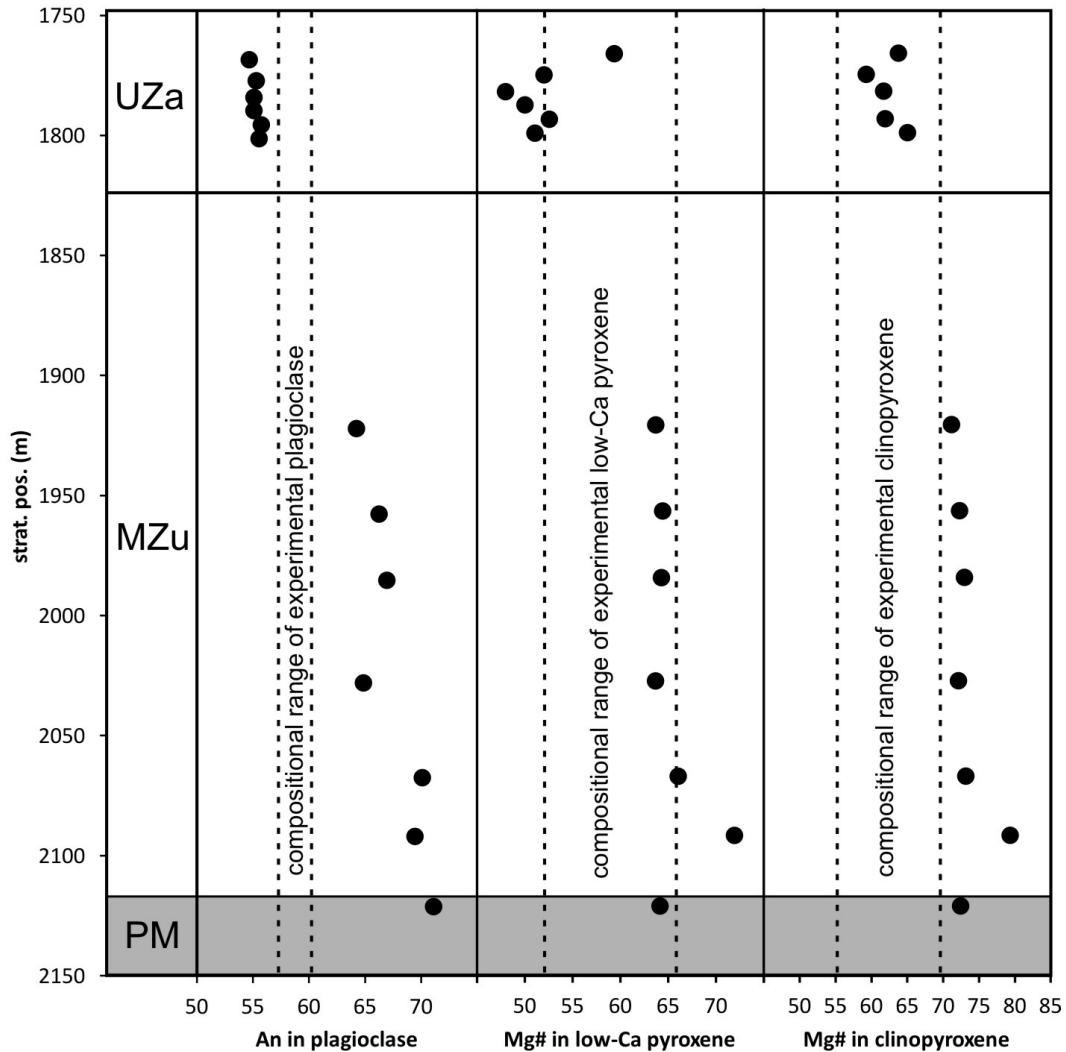
Figure 4.12 Comparison of natural and experimental mineral compositions for plagioclase, low-Ca pyroxenes and clinopyroxens. Natural mineral compositions are shown as black circles for the Upper Main Zone (MZu) and base of Upper Zone a (UZa) stratigraphy above the Pyroxenite Marker (PM) and are obtained in samples from the BK2 drill core (table appendix). Dashed lines mark the range of experimental mineral compositions.

4.5   Conclusions

The results of this study show that the parental magma composition to the UUMZ of the Bushveld Complex must be andesitic in composition rather than basaltic as previously proposed. Using an andesitic starting composition in the crystallization experiments revealed the same mineral assemblage of plagioclase + low-Ca-pyroxene + clinopyroxene as observed above the PM, representing the first cumulates of the UUMZ. The discrepancies observed in mineral compositions between experimental run products and drill core samples show, that the UUMZ most likely contains some amount of residual liquid from the underlying zones, with high Mg and Ca concentrations. There is also evidence from mineral compositions, that small amounts of H_2O were present in the UUMZ parental magma. Addition of these components to the experimentally tested composition F of this study will further stabilize ortho- and clinopyroxenes as well as An-rich plagioclase in the experiments.

Concluding remarks

During this PhD-project, different aspects of the late-stage evolution of the Bushveld Complex, which formed the Upper and Upper Main Zone of this economically and scientifically important intrusion, were investigated. The findings of this study provide a better understanding of the formation mechanisms affecting the magmatic sequence of the upper part of the intrusion.

It is shown in this thesis that the Upper and Upper Main Zone of the Bushveld Complex evolved from an andesitic parental magma containing small amounts of H_2O. The first cumulates have the mineral assemblage plagioclase + low-Ca-pyroxene + clinopyroxene, and the cumulate series is marked by several magma replenishment events. The recent formation model (Yuan et al., 2017) can explain the observed compositional cyclicity by several magma replenishment events in which a plagioclase-laden magma is injected into the Bushveld magma chamber. Based on trace elements in titanomagnetite and clinopyroxene, this study revealed two major compositional shifts correlating with the stratigraphic position of two magma injections identified by Yuan et al. (2017). These shifts towards more evolved compositions are related to injections from different compartments of the sub-Bushveld staging chamber, arguing for a sub-compartmentalized magma chamber as a source of the magma injections. Estimated oxygen fugacities are around FMQ -2 and show only minor variations within the stratigraphy, suggesting constant prevailing fO_2 conditions during crystallization of the Upper Zone. Consequently, it can be concluded that the injected magma has similar oxygen fugacity conditions as the resident magma.

The repeating anorthosite layers are produced by crystal settling of the injected plagioclase crystals. Whereas, the economically important magnetitites are the result of crystallization from a hybrid melt, produced by mixing of resident and injected magma (Yuan et al., 2017). The late stage evolution of Upper Zone with apatite saturated cycles is marked by the onset of silicate liquid immiscibilty producing an Fe- and a Si-rich silicate liquid. The Fe-rich melt is also enriched in P and percolates downwards within the crystal mush. Cumulates of these segregated Fe-P-rich liquids then produced the nelsonite layers observed in the Upper Zone.

References

Arató, R. & Audétat, A. (2017). Experimental calibration of a new oxybarometer for silicic magmas based on vanadium partitioning between magnetite and silicate melt. Geochimica et Cosmochimica Acta 209, 284–295.

Ashwal, L. (1993). Anorthosites. Springer Heidelberg.

Ashwal, L.D., Webb, S.J. & Knoper, M.W. (2005). Magmatic stratigraphy in the Bushveld Northern Lobe: Continuous geophysical and mineralogical data from the 2950 m Bellevue drillcore. South African Journal of Geology 108, 199–232.

Bacon, C.R. & Hirschmann, M.M. (1988). Mg/Mn partitioning as a test for equilibrium between coexisting Fe-Ti oxides. American Mineralogist 73, 57–61.

Bai, Z.-J., Zhong, H., Naldrett, A.J., Zhu, W.-G. & Xu, G.-W. (2012). Whole-rock and mineral composition constraints on the genesis of the Giant Hongge Fe-Ti-V oxide deposit in the Emeishan Large Igneous Province, Southwest China. Economic Geology 107, 507–524.

Baker, D.R. & Eggler, D.H. (1987). Compositions of anhydrous and hydrous melts coexisting with plagioclase, augite, and olivine or low-Ca pyroxene from 1 atm to 8 kbar: application to the Aleutian volcanic center of Atka. American Mineralogist 72, 12-28.

Balan, E., De Villiers, J.P.R., Eeckhout, S.G., Glatzel, P., Toplis, M.J., Fritsch, E., Allard, T., Galoisy, L. & Calas, G. (2006). The oxidation state of vanadium in titanomagnetite from layered basic intrusions. American Mineralogist 91, 953–956.

Barnes, S.J. (1986). The effect of trapped liquid crystallization on cumulus mineral compositions in layered intrusions. Contributions to Mineralogy and Petrology 93, 524–531.

Barnes, S.-J. & Maier, W.D. (2002). Platinum-Group Element Distributions in the Rustenburg Layered Suite of the Bushveld Complex , South Africa. Canadian Institute of Mining and Metallurgy Special Volume 54, p. 431–458

Barnes, S.-J., Maier, W.D. & Curl, E.A. (2010). Composition of the Marginal Rocks and Sills of the Rustenburg Layered Suite, Bushveld Complex, South Africa: Implications for the Formation of the Platinum-Group Element Deposits. Economic Geology 105, 1491–1511.

Basta, E. Z. (1960). Natural and synthetic titano-magnetites. Neues Jahrbuch für Mineralogie - Abhandlungen 94, 1017-1048.

Bédard, J.H.J., Marsh, B.D., Hersum, T.G., Naslund, H.R. & Mukasa, S.B. (2007). Large-scale mechanical redistribution of orthopyroxene and plagioclase in the basement sill, ferrar dolerites, McMurdo Dry Valleys, Antarctica: Petrological, mineral-chemical and field evidence for channelized movement of crystals and melt. Journal of Petrolology 48, 2289–2326.

Berndt, J., Liebske, C., Holtz, F., Freise, M., Nowak, M., Ziegenbein, D., Hurkuck, W. & Koepke, J. (2002). A combined rapid-quench and H_2-membrane setup for internally heated pressure vessels: Description and application for water solubility in basaltic melts. American Mineralogist 87, 1717–1726.

Besson, P. & Poirier, J. P. (1994). The 3100 bp eruption of the Soufrière of Guadeloupe A transmission electron microscopy study of the cryptodome andesite. Bulletin of volcanology, 56(3), 184-192.

Bogaerts, M. & Schmidt, M.W. (2006). Experiments on silicate melt immiscibility in the system Fe_2SiO_4–$KAlSi_3O_8$–SiO_2–CaO–MgO–TiO_2–P_2O_5 and implications for natural magmas. Contributions to Mineralogy and Petrology 152, 257–274.

Bowes, D.R., Hamidullah, S. & Molyneux, T.G. (1997). Petrochemistry and petrogenesis of the Main and Upper Zones of the Bushveld Complex, Sekhukhuneland, Eastern Transvaal, South Africa. Utkal University Special Publication in Geology 2, 259-282.

Bowles F., Howie R., Vaughan D. & Zussman J. (2011). Rock-forming minerals: non-silicates: oxides, hydroxides and sulphides v. 5A. Geological Society, London.

Bown, M.G. & Gay, P. (1959). The identification of oriented inclusions in pyroxene crystals. American Mineralogist, 44(5-6), 592-602.

Buchanan, P.C., Reimold, W.U., Koebert, C. & Kruger, F.J. (2002). Geochemistry of intermediate to siliceous volcanic rocks of the Rooiberg Group, Bushveld Magmatic Province, South Africa. Contributions to Mineralogy and Petrology 144, 131–143.

Buddington, A.F. & Lindsley, D.H. (1964). Iron-titanium oxide minerals and syntetic equivalent. Journal of Petrology 5, 310–357.

Butcher, A.R. & Merkle, R.K.W. (1987). Postcumulus modification of magnetite grains in the upper zone of the Bushveld Complex, South Africa. Lithos 20, 247–260.

Cameron, E.N. (1978). The lower zone of the eastern Bushveld Complex in the Olifants River trough. Journal of Petrology, 19(3), 437-462.

Campbell, I.H. (1978). Some problems with the cumulus theory. Lithos 11, 311–323.

Candela, P.A. & Holland, H.D. (1984). The partitioning of copper and molybdenum between silicate melts and aqueous fluids. Geochimica et Cosmochimica Acta, 48(2), 373-380.

Canil, D. (1997). Vanadium partitioning and the oxidation state of Archaean komatiite magmas. Nature 389, 842–845.

Canil, D. (1999). Vanadium partitioning between orthopyroxene, spinel and silicate melt and the redox states of mantle source regions for primary magmas. Geochimica et Cosmochimica Acta 63(3), 557-572.

Canil, D. & Fedortchouk, Y. (2000). Clinopyroxene-liquid partitioning for vanadium and the oxygen fugacity during formation of cratonic and oceanic mantle lithosphere. Journal of Geophysical Research 105, 26003-26016.

Carr, H.W., & Groves, D.I. (1994). The importance of synmagmatic deformation in the formation of Merensky Reef potholes in the Bushveld Complex. Economic Geology, 89(6), 1398-1410.

Cawthorn, R.G. (2013a). The Residual or Roof Zone of the Bushveld Complex, South Africa. Journal of Petrology 54, 1875–1900.

Cawthorn, R.G. (2013b). Rare earth element abundances in apatite in the Bushveld Complex--A consequence of the trapped liquid shift effect. Geology 41, 603–606.

Cawthorn, R.G. (2014). Rare earth element abundances in apatite in the Bushveld Complex--A consequence of the trapped liquid shift effect: REPLY. Geology 42, e319–e319.

Cawthorn, R.G. (2015). The Bushveld Complex , South Africa. In: Charlier, B., Namur, O., Latypov, R., Tegner, C. (Eds.), Layered Intrusions. Springer Netherlands, pp. 517–587.

Cawthorn, R.G. & Ashwal, L.D. (2009). Origin of Anorthosite and Magnetitite Layers in the Bushveld Complex, Constrained by Major Element Compositions of Plagioclase. Journal of Petrology 50, 1607–1637.

Cawthorn, G., McCarthy, T.S. & Davies, G. (1983). Vertical chemical gradients in a single grain of magnetite from the Bushveld Complex, South Africa. Mineralogical Magazine 47, 27–34.

Cawthorn, R.G., Meyer, P.S. & Kruger, F.J. (1991). Major addition of magma at the pyroxenite marker in the western bushveld complex, South Africa. Journal of Petrology 32, 739–763.

Cawthorn, R.G. & Walraven, F., (1998). Emplacement and Crystallization Time for the Bushveld Complex. Journal of Petrology 39, 1669–1687.

Cawthorn, R.G. & Walsh, K.L. (1988). The use of phosphorus contents in yielding estimates of the proportion of trapped liquid in cumulates of the Upper Zone of the Bushveld Complex. Mineralogical Magazine 52, 81–89.

Cawthorn, R.G. & Webb, S.J. (2001). Connectivity between the western and eastern limbs of the Bushveld complex. Tectonophysics 330, 195–209.

Cawthorn, R.G., Barnes, S.J., Ballhaus, C. & Malitch, K.N. (2005). Platinum-Group Element , Chromium , and Vanadium Deposits in Mafic and Ultramafic Rocks. Economic Geology 100th anni, 215–249.

Champness, P. E., & Lorimer, G. W. (1976). Exsolution in silicates. In: Wenk, H.-R. (Ed.), Electron microscopy in mineralogy. Springer Heidelberg, pp. 174 - 204.

Charlier, B. & Grove, T.L. (2012). Experiments on liquid immiscibility along tholeiitic liquid lines of descent. Contributions to Mineralogy and Petrology 164, 27–44.

Charlier, B., Namur, O. & Grove, T.L. (2013). Compositional and kinetic controls on liquid immiscibility in ferrobasalt-rhyolite volcanic and plutonic series. Geochimica et Cosmochimica Acta 113, 79–93.

Charlier, B., Namur, O., Toplis, M.J., Schiano, P., Cluzel, N., Higgins, M.D. & Auwera, J. V. (2011). Large-scale silicate liquid immiscibility during differentiation of tholeiitic basalt to granite and the origin of the Daly gap. Geology 39, 907–910.

Chung, H.Y. & Mungall, J.E. (2009). Physical constraints on the migration of immiscible fluids through partially molten silicates, with special reference to magmatic sulfide ores. Earth and Planetary Science Letters 286, 14–22.

Connolly, C. & Burnett, D.S. (1999). A study of the minor element concentrations of spinels from two type B calcium-aluminum-rich inclusions : An investigation into pottmtial formation conditions of calcium-aluminum-rich inclusions. Meteoritics & Planetary Science 34, 829–848.

Copley, P.A., Champness, P.E. & Lorimer, G. W. (1974). Electron petrography of exsolution textures in an iron-rich clinopyroxene. Journal of Petrology, 15(1), 41-57.

Czamanske, G.K. & Bohlen, S.R. (1990). The Stillwater Complex and its anorthosites: an accident of magmatic underplating? American Mineralogist 75, 37–45.

Dare, S.A.S., Barnes, S. & Beaudoin, G. (2012). Variation in trace element content of magnetite crystallized from a fractionating sulfide liquid , Sudbury , Canada : Implications for provenance discrimination. Geochimica et Cosmochimica Acta 88, 27–50.

Dare, S.A.S., Barnes, S.J., Beaudoin, G., Méric, J., Boutroy, E. & Potvin-Doucet, C. (2014). Trace elements in magnetite as petrogenetic indicators. Mineralium Deposita 49, 785–796.

Davidson, P.M. & Lindsley, D.H., (1985). Thermodynamic analysis of quadrilateral pyroxenes. Contributions to Mineralogy and Petrology 91, 390-404.

Davies, G. & Cawthorn, R.G. (1984). Mineralogical Data on a Multiple Intrusion in the Rustenburg Layered Suite of the Bushveld Complex. Mineralogical Magazine 48(349), 469-480

Davies, G., Cawthorn, R.G., Barton, J.M. & Morton, M. (1980). Parental magma to the Bushveld complex. Nature 287, 33–35.

Deer, W.A., Howie, R.A. & Zussman, J. (1992). An introduction to the rock-forming minerals. Longman Group Ltd, New York.

Devouard, B., Pósfai, M., Hua, X., Bazylinski, D.A., Frankel, R.B. & Buseck, P.R. (1998). Magnetite from magnetotactic bacteria: Size distributions and twinning. American Mineralogist 83, 1387–1398.

Dixon, S. & Rutherford, M.J., (1979). Plagiogranites as late-stage immiscible liquids in ophiolite and mid-ocean ridge suites: an experimental study. Earth and Planetary Science Letters 45, 45–60.

Doukhan, N., Ingrin, J., Doukhan, J.C. & Latrous, K. (1990). Coprecipitation of magnetite and amphibole in black star diopside; a TEM study. American Mineralogist, 75(7-8), 840-846.

Duchesne, J.-C., Charlier, B. & Vander Auwera, J. (2007). Empirical calibration of the V partitioning between magnetite and ilmenite as an oxybarometer. Eos, Transactions American Geophysical Union 88.

Duke, J.M. (1976). Distribution of the Period Four Transition Elements among Olivine , Calcic Clinopyroxene and Mafic Silicate Liquid : Experimental Results. Journal of Petrology 17, 499–521.

Duran, C.J., Barnes, S.J. & Corkery, J.T. (2016). Trace element distribution in primary sulfides and Fe-Ti oxides from the sulfide-rich pods of the Lac des Iles Pd deposits, Western Ontario, Canada: Constraints on processes controlling the composition of the ore and the use of pentlandite compositions in exploration. Journal of Geochemical Exploration 166, 45–63.

Eales, H.V. (2002). Caveats in defining the magmas parental to the mafic rocks of the Bushveld Complex, and the manner of their emplacement: review and commentary. Mineralogical Magazine 66(6), 815-832.

Eales, H.V. & Cawthorn, R.G. (1996). The Bushveld Complex. Developments in Petrology 15, 181–229.

Feinberg, J.M., Wenk, H.R., Renne, P.R. & Scott, G.R. (2004). Epitaxial relationships of clinopyroxene-hosted magnetite determined using electron backscatter diffraction (EBSD) technique. American Mineralogist, 89(2-3), 462-466.

Fischer, L.A., Wang, M., Charlier, B., Namur, O., Roberts, R.J., Veksler, I.V., Cawthorn, R.G. & Holtz, F. (2016). Immiscible iron- and silica-rich liquids in the Upper Zone of the Bushveld Complex. Earth and Planetary Science Letters 443, 108–117.

Fischer, L.A. & Yuan, Q. (2016). Fe-Ti-V-(P) Resources in the Upper Zone of the Bushveld Complex, South Africa. Papers and Proceedings of the Royal Society of Tasmania 150, 15-22.

Fleet, M.L., Bilcox, G.A. & Barnett, R.L. (1980). Oriented magnetite inclusions in pyroxenes from the Grenville Province. The Canadian Mineralogist, 18(1), 89-99.

Fletcher, W.K. & Wolcott, J. (1991). Transport of magnetite and gold in Harris Creek, British Columbia, and implications for exploration. Journal of Geochemical Exploration 41, 253–274.

Freer, R. & Hauptman, Z. (1978). An experimental study of magnetite-titanomagnetite interdiffusion. Physics of the Earth and Planetary Interiors 16, 223–231.

Freise, M., Holtz, F., Nowak, M., Scoates, J.S. & Strauss, H. (2009). Differentiation and crystallization conditions of basalts from the Kerguelen large igneous province: An experimental study. Contributions to Mineralogy and Petrology 158, 505–527.

Frost, B. R. & Lindsley, D.H. (1991). Occurrence of iron-titanium oxides in igneous rocks. Reviews in Mineralogy and Geochemistry 25(1), 433-468.

Ganino, C., Arndt, N.T., Zhou, M.F., Gaillard, F. & Chauvel, C. (2008). Interaction of magma with sedimentary wall rock and magnetite ore genesis in the Panzhihua mafic intrusion, SW China. Mineralium Deposita, 43(6), 677.

Garzanti, E., Andò, S., France-Lanord, C., Vezzoli, G., Censi, P., Galy, V. & Najman, Y. (2010). Mineralogical and chemical variability of fluvial sediments1. Bedload sand (Ganga–Brahmaputra, Bangladesh). Earth and Planetary Science Letters 299, 368–381.

Geßmann, C.K. & Rubie, D.C. (1998). The effect of temperature on the partitioning of nickel, cobalt, manganese, chromium, and vanadium at 9 GPa and constraints on formation of the Earth's core. Geochimica et Cosmochimica Acta 62, 867–882.

Ghiorso, M.S. & Evans, B.W. (2008). Thermodynamics of rhombohedral oxide solid solutions and a revision of the Fe-Ti two-oxide geothermometer and oxygen-barometer. American Journal of science 308, 957–1039.

Ghiorso, M.S. & Gualda, G.A.R. (2015). An H_2O–CO_2 mixed fluid saturation model compatible with rhyolite-MELTS. Contributions to Mineralogy and Petrology 169, 1–30.

Ghiorso, M.S. & Sack, R.O. (1995). Chemical mass transfer in magmatic processes IV. A revised and internally consistent thermodynamic model for the interpolation and extrapolation of liquid-solid equilibria in magmatic systems at elevated temperatures and pressures. Contributions to Mineralogy and Petrology 119, 197–212.

Giuli, G., Paris, E., Mungall, J., Romano, C., & Dingwell, D. (2004). V oxidation state and coordination number in silicate glasses by XAS. American Mineralogist, 89(11-12), 1640-1646.

Green, T.H. & Watson, E.B. (1982). Crystallization of apatite in natural magmas under high pressure, hydrous conditions, with particular reference to "Orogenic" rock series. Contributions to Mineralogy and Petrology 79, 96–105.

Grove, T.L., Baker, M.B. & Kinzler, R.J. (1984). Coupled CaAl-NaSi diffusion in plagioclase feldspar: Experiments and applications to cooling rate speedometry. Geochimica et Cosmochimica Acta 48, 2113–2121.

Grove, T.L. & Juster, T.C. (1989). Experimental investigations of low-Ca pyroxene stability and olivine-pyroxene-liquid equilibria at 1-atm in natural basaltic and andesitic liquids. Contributions to Mineralogy and Petrology 103, 287–305.

Gualda, G.A.R., Ghiorso, M.S., Lemons, R. V. & Carley, T.L. (2012). Rhyolite-MELTS: A modified calibration of MELTS optimized for silica-rich, fluid-bearing magmatic systems. Journal of Petrology 53, 875–890.

Haggerty, S. E. (1991). Oxide textures; a mini-atlas. Reviews in Mineralogy and Geochemistry 25(1), 129-219.

Hamilton, J. (1977). Sr isotope and trace element studies of the Great Dyke and Bushveld mafic phase and their relation to early Proterozoic magma genesis in southern Africa. Journal of Petrology 18, 24–52.

Hammond, P.A. & Taylor, L.A. (1982). The ilmenite/titano-magnetite assemblage: kinetics of re-equilibration. Earth and Planetary Science Letters, 61(1), 143-150.

Harmer, R.E. & Sharpe, M.R. (1985). Field relations and strontium isotope systematics of the marginal rocks of the eastern Bushveld complex. Economic Geology 80, 813–837.

Harney, D.M., Merkle, R.K. & von Gruenewaldt, G. (1990). Platinum-group element behavior in the lower part of the upper zone, eastern Bushveld Complex; implications for the formation of the main magnetite layer. Economic Geology, 85(8), 1777-1789.

Harrison, T.M. & Bruce, E. (1984). The behavior of apatite during crnstal anatexis : Equilibrium and kinetic considerations. Geochimica et Cosmochimica Acta 48, 1467–1477.

Hart, S.R. & Dunn, T. (1993). Experimental cpx/melt partitioning of 24 trace elements. Contributions to Mineralogy and Petrology 113, 1–8.

Hatton, C.J. & Schweitzer, J.K. (1995). Evidence for synchronous extrusive and intrusive Bushveld magmatism. Journal of African Earth Sciences 21, 579–594.

Hauri, E.H., Wagner, T.P. & Grove, T.L. (1994). Experimental and natural partitioning of Th, U, Pb and other trace elements between garnet, clinopyroxene and basaltic melts. Chemical Geology 117, 149–166.

Hayes, B., Ashwal, L.D., Webb, S.J., Bybee, G.M. & Hayes, B. (2017). Large-scale magmatic layering in the Main Zone of the Bushveld Complex and episodic downward magma infiltration. Contributions to Mineralogy and Petrology, 172(2-3), 13.

Herd, C.D.K. (2006). Insights into the redox history of the NWA 1068/1110 martian basalt from mineral equilibria and vanadium oxybarometry. American Mineralogist 91, 1616–1627.

Herd, C.D.K., Papike, J.J. & Brearley, A.J. (2001). Oxygen fugacity of martian basalts from electron microprobe oxygen and TEM-EELS analyses of Fe-Ti oxides. American Mineralogist 86, 1015–1024.

Herd, C.D.K., Schwandt, C.S., Jones, J.H. & Papike, J. (2002). An experimental and petrographic investigation of Elephant Moraine 79001 lithology A: Implications for its petrogenesis and the partitioning of chromium and vanadium in a martian basalt. Meteoritics & Planetary Science 37, 987–1000.

Hess, H. H. (1941). Pyroxenes of common mafic magmas. Part 1. American Mineralogist, 26(9), 515-535.

Hirschler, A., Lucas, J. & Hubert, J.-C. (1990). Bacterial involvement in apatite genesis. FEMS Microbiology Letters 73, 211–220.

Hirschmann, M.M., Ghiorso, M.S., Davis, F.A., Gordon, S.M., Mukherjee, S., Grove, T.L., Krawczynski, M., . Medard, E. & Till, C.B. (2008). Library of Experimental Phase Relations (LEPR): A database and Web portal for experimental magmatic phase equilibria data. Geochemistry, Geophysics, Geosystems 9(3).

Holloway, J.R., Pan, V. & Gudmundsson, G. (1992). High-Pressure Fluid-Absent Melting Experiments in the Presence of Graphite - Oxygen Fugacity, Ferric Ferrous Ratio and Dissolved CO_2. European Journal of Mineralogy 4, 105–114.

Horn, I., Foley, S., Jackson, S.E. & Jenner, G.A. (1994). Experimentally determined partitioning of high field strength- and selected transition elements between spinel and basaltic melt. Chemical Geology 117, 193–218.

Hövelmann, S. (2014). Experiments on the late-stage evolution of basalts in the Bushveld Complex. MSc Thesis, Universität Hannover.

Husen, A., Almeev, R.R. & Holtz, F. (2016). The effect of H_2O and pressure on multiple saturation and liquid lines of descent in basalt from the Shatsky Rise. Journal of Petrology, 57(2), 309-344.

Irvine, T. N. (1975). Crystallization sequences in the Muskox intrusion and other layered intrusions—II. Origin of chromitite layers and similar deposits of other magmatic ores. Geochimica et Cosmochimica Acta, 39(6-7).

Irvine, T.N. (1982). Terminology for Layered Intrusions. Journal of Petrology 23, 127–162.

Jakobsen, J.K., Veksler, I.V., Tegner, C. & Brooks, C.K. (2005). Immiscible iron- and silica-rich melts in basalt petrogenesis documented in the Skaergaard intrusion. Geology 33, 885.

Jakobsen, J.K., Veksler, I. V., Tegner, C. & Brooks, C.K. (2011). Crystallization of the Skaergaard Intrusion from an Emulsion of Immiscible Iron- and Silica-rich Liquids: Evidence from Melt Inclusions in Plagioclase. Journal of Petrology 52, 345–373.

Jenner, F.E. & O'Neill, H.S.C. (2012). Analysis of 60 elements in 616 ocean floor basaltic glasses. Geochemistry, Geophysics, Geosystems 13, 1–11.

Jenner, G.A., Foley, S., Jackson, S.E., Green, T.H., Fryer, B.J. & Longrich, H.P. (1994). Determination of partition coefficients for trace elements in high pressure-temperature experimental run products by laser ablation microprobe-inductively coupled plasma-mass spectrometry (LAM-ICP-MS). Geochimica et Cosmochimica Acta 58, 5099–5103.

Junge, M., Oberthür, T. & Melcher, F. (2014). Cryptic variation of chromite chemistry, platinum group element and platinum group mineral distribution in the UG-2 chromitite: An example from the karee mine, western Bushveld complex, South Africa. Economic Geology 109, 795–810.

Juster, T.C., Grove, T.L., & Perfit, M.R., (1989). Experimental constraints on the generation of FeTi basalts, andesites, and rhyodacites at the Galapagos spreading center, 85°W and 95°W: Journal of Geophysical Research 94, B7, p. 9251-9274.

Kamenetsky, V.S., Charlier, B., Zhitova, L., Sharygin, V., Davidson, P. & Feig, S.T. (2013). Magma chamber-scale liquid immiscibility in the siberian traps represented by melt pools in native iron. Geology 41, 1091–1094.

Karner, J.M., Papike, J.J., Shearer, C.K., McKay, G., Le, L. & Burger, P. (2007). Valence state partitioning of Cr and V between pyroxene-melt : Estimates of oxygen fugacity for martian basalt QUE 94201. American Mineralogist 92, 1238–1241.

Karner, J.M., Papike, J.J., Sutton, S.R., Shearer, C.K., Burger, P., Kay, G.M.C. & Le, L. (2008). Valence state partitioning of V between pyroxene-melt : Effects of pyroxene and melt composition , and direct determination of V valence states by XANES. Application to Martian basalt QUE 94201 composition. Meteoritics & Planetary Science 43, 1275–1285.

Karner, J.M., Sutton, S.R., Papike, J.J., Shearer, C.K., Jones, J.H. & Newville, M. (2006). Application of a new vanadium valence oxybarometer to basaltic glasses from the Earth, Moon, and Mars. American Mineralogist 91, 270–277.

Kawai, N., Kume, S., & Sasajima, S. (1954). Magnetism of rocks and solid phase transformation in ferromagnetic minerals. Proceedings of the Japan Academy, 30(7), 588-593.

Kgaswane, E.M., Nyblade, A. a., Durrheim, R.J., Julià, J., Dirks, P.H.G.M. & Webb, S.J. (2012). Shear wave velocity structure of the Bushveld Complex, South Africa. Tectonophysics 554–557, 83–104.

Kilinc, A., Carmichael, I.S.E., Rivers, M.L. & Sack, R.O. (1983). The ferric-ferrous ratio of natural silicate liquids equilibrated in air. Contributions to Mineralogy and Petrology 83, 136–140.

Kinnaird, J.A., Hutchinson, D., Schurmann, L., Nex, P. a M. & de Lange, R. (2005). Petrology and mineralisation of the southern Platreef: Northern limb of the Bushveld Complex, South Africa. Mineralium Deposita 40, 576–597.

Kinzler, R.J. (1997). Melting of mantle peridotite at pressures approaching the spinel to garnet transition: Application to mid-ocean ridge basalt petrogenesis. Journal of Geophysical Research: Solid Earth, 102(B1), 853-874.

Klemm, D.D., Ketterer, S., Reichhardt, F., Steindl, J. & Weber-Diefenbach, K. (1985). Implication of vertical and lateral compositional variations across the pyroxene marker and its associated rocks in the upper part of the main zone in the eastern Bushveld complex. Economic Geology 80, 1007–1015.

Kruger, F.J. (1992). The origin of the Merensky cyclic unit: Sr-isotopic and mineralogical evidence for an alternative orthomagmatic model. Australian Journal of Earth Sciences 39, 255–261.

Kruger, F.J. (1994). The Sr-isotopic stratigraphy of the western Bushveld Complex. South African Journal of Geology 97, 393–398.

Kruger, F.J., Cawthorn, R.G. & Walsh, K.L. (1987). Strontium isotopic evidence against magma addition in the Upper Zone of the Bushveld Complex. Earth and Planetary Science Letters 84, 51–58.

Kruger, F.J. & Smart, R. (1987). Diffusion of trace elements during bottom crystallization of double-diffusive convection systems: the magnetitite layers of the Bushveld Complex. Journal of Volcanology and Geothermal Research, 34(1-2), 133-142.

Lally, J.S., Heuer, A.H., Nord, G. L. & Christie, J.M. (1975). Subsolidus reactions in lunar pyroxenes: an electron petrographic study. Contributions to Mineralogy and Petrology, 51(4), 263-281.

Lattard, D. (1995). Experimental evidence for the exsolution of ilmenite from titaniferous spinel. American Mineralogist 80(9-10), 968-981.

Latypov, R. (2009). Testing the validity of the petrological hypothesis "no phenocrysts, no post-emplacement differentiation". Journal of Petrology 50, 1047–1069.

Laubier, M., Grove, T.L. & Langmuir, C.H. (2014). Trace element mineral / melt partitioning for basaltic and basaltic andesitic melts : An experimental and laser ICP-MS study with application to the oxidation state of mantle source regions. Earth and Planetary Science Letters 392, 265–278.

Lindsley, D.H. (1981). Some experiments pertaining to the magnetite-ulvospinel miscibility gap. American Mineralogist, 66(7-8), 759-762.

Lindsley, D.H. & Andersen, D.J. (1983). A two-pyroxene thermometer. Journal of Geophysical Research 88, A887–A906.

Lindstrom, D.J. (1976). Experimental study of the partitioning of the transition metals between clinopyroxene and coexisting silicate liquids. PhD Thesis, University of Oregon.

Lipin, B.R. (1993). Pressure increases, the formation of chromite seams, and the development of the ultramafic series in the Stillwater Complex, Montana. Journal of Petrology, 34(5), 955-976.

Liu, P.-P., Zhou, M.-F., Chen, W.T., Boone, M. & Cnudde, V. (2014). Using Multiphase Solid Inclusions to Constrain the Origin of the Baima Fe-Ti-(V) Oxide Deposit, SW China. Journal of Petrology 55, 951–976.

Liu, Y., Hu, Z., Gao, S., Günther, D., Xu, J., Gao, C. & Chen, H. (2008). In situ analysis of major and trace elements of anhydrous minerals by LA-ICP-MS without applying an internal standard. Chemical Geology 257, 34–43.

Maier, W.D., Arndt, N.T. & Curl, E.A. (2000). Progressive crustal contamination of the Bushveld Complex: evidence from Nd isotopic analyses of the cumulate rocks. Contributions to Mineralogy and Petrology 140, 316–327.

Maier, W.D., Barnes, S.J., Gartz, V. & Andrews, G. (2003). Pt-Pd reefs in magnetitites of the Stella layered intrusion, South Africa: A world of new exploration opportunities for platinum group elements. Geology 31, 885–888.

Maier, W.D., Barnes, S. & Groves, D.I. (2013). The Bushveld Complex, South Africa: formation of platinum–palladium, chrome- and vanadium-rich layers via hydrodynamic sorting of a mobilized cumulate slurry in a large, relatively slowly cooling, subsiding magma chamber. Mineralium Deposita 48, 1–56.

Maier, W.D., Barnes, S.J. & Van Der Merwe, M.J. (2001). Platinum-group elements in the Pyroxenite Marker, Bushveld Complex: Implications for the formation of the Main Zone. South African Journal of Geology 104, 301–308.

Mallmann, G. & O'Neill, H.S.C. (2009). The crystal/melt partitioning of V during mantle melting as a function of oxygen fugacity compared with some other elements (Al, P, Ca, Sc, Ti, Cr, Fe, Ga, Y, Zr and Nb). Journal of Petrology 50, 1765–1794.

Marsh, B.D. (2004). A magmatic mush column rosetta stone: The McMurdo Dry Valleys of Antarctica. Eos, Transactions American Geophysical Union 85, 497.

Marsh, B.D. (2013). On some fundamentals of igneous petrology. Contributions to Mineralogy and Petrology 166, 665–690.

Martin, B. & Kushiro, I. (1991). Immiscibility synthesis as an indication of cooling rates of basalts. Journal of Volcanology and Geothermal Research 45, 289–310.

Mathez, E.A., VanTongeren, J.A. & Schweitzer, J. (2013). On the relationships between the Bushveld Complex and its felsic roof rocks, part 1: Petrogenesis of Rooiberg and related felsites. Contributions to Mineralogy and Petrology 166, 435–449.

Mathison, C.I. & Ahmat, A. L. (1996). The Windimurra Complex, Western Australia. In Cawthorn, R.G. (ed.), Layered intrusions: Amsterdam, Elsevier, p. 485–510.

McCarthy, T.S., Cawthorn, R.G., Wright, C.J. & McIver, J.R. (1985). Mineral layering in the Bushveld Complex; implications of Cr abundances in magnetite from closely spaced magnetitite and intervening silicate-rich layers. Economic Geology 80, 1062–1074.

McDonald, I. & Holwell, D.A. (2007). Did lower zone magma conduits store PGE-rich sulphides that were later supplied to the Platreef? South African Journal of Geology, 110(4), 611-616.

Molyneux, T.G. (1974). A geological investigation of the Bushveld Complex in Sekhukhuneland and part of the Steelpoort valley. South African Journal of Geology 77, 329–338.

Morse, S.A. (1975). Plagioclase lamellae in hypersthene, Tikkoatokhakh Bay, Labrador. Earth and Planetary Science Letters, 26(3), 331-336.

Mücke, A. (2003). Magnetite, ilmenite and ulvite in rocks and ore deposits: petrography, microprobe analyses and genetic implications. Mineralogy and Petrology 77(3), 215-234.

Mungall, J.E. & Su, S. (2005). Interfacial tension between magmatic sulfide and silicate liquids: Constraints on kinetics of sulfide liquation and sulfide migration through silicate rocks. Earth and Planetary Science Letters 234, 135–149.

Nadoll, P. & Koenig, A.E. (2011). LA-ICP-MS of magnetite: methods and reference materials. Journal of Analytical Atomic Spectrometry, 26(9), 1872-1877.

Namur, O., Charlier, B., Toplis, M.J., Higgins, M.D., Liégeois, J.P. & Vander Auwera, J., (2010). Crystallization sequence and magma chamber processes in the ferrobasaltic Sept Iles layered intrusion, Canada. Journal of Petrology 51, 1203–1236.

Namur, O., Charlier, B., Pirard, C., Hermann, J., Liégeois, J.-P. & Vander Auwera, J. (2011). Anorthosite formation by plagioclase flotation in ferrobasalt and implications for the lunar crust. Geochimica et Cosmochimica Acta 75, 4998–5018.

Namur, O., Charlier, B. & Holness, M.B. (2012). Dual origin of Fe-Ti-P gabbros by immiscibility and fractional crystallization of evolved tholeiitic basalts in the Sept Iles layered intrusion. Lithos 154, 100–114.

Namur, O., Abily, B., Boudreau, A.E., Blanchette, F., Bush, J.W.M., Ceuleneer, G., Charlier, B., Donaldson, C.H., Duchesne, J.-C., Higgins, M.D., Morata, D., Nielsen, T.F.D., O'Driscoll, B., Pang, K.N., Peacock, T., Spandler, C.J., Toramaru, A. & Veksler, I. V. (2015). Igneous Layering in Basaltic Magma Chambers. In: Charlier, B., Namur, O., Latypov, R., Tegner, C. (Eds.), Layered Intrusions. Springer Netherlands, pp. 75–152.

Newberry, N.G., Peacor, D.R., Essene, E.J. & Geissman, J.W. (1982). Silicon in magnetite: High resolution microanalysis of magnetite-ilmenite intergrowths. Contributions to Mineralogy and Petrology 80, 334–340.

Nicholls, J., Carmichael, I.S.E. & Stormer, J.C. (1971). Silica activity and P total in igneous rocks. Contributions to Mineralogy and Petrology 33, 1–20.

Nystrom, J.O. & Henriquez, F. (1994). Magmatic features of iron ores of the Kiruna type in Chile and Sweden: ore textures and magnetite geochemistry. Economic Geology 89, 820–839.

O'Neill, H.S.C. & Eggins, S.M. (2002). The effect of melt composition on trace element partitioning: an experimental investigation of the activity coefficients of FeO, NiO, CoO, MoO 2 and MoO 3 in silicate melts. Chemical Geology, 186(1), 151-181.

Owens, B.E. & Dymek, R.F. (1992). Fe-Ti-P-rich rocks and massif anorthosite; problems of interpretation illustrated from the Labrieville and St-Urbain plutons, Quebec. The Canadian Mineralogist, 30(1), 163-190.

Pang, K., Li, C., Zhou, M. & Ripley, E.M. (2009). Mineral compositional constraints on petrogenesis and oxide ore genesis of the late Permian Panzhihua layered gabbroic intrusion, SW China. Lithos 110, 199–214.

Panjasawatwong, Y., Danyushevsky, L. V, Crawford, A.J. & Harris, K.L. (1995). An Experimental-Study of the Effects of Melt Composition on Plagioclase - Melt Equilibria at 5-Kbar and 10-Kbar - Implications for the Origin of Magmatic High-an Plagioclase. Contributions to Mineralogy and Petrology 118, 420–432.

Papike, J.J., Burger, P., Bell, A.S., Shearer, C.K., Le, L., Jones, J. & Provencio, P. (2014). Valence state partitioning of V between pyroxene and melt for martian melt compositions Y 980459 and QUE 94201 : The effect of pyroxene composition and crystal structure. American Mineralogist 99, 1175–1178.

Papike, J.J., Burger, P. V., Bellll, A.S., Le, L., Shearer, C.K., Sutton, S.R., Jones, J. & Newvilllle, M. (2013). Developing vanadium valence state oxybarometers (spinel-melt, olivine-melt, spinel-olivine) and V/(Cr+Al) partitioning (spinel-melt) for martian olivine-phyric basalts. American Mineralogist 98, 2193–2196.

Pearce, N.J.G., Perkins, W.T., Westgate, J.A., Gorton, M.P., Jackson, S.E., Neal, C.R. & Chenery, S.P. (1997). A compilation of new and published major and trace element data for NIST SRM 610 and NIST SRM 612 glass reference materials. Geostandards and Geoanalytical Research 21, 115–144.

Philpotts, A.R. (1982). Compositions of immiscible liquids in volcanic rocks. Contributions to Mineralogy and Petrology 80, 201–218.

Phinney, W.C. (1992). Partition coefficients for iron between plagioclase and basalt as a function of oxygen fugacity: Implications for Archean and lunar anorthosites. Geochimica et Cosmochimica Acta 56, 1885–1895.

Pouchou, J. & Pichoir, F. (1991). Quantitative Analysis of Homogeneous or Stratified Microvolumes Applying the Model "PAP,". In: Heinrich, K.F.J., Newbury, D.E. (Eds.), Electron Probe Quantitation. Plenum Press, New York, pp. 31–75.

Price, G. D. (1980). Exsolution microstructures in titanomagnetites and their magnetic significance. Physics of the Earth and Planetary Interiors 23(1), 2-12.

Price, G. D. (1981). Subsolidus phase relations in the titanomagnetite solid solution series. American Mineralogist 66, 751- 758.

Pucher, R. (1969). On the oxidation and reduction of natural magnetites. Geophysical Journal International 18(5), 489-497.

Putirka, K. (1999). Clinopyroxene + liquid equilibria to 100 kbar and 2450 K. Contributions to Mineralogy and Petrology 135, 151–163.

Putirka, K.D. (2005). Igneous thermometers and barometers based on plagioclase + liquid equilibria: Tests of some existing models and new calibrations. American Mineralogist 90, 336–346.

Putirka, K.D. (2008). Thermometers and Barometers for Volcanic Systems. Reviews in Mineralogy and Geochemistry 69, 61–120.

Raedeke, L.D. (1982). Petrogenesis of the Stillwater Complex. PhD Thesis, University of Washington.

Reynolds, I.M. (1985a). Contrasted mineralogy and textural relationships in the uppermost titaniferous magnetite layers of the Bushveld complex in the Bierkraal area north of Rustenburg. Economic Geology 80(4), 1027-1048.

Reynolds, I.M. (1985b). The nature and origin of titaniferous magnetite-rich layers in the upper zone of the Bushveld Complex; a review and synthesis. Economic Geology 80, 1089–1108.

Rhodes, J.M., Dungan, M.A., Blanchard, D.P. & Long, P.E. (1979). Magma mixing at mid-ocean ridges: Evidence from basalts drilled near 22° N on the Mid-Atlantic Ridge. Tectonophysics 55, 35–61.

Righter, K., Leeman, W.P. & Hervig, R.L. (2006). Partitioning of Ni , Co and V between spinel-structured oxides and silicate melts : Importance of spinel composition. Chemical Geology 227, 1–25.

Righter, K., Pando, K.M., Danielson, L. & Lee, C.T. (2010). Partitioning of Mo, P and other siderophile elements (Cu, Ga, Sn, Ni, Co, Cr, Mn, V, and W) between metal and silicate melt as a function of temperature and silicate melt composition. Earth and Planetary Science Letters, 291(1), 1-9.

Riker, J.M., Cashman, K. V., Rust, A.C. & Blundy, J.D. (2015). Experimental constraints on plagioclase crystallization during H_2O- and H_2O-CO_2-saturated magma decompression. Journal of Petrology 56, 1967–1998.

Robinson, P., Jaffe, H.W., Ross, M. & Klein, C. (1971). Orientation of exsolution lamellae in clinopyroxenes and clinoamphiboles: consider- ation of optimal phaseboundaries. American Mineralogist, 56(5-6), 909.

Roeder, P.L. & Osborn, E.F. (1966). Experimental data for the system MgO-FeO-Fe_2O_3-$CaAl_2Si_2O_8$-SiO_2 and their petrologic implications. American Journal of Science 264, 428–480.

Roelofse, F. & Ashwal, L.D. (2012). The Lower Main Zone in the Northern Limb of the Bushveld Complex - A >1.3 km Thick Sequence of Intruded and Variably Contaminated Crystal Mushes. Journal of Petrology 53, 1449–1476.

Roelofse, F., Ashwal, L.D. & Romer, R.L. (2015). Multiple, isotopically heterogeneous plagioclase populations in the Bushveld Complex suggest mush intrusion. Chemie der Erde - Geochemistry 75, 357–364.

Ross, M. & Huebner, J.S. (1979). Temperature-composition relationships between naturally occurring augite, pigeonite, and orthopyroxene at one bar pressure. Am Mineral, 64, 1133-1155.

Rudnick, R.L. & Gao, S. (2003). Composition of the Continental Crust. In: Holland, H.D., Turekian, K.K. (Eds.), Treatise on Geochemistry. Pergamon, Oxford, pp. 1–64.

SACS (South African Committee for Stratigraphy) (1980). Lithostratigraphy of the Republic of South Africa, South West Africa/Namibia, and the Republics of Bophuthatswana, Transkei and Venda. In: Kent, L.E. (ed.) Stratigraphy of South Africa, Part 1. Geological Survey of South Africa, p. 690.

Sauerzapf, U., Lattard, D., Burchard, M. & Engelmann, R. (2008). The titanomagnetite-ilmenite equilibrium: New experimental data and thermo-oxybarometric application to the crystallization of basic to intermediate rocks. Journal of Petrology 49, 1161–1185.

Schnetzler, C.C. & Philpotts, J.A. (1970). Partition coefficients of rare-earth elements between igneous matrix material and rock-forming mineral phenocrysts-II. Geochimica et Cosmochimica Acta 34, 331–340.

Schuth, S., Horn, I., Brüske, A., Wolff, P.E. & Weyer, S. (2017). First vanadium isotope analyses of V-rich minerals by femtosecond laser ablation and solution-nebulization MC-ICP-MS. Ore Geology Reviews, 81, 1271-1286.

Schweitzer, J.K., Hatton, C.J. & De Waal, S.A. (1997). Link between the granitic and volcanic rocks of the Bushveld Complex, South Africa. Journal of African Earth Sciences 24, 95–104.

Scoon, R.N. & Mitchell, A.A. (1994). Discordant iron-rich ultramafic pegmatites in the bushveld complex and their relationship to iron-rich intercumulus and residual liquids. Journal of Petrology 35, 881–917.

Scoon, R.N. & Mitchell, A.A. (2012). The Upper Zone of the Bushveld Complex at Roossenekal, South Africa: Geochemical stratigraphy and evidence of multiple episodes of magma replenishment. South African Journal of Geology 115, 515–534.

Scoon, R.N. & Mitchell, A.A. (2014). Discussion of "The Bushveld Complex, South Africa: Formation of platinum-palladium, chrome- and vanadium-rich layers via hydrodynamic sorting of a mobilized cumulate slurry in a large, relatively slowly cooling, subsiding magma chamber" by Maier et al. (2013) Mineralium Deposita 48, 1-56. Mineralium Deposita 49, 399–404.

Sievwright, R.H., Wilkinson, J.J., O'Neill, H.S.C. & Berry, A.J. (2017). Thermodynamic controls on element partitioning between titanomagnetite and andesitic – dacitic silicate melts. Contributions to Mineralogy and Petrology 172, 1–33.

Sisson, T.W. & Grove, T.L. (1993). Experimental investigations of the role of H_2O in calc-alkaline differentiation and subduction zone magmatism. Contributions to Mineralogy and Petrology 113, 143–166.

Skulski, T., Minarik, W. & Watson, E.B. (1994). High-pressure experimental trace-element partitioning between clinopyroxene and basaltic melts. Chemical Geology 117, 127–147.

Song, X.-Y., Qi, H.-W., Hu, R.-Z., Chen, L.-M., Yu, S.-Y. & Zhang, J.-F. (2013). Formation of thick stratiform Fe-Ti oxide layers in layered intrusion and frequent replenishment of fractionated mafic magma: Evidence from the Panzhihua intrusion, SW China. Geochemistry, Geophysics, Geosystems 14, 712–732.

Spencer, K.J. & Lindsley, D.H. (1981). A solution model for coexisting Fe-Ti oxides. American Mineralogist 66, 1189–1201.

Tacker, R.C. & Candela, P.A. (1987). Partitioning of molybdenum between magnetite and melt; a preliminary experimental study of partitioning of ore metals between silicic magmas and crystalline phases. Economic Geology, 82(7), 1827-1838.

Tan, W., Liu, P., He, H., Wang, C. Y. & Liang, X. (2017). Mineralogy and origin of exsolution in Ti-rich magnetite from different magmatic Fe-Ti oxide-bearing intrusions. The Canadian Mineralogist 54(3), 539-553.

Tanner, D., Mavrogenes, J. a., Arculus, R.J. & Jenner, F.E. (2014). Trace Element Stratigraphy of the Bellevue Core, Northern Bushveld: Multiple Magma Injections Obscured by Diffusive Processes. Journal of Petrology 55, 859–882.

Tegner, C. & Cawthorn, R.G. (2010). Iron in plagioclase in the Bushveld and Skaergaard intrusions: Implications for iron contents in evolving basic magmas. Contributions to Mineralogy and Petrology 159, 719–730.

Tegner, C., Cawthorn, R.G. & Kruger, F.J. (2006). Cyclicity in the Main and Upper Zones of the Bushveld Complex, South Africa: Crystallization from a Zoned Magma Sheet. Journal of Petrology 47, 2257–2279.

Thy, P., Lesher, C.E. & Tegner, C. (2009). The Skaergaard liquid line of descent revisited. Contributions to Mineralogy and Petrology 157, 735–747.

Toplis, M.J. & Carroll, M.R. (1995). An Experimental Study of the Influence of Oxygen Fugacity on Fe-Ti Oxide Stability, Phase Relations, and Mineral- Melt Equilibria in Ferro-Basaltic Systems. Journal of Petrology 36, 1137–1170.

Toplis, M.J. & Carroll, M.R. (1996). Differentiation of Ferro-Basaltic Magmas under Conditions Open and Closed to Oxygen : Implications for the Skaergaard Intrusion and Other Natural Systems. Journal of Petrology 37, 837–858.

Toplis, M.J. & Corgne, A. (2002). An experimental study of element partitioning between magnetite, clinopyroxene and iron-bearing silicate liquids with particular emphasis on vanadium. Contributions to Mineralogy and Petrology 144, 22–37.

Trumbull, R.B., Ashwal, L.D., Webb, S.J. & Veksler, I.V. (2015). Drilling through the largest magma chamber on Earth: Bushveld Igneous Complex Drilling Project (BICDP). Scientific Drilling 19, 33–37.

Turnock, A.C. & Eugster, H.P. (1962). Fe—Al Oxides: Phase Relationships below 1,000 C. Journal of Petrology 3(3), 533-565.

U.S. Geological Survey (2015). Mineral commodity summaries 2015, U.S. Geological Survey.

VanTongeren, J.A. (2018). Mixing and Unmixing in the Bushveld Complex Magma Chamber. In: Mondal, S.K. & Griffin, W.L. (Eds.), Processes and Ore Deposits of Ultramafic-Mafic Magmas through Space and Time, pp. 113-138.

VanTongeren, J.A., Mathez, E.A., Kelemen, P.B. (2010). A felsic end to Bushveld differentiation. Journal of Petrology 51, 1891–1912.

VanTongeren, J.A. Mathez, E.A. (2012). Large-scale liquid immiscibility at the top of the Bushveld Complex, South Africa. Geology 40, 491–494.

VanTongeren, J.A. & Mathez, E.A. (2013). Incoming magma composition and style of recharge below the pyroxenite marker, eastern Bushveld Complex, South Africa. Journal of Petrology 54, 1585–1605.

VanTongeren, J.A. & Mathez, E. (2014). Rare earth element abundances in apatite in the Bushveld Complex—A consequence of the trapped liquid shift effect: COMMENT. Geology.

Veksler, I.V., Kähn, J., Franz, G. & Dingwell, D.B. (2010). Interfacial tension between immiscible liquids in the system K_2O-FeO-Fe_2O_3-Al_2O_3-SiO_2 and implications for the kinetics of silicate melt unmixing. American Mineralogist 95, 1679–1685.

Veksler, I.V. & Charlier, B. (2015). Silicate Liquid Immiscibility in Layered Intrusions. In: Charlier, B., Namur, O., Latypov, R., Tegner, C. (Eds.), Layered Intrusions. Springer Netherlands pp. 229–258.

Vincent, E. A., Wright, J. B., Chevallier, R., & Mathieu, S. (1957). Heating experiments on some natural titaniferous magnetites. Mineralogical Magazine 31(239), 624-655.

von Gruenewaldt, G. (1971). A petrographical and mineralogical investigation of the rocks of the bushveld igneous complex in the tauteshoogte-roossenekal area of the eastern transvaal. PhD Thesis, University of Pretoria.

von Gruenewaldt, G. (1973). The Main and Upper Zones of the Bushveld Complex in the Roossenekal area, eastern Transvaal. Transactions of the Geological Society of South Africa 76, 207–227.

von Gruenewaldt, G. (1993). Ilmenite-apatite enrichments in the upper zone of the Bushveld Complex: a major titanium-rock phosphate resource. International Geology Review 35, 987–1000.

von Gruenewaldt, G., Klemm, D.D., Henckel, J. & Dehm, R.M. (1985). Exsolution features in titanomagnetites from massive magnetite layers and their host rocks of the Upper Zone, eastern Bushveld Complex. Economic Geology 80, 1049–1061.

Wadhwa, M. (2001). Redox State of Mars' Upper Mantle and Crust from Eu Anomalies in Shergottite Pyroxenes. Science 291, 1527–1530.

Wager, L.R. & Brown, G.M. (1968). Layered Igneous Rocks. Oliver and Boyd, London.

Wallmach, T., Hatton, C.J., De Waal, S.A., Gibson, R.L., 1995. Retrogressive hydration of calc-silicate xenoliths in the eastern Bushveld complex: evidence for late magmatic fluid movement. J. African Earth Sci. 21, 633–646.

Webb, S.J., Cawthorn, R.G., Nguuri, T. & James, D. (2004). Gravity modeling Bushveld complex connectivity supported by Southern African Seismic Experiment results. South African Journal of Geology 107, 207–218.

Wilkinson, J.F.G. (1986). Classification and Average Chemical Compositions of Common Basalts and Andesites. Journal of Petrology 27, 31–62.

Willemse, J. (1969). The vanadiferous magnetic iron ore of the Bushveld Igneous Complex. Economic Geology Monograph 4, 137–208.

Wilson, J.R. & Sorensen, H.S. (1996). The Fongen-Hyllingen Layered Intrusive Complex, Norway. Developments in Petrology 15, 303–329.

Yuan, Q., Namur, O., Fischer, L.A., Roberts, R.J., Lü, X. & Charlier, B. (2017). Pulses of plagioclase-laden magmas and stratigraphic evolution in the Upper Zone of the Bushveld Complex, South Africa. Journal of Petrology, 58(8), 1619-1643.

Zeh, A., Ovtcharova, M., Wilson, A.H. & Schaltegger, U. (2015). The Bushveld Complex was emplaced and cooled in less than one million years – results of zirconology, and geotectonic implications. Earth Planet. Sci. Lett. 418, 103–114.

Zhou, M.F., Robinson, P.T., Lesher, C.M., Keays, R.R., Zhang, C.J. & Malpas, J. (2005). Geochemistry, petrogenesis and metallogenesis of the Panzhihua gabbroic layered intrusion and associated Fe–Ti–V oxide deposits, Sichuan Province, SW China. Journal of Petrology, 46(11), 2253-2280.

Zhou, M.F., Arndt, N.T., Malpas, J., Wang, C.Y. & Kennedy, A. K. (2008). Two magma series and associated ore deposit types in the Permian Emeishan large igneous province, SW China. Lithos, 103(3), 352-368.

Zhu, Y., Chen, J., Xue, Y., Feng, W. & Jiang, J. (2017). Spinel and orthopyroxene exsolved from clinopyroxene in the Haladala pluton in the middle Tianshan (Xinjiang, China). Mineralogy and Petrology, 1-15.

Supplemental figure and tables
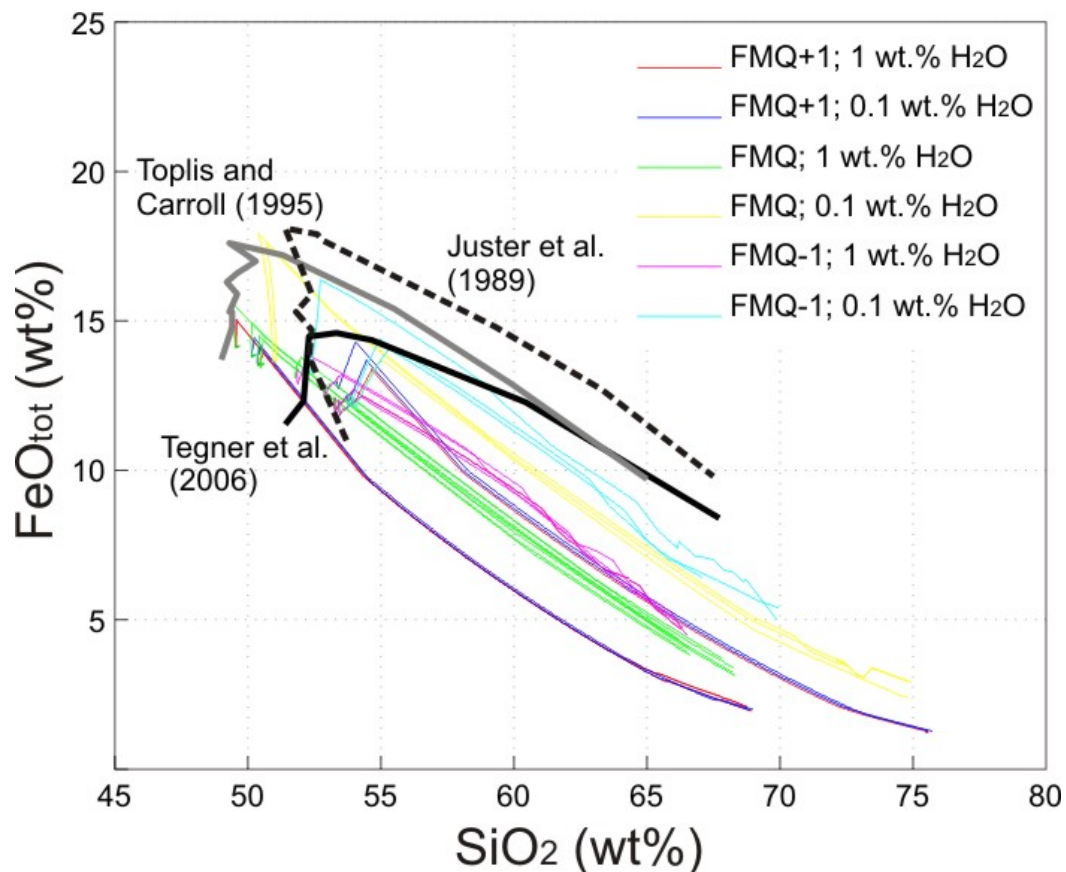
Supplemental Figure S1

Figure S1 FeO$_{tot}$ vs. SiO$_2$ (wt%) diagram showing potential liquid lines of descent (LLD) for the Upper and Upper Main Zone (UUMZ) of the Bushveld Complex. Colored lines represent results of MELTS calculations (Ghiorso and Sack, 1995) at three different oxygen fugacity conditions (FMQ+1, FMQ and FMQ-1 with FMQ being the fayalite-magnetite-quartz buffer). We used 8 starting compositions (see Supplemental Table S6 in the supplementary material) representing a mixture between the bulk composition of the UUMZ (VanTongeren et al., 2010) and 15 - 25 wt% of a rhyolite formation (Damwal, Kwaggasnek, Schrikkloof and Rashoop). Calculations were performed for initial H$_2$O contents of 0.1 and 1.0 wt%. We only present LLD in which orthopyroxene crystallizes as the first cumulus phase. For comparison, we plotted liquids of Tegner et al. (2006) calculated using a forward fractional crystallization model and experimental melts produced from ferrobasaltic starting compositions (Galapagos: Juster et al., 1989; Skaergaard: Toplis and Carroll, 1995). Figure from Fischer et al. (2016).

Supplemental Tables

S1   List of samples

S2   List of minerals used as reference for mineral mode determination

S3   Mineral modes obtained via MLA (from Yuan et al. 2017)

S4   Mineral compositions in samples BK1-1085 and BK1-1094 from Fischer et al. (2016)

S5   Compositions of melt inclusions in apatite from samples BK1-1085 and BK1-1094 from Fischer et al. (2017).

S6   Composition of parental magmas to the Upper Main and Upper Zones from Fischer et al. (2016).

S7   Experimental data set with mineral/melt partition coefficients from literature

S8   Magnetite major and trace element composition and 1σ standard deviation.

S9   Magnetite major and trace element composition and 1σ standard deviation.

Curriculum Vitae

■ Personal Details

Lennart Alexander Fischer
14.08.1988 in Würzburg, German citizenship

■ Work experience

12/2013 - today	**Research assistant** Institut für Mineralogie, Leibniz Universität Hannover, Germany
03/2015 - 02/2016	**University Associate** University of Tasmania, Australia ARC Centre of Excellence in Ore Deposits (CODES)
09/2009 - 11/2013	**Student assistant** Institut für Mineralogie, Leibniz Universität Hannover
04/2009 - 03/2010	**Student assistant** Institut für Geologie, Leibniz Universität Hannover

■ Education

12/2013 - today	**PhD student** Leibniz Universität Hannover, Germany Thesis: „The Upper Zone of the Bushveld Complex, South Africa: Parental Magma and Crystallization Processes"
10/2011 - 09/2013	**Master's studies in Earthscience with focus on Mineralogy/Geochemistry** Leibniz Universität Hannover Thesis: „Experimental study on hydrous partial melting of hydrothermally altered dolerite: Generation of felsic melts within fast-spreading oceanic crust"
09/2008 - 09/2011	**Bachelor's studies in Earhtscience** Leibniz Universität Hannover Thesis: „Experimental hydrous partial melting of gabbro: A new approach to enlarge melt pools by adding synthetic glass"
08/2001 - 05/2008	**Abitur** Gymnasium Horn, Bremen, Germany

List of publications

■ Journals (peer reviewed)

Yuan, Q., Namur, O., Fischer, L.A., Roberts, R.J., Lü, X., Charlier, B. (2017): Pulses of plagioclase-laden magmas and stratigraphic evolution in the Upper Zone of the Bushveld Complex, South Africa. *Journal of Petrology, 58(8), 1619-1643.*

Rossi, S., Petrelli, M., Gonzalez, D., Morgavi, D., Fischer, L.A., Vetere, F., Perugini, D. (2017): Exponential decay of concentration variance during magma mixing: robustness of a volcanic chronometer and implications for the homogenization of chemical heterogeneities in magmatic systems. *Lithos, 286, 396-407*

Erdmann, M., France, L., Fischer, L.A., Deloule, E., Koepke, J. (2017): Partitioning of trace elements during anatectic processes occurring at MOR magma chamber margins. Chemical Geology, *456, 43-57*

Burianek, M., Teck, M., Niekamp, C., Birkenstock, J., Spieß, I., Medenbach, O., Fischer, L.A., Wolff, P.E., Neumann, J., Fischer, R.X. (2016): Crystal growth, crystal structure, optical properties, and phase transition of BaCaBO3F. *Crystal Growth & Design, 16 (8), 4411-4420.*

Fischer, L.A., Erdmann, M., France, L., Wolff, P.E., Deloule, E., Zhang, C., Godard, M., Koepke, J. (2016): Trace element evidence for anatexis at oceanic magma chamber roofs and the role of partial melts for contamination of fresh MORB. *Lithos, 260, 1-8.*

Fischer, L.A. and Yuan, Q. (2016): Fe-Ti-V-(P) Resources in the Upper Zone of the Bushveld Complex, South Africa. *Papers and Proceedings of the Royal Society of Tasmania, 150 (1).*

Fischer, L.A., Wang, M., Charlier, B., Namur, O., Roberts, R.J., Veksler, I.V., Cawthorn, R.G. Holtz, F. (2016): Immiscible iron-and silica-rich liquids in the Upper Zone of the Bushveld Complex. *Earth and Planetary Science Letters, 443, 108-117.*

Erdmann, M., Fischer, L.A., France, L., Koepke, J. (2015): Anatexis at the roof of an oceanic magma chamber at IODP Site 1256 (equatorial Pacific): An Experimental Study. *Contributions to Mineralogy and Petrology, 169 (4), 1-28.*

Fischer, R.X., Tikhonova V., Birkenstock J., Fischer L.A., Herrmann K., Mengel K., Schneider H. (2015): Sillimullite, a mineral intermediate between mullite and sillimanite. *American Mineralogist, 100(7), 1493-1501.*

■ Conference abstracts (selection)

Fischer, L.A., Namur O., Horn, I., Holtz F., Charlier B. (2017): Vanadium distribution in the Upper Zone of the Bushveld Complex: Constrains on fO_2. GeoBremen, Bremen Germany

Fischer, L.A., Namur O., Wang, M., Holtz F., Charlier B. (2017): Silicate liquid immiscibility in the Upper Zone of the Bushveld Complex. SEG meeting, Beijing, China

Fischer, L.A., Charlier, B., Namur, O., Roberts, J., Holtz, F. (2016): Melt inclusions reveal immiscibility in the Upper Zone of the Bushveld Complex. *EMC meeting, Rimini, Italy*

Fischer, L.A., Charlier, B., Namur, O., Holtz, F. (2015): Formation of the largest platinum deposit on Earth - What we learn from micron-scale observations. *Biennial Conference of the Australian Association of von Humboldt Fellows, Hobart, TAS, Australia*

Fischer, L.A., Charlier, B., Namur, O., Roberts, J., Holtz, F. (2015): Immiscible iron- and silica-rich liquids in the Upper Zone of the Bushveld complex. *SEG Conference 2015, Hobart, TAS, Australia*

Fischer, L.A., Erdmann M., France L., Deloule E., Koepke J. (2013): Generation of felsic melts within fast-spreading oceanic crust: Experimental partial melting of hydrothermally altered sheeted dike. *AGU Fall Meeting 2013, San Francisco*

Fischer, L.A., Erdmann M., France L., Deloule E., Koepke J. (2013): Experimental study on hydrous partial melting of hydrothermally altered dolerite: Generation of felsic melts within fast-spreading oceanic crust. *DMG Joint Meeting, Tübingen*

Fischer, L.A., Brophy, J.G., Erdmann, M., Koepke, J. (2012): Experimental hydrous partial melting of gabbro: A new approach to enlarge melt pools by adding synthetic glass. *EMPG conference, Kiel*